Title
Device Physics and Recombination in Polymer:Fullerene Bulk-Heterojunction Solar Cells

Author
Hawks, Steven

Publication Date
2015

Peer reviewed|Thesis/dissertation

UNIVERSITY OF CALIFORNIA

Los Angeles

Device Physics and Recombination in Polymer:Fullerene Bulk-Heterojunction Solar Cells

A dissertation submitted in partial satisfaction

of the requirements for the degree

Doctor of Philosophy in Materials Science and Engineering

by

Steven Aaron Hawks

2015

Abstract of the Dissertation

Device Physics and Recombination in Polymer:Fullerene Bulk-Heterojunction Solar Cells

by

Steven Aaron Hawks
Doctor of Philosophy in Materials Science and Engineering
University of California, Los Angeles, 2015
Professor Sarah H. Tolbert, Chair

My thesis focuses on improving and understanding a relatively new type of solar cell materials system: polymer:fullerene bulk-heterojunction (BHJ) blends. These mixtures have drawn significant interest because they are made from low-cost organic molecules that can be cast from solution, which makes them a potential cheap alternative to traditional solar cell materials like silicon. The drawback, though, is that they are not as efficient at converting sunlight into electricity. My thesis focuses on this issue, and examines the loss processes holding back the efficiency in polymer:fullerene blends as well as investigates new processing methods for overcoming the efficiency limitations. The first chapter introduces the subject of solar cells, and polymer:fullerene solar cells in particular. The second chapter presents a case study on recombination in the high-performance PBDTTT polymer family, wherein we discovered that nongeminate recombination of an anti-Langevin origin was the dominant loss process that ultimately limited the cell efficiency. Electroluminescence measurements revealed that an electron back-transfer process was prevalent in active layers with insufficient $PC_{71}BM$ content. This work ultimately made strong headway in understanding what factors limited the relatively unexplored but highly efficient PBDTTT family of polymers. In the next chapter, I further explore the recombination mechanisms in polymer:fullerene BHJs by examining the dark diode ideality factor as a function of temperature in several polymer:fullerene materials systems. By re-deriving the diode law for a polymer:fullerene device with Shockley-Read-Hall recombination, we were able to confirm that trap-assisted recombination through an exponential band-tail of localized states is the dominant recombination process in many polymer:fullerene active layers. In the third chapter, I present a generalized theoretical framework for understanding current transients

in planar semiconductor devices, like those discussed above. My analysis reveals that the apparent free-carrier concentration obtained via the usual integral approach is altered by a non-trivial factor of two, sometimes leading to misinterpretations of the charge densities and overall device physics. This new perspective could have far-reaching effects on semiconductor research and technology. Finally, in the last two chapters, I discuss the device physics associated with a relatively novel method for fabricating nanoscale polymer:fullerene BHJs: solution sequential processing (SqP). In particular, I compare recombination in SqP vs. traditionally processed blend-cast devices, and demonstrate that SqP is a more scalable method for making BHJ solar cells. In the final chapter, I examine an unexpected discovery that occurred while working on the content in Chapter 5. Specifically, Chapter 6 examines electrode metal penetration in the SqP quasi-bilayer active layer architecture. Therein, we unexpectedly found that evaporated metal can readily penetrate into fullerene-rich layers, up to $\sim$70 nm or more. The details and consequences of this surprising occurrence are discussed in detail.

The dissertation of Steven Aaron Hawks is approved.

Qibing Pei

Benjamin J. Schwartz

Sarah H. Tolbert, Committee Chair

University of California, Los Angeles

2015

To my parents Aaron and Gina,

the most remarkable people that I know.

TABLE OF CONTENTS

LIST OF FIGURES

List of Tables

ACKNOWLEDGMENTS

There are a lot of people to thank. I would like to start with my family: my mom, dad, sister, and all the grandparents, who put so much love and happiness in my life growing up. They were always there for me every step of the way, including graduate school. In particular, I cannot thank my parents enough for putting me in the position to be where I am today. They are truly the best; I am very blessed. I would also like to thank Emily, of course, who stuck with me throughout graduate school and even came down to LA—a four letter word—so that we could be together.

In terms of graduate studies, I would like to thank Prof. Yang Yang for giving me the chance to work in his lab and learn what it took to do high-level research. Ankit, Dr. Zhu, Dr. You, Renee, Dr. He, Wenbing!, Eric, Kitty, and all the rest of the YY club, thanks for being great friends and coworkers. Special thanks to the ICL people (Flo, Dan, Stoichko, Safa,...), who were all terrific and instrumental in helping me grow as a researcher. Of that group, Thomas deserves special thanks for being a true mentor and having an infinite patience and willingness to help noobs like myself.

Special thanks to Bob Street at PARC. A man of great patience, incredible depth of knowledge, and uncanny intuition. A venerable master. It was a pleasure working with you, and Chapter 3 owes largely to you.

Now for the Schwartz lab (may the Schwartz be with you). First and foremost a special thanks to the man himself, Big Ben. I've learned so much from you and had a blast doing it. In science and on the bike, you're certainly no slouch. On the subject of Bens, thanks to Little Ben for being a great office mate and helping me become more of an aficionado on fine cinema (like Dredd). Thanks to Jordan and Master Guang, two of the best coworkers anyone could ever ask for. The young pups: Matt, Taylor, T-sizzle, Voss...you're all ok too. ;) Lastly, of course, thanks to Sarah for being my "on paper" advisor but also an outstanding source of advice on all subjects.

Some elements of **Chapter 1** are partially adapted from S. Hawks and E. Robertson, "Fabrication and Characterization of P3HT:PCBM Bulk-Heterojunction "Plastic" Solar Cells," California Polytechnic State University Senior Project, 2010. I wrote the sections adapted in this thesis and Emily Robertson helped edit them. The project advisors were: Kathy Chen and Robert Echols.

Chapter 2 and Appendix B are versions of Reference 150, reproduced with permission from John Wiley and Sons under license number 3683720043722. This chapter was supported in part by the NSF IGERT: Materials Creation Training Program (MCTP)-DGE-0654431 and NSF CHE-1112569, and I would like to thank Dr. Chad Risko for useful discussions and Letian Dou for aid with Figure 1. I wrote the paper, initiated the project, and fabricated/measured all the devices. Florent Deledalle measured and evaluated the transient data. Jizhong Yao and Dylan G. Rebois measured the EL. Thomas Kirchartz played a major intellectual role in formulating the paper's conclusions and interpreting the results. The PIs and/or project directors were Gang Li, Jenny Nelson, Yang Yang, Thomas Kirchartz, and James R. Durrant.

Chapter 3 is a version of Reference 205, reproduced with permission from the AIP family of journals. This chapter was supported in part by the NSF IGERT: Materials Creation Training Program (MCTP)-DGE-0654431 and the Molecularly Engineered Energy Materials (MEEM), an Energy Frontier Research Center funded by the US Department of Energy, Office of Science, Office of Basic Energy Sciences under Award No. DE-SC0001342. I performed all the measurements and played a significant role in writing the manuscript as well as developing its conclusions. Robert Street initiated the project, derived the model, and wrote most of the manuscript. The PIs and/or project directors were: Gang Li, Yang Yang, and Robert A. Street.

Chapter 4 and Appendix C are versions of Reference 358, reproduced with permission from the APS family of journals. This chapter was supported in part by the Molecularly Engineered Energy Materials (MEEM), an Energy Frontier Research Center funded by the U.S. Department of Energy, Office of Science, Office of Basic Energy Sciences under Grant No. DE-SC0001342 and from the National Science Foundation Grant No. CHE-1112569. I wrote the manuscript and derived all equations. Benjamin Y. Finck performed the D-D simulations. The PI was Benjamin J. Schwartz.

Chapter 5 and Appendix D are versions of Reference 201, reproduced with permission from the ACS family of journals. This chapter was supported in part by the Molecularly Engineered Energy Materials (MEEM), an Energy Frontier Research Center funded by the US Department of Energy, Office of Science, Office of Basic Energy Sciences under Award Number DE-SC0001342 and by the National Science foundation under grant NSF CHE-1112569. The X-ray diffraction studies

presented in this manuscript were carried out at the Stanford Synchrotron Radiation Lightsource. Use of the Stanford Synchrotron Radiation Lightsource, SLAC National Accelerator Laboratory, is supported by the U.S. Department of Energy, Office of Science, Office of Basic Energy Sciences under Contract No. DE-AC02-76SF00515. The XPS instrument used in this work was obtained with support from the NSF, award number 0840531. I came up with the redissolving method, performed most of the measurements, made all the devices except for the large area cells, and wrote the manuscript. Guangye Zhang and Jordan C. Aguirre performed some of the electronic characterization of the devices. Jordan C. Aguirre made and characterized the large-area cells. Laura Schelhas performed the XPS experiments. Robert Thompson did the EF-TEM tomography. Rachel Huber and Amy Ferreira took all of the grazing incident wide angle x-ray spectroscopy on the films. The PIs and/or project directors were: Andrew A. Herzing, Sarah H. Tolbert, and Benjamin J. Schwartz.

Chapter 6 and Appendix E are versions of work submitted to *ACS Applied Materials and Interfaces*, reproduced with permission from the ACS family of journals. I would like to acknowledge Dr. Jia Ming Chen for ample administrative assistance, Dr. Liane Slaughter for insightful discussions, Noah Bodzin for making the X-TEM samples via FIB, and Amy Ferreira for preparation of the Pt-based samples. This chapter was supported in part by the Molecularly Engineered Energy Materials (MEEM), an Energy Frontier Research Center funded by the US Department of Energy, Office of Science, Office of Basic Energy Sciences under Award Number DE-SC0001342 and by the National Science foundation under grant NSF CHE-1112569. The XPS instrument used in this work was obtained with support from the NSF, award number 0840531. I wrote the article and performed part of the measurements. Guangye Zhang performed most of the measurements and helped write the article. Chilan Ngo did the TEM work, Laura T. Schelhas did the XPS work, D. Tyler Scholes helped with TEM sample prep, Hyeyeon Kang performed SEM analysis, and Jordan C. Aguirre helped fabricate some of the doping samples. The PIs were: Benjamin J. Schwartz and Sarah H. Tolbert.

VITA

2010–2012	MS Materials Science and Engineering Engineering, University of California Los Angeles (UCLA), Los Angeles
2005–2010	BS Materials Engineering, California Polytechnic State University, San Luis Obispo, Magna Cum Laude, with Honors
2005–2010	BA Physics, California Polytechnic State University, San Luis Obispo, Magna Cum Laude, with Honors
2015	French American Doctoral Exchange Seminar (FADEx) Laureate
2013	CLAD Certified LabVIEW programmer
2011–2013	UCLA Materials Creation Training Program (MCTP) Fellowship Trainee
2010–2011	UCLA University Fellowship Recipient
2008, 2009	Cal Poly Honors Program NSF Scholarship recipient
2008	TMS SMD Scholarship (SMD Scholar)
2008	ASM-SAMPE Scholarship recipient
2008	ASM-LA Chapter Scholarship recipient
2008	Gregory Stines Memorial Scholarship

Publications and Presentations

Hawks, S. A.; Finck, B. Y.; Schwartz, B. J. Theory of Current Transients in Planar Semiconductor Devices: Insights and Applications to Organic Solar Cells. *Phys. Rev. Appl.* **2015**, *3*, 044014.

Aguirre, J. C.; **Hawks, S. A.**; Ferreira, A. S.; Yee, P.; Subramaniyan, S.; Jenekhe, S. A.; Tolbert, S.H.; Schwartz, B. J. Sequential Processing for Organic Photovoltaics: Design Rules for Morphology Control by Tailored Semi-Orthogonal Solvent Blends. *Adv. Energy Mater.* **2015**, 1402020.

Street, R. A.; **Hawks, S. A.**; Khlyabich, P. P.; Li, G.; Schwartz, B. J.; Thompson, B. C.; Yang, Y. Electronic Structure and Transition Energies in Polymer–Fullerene Bulk Heterojunctions. *J. Phys. Chem. C* **2014**, *118*, 21873–21883.

Hawks, S. A.; Aguirre, J. C.; Schelhas, L. T.; Thompson, R. J.; Huber, R. C.; Ferreira, A. S.; Zhang, G.; Herzing, A. A.; Tolbert, S. H.; Schwartz, B. J. Comparing Matched Polymer:Fullerene Solar Cells Made by Solution-Sequential Processing and Traditional Blend Casting: Nanoscale Structure and Device Performance. *J. Phys. Chem. C* **2014**, *118*, 17413–17425.

Hawks, S. A.; Li, G.; Yang, Y.; Street, R. A. Band Tail Recombination in Polymer:fullerene Organic Solar Cells. *J. Appl. Phys.* **2014**, *116*, 074503.

Hawks, S. A.; Deledalle, F.; Yao, J.; Rebois, D. G.; Li, G.; Nelson, J.; Yang, Y.; Kirchartz, T.; Durrant, J. R. Relating Recombination, Density of States, and Device Performance in an Efficient Polymer:Fullerene Organic Solar Cell Blend. *Adv. Energy Mater.* **2013**, *3*, 1201–1209.

Chen, C.-C.; Dou, L.; Zhu, R.; Chung, C.-H.; Song, T.-B.; Zheng, Y. B.; **Hawks, S. A.**; Li, G.; Weiss, P. S.; Yang, Y. Visibly Transparent Polymer Solar Cells Produced by Solution Processing. *ACS Nano* **2012**, *6*, 7185–7190.

You, J.; Chen, C.-C.; Dou, L.; Murase, S.; Duan, H.-S.; **Hawks, S. A.**; Xu, T.; Son, H. J.; Yu, L.; Li, G.; *et al.* Metal Oxide Nanoparticles as an Electron-Transport Layer in High-Performance and Stable Inverted Polymer Solar Cells. *Adv. Mater.* **2012**, *24*, 5267–5272.

Mitchell Hopper, E.; Peng, H.; **Hawks, S. A.**; Freeman, A. J.; Mason, T. O. Defect Mechanisms in the $In_2O_3(ZnO)_k$ System ($k = 3,5,7,9$). *J. Appl. Phys.* **2012**, *112*, 093712.

Kirchartz, T.; Gong, W.; **Hawks, S. A.**; Agostinelli, T.; Mackenzie, R. C. I.; Yang, Y.; Nelson, J. Sensitivity of the Mott-Schottky Analysis in Organic Solar Cells. *J. Phys. Chem. C* **2012**, *116*, 7672–7680.

Hawks, S. A.; Li, G.; Yang, Y.; Street, R.A. Band-Tail Recombination and the Ideality Factor in Polymer-Fullerene Bulk Heterojunction Solar Cells. *MRS Spring Meeting*, Oral Presentation, D1.02, 2015.

Hawks, S. A.; Li, G.; Yang, Y.; Street, R.A. Understanding Recombination in Polymer:Fullerene Organic Solar Cells Through the Dark Ideality Factor. *French American Doctoral Exchange Seminar (FADEx)*, Oral Presentation, 2015.

Hawks, S. A.; Zhang, G.; Schelhas, L.T.; Kang, H.; Aguirre, J.C.; Tolbert, S.H.; Schwartz, B.J. Extensive Penetration of Evaporated Metal into Fullerene Layers: Implications for Organic Solar Cells and Possibilities for Novel Device Structures. *MRS Spring Meeting*, Poster D10.39, 2015.

Hawks, S. A.; Aguirre, J.C.; Schelhas, L.T.; Thompson, R.; Huber, R.; Ferreira, A.; Zhang, G.; Herzing, A.A.; Tolbert, S.H.; Schwartz, B.J. Comparing Matched Polymer:Fullerene Solar Cells Made by Solution-Sequential Processing and Traditional Blend Casting: Nanoscale Structure and Device Performance. *The 6th International Conference on Excited State Processes in Electronic and Bio Nanomaterials (ESP2014)*, Poster, 2014.

Hawks, S. A.; Deledalle, F.; Kirchartz, T.; Li, G.; Durrant, J.; Yang Y. The Influence of Blend Composition on Density of States and Recombination in an Efficient Polymer:Fullerene Organic Solar Cell System. *MRS Spring Meeting*, Poster B6.114, 2013.

Hawks, S. A.; Yang Y. Analytic Considerations for Studying Bipolar Transport in Polymer:Fullerene Organic Photovoltaic Devices with the CELIV Technique. *International Conference on Science and Technology of Synthetic Metals*, Poster PIII-37, 2012.

CHAPTER 1

Introduction

Solar energy harvested directly through photovoltaic (PV) modules could easily form the backbone of our national energy supply, as just ∼10,000 square miles of 10% efficient solar cells would fulfill all of our energy needs.[1] Moreover, at any given moment, approximately 580 TW of readily accessible solar power is available for use worldwide, which dwarfs the projected 16.9 TW of instantaneous global power needed by 2030.[2] Unfortunately, though, serious challenges obstruct the widespread commercialization of PV technologies, making it necessary for research in applied science to drive down costs, improve efficiencies, and increase the stability of photoactive materials/devices. At present, the main problem is that PV cells are not economically competitive with other forms of energy, largely due to the need for expensive substrates, energy-intensive processing steps, and non-earth abundant materials.[3]

Organic solar cells, on the other hand, are a relatively new class of photovoltaics that present a possible way around the processing challenges that are inherent to traditional inorganic devices. In particular, polymer:fullerene bulk-heterojunction (BHJ) organic photovoltaics (OPVs) have received substantial attention as low cost, light weight, and mechanically flexible solar cells.[4] These thin-film OPVs are cast from blended solutions of conjugated polymers and fullerene derivatives,[5] and because they dissolve in solution, the possible production capacities are immense, resulting in significantly lower manufacturing costs when compared to their traditional inorganic counterparts.[6] Thus, polymer:fullerene BHJ OPVs could be the low cost, light weight, and mechanically flexible solar cells that help free society from the grip of fossil fuels, allowing for global climate stabilization due to reduced CO_2 emissions, less tenuous foreign relations, and an indefinite sustainable energy supply.

1.1 Extracting Power from a Solar Cell

A solar cell converts light directly into electricity. The power-conversion efficiency (PCE) of a such a device is calculated by dividing the maximum electrical power-density that it produces by the incident light intensity. For a diode, this mathematically corresponds to

$$\eta = \frac{|JV|_{max}}{I_{light}} = \frac{J_{SC}V_{OC}FF}{I_{light}} \tag{1.1}$$

where η is the power-conversion efficiency, $|JV|_{max}$ is the maximum output power-density of the solar cell in W/m^2, I_{light} is the incident light intensity in W/m^2, J_{SC} is the short-circuit current density in A/m^2 (the maximum amount of photocurrent that the cell can produce on its own), V_{OC} is the open-circuit voltage in V (the maximum amount of photovoltage that the cell can produce on its own), and FF is the fill factor from

$$FF = \frac{|JV|_{max}}{J_{SC}V_{OC}} \tag{1.2}$$

See Figure 1.1a for a visualization of these terms. For standardized solar cell testing, the air mass 1.5 global (AM 1.5G, Figure 1.1b) solar spectrum is substituted (I_{light} = 1000 W/m^2) into Eqn. (1.1) to give

$$\eta_{AM1.5G} = J_{SC}V_{OC}FF \tag{1.3}$$

where $\eta_{AM1.5G}$ is the power-conversion efficiency under the AM 1.5G solar spectrum in percent, J_{SC} is the short circuit-current density in mA/cm^2, and a dimensional mW-cm^2 is implied on the right hand side.

Another way of obtaining the device's J_{SC} is by integrating the external quantum efficiency (EQE) over the AM 1.5G photon spectrum, or

$$J_{SC,EQE} = q\int_{280}^{4000} EQE\,(\lambda)\,\phi_{AM\ 1.5G}\,(\lambda)\,d\lambda \tag{1.4}$$

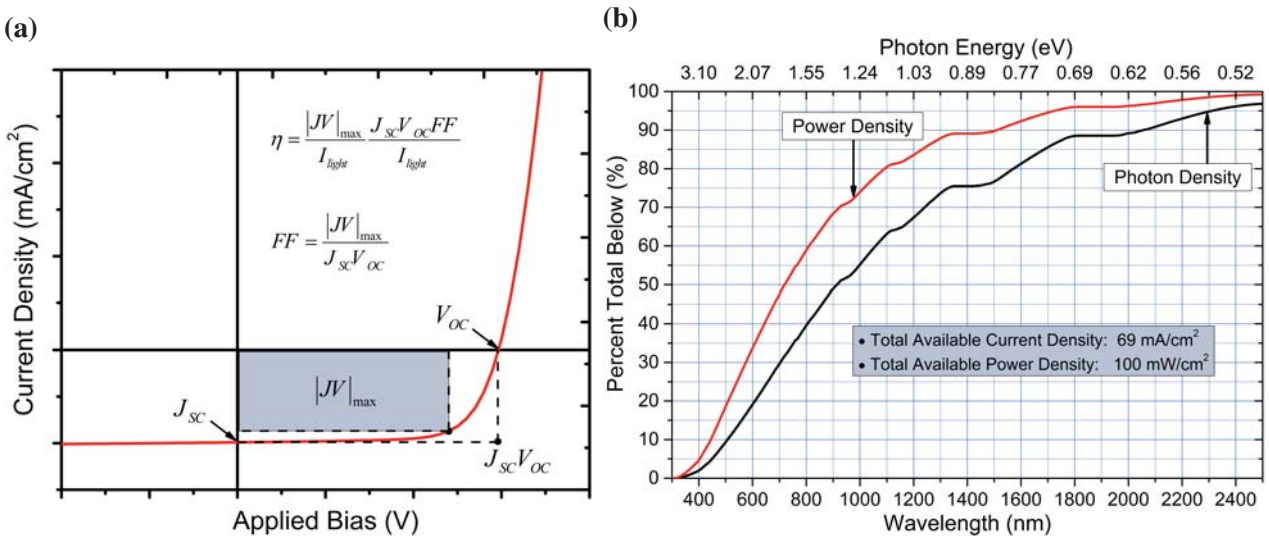

Figure 1.1: (a) A schematic *J-V* curve of an illuminated solar cell illustrating the parameters described in Eqns. (1.1)-(1.3). (b) The AM 1.5G solar spectrum in integrated form. The ideal absorption onsets according to Shockley-Queisser theory are between 1.1-1.44 eV as shown in Figure 1.2.

where $J_{SC,EQE}$ is the predicted short-circuit current density under AM 1.5G illumination, λ is the wavelength of light in nm, $\phi_{AM\ 1.5G}$ is the AM 1.5G photon flux spectrum in $cm^{-2}\,s^{-1}\,nm^{-1}$, q is the fundamental unit of charge in coulombs, and $EQE(\lambda)$ is the device's external quantum efficiency as a function of wavelength, which is defined as a ratio of quanta: (# of electrons of photocurrent)/(# of incident photons). For testing purposes, it is important to check if the $J_{SC,EQE}$ and the J_{SC} measured under simulated AM 1.5G illumination conditions match reasonably well and that the light intensity conditions are reasonable in the EQE experiment.[7,8] For a detailed standard operating procedure of the Schwartz lab EQE setup that I built, see Appendix A.

The ideal *J-V* curve parameters for a solar cell illuminated by the AM 1.5G solar spectrum can be calculated from a general standpoint via detailed balance theory.[9] This was performed initially in the seminal work of Shockley and Queisser (Figure 1.2),[10] establishing the thermodynamic limit of photovoltaic energy conversion for a single junction solar cell. The Shockley-Queisser approach assumes a step function absorption profile that turns on at the energy gap of the semiconductor and is unity (total absorption) for photon energies above the band gap. Organic solar cells deviate strongly from this limit primarily due to non-ideal recombination,[11,12] imperfect light absorption,[13] and the need to dissociate excitons (strongly bound electron-hole pairs).[14] The focus of this thesis will be primarily in the former category of non-ideal recombination.

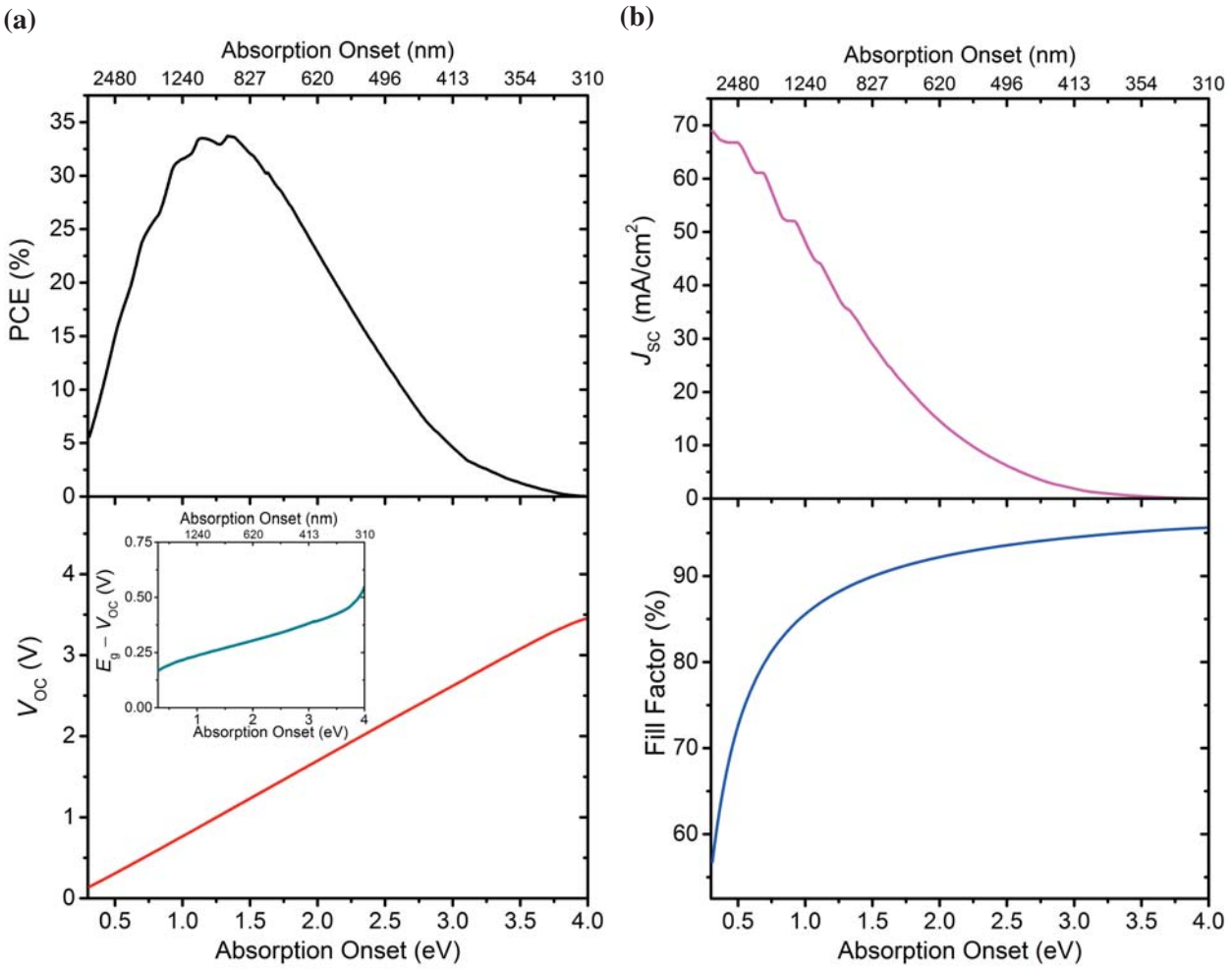

Figure 1.2: (a) The ideal PCE and open-circuit voltage parameters for a solar cell illuminated by the AM 1.5G solar spectrum calculated via the Shockley-Queisser approach with a perfect back reflector. The inset of the lower panel is the difference between the semiconductor absorption onset (i.e., energy gap) and the ideal open-circuit voltage. (b) The ideal short-circuit current density and fill factor parameters for a solar cell illuminated by the AM 1.5G solar spectrum calculated by the Shockley-Queisser approach with a perfect back reflector.

1.2 Introduction to Polymer:Fullerene Organic Photovoltaics

To execute the photovoltaic process, bulk-heterojunction OPVs primarily utilize two classes of materials: semiconducting polymers and fullerene derivatives. Semiconducting polymers are distinguished from normal polymers by their π-conjugated carbon backbone. That is, they have alternating single and double carbon-carbon bonds along their main chain. This distinctive bonding structure gives rise to unique electrical properties because π-orbital electrons in the double bonds delocalize along the polymer chain.[15] Another characteristic of conjugated polymers is strong interchain Van der Waals forces through the π-orbitals. This is not surprising, considering, for instance, that the same carbon-carbon interaction holds individual sheets of graphene together in graphite. As a consequence, conjugated polymers tend to aggregate in a chain-on-top-of-chain orientation, referred to as π-π stacking. In terms of electrical properties, π-π stacking lowers the electronic band gap and increases carrier mobility due to interchain π-orbital overlap. Unfortunately, though, this interaction is so strong that it inhibits solubility. Thus, in order to make conjugated polymers soluble, attachment of insulating side groups to the conjugated backbone is often required.[16] For similar reasons, spherical fullerene (C_{60}) molecules must be functionalized with alkyl and/or aromatic groups to afford solubility. Fullerene derivatives are used in conjunction with semiconducting polymers in OPVs because of their large electron affinity, which is necessary to create at type II heterojunction (Figure 1.3b) for splitting excitons, and their satisfactory charge-transport properties.

The mechanisms by which this dual-material system converts light energy into electrical energy are strikingly different than those employed by traditional inorganic cells. A silicon solar cell, for instance, makes use of a homojunction between *n* and *p* doped regions to separate photogenerated free charge, whereas OPVs must exploit an interface between two dissimilar semiconductors (heterojunction) in order to separate excitons into free carriers (Figure 1.3b; see photogeneration section below). To create these interfaces, one can blend a semiconducting polymer ('*p*-type' electron *donor* material) and functionalized fullerene ('*n*-type' electron *acceptor* material) in solution, and then cast them into a thin film.[17] The blending process intimately mixes each component, resulting in a cast film with incredibly high heterojunction area, hence 'bulk' heterojunction (Figure 1.3a). To make an OPV device, the polymer-fullerene photoactive layer is sandwiched between electrodes

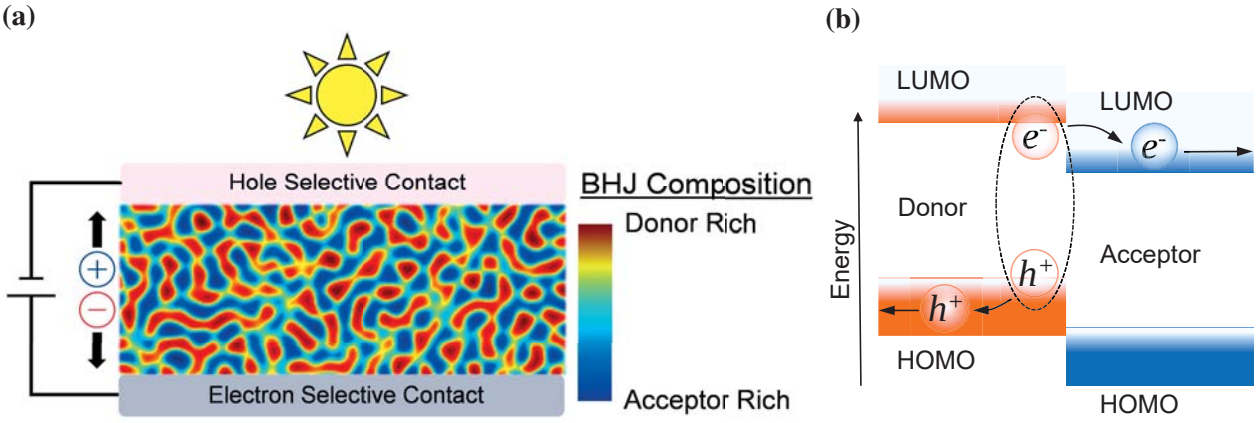

Figure 1.3: (a) An illustration of the simplest possible bulk-heterojunction solar cell. The active layer is usually ∼100 nm thick, though highly efficient bulk-heterojunction devices have been made with an active layer as thick as 1 μm.[19] For simplicity, we omit functional layers in-between the active layer and electrode(s). (b) Schematic process of free carrier photogeneration in the BHJ as described in the photogeneration section below.

with different work functions (Figure 1.3a), often with buffer layers in-between for improved performance.[18]

Donor:acceptor bulk-heterojunction blends, as schematically illustrated above, have yielded solar cell single-junction efficiencies above 7% for numerous different polymer:fullerene combinations,[19–21] and are even now reaching above 10% in certain cases.[22]

1.2.1 P3HT:PCBM—The Archetypal Bulk-Heterojunction System

What the *p-n* junction silicon solar cell is to inorganic photovoltaics, P3HT:PCBM bulk-heterojunction solar cells are to polymer:fullerene organic photovoltaics.[23] Figure 5 shows the chemical structure of these "workhorse" OPV materials. Many investigators have reported power conversion efficiencies over 4% with P3HT:PCBM-based devices.[24] This materials combination makes an excellent bulk-heterojunction active layer for several reasons: P3HT efficiently absorbs light out to 650 nm, even in thin (∼100-220 nm) active layers, excitons can efficiently dissociate at the P3HT:PCBM interface due a large LUMO-LUMO offset, the P3HT:PCBM blends generate a reasonable ∼0.6 V open-circuit voltage, the active layer morphology can be optimized through processing treatments such as solvent and thermal annealing, and high-quality P3HT and PCBM materials are available commercially at reasonable prices.[6] When mixed with 'good' solvents

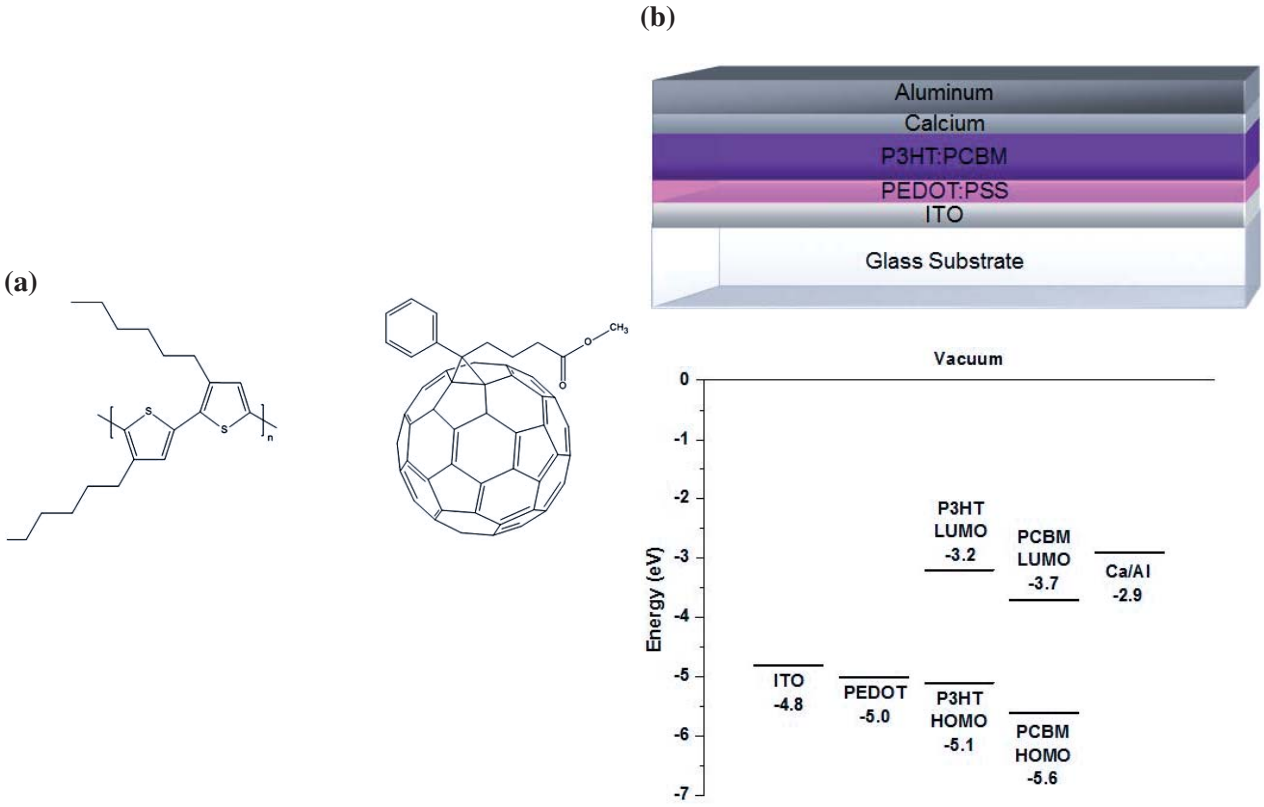

Figure 1.4: The chemical structure of regioregular P3HT (left) and PCBM (right). The percent regioregularity in a polymer refers to the fraction of mer units attached in the head-to-tail orientation. If the entire P3HT polymer chain was oriented like in (a), then it would be 100% regioregular. (b) The 'standard' polymer:fullerene BHJ OPV device structure Glass/ITO/PEDOT/Active-Layer/Ca/Al with its corresponding energy level diagram for the case of P3HT:PCBM being the active layer.

like chlorobenzene, dichlorobenzene, or cholorform, P3HT:PCBM active layers can be cast with domain sizes on the sub 5 nm scale.[25,26] Such small phase regions result in excellent exciton quenching efficiencies; however, highly disordered extraction pathways prevent free charge from escaping the device. Luckily, a short (5-10 min) low temperature (100-150°C) anneal and/or a slow active-layer drying process induces sufficient component demixing and individual phase ordering, giving drastically better electrical properties. The act of solvent/thermal annealing of as-cast P3HT:PCBM results in larger carrier mobility, increased charge-transfer state dissociation efficiency, slower recombination, and improved contact with the top electrode.[27–34] These enhanced properties are mostly a result of more-ordered individual phases, and together they translate into drastically increased device performance, often by more than a factor of two.[35]

The anode and cathode typically used to sandwich this polymer blend are indium-tin oxide (ITO) and calcium/aluminum, respectively. Also, a poly(3,4-ethylenedioxythiophene):poly(styrene-sulfonate) (PEDOT:PSS) buffer layer inserted between the ITO anode and active layer further improves device performance. The approximate energy-level diagram and device structure of an ITO (∼150 nm)/PEDOT (∼30-40 nm)/PCBM:P3HT (∼80-220 nm)/Ca (∼10 nm)/Al (∼50-100 nm) OPV device are presented in Figure 1.4b. The PEDOT:PSS (PEDOT) buffer layer increases device performance because it improves hole extraction due to its higher work function relative to ITO, it increases the smoothness of the electrode/active-layer contact, and it increases the open-circuit voltage by forming a better ohmic contact.[36–38] Examples of exemplary solar cell performance in this device structure are shown in Figure 1.5. It should also be noted that transition metal oxides also make excellent buffer layers for polymer:fullerene BHJ OPVs, especially in the 'inverted' device structure.[39] These inverted structures have a built-in potential that runs opposite to that in a PEDOT/Ca/Al device shown in Figure 1.4b and can have favorable stability and light management properties.[40–46]

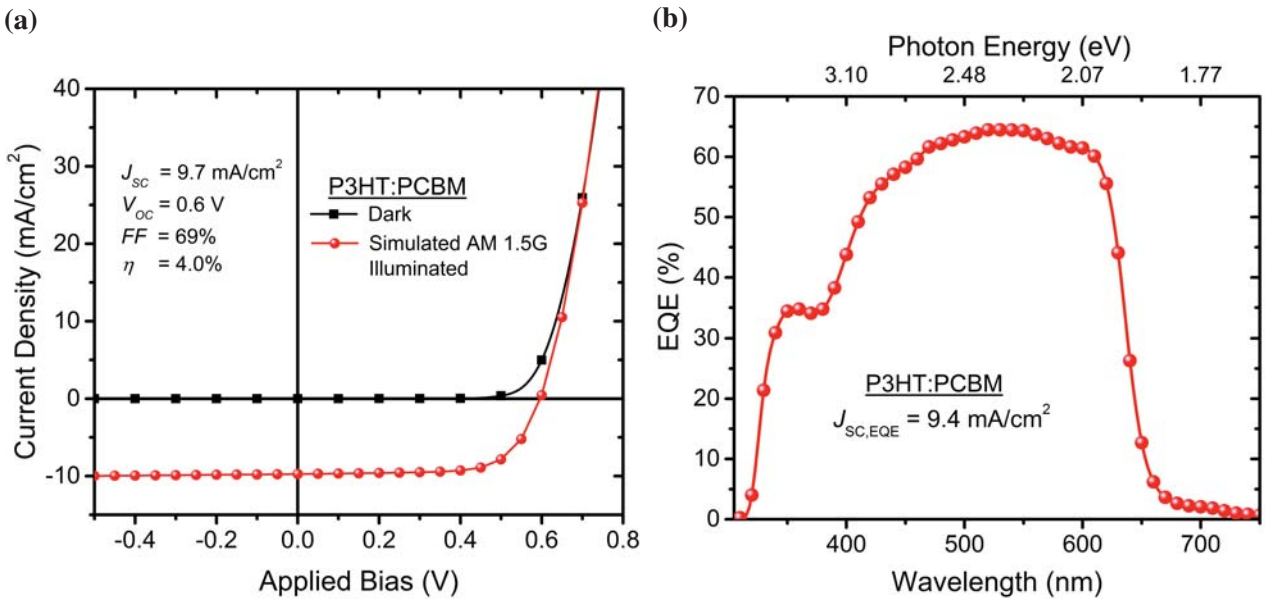

Figure 1.5: (a) Example *J-V* curves for the P3HT:PCBM device shown in Figure 1.4 with an active layer thickness of 220 nm. (b) The corresponding EQE of the P3HT:PCBM device shown in (a).

1.3 Device Physics of Polymer:Fullerene OPVs

The essential processes occurring within an operating polymer:fullerene BHJ OPV are schematically summarized in Figure 1.6. First, the active layer must absorb as many of the incident AM 1.5G solar photons as possible, and the resulting excitons that are generated from these absorption events must be efficiently dissociated into free carriers. Below I discuss in detail what it takes to dissociate excitons into free carriers in these conjugated organic systems and why the BHJ morphology (Figure 1.3a) is critical to realizing this process. Furthermore, I discuss why just simple light absorption and light management within these devices is also highly non-trivial due to interference effects. Figure 1.6 also shows the two fundamental electrical processes, transport and recombination, that come together to ultimately determine the electronic quality of the device. I discuss how these processes play out in a typical polymer:fullerene BHJ OPV device band diagram.

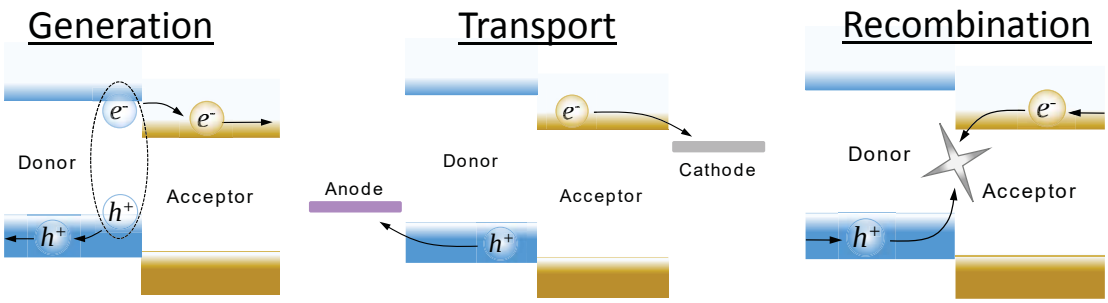

Figure 1.6: The essential processes in polymer:fullerene BHJ OPVs. Generation by incident photons must yield free carriers, transport to the contacts must be efficient, and non-ideal recombination processes must be suppressed.

1.3.1 Photogeneration in Organic Semiconductors

When illuminated, a sequence of events must occur within an OPV to convert incident light into electrical energy. First, of course, photons must be absorbed by the semiconducting polymer and/or fullerene derivative, which is primarily dictated by each materials optical band gap, molecular density of states, and degree of crystallinity.[47] Both materials contribute to absorption and photocurrent, typically with the fullerene dominating in the ultraviolet and the polymer dominating in the visible. When a photon of sufficient energy is absorbed in the polymer, an electron in its highest occupied molecular orbital (HOMO) is excited across the band gap to the lowest unoccupied molecular orbital (LUMO) (Figure 1.3b). These absorbed photons in the polymer generate excitons, as opposed to free electrons and holes like that created in most crystalline inorganic semiconductors. Tightly bound excitons occur in organic molecules because of strong reorganization energies that confine electron-hole pairs to their respective molecule and because of low relative dielectric constants ($\varepsilon_r \approx$ 2-4) that fail to screen the Coulomb attraction. These properties of disordered conjugated-polymer systems make room-temperature thermal energy insufficient to dissociate electron-hole pairs.[48] For π-conjugated polymers, the energy required to dissociate excitions is typically on the order of 0.3 eV.[49,50] In order to harvest their energy, excitons must be dissociated into free charge carriers. Therefore, a dissociation mechanism is required that occurs on a timescale much shorter than exciton recombination. Conveniently, if an exciton encounters a donor:acceptor heterojunction, it will partially disassociate by ultrafast (femtosecond) electron transfer from the LUMO of the polymer to the LUMO of the fullerene, as shown schematically in Figure 1.3b.[51,52] In pristine semiconducting

polymers, excitons can only diffuse approximately 10 nm before decaying.[53] Hence, if an exciton in the polymer cannot 'find' a heterojunction within ∼10 nm, it will decay and its energy will be lost with respect to harvesting. This property of semiconducting polymers makes the relative domain sizes of each component and their respective purity in the bulk heterojunction a critical performance parameter. The ideal donor:acceptor blend would intimately mix in solution and, upon casting, spontaneously demix into separate phase domains small enough to efficiently dissociate excitons while maintaining excellent charge-transport characteristics (Figure 1.6).

1.3.2 Absorption and Light Management

Light absorption in polymer:fullerene BHJ OPV thin-film systems is often poorly described by the simple Beer-Lambert law because the layers involved are typically thin (∼100 nm) and smooth, making wave optics necessary to describe the internal optical electric fields. The classic formalism to optically describe 1-D stratified media is the so-called transfer matrix method.[54–68] The transfer matrix approach takes into account the infinite number of reflections between all layer interfaces in the system, treating each interface as perfectly coherent (i.e., not rough/scattering) Fresnel reflector. These reflections from all the layer interfaces within the device (e.g., Figure 1.4b) cause interference effects that can dramatically alter the absorption characteristics of the active layer.[46,69–74]

Figure 1.7a gives an example of how this interference manifests in a typical regular (ITO 150 nm/PEDOT 35 nm/PCBM:P3HT variable/Ca 10 nm/Al 80 nm) and inverted (ITO 150 nm/ZnO 35 nm/PCBM:P3HT variable/MoO_3 15 nm/Ag 80 nm) P3HT:PCBM device. Notice that the maximum possible J_{SC} due to absorbed light does not increase in a monotonic exponential way as expected from Beer's law. Instead, there are certain active-layer thickness ranges where thicker layers (more material) actually results in *less* net absorption. Where the peaks and valleys of Figure 1.7a occur also depend strongly on the other layers within the device, as exemplified in Figure 1.7a by the difference in the maximum possible J_{SC} vs. active-layer thickness curves for both normal and inverted devices. Moreover, the corresponding absorption profile within the active-layer itself is highly non-exponential (Figure 1.7b). Indeed, Figure 1.7b shows a more sinusoidal-esque exciton generation distribution within the P3HT:PCBM photoactive layer for the case of a 100 nm film thickness. This is highly important when

considering that the contacts (e.g., Ca/Al) can cause excessive exciton quenching,[75] and thus a peak in the generation profile near that interface would likely result in a lower internal quantum efficiency.

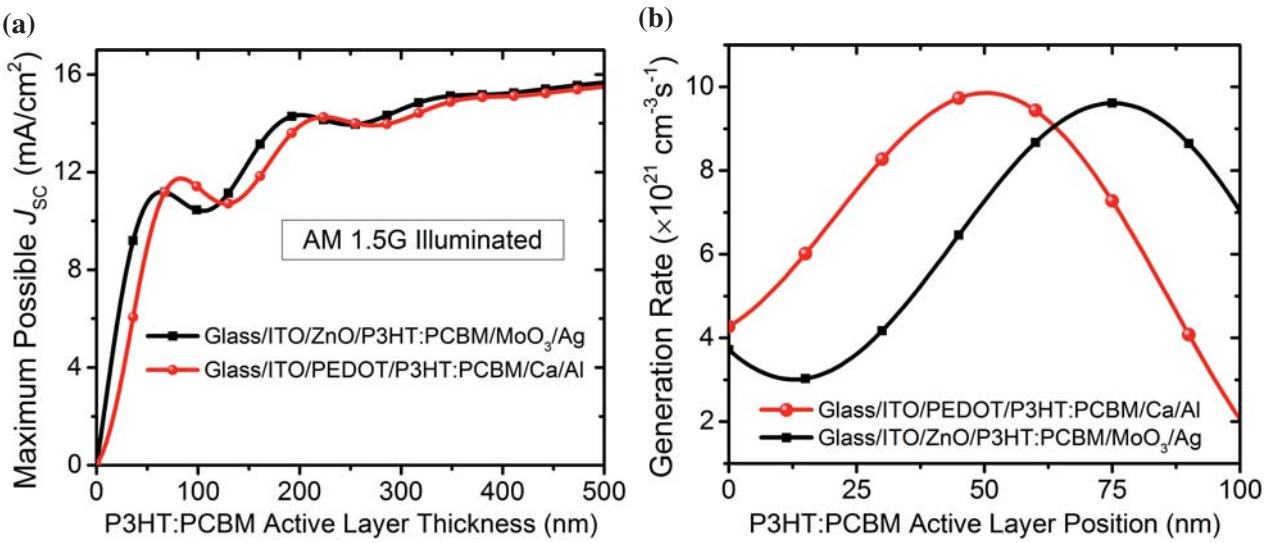

Figure 1.7: Representative active-layer absorption characteristics of a typical polymer:fullerene device made from P3HT:PCBM. (a) Representative maximum short-circuit current density measured under AM 1.5G illumination for two typical BHJ OPV device structures. (b) The corresponding exciton generation profiles within the active layer for a thickness of 100 nm showing strongly non-Beer's Law like distributions.

1.3.3 Currents, Band Diagrams, and the Built-In Potential

The typical polymer:fullerene BHJ OPV active layer is thin (∼100 nm), undoped, and has a low dielectric constant ($\varepsilon_r \approx$ 2-4), which when pared with contacts that have highly asymmetric work functions, means that the device band diagram must look something like Figure 1.8a in the dark and Figure 1.8b in the light. This diagram implies that there is little space charge (what little there is is mostly near the contacts) and that there is a nearly constant electric field across the active layer in the dark at zero applied bias.

The polymer:fullerene BHJ OPV band diagrams of Figure 1.8 are composed of the relevant energy levels for transport and recombination (i.e., the polymer HOMO $E_{\mathrm{HOMO,D}}$ and fullerene LUMO $E_{\mathrm{LUMO,A}}$), the (quasi-)Fermi levels for electrons ($E_{\mathrm{f,n}}$) and holes

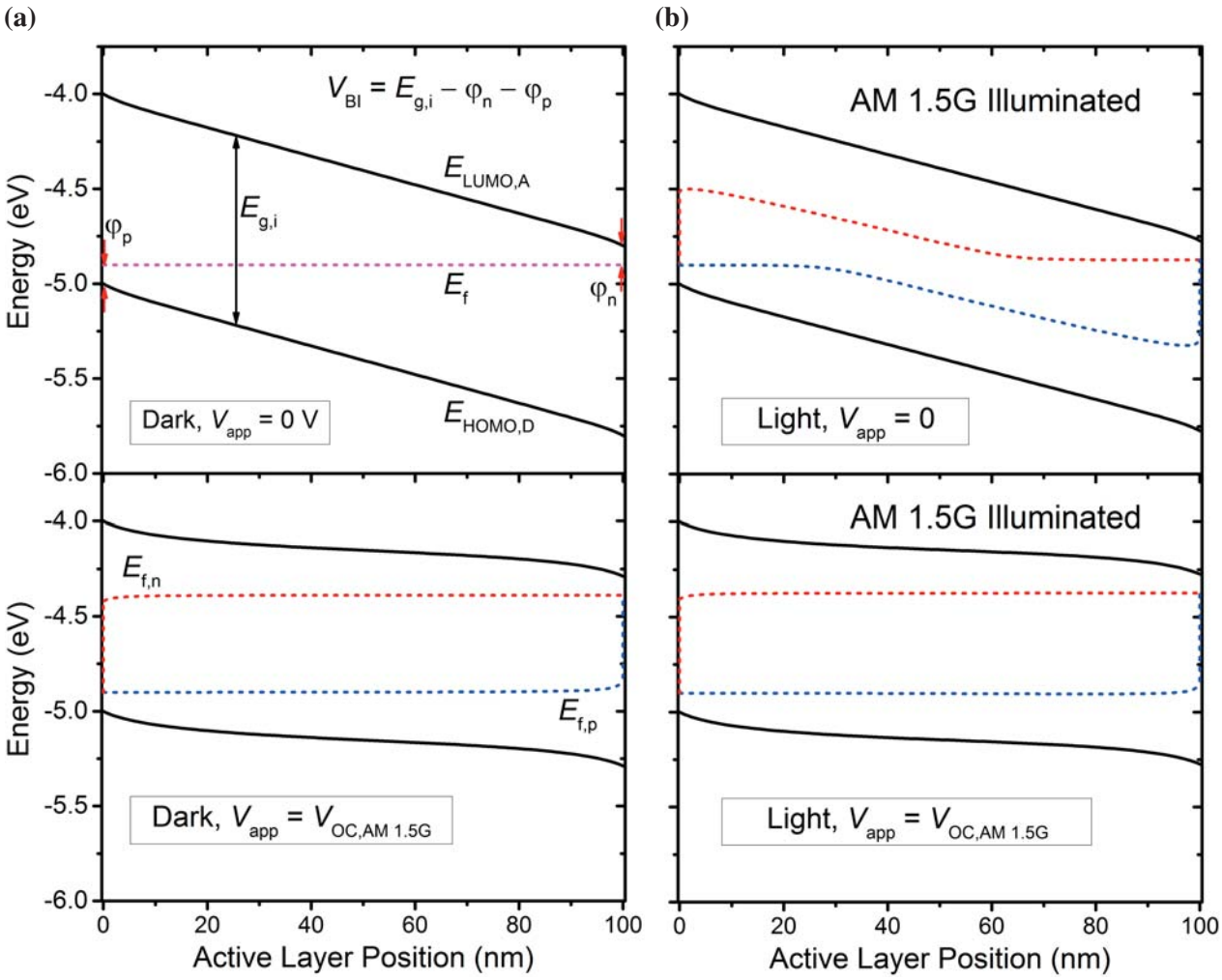

Figure 1.8: (a) A representative band diagram of a typical polymer:fullerene BHJ OPV in the dark and at low forward bias simulated by the AFORS-HET drift-diffusion software. (b) The same device but under AM 1.5G illumination. There is a small bias at short circuit under illumination due to the finite external series resistance. The active layers are typically thin (∼100 nm), undoped, and have low dielectric constants, thus giving the linear band structure as shown above. Symbols are defined in the text.

($E_{\mathrm{f,p}}$), the interfacial energy gap ($E_{\mathrm{g,i}} = E_{\mathrm{LUMO,A}} - E_{\mathrm{HOMO,D}}$), and the contact Schottky barriers (ϕ_n and ϕ_p). The underlying physics behind these band diagrams is summarized by the 1-D van Roosbroeck equations with the corresponding boundary conditions:

Continuity Equations

$$\frac{dn}{dt} = G - R + G_e^D - R_e^D + G_e^A - R_e^A + \frac{1}{q}\frac{dJ_n}{dx} \tag{1.5}$$

$$\frac{dp}{dt} = G - R + G_h^D - R_h^D + G_h^A - R_h^A - \frac{1}{q}\frac{dJ_p}{dx} \tag{1.6}$$

Current Equations

$$J_n = qn\mu_n \left(E - \frac{d\chi}{dx} - kT\frac{d\ln(N_{\mathrm{C}})}{dx} \right) + qD_n\frac{dn}{dx} \tag{1.7}$$

$$J_p = qp\mu_p \left(E - \frac{d\left(\chi + E_{\mathrm{g,i}}\right)}{dx} + kT\frac{d\ln(N_{\mathrm{V}})}{dx} \right) - qD_p\frac{dp}{dx} \tag{1.8}$$

$$\frac{D_n}{\mu_n} = \frac{n}{q\frac{dn}{dE_{\mathrm{f,n}}}} \approx \frac{kT}{q} \text{ if } n \ll N_{\mathrm{C}} \tag{1.9}$$

$$\frac{D_p}{\mu_p} = \frac{p}{q\frac{dp}{dE_{\mathrm{f,p}}}} \approx \frac{kT}{q} \text{ if } p \ll N_{\mathrm{V}} \tag{1.10}$$

$$J_D = \varepsilon\frac{dE}{dt} \tag{1.11}$$

$$J_{\mathrm{tot}} = J_n + J_p + J_D \tag{1.12}$$

Electrodynamics

$$\frac{dE}{dx} = \frac{q}{\varepsilon}(p - n + N_{\mathrm{D}}^{+} - N_{\mathrm{A}}^{-}) \tag{1.13}$$

Boundary Conditions

$$V_{\mathrm{app}} = \int_0^d (E_0 - E)\, dx \tag{1.14}$$

$$J_n(0) = qS_{\mathrm{n,0}}\left[n(0) - n_0(0)\right] \tag{1.15}$$

$$J_p(0) = -qS_{\mathrm{p,0}}\left[p(0) - p_0(0)\right] \tag{1.16}$$

$$J_n(d) = -qS_{\mathrm{n,d}}\left[n(d) - n_0(d)\right] \tag{1.17}$$

$$J_p(d) = qS_{\mathrm{p,d}}\left[p(d) - p_0(d)\right] \tag{1.18}$$

$$n(d) = N_{\mathrm{C}}\exp\left(-\frac{\phi_{\mathrm{n}}}{kT}\right) \tag{1.19}$$

$$n(0) = N_{\mathrm{c}} \exp\left(-\frac{E_{\mathrm{g,i}} - \phi_{\mathrm{p}}}{kT}\right) \tag{1.20}$$

$$p(0) = N_{\mathrm{v}} \exp\left(-\frac{\phi_{\mathrm{p}}}{kT}\right) \tag{1.21}$$

$$p(d) = N_{\mathrm{v}} \exp\left(-\frac{E_{\mathrm{g,i}} - \phi_{\mathrm{n}}}{kT}\right) \tag{1.22}$$

where all symbols are defined in Table 1.1.

Physically, Eqs. (1.5) and (1.6) account for the continuity of free carriers and simply add or subtract the contributions of both bulk and trap-mediated recombination/generation to the free carrier populations. Eqs. (1.7) and (1.8) are the composition-dependent drift-diffusion equations for electrons and holes. Note that the only shared term is the electric field, E, and that gradients in material properties like electron affinity, effective density of states, and ionization potential act as effective electric fields only on their respective carriers. In terms of charge transport, Eqs. (1.9) and (1.10) relate the electron and hole mobilities to their respective diffusion coefficients. The ratio of D/μ is typically given by the simple Einstein relation that is equal to kT/q; however, for large carrier concentrations, this relation breaks down, and the generalized Einstien relation must be used (Eqs. (1.9) and (1.10)).[76,77] The total (time-dependant) current (Eq. (1.12)) that is measured in an experiment is given by the sum of the electron, hole, and displacement currents (Eq. (1.11)). Electrostatically and dynamically, the charges within the semiconductor (both free n,p and localized N_{D}^{+}, N_{A}^{-}) must also always obey Gauss's law (Eq. (1.13)).

In terms of boundary conditions, arguably the most important relation is that of Eq. (1.14), which defines the experimentally applied voltage to the cell. Together with Eq. (1.12) and the associate sub-equations, Eq. (1.14) links the experimental J-V curves to the theory presented herein. Eq. (1.14) states that a measured or applied voltage must manifest as a departure of the integrated electric-field distribution from its equilibrium value in the dark. This equation is general to any solar cell or optoelectronic device, and arises from the fact that the vacuum levels must be continuous (but not necessarily differentiable) as one spatially transitions from the semiconductor device into the metal-wire based circuit.[78] The reasoning behind this statement is that an applied voltage creates a difference between the metal electrode Fermi levels, and since an applied voltage cannot change

Table 1.1: Parameter Definitions

Parameter Symbol	Definition	Typical Unit
n, p	Mobile electron and hole concentrations, respectively	cm^{-3}
N_D^+	Ionized donor-type (neutral when filled) traps	cm^{-3}
N_A^-	Ionized acceptor-type (neutral when empty) traps	cm^{-3}
G	Generation rate of mobile-carrier pairs (Figure 1.7b)	$cm^{-3}s^{-1}$
R	Recombination rate of mobile-carrier pairs (Figure 1.9)	$cm^{-3}s^{-1}$
$G_{e,h}^{D,A}$	Generation rates of mobile carriers from localized donor- and acceptor-type trap sites (Figure 1.9)	$cm^{-3}s^{-1}$
$R_{e,h}^{D,A}$	Recombination rates of mobile charge into localized donor- and acceptor-type trap sites (Figure 1.9)	$cm^{-3}s^{-1}$
E	Electric field	V/cm
ε	Semiconductor permittivity $= \varepsilon_r \varepsilon_0$	F/cm
q	Absolute value of the electron charge $= 1.6 \times 10^{-19}$	C
$J_{n,p}$	Electric current due to mobile electrons and holes, respectively	mA/cm^2
$\mu_{n,p}$	Electron and hole mobilities, respectively	cm^2/V-s
$D_{n,p}$	Electron and hole diffusion coefficients, respectively	cm^2/s
d	Active layer thickness	nm
k	Boltzmann constant $= 8.62 \times 10^{-5}$	eV/K
T	Cell temperature	K
J_D	Maxwell's displacement current	mA/cm^2
J_{tot}	Experimentally measured total electric current	mA/cm^2
V_{app}	Applied cell voltage	V
E_0	Equilibrium electric field distribution	V/cm
n_0, p_0	Equilibrium electron and hole concentrations, respectively	cm^{-3}
$S_{p,0}$, $S_{p,d}$	Hole surface recombination velocities	cm/s
$S_{n,0}$, $S_{n,d}$	Electron surface recombination velocities	cm/s
χ	Semiconductor Electron Affinity	eV
$E_{g,i}$	Donor-Acceptor interfacial band gap	eV
$\chi + E_{g,i}$	Semiconductor ionization potential	eV
$\phi_{n,p}$	Schottky barrier heights	eV
N_C,N_V	Conduction and valence band effective density of states	cm^{-3}

the work function of an entire metal-wire terminal, only shifts in the electric potential (integrated electric field) across the device relative to equilibrium can manifest as a voltage. Such a conclusion is not necessarily obvious, as certain researchers have even incorrectly questioned the validity of Eq. (1.14).[79]

The carrier concentration boundary conditions are given by Eqns. (1.19)-(1.22) (assuming Boltzmann statistics), which relate the carrier densities at the boundaries of the active layer to the energetic distance between the metal-electrode Fermi level and the respective semiconductor band edge (i.e., the Schottky barrier height). Finally, $S_{\mathrm{p,0}}$, $S_{\mathrm{p,d}}$, $S_{\mathrm{n,0}}$, and $S_{\mathrm{n,d}}$ are the surface recombination velocities for each interface/carrier combination. These are surface kinetic parameters that describe how well the interfaces bounding the active layer pass current of a certain type. An infinite surface recombination velocity implies that the interface passes current so readily that no charge ever gets built up or depleted at the interface (the carrier concentrations always remain at their equilibrium values). Conversely, a surface recombination velocity of zero implies a totally blocking interface that never passes current of that particular carrier. Ideally, for a solar cell, perfectly 'selective contacts' mean that one contact has an infinite surface recombination velocity for one carrier and zero for the other, but vice versa is true for the opposite contact.

An important solar cell parameter that is strongly related to the boundary conditions is the built-in potential (V_{BI}). This is a somewhat vague and imprecise term, since there is no specification as to what this potential really represents; i.e., is it a built-in diffusional, compositional, or electric potential? Typically, though, what is meant by V_{BI} is just the electric potential difference (integral of the electric field distribution) in the dark. In order get a better sense of V_{BI} for the typical OPV, we can derive it on relatively general grounds for an active-layer of uniform composition (no gradients in χ, etc.). To do so, one needs to realize that in the dark $J_n = J_p = 0$ or else there would be Joule heating and the device could fuel a perpetual motion machine.[80] Thus, combining Eqns. (1.7)-(1.8) with Eqns. (1.19)-(1.22) and $J_n = J_p = 0$ and solving gives the simple drift-diffusion V_{BI} for a uniform composition 1-D active layer device:

$$qV_{\mathrm{BI}} = E_{\mathrm{g,i}} - \phi_{\mathrm{n}} - \phi_{\mathrm{p}} \tag{1.23}$$

where $\phi_{n,p}$ (Table 1.1) are the height of the Schottky energy barriers at the cathode and anode contact (Figure 1.8a), respectfully, and $N_{C,V}$ are the effective density of states of the fullerene LUMO and polymer HOMO, respectively. Notably, this equation is the same for a classic *p-n* homojunction, except therein it is typically assumed that the ϕ values represent the doping levels on the left and right of the junction instead of the Schottky barrier heights. Eqn. (1.23) is highly important to OPV performance because it sets up the equilibrium electric field distribution (E_0), which serves to drive excess photogenerated carriers out of the device before they recombine back to the ground state. This built-in electric field due to the use of asymmetric contact work functions (small ϕ_n,ϕ_p) typically serves as the necessary conduction asymmetry for achieving photovoltaic action in OPV devices.

1.3.4 Recombination

The main recombination processes that are typically considered in polymer:fullerene BHJ OPV research are schematically indicated in Figure 1.9. Since recombination is a heavily discussed topic in the coming chapters, here I only briefly introduce the basic processes and relevant terms used in forthcoming detailed discussions.

In terms of parlance, 'geminate' and 'nongeminate' recombination are two main terms that are used to refer to recombination in polymer:fullerene BHJ OPV active layers. 'Bimolecular' recombination was fashionable for a time, but has since been replaced by 'nongeminate'. Geminate recombination refers to a recombination event involving a bound electron-hole pair either as an exciton or as a charge-transfer (CT) state at a polymer:fullerene interface. In either case, geminate recombination occurs before free-carrier generation. Nongeminate recombination, on the other hand, refers to everything else, including trap-assisted, band-to-band, and surface recombination. The two most popular functional forms used for describing steady-state nongeminate recombination are the Langevin model (Eqn. (1.24)) and the Shockley-Read-Hall (SRH) model (Eqn. (1.25)):

$$R_{\text{Langevin}} = \frac{q\gamma(\mu_n + \mu_p)}{\varepsilon}\left(np - n_i^2\right) \tag{1.24}$$

$$R_{\mathrm{SRH}}(E_t) = R_{e,h}^{D,A} - G_{e,h}^{D,A} = \frac{c_n c_p N_t(E_t)}{c_n(n+n_g)+c_p(p+p_g)}\left(np-n_i^2\right) \tag{1.25}$$

$$p_g = N_{\mathrm{V}} \exp\left(-\frac{E_t - E_V}{kT}\right) \tag{1.26}$$

$$n_g = N_{\mathrm{C}} \exp\left(-\frac{E_C - E_t}{kT}\right) \tag{1.27}$$

$$n_i^2 = N_{\mathrm{C}} N_{\mathrm{V}} \exp\left(-\frac{E_g}{kT}\right) \tag{1.28}$$

where γ is the Langevin recombination reduction factor, n_i^2 is the square of the intrinsic carrier concentration, $N_t(E_t)$ is the trap concentration at the trap energy E_t, $E_C = E_{\mathrm{LUMO,A}}$ is the conduction band edge, $E_V = E_{\mathrm{HOMO,D}}$ is the valence band edge, $c_{n,p}$ are the electron/hole capture coefficients for the traps $N_t(E_t)$ at energy E_t, p_g and n_g are thermal emission coefficients that represent contributions from $G_{e,h}^{D,A}$ in Figure 1.9.

Much of the forthcoming discussion is in regards to the application of these recombination

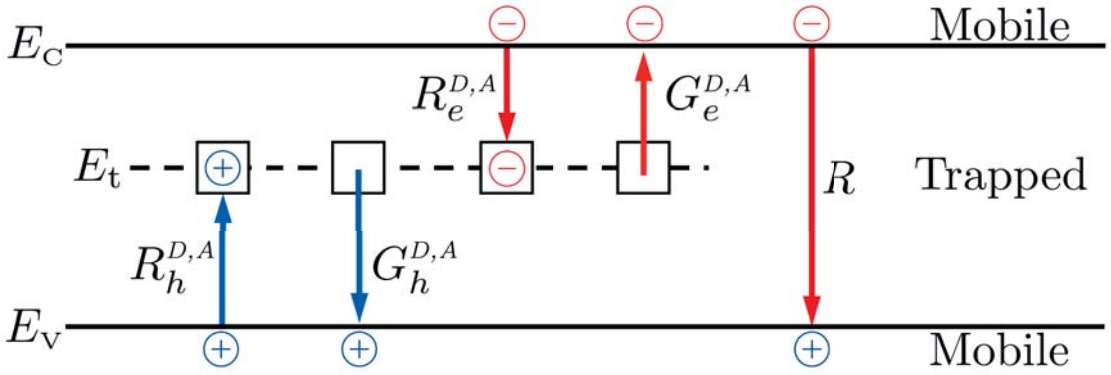

Figure 1.9: The essential recombination processes in polymer:fullerene BHJ OPVs: trap-assisted and band-to-band. Auger and surface recombination are typically not examined, though may play a role (especially surface recombination).

models to the polymer:fullerene BHJ OPV devices, and thus I refer to the coming chapters for a more extensive introduction and detailed analysis. In particular, Chapter 2 shows experimentally that Eqn. (1.24) cannot be the dominant recombination pathway in a certain class of high-performance polymer:fullerene materials, and instead that trap assisted recombination (Eqn. (1.25)) through an exponential distribution of trap states is the likely dominant pathway. Chapter 3 further ellaborates along these lines by providing direct evidence for SRH recombination through band-tail states being

the primary recombination process.

1.4 Thesis Breakdown and Outlook

This thesis is composed of six chapters on the topic of recombination and device physics of polymer:fullerene BHJ solar cells and solution sequential processing. Below is a summary of each forthcoming chapter and how each project made original and impactful contributions to the field.

1.4.1 Chapter 2: Relating Recombination, Density of States, and Device Performance in an Efficient Polymer:Fullerene Organic Solar Cell Blend

This chapter is taken directly from the published work of Reference 150.

In this chapter, we explore the interrelation between density of states, recombination kinetics, and device performance in efficient poly[4,8-bis-(2-ethylhexyloxy)-benzo[1,2-b:4,5-b]dithiophene-2,6-diyl-alt-4-(2-ethylhexyloxy-1-one) thieno[3,4-b]thiophene-2,6-diyl]:[6,6]-phenyl-C 71 -butyric acid methyl ester (PBDTTT-C:$PC_{71}BM$) bulk-heterojunction organic solar cells. We modulate the active-layer density of states by varying the polymer:fullerene composition over a small range around the ratio that leads to the maximum solar cell efficiency (50-67 wt% $PC_{71}BM$). Using transient and steady-state techniques, we find that nongeminate recombination limits the device efficiency and, moreover, that increasing the $PC_{71}BM$ content simultaneously increases the carrier lifetime and drift mobility in contrast to the behavior expected for Langevin recombination. Changes in electronic properties with fullerene content are accompanied by a significant change in the magnitude or energetic separation of the density of localized states. Our comprehensive approach to understanding device performance represents significant progress in understanding what limits these high-efficiency polymer:fullerene systems.

1.4.2 Chapter 3: Band tail recombination in polymer:fullerene organic solar cells

This chapter is taken directly from the published work of Reference 205, with much credit also going to Robert A. Street.

In this chapter, recombination through band tail localized states is studied analytically and by measurement of the forward-bias dark current as a function of temperature in three different organic bulk-heterojunction solar cells. The Shockley-Read-Hall mechanism is analyzed for the specific case of recombination between mobile carriers and an exponential distribution of localized band tail states. The analysis gives a simple relation between the dark current ideality factor and the band tail slope. Assumptions of the model are verified by numerical drift-diffusion modeling. Diode current-voltage measurements give good agreement with the analytical model, confirming that the band tail recombination mechanism applies to at least some organic solar cells. Deep traps provide a secondary recombination channel in some devices.

1.4.3 Chapter 4: Theory of Current Transients in Planar Semiconductor Devices: Insights and Applications to Organic Solar Cells

This chapter is taken directly from the published work of Reference 358.

In this chapter, I explore time-domain current measurements, which are widely used to characterize semiconductor material properties, such as carrier mobility, doping concentration, carrier lifetime, and the static dielectric constant. It is therefore critical that these measurements be theoretically understood if they are to be successfully applied to assess the properties of materials and devices. I derive generalized relations for describing current-density transients in planar semiconductor devices at uniform temperature. By spatially averaging the charge densities inside the semiconductor, I am able to provide a rigorous, straightforward, and experimentally relevant way to interpret these measurements. The formalism details several subtle aspects of current transients, including how the electrode charge relates to applied bias and internal space charge, how the displacement current can alter the apparent free-carrier current, and how to understand the integral of a charge-extraction transient. I also demonstrate how the formalism can be employed to derive the current transients arising from simple physical models, like those used to describe charge extraction by linearly increasing voltage (CELIV) and time-of-flight experiments. In doing so, I find that there is a nonintuitive factor-of-2 reduction in the apparent free-carrier concentration that has been missed, for example, in the application of charge-extraction models. Finally, to validate my theory and better understand the different current contributions, I perform a full time-domain drift-diffusion

simulation of a CELIV trace and compare the results to my formalism. As expected, my analytic equations match precisely with the numerical solutions to the drift-diffusion, Poisson, and continuity equations. Thus, overall, my formalism provides a straightforward and general way to think about how the internal space-charge distribution, the electrode charge, and the externally applied bias translate into a measured current transient in a planar semiconductor device.

1.4.4 Chapter 5: Comparing Matched Polymer:Fullerene Solar Cells Made by Solution-Sequential Processing and Traditional Blend Casting: Nanoscale Structure and Device Performance

This chapter is taken directly from the published work of Reference 201.

Polymer:fullerene bulk heterojunction (BHJ) solar cell active layers can be created by traditional blend casting (BC), where the components are mixed together in solution before deposition, or by sequential processing (SqP), where the pure polymer and fullerene materials are cast sequentially from different solutions. Presently, however, the relative merits of SqP as compared to BC are not fully understood because there has yet to be an equivalent (composition- and thickness-matched layer) comparison between the two processing techniques. The main reason why matched SqP and BC devices have not been compared is because the composition of SqP active layers has not been accurately known. In this chapter, I present a novel technique for accurately measuring the polymer:fullerene film composition in SqP active layers, which allows me to make the first comparisons between rigorously composition- and thickness-matched BHJ organic solar cells made by SqP and traditional BC. I discover that, in optimal photovoltaic devices, SqP active layers have a very similar composition as their optimized BC counterparts ($\approx$44-50 mass % PCBM). We then present a thorough investigation of the morphological and device properties of thickness- and composition-matched P3HT:PCBM SqP and BC active layers in order to better understand the advantages and drawbacks of both processing approaches. For my matched devices, we find that small-area SqP cells perform better than BC cells due to both superior film quality and enhanced optical absorption from more crystalline P3HT. The enhanced film quality of SqP active layers also results in higher performance and significantly better reproducibility in larger-area devices, indicating that SqP is more amenable to scaling than the traditional BC approach. X-ray diffraction, UVvis absorption,

and energy-filtered transmission electron tomography collectively show that annealed SqP active layers have a finer-scale blend morphology and more crystalline polymer and fullerene domains when compared to equivalently processed BC active layers. Charge extraction by linearly increasing voltage (CELIV) measurements, combined with X-ray photoelectron spectroscopy, also show that the top (non-substrate) interface for SqP films is slightly richer in PCBM compared to matched BC active layers. Despite these clear differences in bulk and vertical morphology, transient photovoltage, transient photocurrent, and subgap external quantum efficiency measurements all indicate that the interfacial electronic processes occurring at P3HT:PCBM heterojunctions are essentially identical in matched-annealed SqP and BC active layers, suggesting that device physics are surprisingly robust with respect to the details of the BHJ morphology.

1.4.5 Chapter 6: Extensive Penetration of Evaporated Electrode Metals into Fullerene Films: Intercalated Metal Nanostructures and Influence on Device Architecture

This chapter is taken straight from work submitted to *ACS Applied Materials and Interfaces*, with contributions from Guangye Zhang, Chilan Ngo, Laura T. Schelhas, D. Tyler Scholes, Hyeyeon Kang, and Jordan C. Aguirre.

Although it is known that evaporated metals can penetrate through a few nm of different types of organic molecules, there has been little work aimed at exploring the behavior of the common electrode metals used in devices based on fullerene derivatives, such as organic photovoltaics (OPVs) and methylammonium lead halide perovskite solar cells. In this paper, we show that when commonly-used electrode metals (e.g., Au, Ag, Al, Ca, etc.) are evaporated onto films of fullerene derivatives (such as [6,6]-phenyl-C_{61}-butyric acid methyl ester (PCBM)), the metal penetrates many tens of nanometers into the fullerene layer. This penetration decreases the effective electrical thickness of fullerene-based sandwich structure devices, as measured by the device's geometric capacitance, and thus significantly alters the device physics. For the case of Au/PCBM, the metal penetrates a remarkable 70 nm, and we see penetration of similar magnitude in a wide variety of fullerene derivative/evaporated metal combinations. Moreover, using cross-sectional transmission electron microscopy, we show that when gold is evaporated onto poly(3-hexylthiophene) (P3HT)/PCBM sequentially-processed OPV quasi-bilayers, Au nanoparticles with diameters of $\sim$3-

20 nm are formed and are dispersed entirely throughout the fullerene-rich overlayer. The plasmonic absorption and scattering from these nanoparticles are readily evident in the optical transmission spectrum, demonstrating that the interpenetrated metal significantly alters the optical properties of fullerene-rich active layers. Overall, these discoveries open up a number of possibilities in terms of contact engineering and light management within devices that use fullerene derivatives, so that it is critical that researchers are aware of the profound electronic and optical consequences of exposing fullerene-derivative films to evaporated electrode metals.

CHAPTER 2

Relating Recombination, Density of States, and Device Performance in an Efficient Polymer:Fullerene Organic Solar Cell Blend

2.1 Introduction

Polymer:fullerene bulk heterojunction (BHJ) solar cells have recently witnessed tremendous advancements in active-layer performance due to materials and processing optimization.[14,19–21,81–83] The development of novel interlayers and polymers with favorable absorptive, electrical, and morphological properties have enabled single-junction efficiencies to exceed 9%.[84] In a number of efficient BHJ systems, investigators have shown that nongeminate recombination is the key loss mechanism that limits the power conversion efficiency.[85–93] The influence of nongeminate recombination on the shape of the current/voltage curve has even been demonstrated quantitatively in several polymer:fullerene systems.[90–95] Nongeminate recombination is controlled by the recombination kinetics—usually experimentally represented through charge-carrier lifetimes—and the density of states (DoS) of the semiconductor. While the theoretical relation between the DoS, recombination kinetics, and device performance (e.g., open-circuit voltage (V_{oc}) have been discussed,[80,96,97] there have been few studies on polymer:fullerene systems that monitor the DoS explicitly, and study the impact on recombination kinetics, V_{oc}, and overall device performance.[98–100] In addition, there has been comparatively little experimental work on understanding the precise physical origin of the recombination dynamics, and how the kinetics of recombination depends on the kinetics of transport.[101–105]

In this work, we explicitly examine the DoS, recombination dynamics, device performance, and

their interdependence in a representative, high-efficiency, BHJ organic photo voltaic (OPV) active layer composed of poly[4,8-bis-(2- ethylhexyloxy)-benzo[1,2-b:4,5-b]dithiophene-2,6-diyl-alt-4-(2-ethylhexyloxy-1-one)thieno[3,4-b]thiophene-2,6-diyl] (PBDTTT-C) and [6,6]-phenyl-C_{71}-butyric acid methyl ester ($PC_{71}BM$) (Figure 2.1).[106] We do so by combining electroluminescence spectroscopy (EL), transient photovoltage (TPV), and charge extraction (CE) measurements.[87–89] To modulate the DoS, we examine different blend compositions around the composition at which the photovoltaic performance of PBDTTT-C:$PC_{71}BM$ solar cells is optimized. We find that the principal recombination mechanism in this system is of nongeminate character, and that the recombination kinetics scale with drift-mobility in the opposite way that would be predicted by a Langevin-type model. Namely, the highest fullerene loading leads to both the highest mobility and the longest charge-carrier lifetime. The improved carrier lifetimes and drift-mobility with increasing $PC_{71}BM$ content are accompanied by a significant change in the magnitude or width of the DoS. Our assignment of dominant carrier losses to nongeminate recombination is validated by reconstructions of the J-V curves and V_{oc} predictions at different light intensities and blend compositions. In addition, we find a strong correlation between the blend CT-state energy, V_{oc}, and $PC_{71}BM$ content, which has previously been observed in several other polymer systems over a wide composition range, despite vastly different processing conditions, and molecular structures.[107–111] In this regard, our results are consistent with the hypothesis that a major reason behind the success of PCBM-based acceptors is the tendency to form a unique morphology ideal for charge separation and extraction.[107,112,113]

We chose to investigate PBDTTT-C because of its facile synthesis, excellent performance, and close similarity to some of the highest efficiency BHJ donor polymers known to date.[21,84,114–122] The PBDTTT:$PC_{71}BM$ BHJ system is interesting because it achieves high photovoltaic performance despite detailed morphological studies suggesting that it forms a complex and mostly amorphous morphology with relatively weak polymer/ fullerene aggregation where it is presently unclear how such excellent photovoltaic performance manifests.[16,123–126]

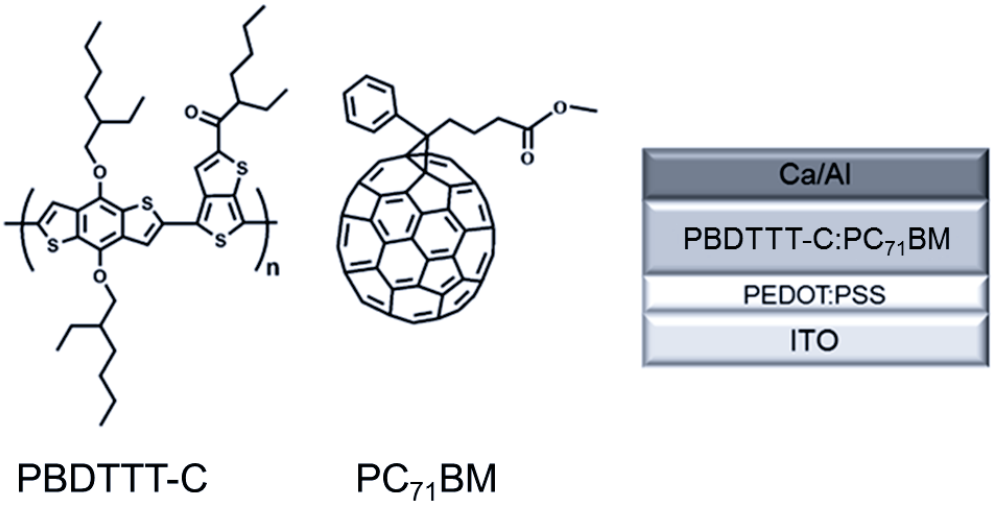

Figure 2.1: This work examines the PBDTTT-C:$PC_{71}BM$ system at three different compositions, 50 wt% $PC_{71}BM$, 60 wt% $PC_{71}BM$, and 67 wt% $PC_{71}BM$ wt. ratio PBDTTT-C:$PC_{71}BM$ (50-67 wt% $PC_{71}BM$). The device architecture chosen for study was ITO/PEDOT:PSS/PBDTTT-C:$PC_{71}BM$/Ca/Al.

2.2 Results and Discussion

2.2.1 *J-V* Characteristics

Herein we study devices made from three different PBDTTT-C: $PC_{71}BM$ compositions; namely, 50 wt% $PC_{71}BM$, 60 wt% $PC_{71}BM$, and 67 wt% $PC_{71}BM$. In order to understand the differences in performance from a general standpoint, we optimized each blend individually for active-layer thickness (Figure 2.2). In agreement with previous reports,[106] we find that the optimal blend weight ratio has 60 wt% $PC_{71}BM$. In Figure 2.2 the active-layer spin speed was used as a relative unit for thickness because a measurement of the absolute thickness of all active layers was not necessary for the following *J-V* comparisons. From the trends in Figure 2.2 we see that both the 60 wt% $PC_{71}BM$ and 67 wt% $PC_{71}BM$ devices are able to maintain high fill factors at thicknesses where the J_{sc} is locally maximized. The 50 wt% $PC_{71}BM$ blend, on the other hand, begins to suffer losses in fill factor while the J_{sc} is still increasing with increasing thickness. Based on typical absorbed photon flux vs. active-layer thickness plots for BHJ OPVs,[24,55,127,128] we hypothesize that, in this case, the charge-collection efficiency is greater in films with higher fullerene content, allowing the active layers to be optimized at the first absorption maximum.[24,55,127,128] Thus, it appears that the favorable overall absorption of higher PBDTTT-C content active layers (50 wt% $PC_{71}BM$) cannot

be exploited due to excessive nongeminate losses with modest increases in active-layer thickness. This assessment of the *J*-*V* characteristics and device performance is supported by our transient optoelectronic measurements discussed below.

We also observed a robust trend in V_{oc} with fullerene loading for the compositions examined herein; namely, that the open-circuit voltage is always higher for lower fullerene content (Figure 2.2c). Though the differences in V_{oc} between blends is only on the order of $\sim$10 mV, this trend was consistently reproduced from different polymer and $PC_{71}BM$ batches, as well as from many devices fabricated at different laboratories (ICL and UCLA). The observation that V_{oc} decreases with higher PCBM content over a wide composition range has also been found in other polymer systems.[107,108,110,111,129–131] Sparing contact effects, the V_{oc} is a function of energy levels and the steady-state carrier concentration determined by the balance between generation and recombination.[9,85,94,97,132] Earlier investigations into the reason for the composition dependence of V_{oc} found that the change in V_{oc} with fullerene content can be explained with changes in the CT-state energy and that kinetic arguments were not necessary to explain the trends.[107,110] To verify whether this is the case in our devices as well, and to better understand how the PBDTTT-C: $PC_{71}BM$ composition affects energy levels, recombination, and the overall device performance, we performed transient optoelectronic measurements and electroluminescence studies.

2.2.2 Transient Optoelectronic Analysis

We performed TPV and CE experiments on the different blend-ratio devices; descriptions of these techniques and their use in characterizing organic solar cells are well-documented elsewhere.[33,87–94,97] These techniques allow us to probe the typically non-linear relationship between carrier density and recombination, which plays a major role in determining the shape of the *J*-*V* curve and thus also the power conversion efficiency. Table 2.1 summarizes the typical *J*-*V* characteristics and device parameters relevant to the following analysis. We note that the carrier concentration data was obtained from CE measurements by correcting for both the charge on the electrodes (using the geometric capacitance) and any incurred carrier losses during extraction.[88] We analyze our transient data using the empirical and approximate relations[133]

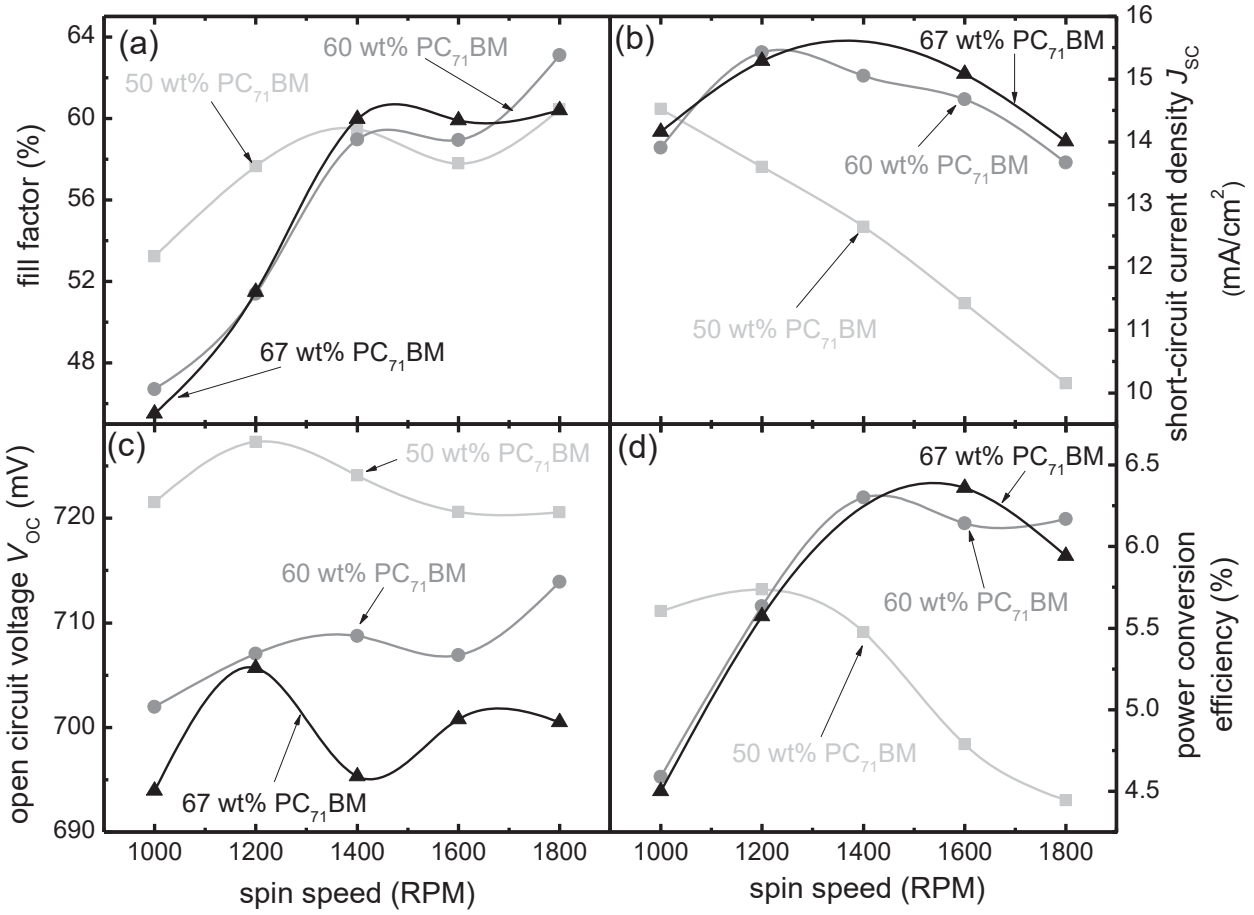

Figure 2.2: (a) Fill Factor, (b) J_{SC} , (c) V_{OC} , and (d) PCE dependence on spin speed for the compositions examined in this study. All data points are averaged over 6 devices, and the solid lines are added as guides to the eye.

Table 2.1: *J-V* Characteristics and device parameters of different blend compositions processed under identical conditions. The device characteristics were averaged over 4 devices ($\pm$ standard deviation). Thickness measurements were averaged over $\geq$ 4 locations and taken with an AFM. The built-in voltage was derived from the intersection of light and dark curves.

Composition	V_{OC} (V)	J_{SC} (mA/cm^2)	Fill Factor (%)	Efficiency (%)	Active Layer Thickness (nm)	Dielectric Constant (ε_r)	Built-in Voltage (V)
50 wt% PC$_{71}$BM	715 ± 3	11.4 ± 0.1	61.3 ± 0.5	4.98 ± 0.1	67 ± 4	3.7	0.79
60 wt% PC$_{71}$BM	708 ± 1	13.6 ± 2	64.5 ± 0.5	6.22 ± 0.1	82 ± 2	3.8	0.805
67 wt% PC$_{71}$BM	698 ± 3	14.6 ± 0.3	60.8 ± 1.2	6.18 ± 0.1	105 ± 5	3.9	0.78

$$\tau_{\Delta n} = \tau_{\Delta n0} \exp\left(-\frac{qV_{oc}}{\theta kT}\right) \tag{2.1}$$

$$n = n_0 \exp\left(-\frac{qV_{oc}}{mkT}\right) \tag{2.2}$$

$$\delta = \frac{m}{\theta} + 1 \tag{2.3}$$

$$\tau = \tau_{\Delta n}\delta = \frac{1}{k_{rec}n} = \frac{n^{\delta-2}}{\delta\tau_{\Delta n0}n_0^{\delta-1}} \tag{2.4}$$

where $\tau_{\Delta n}$ is the small perturbation lifetime obtained from fitting TPV decays to a monoexponential decay, τ the total carrier lifetime, and n is the average excess carrier concentration in the active layer relative to short circuit in the dark. The slope of $\tau(V_{oc})$ and $n(V_{oc})$ are defined by m and θ, and δ is the reaction order.[133, 134]

Figure 2.3a shows $n(V_{oc})$ as measured by CE, and (c) gives the total carrier lifetime as a function of average carrier concentration. We first see from Figure 2.3 a that for a given average carrier density, the $V_{oc}(n)$ is consistently different across blend ratios, where V_{oc}(50 wt% $PC_{71}BM$) > V_{oc}(60 wt% $PC_{71}BM$) > V_{oc}(67 wt% $PC_{71}BM$) for a given n = constant. Thus, for identical average charge densities n, the quasi-Fermi level splitting is larger for lower fullerene content, which indicates a significant composition-induced shift in the density of states. For lower fullerene loadings, the band tails of the polymer HOMO and $PC_{71}BM$ LUMO are either further separated from each other in energy, lower in magnitude, or a combination of both when compared to the higher $PC_{71}BM$ loading cases. We have schematically indicated this apparent shift in the density of states in Figure 2.3b. While the magnitude or energetic separation of the density of states around the band edges changes with composition, the slope of n vs. V_{oc}, and therefore the shape of the DoS, is not significantly affected.[135]

In order to analyze the recombination kinetics, we examine the total carrier lifetime as a function of average carrier density (Figure 2.3c). Much like Figure 2.3a, Figure 2.3c shows that τ (n) is also shifted across compositions. However, despite the larger V_{oc} values, τ (n = constant) goes as τ(50 wt% $PC_{71}BM$) < τ(60 wt% $PC_{71}BM$) < τ(67 wt% $PC_{71}BM$). Thus, nongeminate recombination is

actually fastest in the 50 wt% $PC_{71}BM$ blend, followed by the slower 60 wt% $PC_{71}BM$ and 67 wt% $PC_{71}BM$ blends, respectively. This indicates that the small differences in V_{oc} are due to two effects that partly compensate each other, namely a change in DoS and a shift in recombination dynamics. The higher magnitude and/or energetic shift in DoS induced by higher fullerene content is partly compensated by a concomitant reduction of the recombination rate, which, taken together, leads to only a slightly lower open-circuit voltage when compared to a lower fullerene content case.

The dominating recombination mechanism responsible for the trends in $\tau(n)$ of Figure 2.3c is of fundamental interest to understanding what limits the efficiency of a given active layer. A common approach for describing nongeminate recombination is via a Langevin-type mechanism, where the recombination coefficient k_{rec} is directly proportional to the carrier mobility (μ).[136] To examine the validity of a Langevin-type model, we used the technique described in Reference 137 to evaluate carrier drift mobilities as a function of average carrier concentration (Figure 2.4 a). From Figure 2.4 a we see that the mobility is weakly carrier-density dependent, offsetting between compositions, and actually largest for the 67 wt% $PC_{71}BM$ blend, following μ(67 wt% $PC_{71}BM$) $>$ μ(60 wt% $PC_{71}BM$) $>$ μ(50 wt% $PC_{71}BM$). For comparison, we plot the nongeminate recombination coefficient also in Figure 2.4 a as calculated from Equation (4) . The data in Figure 2.4 a and Figure 2.3c have exactly the opposite trend one would expect if Langevin-type recombination were dominant. In this particular case, larger $PC_{71}BM$ content increases the mobility and simultaneously decreases the recombination rate. Moreover, it is clear that the nongeminate recombination coefficient and the mobility have significantly different dependencies on average carrier density, which has been previously noted by Rauh *et al.*[105] In the following electroluminescence section, we provide further evidence that, in this case, phase-segregation effects are likely the dominating factor in determining the nongeminate recombination properties.

To combine these dynamical constants into one effective assay of the electrical properties of the blend, we plot the mobility-lifetime product in Figure 2.4b using the data from Figure 2.3c and Figure 2.4a that overlap in carrier density. Clearly, higher $PC_{71}BM$ concentrations result in vastly superior electrical properties in this composition range. The differences in $\mu\tau(n)$ between the 50 wt% $PC_{71}BM$ and 67 wt% $PC_{71}BM$ blends approaches an order of magnitude over the measured carrier concentration range, which explains why the 50 wt% $PC_{71}BM$ blend has suboptimal photovoltaic

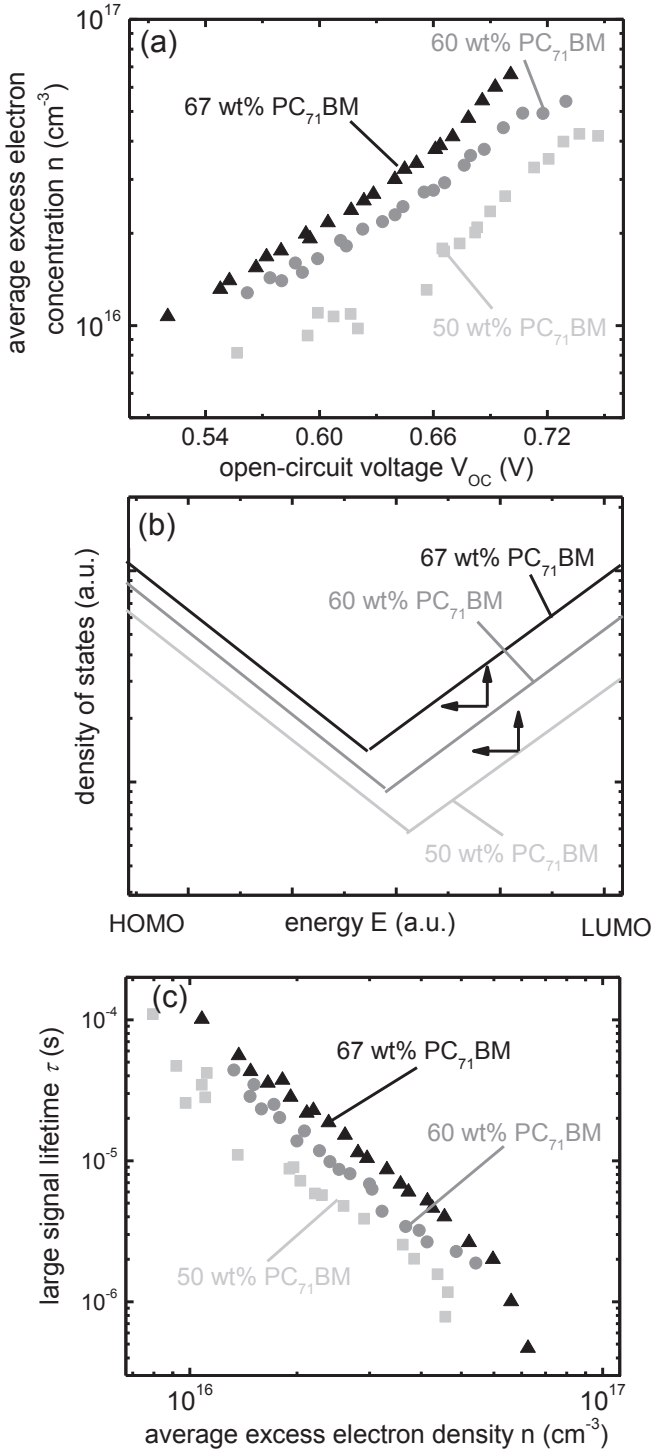

Figure 2.3: (a) The average carrier concentration as a function of V_{oc} and (c) the total carrier lifetime as a function of average carrier concentration for all PBDTTT-C:$PC_{71}BM$ weight ratios studied herein. (b) is a schematic showing how the density of states shifts with composition. Note that an increase in the absolute density of states at given energy or a shift of the DoS in energy are indistinguishable from a charge extraction measurement. We cannot discern whether the change is primarily in the HOMO or LUMO or whether both change equally.

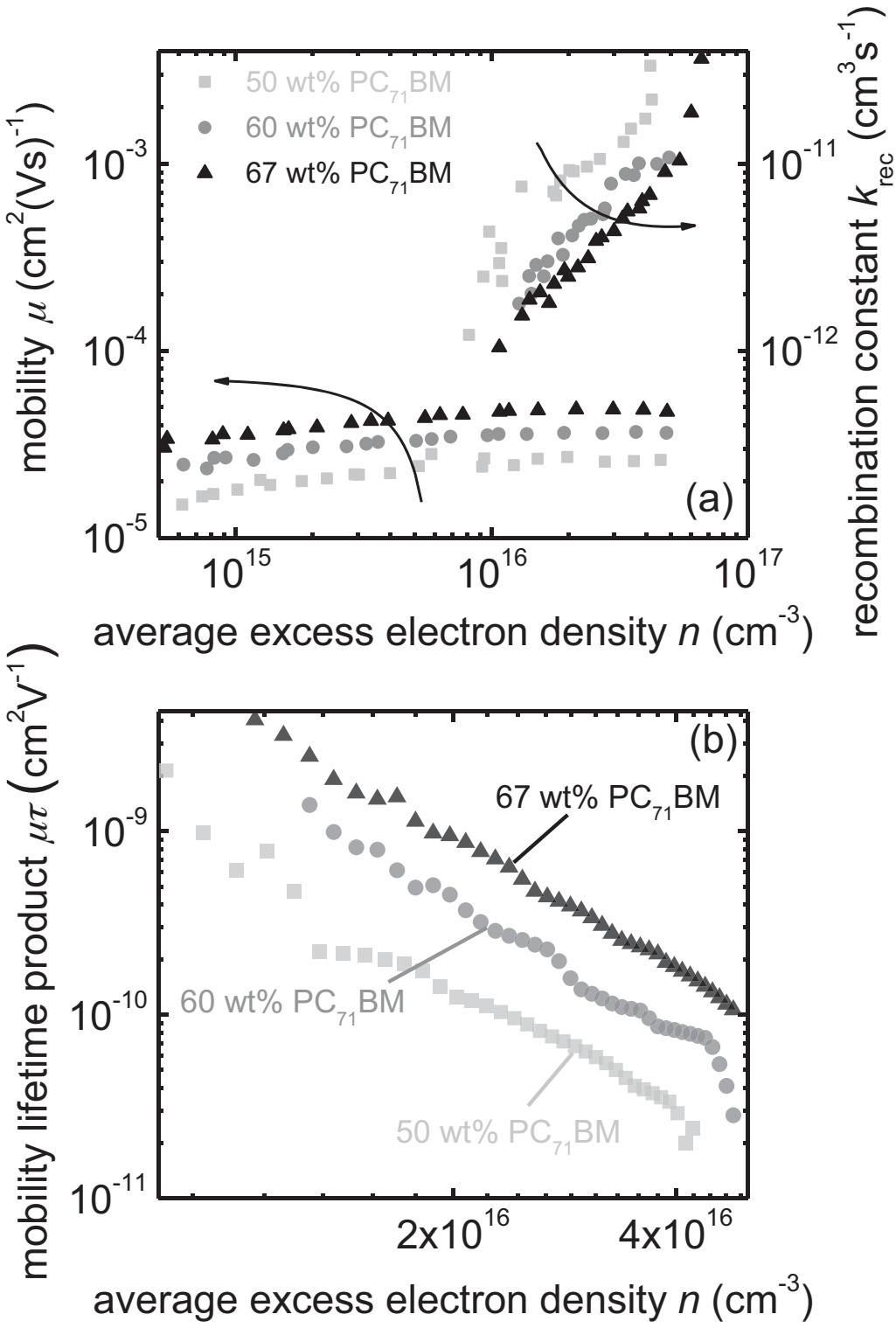

Figure 2.4: (a) Average carrier mobilities of the different blend ratios under study measured by the method in Reference 137 and the effective nongeminate recombination coefficient as a function of average carrier concentration. (b) The resulting mobility-lifetime product (lifetime from Figure 2.3 c) as a function of average carrier concentration. Note the different scales for the charge density *n*.

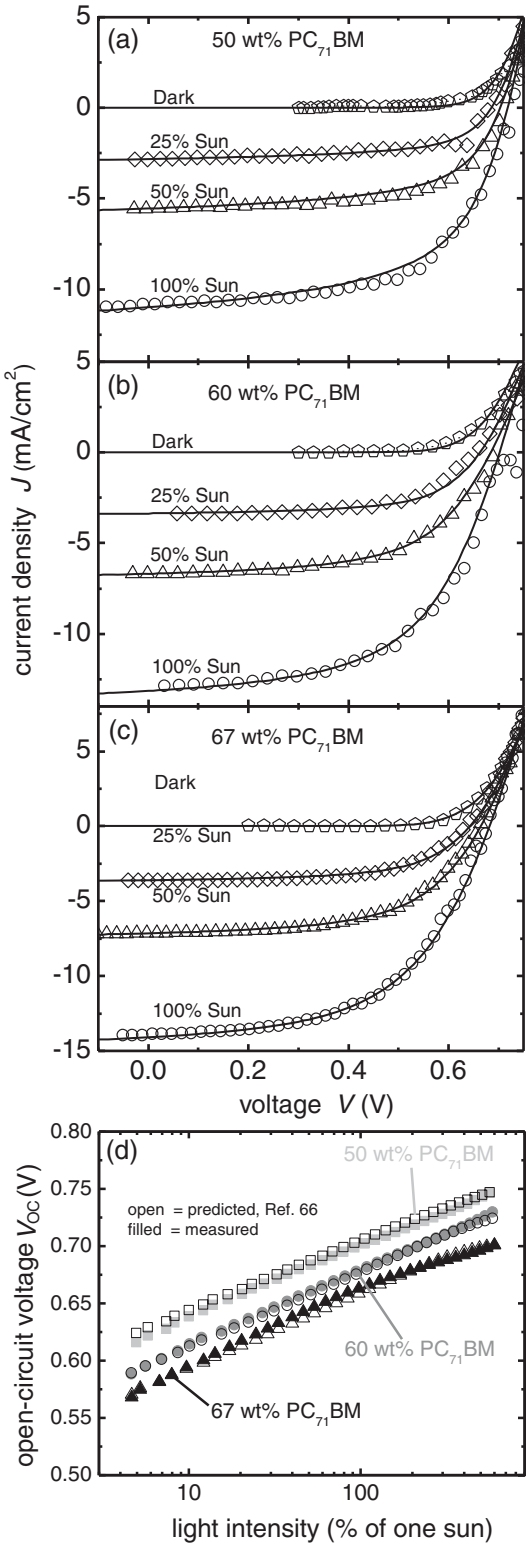

Figure 2.5: (a-c) *J-V* reconstructions comparing experimentally measured (solid lines) and reconstructed values (open points) based on the method detailed in References 90 and 92. (d) The light intensity dependence of V_{oc} for each blend and the corresponding predicted V_{oc} using the methods detailed in Reference 94.

properties.[138] In this case, the relative improvements of $\mu\tau(n)$ appear to afford acceptable fill factors at active-layer thicknesses corresponding roughly to the first absorption maximum for the 60 wt% $PC_{71}BM$ and 67 wt% $PC_{71}BM$ blends, but not the 50 wt% $PC_{71}BM$ blend (Figure 2.2).

Finally, in order to further understand the nature of these differences in recombination characteristics, we attempt to reconstruct the *J*-*V* curves and predict open-circuit voltages assuming that the generation rate is independent of voltage and that nongeminate recombination is the dominating loss process throughout the photovoltaic operating regime. Figure 2.5a-c shows the *J*-*V* reconstructions and Figure 2.5d the attendant V_{oc} predictions of all blend ratios using the methods detailed in previous works (dark *J*-*V* reconstructions are provided on a logarithmic scale in Figure S1).[90,91,94] The excellent agreement between measured and predicted values for all blend ratios in Figure 2.5 suggests that non-geminate recombination alone is sufficient to understand the shape of the *J*-*V* curves and the magnitudes of the open-circuit voltages for all compositions. In the final section below, we examine the electroluminescence spectra of the different blends to further specify the nature of this nongeminate, non-Langevin, type of recombination and, moreover, better understand why it is so sensitive to blend composition.

2.2.3 Electroluminescence

Figure 2.6 a shows the electroluminescence spectra for each of the PBDTTT-C:$PC_{71}BM$ weight ratios and the pure PBDTTT-C polymer. The normalized 50 wt% $PC_{71}BM$ blend EL resembles that of the pure polymer, but with the high-energy cutoff $\sim$0.1 eV redshifted and a stronger low-energy emission tail. When progressing through the composition range, the EL spectra continue to redshift and appear to be in a transitionary phase at the optimal 60 wt% $PC_{71}BM$ blend ratio. Further examination shows that the photon energy corresponding to the maximum emission intensity (E max) for the 60 wt% $PC_{71}BM$ blend was strongly voltage-dependent, where under injection conditions of $\leq$ 40 mA/cm^2 the spectrum resembles that of the 67 wt% $PC_{71}BM$ device, but with increased current it shifts rapidly to resemble the 50 wt% $PC_{71}BM$ (Figure 2.6b). This luminescence transition, consistent with our charge extraction data, is an indicator of the important DoS evolution that takes place over a relatively narrow composition range. While the optimal 60 wt% $PC_{71}BM$ device EL was sensitive to injection conditions, the relative spectral intensities of the 50 wt%

$PC_{71}BM$ and 67 wt% $PC_{71}BM$ blends were insensitive to injection, which is similar to what has been found for other polymer:PCBM systems.[139]

Looking closer at the blend EL spectra in Figure 2.6a, they appear to be composed of primarily two emission bands: one with peak intensity around ∼1.0-1.15 eV and the other at ∼1.4 eV. In order to quantitatively assess this observation, we reduced and deconvoluted each spectrum into two Gaussian emission profiles,[109] attributing the higher-energy Gaussian at ∼1.4 eV to pure polymer emission and the low-energy Gaussian centered around ∼1.1 eV to CT-state emission (Figure B.1). The presence of PBDTTT-C singlet activation in the electroluminescence spectra is consistent with the findings of Faist *et al.*[140] for the case where the donor has an optical band gap of < 1.7 eV ($E_{g,\text{PBDTTT-C}} \approx 1.6$ eV) and the donor/acceptor CT-energy is near the singlet energy of one of the pure materials. Based upon this finding, we hypothesize that, in this case, the CT energy is quite close to the polymer's singlet energy and the DoS modulation from fullerene loading significantly affects the singlet activation process. Faist *et al.*[140] qualitatively found that singlet activation of one component correlated with reduced photovoltaic performance, which is in agreement with the case here, where the poorly performing 50 wt% $PC_{71}BM$ blend shows by far the most singlet activation, followed consecutively by the electrically superior 60 wt% $PC_{71}BM$ and 67 wt% $PC_{71}BM$ compositions (Figure B.1). A number of photophysical processes can be activated when the blend energy levels are brought in too close proximity;[141,142] however, in this instance, it appears that injected electrons on the $PC_{71}BM$ can more easily transfer onto the PBDTTT-C for cases with less $PC_{71}BM$ loading. This effect would partially nullify the physical separation of charges by material phase segregation, leading to the observed higher nongeminate recombination rates for lower fullerene loadings. It may also seem likely that, in addition to the nongeminate losses detailed above, the 50 wt% $PC_{71}BM$ blend suffers more geminate recombination due to a smaller driving force for interfacial charge separation. However, we note that transient absorption measurements (Figures S3-S5) found strong generation yields for all the compositions studied herein and even a strong polaron yield for neat PBDTTT-C.

For further verification of the connection between our EL and optoelectronic measurements, we take the reduced CT emission band's center of gravity (E_{CT}) and plot it against the V_{oc} at equivalent active-layer charge densities (Figure 2.6c). We find for the case of V_{oc} ($n = 2 \times 10^{16}$ cm^{-3}) and for

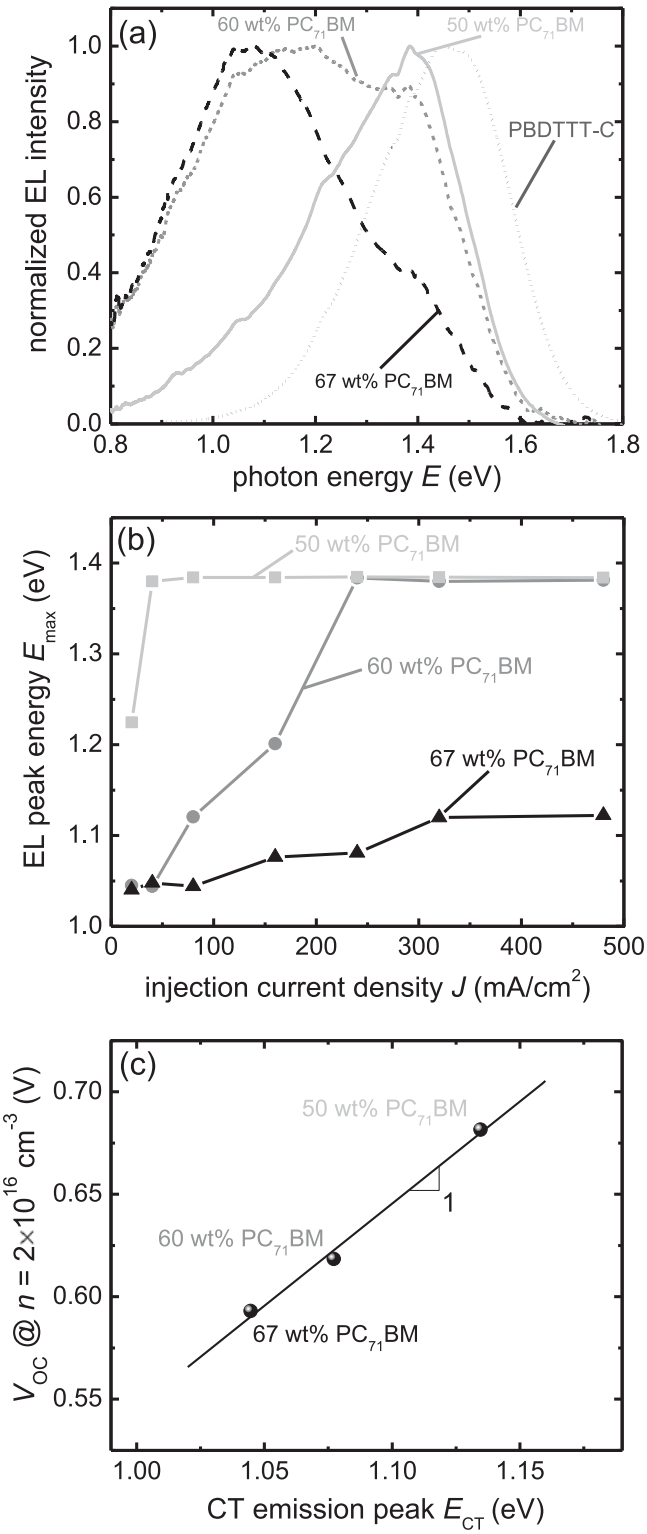

Figure 2.6: (a) Electroluminescence spectra of the different blend films and pure PBDTTT-C (all at J = 160 mA/cm^2). (b) Shift in the EL emission maximum with injection conditions. (c) The linear relationship between CT emission band peak position (at J = 80 mA/cm^2) and V_{OC} at equal carrier concentrations.

EL injection conditions of J = 80 mA/cm^2 that the CT emission band's center of mass and V_{oc} scale on precisely a 1-to-1 basis. We note that the CT emission band's center of mass varied weakly with injection conditions (Figure B.2) and that the slopes also varied marginally with different V_{oc} (n = constant). Despite these variations, we found that plots of V_{oc} (n = constant) vs. E_{CT} were always linear with slopes near unity. Thus, the offset between open-circuit voltages of different compositions at equivalent carrier densities are reproduced well by our EL analysis, indicating that EL reflects the same DoS that is measured with charge extraction.

Despite significantly different chemical structures, polymer:PCBM stoichiometries, and optimization conditions, similar relationships between PCBM composition, V_{oc}, and E_{CT} have been reported for other conjugated polymer:PCBM blends.[109,110,112] These prior studies have also found that V_{oc} scales with the CT-state energy in an expected 1-to-1 fashion.[110,143] Primarily two explanations have emerged regarding the observed interrelation between PCBM content, V_{oc}, and E_{CT}: (i) the V_{oc} and CT-state energy decrease with increasing PCBM content due to an increase in the relative dielectric constant of the film,[112] and/or (ii) nanoscale crystallization due to added PCBM stabilizes the LUMO energy[144] and thus decreases the V_{oc} and redshifts the CT-state emission.[107,109] Considering the work of Piersimoni *et al.*[107] and Jamieson *et al.*,[113] and because this effect is witnessed over several different polymer/fullerene systems, we believe that morphological differences are the primary cause for such trends. Additionally, Agostinelli *et al.*[145] found that the refractive index of P3HT:PCBM BHJs was only weakly dependent on composition, which further suggests that a change in relative dielectric constant could not fully account for these trends. Composition-induced $PC_{71}BM$ aggregation would be consistent with our $n$vs. V_{oc} and EL data for the reasons stated above; however, it is difficult to hypothesize about microstructural changes without direct evidence. It is presently unclear whether a change in the density of states with composition as observed for PBDTTT-C:$PC_{71}BM$ blends could be a general feature of polymer:PCBM systems. Given that the energy of the charge transfer state electroluminescence typically shifts with composition in various polymer:PCBM blends but not necessarily with other fullerene-based acceptors,[107,109,110,113] our data could be revealing as to why PCBM works so well with an array of different polymers.

2.3 Conclusions

In summary, we find that the dominant recombination mechanism in optimized PBDTTT-C:$PC_{71}BM$ solar cells is of non-Langevin and nongeminate character. Our assumptions regarding recombination are supported by accurate *J-V* reconstructions at multiple light intensities for all the blend compositions examined. Moreover, both the carrier lifetime and the effective drift mobility increase with $PC_{71}BM$ loading, directly opposite to what one would expect if Langevin-type kinetics dominated. Using electroluminescence spectroscopy and charge extraction measurements, we show that increased fullerene loading in this range energetically narrows and/or increases the magnitude of the DoS active in solar cell operation. This significant change in the DoS was not strongly refl ected in V_{oc} measurements because of a concomitant decrease in carrier lifetime. From a cell efficiency standpoint, we conclude that the poor electronic properties of the 50 wt% $PC_{71}BM$ blend do not permit higher active-layer thicknesses that would lead to increased light absorption, whereas the higher wt% $PC_{71}BM$ devices are able to reach the first active-layer absorption maximum without significant nongeminate losses.

2.4 Experimental Section

Device Fabrication and Characterization: PBDTTT-C:$PC_{71}BM$ is optimized with $\sim$6 higher molar ratios of fullerene to polymer-repeat unit than P3HT-like systems.[144] The most effective optimization procedure for these high-performance PBDTTT:$PC_{71}BM$ BHJs often includes the addition of $\sim$3% v/v 1,8-Diiodooctane (DIO) as a solvent additive, thin active layers of $\sim$100 nm or less, compositions with higher weight fractions of $PC_{71}BM$ than polymer, and no need for solvent or thermal annealing.[21,106,114,146]

To make devices, indium-tin oxide (ITO) coated glass substrates were sequentially sonicated in acetone and isopropyl alcohol for 15 minutes, followed by drying with compressed N_2. The substrates were then loaded into a UV ozone reactor for 7 minutes of further cleaning and surface treatment in a 0.2 mbar oxygen/ozone atmosphere. Immediately following ozone treatment, the PEDOT (CLEVIOS P VP Al 4083) solution was spin coated directly from a 0.2 μm GHP membrane

filter to give a ∼30 nm thick film, which was then annealed at 140°C for 15 min. While still at temperature, the PEDOT coated substrates were loaded into a N_2 atmosphere glove box (< 1 ppm H_2O) and allowed to cool. At least one day prior to spin coating, the active-layer solutions were prepared from various weight ratios of $PC_{71}BM$ (Solenne or Nano-C) and PBDTTT-C (Solarmer). All solutions employed 1,2-dichlorobenzene (DCB) as the solvent and contained 1,8-diiodooctane (3% v/v) purchased from Sigma- Aldrich. We held the concentration of PBDTTT-C in DCB constant at 10 mg/ml for all solutions, while the $PC_{71}BM$ concentration was varied from 10 mg/ml (50 wt% $PC_{71}BM$), to 15 mg/ml (60 wt% $PC_{71}BM$), to 20 mg/ml (67 wt% $PC_{71}BM$). The dry materials for each solution were weighed in ambient conditions, and the solvents were added in a N_2 atmosphere glove box. Devices made at ICL were spun coat from each of these blend solutions onto the PEDOT covered substrates at various spin speeds (Figure 2.2) for 40 s. Devices made at UCLA (Table 2.1) were made from identical procedures as described above, save for slightly different parameters due to inherent equipment variability. The presented transient optolectronic analysis is from the devices summarized in Table 2.1; however, the same trends in the transient data were found on devices made at ICL (Figure 2.2). After spin coating the active layer, we deposited Ca/Al electrodes to create devices with active areas of 4.5 mm^2 or 10 mm^2. To add the electrodes, we first deposited 10-20 nm of Ca at a pressure of 1-2.3 $\times 10^{-6}$ mbar and a rate of 0.5 Å/s, followed by a deposition of 100 nm at a rate of 1 Å/s. Before the shutter was opened in each case, ∼20 nm of metal was evaporated off to ensure purity. The final device structure was ITO/PEDOT/PBDTTT-C:$PC_{71}BM$/ Ca/Al.

The *J*-*V* characteristics in Figure 2.2 were obtained under simulated AM 1.5G illumination using a xenon lamp with a water IR filter. The *J*-*V* measuremtents in Table 2.1 were taken under simulated AM 1.5G illumination using an Oriel 9600 solar simulator. All *J*-*V* measurements were obtained with a Keithley 2400 sourcemeter, and the light intensity was calibrated with an IR cutoff filter equipped silicon photodiode.

TAS: Transient absorption spectroscopy was carried out in transmission mode on samples consisting of ITO/PEDOT/PBDTTT-C: $PC_{71}BM$, which were processed in identical fashion as those made into devices. The pump beam was selected to be at 650 nm, exciting PBDTTT-C, while the probe beam was at 1190 nm, around the absorption maximum of polarons in the 60 wt% $PC_{71}BM$ system (Figure B.3). The pump excitation was performed with a OPO Nd:YAG laser

(Opotek LD 355) at 5 Hz and was varied from 0.25-6 μJ/cm^2 pulse fluence (Figure B.4). The probe beam was monitored by a InGaAs Hamamatsu G83 70-82 photodetector amplified by a Costronics 2004 Optical Transient Amplifier connected to a Tektronix TDS220 digital oscilloscope.
TPC/TPV/CE: We performed charge extraction, transient photocurrent, and transient photovoltage measurements and analysis in exact accordance with that detailed previously.[87–91]

Electroluminescence: Electroluminescence was measured using a Princeton Instruments Acton SP 2500 spectrograph combined with a liquid nitrogen-cooled InGaAs photodiode array (Acton OMAV:1024). The spectral intensity was corrected with the spectrum from a calibrated halogen lamp.[139, 140]

2.5 Supporting Information

Supporting Information is available in Appendix B.

CHAPTER 3

Band tail recombination in polymer:fullerene organic solar cells

3.1 Introduction

Organic bulk heterojunction (BHJ) solar cells based on polymer:fullerene blends have increased rapidly in efficiency due to the introduction of optimized new materials and the improvement of device architecture.[84, 147–149] Present devices are largely limited by the compromise between optical absorption and fill factor.[150] Thicker devices typically absorb more of the incident light but also have increased recombination due to the need to collect charge over a longer distance and at a lower internal electric field. It is therefore important to reduce the recombination to achieve higher efficiency, and hence it is important to understand the recombination processes in detail. Several recombination mechanisms have been studied in BHJ devices, including geminate and Langevin recombination, as well as recombination through localized (trap) states.[149] Since BHJ cells use disordered materials, there is a strong theoretical expectation and significant experimental evidence for the presence of localized band-tail states. Thus, it is reasonable to expect that band tail states also play a significant role in the recombination of mobile carriers.

Along these lines, this paper aims to develop and test a recombination model for the forward-bias dark current in BHJ solar cells based on an exponential distribution of localized band-tail states and the Shockley-Read-Hall mechanism. We demonstrate the validity of the model by analyzing the dark diode ideality factor as a function of temperature in several different BHJ materials systems. The photocurrent spectral response (PSR) as well as numerical drift-diffusion modeling are used to verify the model predictions.

3.2 The Dark Diode Current Ideality Factor

The dark diode current in low forward bias is characterized by an exponential dependence on voltage (V) that goes like $\exp\left(\frac{qV}{n_{id}kT}\right)$ with an ideality factor n_{id}. The exponential region corresponds to small current-density values where the magnitude of the drift and diffusion components in the recombination zone outweighs the total current, which minimizes the influence of transport and contact effects. The diode ideality factor is characteristic of the recombination mechanism. For the classic models, band-to-band or Schottky contact recombination gives $n_{id} \approx 1$, while Shockley-Read-Hall (SRH) recombination through midgap traps gives $n_{id} \approx 2$.[151–153]

Most BHJ solar cells have room temperature ideality factors measured by the dark diode current of $\sim$1.3-2,[154–157] and so the associated recombination mechanisms are not immediately apparent. Several papers attribute this intermediate ideality factor to the presence of a distribution of localized states, including band-tail states,[133–135] but a direct experimental connection between n_{id} and the measured band-tail slope has not been fully explored. Some experimental data already suggest the importance of band-tail recombination and even correlate the ideality factor with the band-tail slope.[158] However, the ideality factor is also influenced by the presence of other deep states that provide a separate recombination channel. For instance, the ideality factor increases when deep traps are induced by exposure to radiation in both poly[carbazole-dithienyl-benzothiadiazole):phenyl-C_{61}-butyric acid methyl ester (PCDTBT:PCBM) and poly(3-hexyl thiophene) (P3HT):PCBM solar cells.[159] Hence, the ideality factor may reflect more than one recombination mechanism, and the dominant mechanism may depend on the specific material and device condition. The ideality factor can also be obtained from the light intensity dependence of the open-circuit voltage (V_{oc}). Reports of this measurement in organic BHJ solar cells have included discussion of whether the dark and illuminated ideality factors are the same or different.[154,157]

The ideality factor can also be measured in single carrier devices. In such structures, bulk electron-hole recombination is excluded so that the ideality factor will therefore generally be different, and is usually associated with the Schottky contact.[154] Single carrier devices also exhibit pronounced space charge limited current transport.

There have been various attempts to model the ideality factor of organic diodes. This can

be done by solving the drift-diffusion equations with assumed recombination mechanisms and contact boundary conditions.[133,135] Early calculations of current-voltage behavior assume either geminate or Langevin-type recombination and have generally neglected the presence of band-tail states.[160,160–163] Giebink *et al.*[164,165] give an analytical model for the dark forward current, including the presence of band-tail states, but the analysis is for a planar heterojunction diode rather than a BHJ structure. The first analysis of the dark current ideality factor which assumed an exponential band-tail density of states $\exp(E/E_0)$ was by van Berkel *et al.*[166] and gave for the ideality factor,

$$\frac{1}{n_{id}} = \frac{1}{2} + \frac{kT}{2E_0} \tag{3.1}$$

Various authors have recently derived or used the same or a similar relation in the context of organic bulkheterojunction solar cells.[133–135] However, we show that Eq. (3.1) fails to account for thermal emission from traps.

3.3 Shockley-Read-Hall Analysis of Band Tail Recombination

The assumed BHJ cell energy band structure is shown schematically in Figure 3.1. Electrons are injected from the cathode and move in the fullerene lowest unoccupied molecular orbital (LUMO), holes are injected from the anode and move in the polymer

highest occupied molecular orbital (HOMO), and recombination occurs at the distributed interface between the polymer and fullerene domains. The presence of localized band-tail states is well documented, and current flow in disordered semiconductors is generally described in terms of a transport energy that separates mobile states and localized band-tail states.[135,155,167,168] In forward bias, the occupancy of states by electrons and holes are described by quasi-Fermi energies (qFE), which are indicated along with the various parameters in the figure. Figure 3.1(b) shows the density of states with exponential band tails. The Shockley-Read-Hall (SRH) mechanism[151–153] assumes capture and thermal emission of electrons and holes through trap states with a state density N_t at a

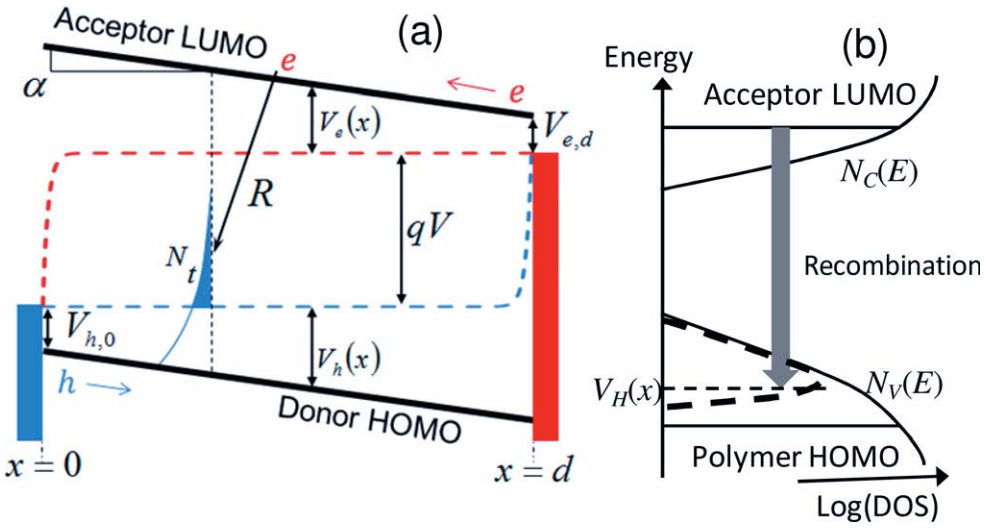

Figure 3.1: (a) Band diagram for the BHJ cell under forward bias, showing the quasi-Fermi energies (dashed lines) and various parameters. (b) The assumed density of states distribution with an exponential distribution of band-tail states. The equilibrium trapped hole concentration which peaks at the qFE is indicated.

trap energy E_t, leading to a recombination rate,

$$R_{\text{SRH}}(E_t) = R_{e,h}^{D,A} - G_{e,h}^{D,A} = \frac{c_n c_p N_t(E_t)}{c_n(n+n_g) + c_p(p+p_g)}\left(np - n_i^2\right) \tag{3.2}$$

where the terms are defined in Chapter 1 Eqns. (1.26)-(1.28) and Figure 1.9. For definiteness, the model assumes a broader exponential band tail on the HOMO with slope E_0 and a narrower band tail on the LUMO, which is probably the situation in most BHJ cells. The opposite situation in which the LUMO band tail is broader than the HOMO band tail will give an equivalent result.

There are three main recombination transitions to consider: between mobile states at or above the transport energy, between a mobile state and a localized band-tail state, and between two localized band-tail states. Recombination between localized states has a very low probability because the states are physically separated and can only recombine by tunneling, and at the typical electron and hole densities ($\sim 10^{16}\text{cm}^{-3}$) the average separation is large and hence the tunneling probability is very small. When $E_0 > kT$ for the wider band tail, the majority of carriers are in the band tail rather than being in mobile states, and the ratio can be 100-1000, which is also related to the ratio of the free and trap-limited mobility. Hence, we expect that recombination from a mobile state in the fullerene LUMO to a localized band-tail state in the polymer HOMO is much more probable

than transitions between mobile states, and thus this is the mechanism we analyze. Several others have reached the same conclusion for organic BHJ devices and other diodes.[134,135,169] All of the possible recombination transitions in the BHJ cell are between an electron in the fullerene and a hole in the polymer and so necessarily involve a tunneling component across the interface.

Analysis of the SRH mechanism usually makes a simplifying assumption that the energy level(s) of the recombination centers either lie between the quasi-Fermi energies or outside of them. In many situations, the relative energy of the qFE and the recombination center can change with the illumination intensity and temperature, etc. For recombination centers lying between the qFEs where thermal emission is negligible, the recombination rate simplifies to,

$$R_{\mathrm{SRH}}(E_t) = \frac{c_n c_p N_t(E_t) np}{c_n n + c_p p} \tag{3.3}$$

The band tail recombination model presents an unusual situation for the SRH analysis. As shown in Figure 3.1(b), the population of trapped holes, which are herein the presumed recombination centers, peaks at the qFE because the hole density drops off at higher energy due to the band tail density of states and falls off at low energy due to the Fermi function. Hence neither of the usual simplifying assumptions applies since the recombination centers are at, or very close to, the qFE. Furthermore, provided that the qFE stays within the band tail distribution, the recombination centers remain at the qFE, independent of temperature, light intensity, and position in the device.

In terms of the SRH equation (Eq. (3.2)), our model assumes that electron-emission barrier is large enough that thermal excitation of electrons is negligible, while hole-emission barrier is small enough that the trapped holes are in thermal equilibrium with the mobile holes. The validity of these assumptions is discussed below. For the band diagram and the parameters shown in Figure 3.1(a), the mobile electron n and hole p concentrations as a function of position x and applied bias are,

$$n(x) = N_{\mathrm{C}} \exp\left(-\frac{V_e(x)}{kT}\right) \tag{3.4}$$

$$p(x) = N_{\mathrm{V}} \exp\left(-\frac{V_h(x)}{kT}\right) \tag{3.5}$$

$V_h(x)$ and $V_e(x)$ are the separation of the qFE and the HOMO and LUMO band edges as a function of position. The density of recombination centers $N_t(x)$ is approximated to the density of states in the exponential band-tail states above the quasi-Fermi energy (assuming a low temperature Fermi function),

$$N_t(x) = N_c \exp\left(-\frac{V_h(x)}{E_0}\right) \tag{3.6}$$

By straightforward kinetics, the total electron recombination rate is the product of the electron density, the hole trap density, and the recombination rate constant, integrated across the device,

$$R = \int_0^d c_n n(x) N_t(x) dx \tag{3.7}$$

$$= c_n N_c N_v \int_0^d \exp\left(-\frac{V_h(x)}{E_0}\right) \exp\left(-\frac{V_e(x)}{kT}\right) dx \tag{3.8}$$

Assuming a linear band profile for the cell of thickness d,

$$V_h(x) = V_{h0} + \alpha x \tag{3.9}$$

$$V_e(x) = V_{e0} + \alpha (d - x) \tag{3.10}$$

then,

$$R = c_n N_c N_v \exp\left(-\frac{V_{e0}}{kT}\right) \exp\left(-\frac{V_{h0} + \alpha d}{E_0}\right) \int_0^d \exp\left(-\alpha(d-x)\left(\frac{1}{kT} - \frac{1}{E_0}\right)\right) dx \tag{3.11}$$

Since E_0 is larger than kT, the exponent in the integral is negative and has its largest value when $x = d$, so that most of the current flows on the cathode side of the cell. Equations (3.9) and (3.10) and the parameters in Figure 3.1(a) give,

$$E_g = V_{h0} + V_{e0} + \alpha d + qV \tag{3.12}$$

$$V_{h0} + \alpha d = E_g - V_{e0} - qV \tag{3.13}$$

where EG is the interface band gap between the polymer HOMO and the fullerene LUMO. The built-in potential is $qV_{\text{BI}} = E_g - V_{h0} - V_{e0}$ (same as Eqn. (1.23)), and thus $\alpha d = q(V_{\text{BI}} - V)$. V_{e0} and V_{h0} are the Schottky energy barriers at the electron and hole contacts, respectively. The dark current is the excess integrated recombination rate relative to $V = 0$,

$$J_D(V) = \beta q d c_n N_{\text{C}} N_{\text{V}} \exp\left(-\frac{V_{e0}}{kT}\right) \exp\left(-\frac{E_g - V_{e0}}{E_0}\right) \left[\exp\left(\frac{qV}{E_0}\right) - 1\right] \tag{3.14}$$

The dimensionless parameter β is,

$$\beta = s\left[1 - \exp\left(-\frac{1}{s}\right)\right] \tag{3.15}$$

$$s = \frac{1}{q(V_{\text{BI}} - V)} \frac{E_0 kT}{E_0 - kT} \tag{3.16}$$

and the ideality factor for this model is from Eq. (3.14),

$$n_{id} = \frac{E_0}{kT} \tag{3.17}$$

The model therefore predicts that the slope of the diode region of the dark current is independent of temperature (apart from any temperature dependence of E_0) and that $n_{id}kT$ is equal to the band-tail slope.

Equation (3.17) is manifestly different from Eq. (3.1), which was also obtained from SRH analysis of a similar situation. The difference is that Eq. (3.1) used the approximation of Eq. (3.3) that the recombination centers are between the qFEs and hence neglects thermal emission. A consequence is that the dominant recombination traffic is forced to be at the center of the device $x = d/2$ where $n \approx p$, and with this added condition, Eq. (3.1) follows from Eqs. (3.4)-(3.6). However, Eq. (3.3) is not appropriate for band tail recombination since the active traps are at the qFE, as discussed above. Equation (3.3) omits the SRH term governing the thermal population of the recombination centers, but the assumption of a flat qFE requires a thermal equilibrium hole population. Equations (3.14) and (3.17) result when recombination is allowed to be throughout the device and the analysis shows that the dominant recombination is closer to the cathode rather

than in the center of the device. Tzabari and Tessler also discuss the need to include the thermal excitation terms in Eq. (3.2) for the case of shallow hole traps.[170]

Under some experimental conditions, the qFE might not be flat across the device, and in particular the hole qFE will move up near the cathode if the recombination traffic is such that hole thermal equilibrium cannot be maintained across the device, for example, from transport limitations. In this case, the maximum current is at $x < d$. The dependence of current on voltage for this case is obtained by evaluating the integrand in Eq. (3.8) for an arbitrary value of x and using Eqs. (3.9)-(3.13) to derive the exponential voltage dependence. This calculation leads to,

$$\frac{1}{n_{id}} = 1 - \frac{x}{d}\left(1 - \frac{kT}{E_0}\right) \tag{3.18}$$

which reduces to Eq. (3.1) for $x = d/2$ and Eq. (3.17) for $x = d$.

An exponential band tail is well known to result in dispersive transport, characterized by a dispersion parameter $\alpha_{tr} = kT/E_0$. Hence an interesting relation is that when charge transport and recombination both arise from the band tail states, then $n_{id}\alpha_{tr} = 1$.

3.4 Experimental Results

3.4.1 Experimental methods

Three different well-performing BHJ solar cells were used in these studies. P3HT:PCBM and PBDTT-DPP:PCBM cells were fabricated at UCLA, and PCDTBT:PCBM devices were made at UC Santa Barbara. The details of the device fabrication are described elsewhere.[29,171,172] The P3HT:PCBM cell fabrication used the solvent annealing approach, which gives a high degree of polymer crystallinity. Measurement of the steady-state dark current was made with the devices mounted in an evacuated variable-temperature cryostat and measured by a Keithley 6487 picoammeter. The PSR measurement was made with a monochromatic light source using lock-in amplifier techniques as described elsewhere.[158,167] The PSR signal is normalized to the power of the incident light. The light intensity dependence of the open-circuit voltage was made with a white light emitting diode module (Helieon 1200 lm), using a silicon photodiode and a Keithley 6487

picoammeter to monitor the light intensity. To minimize heating, the devices were only illuminated for ∼1-2 s at each light intensity.

3.4.2 Experimental measurements

Figure 3.2 shows examples of the dark forward bias current-voltage $J_D(V)$ characteristics for the three different polymer:PCBM blends at temperatures between ∼180 and 330 K. The slope of the exponential region of the diode current is evidently not strongly temperature dependent and hence the ideality factor changes with temperature, contrary to predictions by the classic models of the diode dark current. The ideality factor was extracted by two methods: the first method was from fits to the dark diode equation,

$$J_D(V) = J_0 \left[\exp\left(\frac{q(V - JR_s)}{n_{id}kT} \right) - 1 \right] + \frac{V - JR_s}{R_{sh}} \tag{3.19}$$

where R_s is the series resistance and R_p is the parallel shunt resistance. The fit is performed by using measured values of $J_D(V)$ to evaluate the right hand side of Eq. (3.19). The lines in Figure 3.2 are fits to this equation. The second method was from the function,

$$n_{id}kT = q \min\left(\frac{dV}{d\ln(J_D(V))} \right) \tag{3.20}$$

which is from the steepest slope of the exponential region in a semi-log plot. The $J_D(V)$ data show typical series and shunt resistances, although the shunt resistance for the P3HT:PCBM cell was particularly high and so the exponential region extends over a larger voltage range. The P3HT:PCBM series resistance was not accurately ohmic and probably includes a significant space-charge limited current or other non-Ohmic contributions,[173] thus the data were only fitted over a limited voltage range over the series-resistance region.

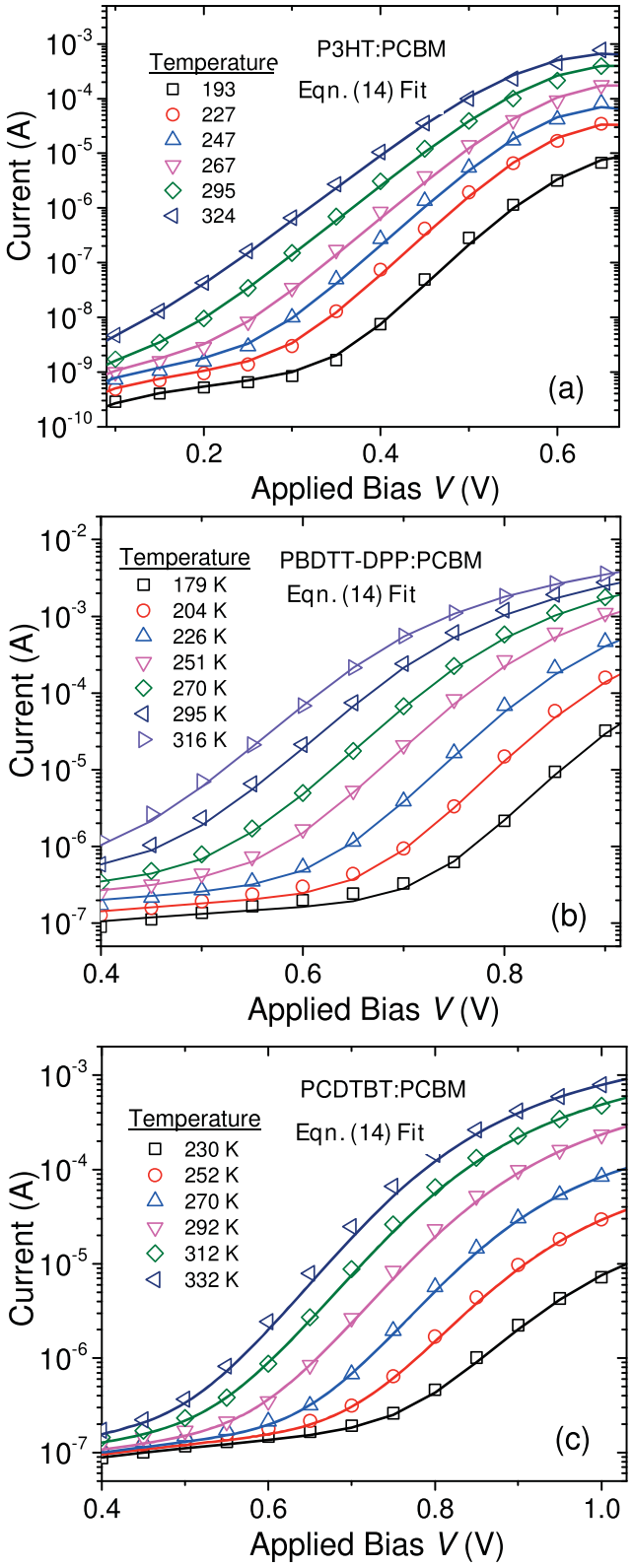

Figure 3.2: Dark current voltage characteristics at various temperatures as indicated, for the three different BHJ solar cells (a) P3HT:PCBM (b) PBDTTDPP: PCBM (c) PCDTBT:PCBM. The points are data and the solid lines are fits to the diode equation Eq. (3.19).

The exponential slope factor $n_{id}kT$ is shown in Figure 3.3 as a function of temperature. The data for P3HT:PCBM and PBDTT-DPP:PCBM show both methods of extraction from Eqs. (3.19) and (3.20), and the results differ by no more than 2 meV, which is roughly the uncertainty in the fit to Eq. (3.19). The PCDTBT:PCBM data show results from two different samples. The values of $n_{id}kT$ are weakly dependent on temperature, increasing slightly for P3HT:PCBM and PBDTT-DPP:PCBM, and either flat or decreasing for PCDTBT:PCBM. Others have also reported polymer:fullerene current-voltage characteristics that, by inspection, have weakly temperature dependent values of $n_{id}kT$.[156,174] Hence, it is more appropriate to examine the actual slope factor $n_{id}kT$ rather than n_{id} alone.

An independent measurement of the band-tail slope is needed to evaluate the recombination model. Several experiments have provided estimates of the slope of the band tail in BHJ cells, but the resulting values are widely varying.[134,167,168,175,176] We use the photocurrent spectral response (PSR) technique, which measures the optical absorption of excitations that generate photocurrent, including bulk exciton absorption, charge-transfer absorption, and localizedstate transitions.[167,177] There is significant precedent for the use of a PSR-like technique to characterize the sub-gap electronic structure of inorganic amorphous solids.[178–180] In bulk-heterojunction organics, we typically observe a PSR that has an exponential slope at energies below the charge transfer (CT) band gap, which we have interpreted as corresponding to the slope of the wider band tail.[167] Experimental evidence for this interpretation of the PSR exponential slope is that the same value of band-tail slope is deduced from transient photocurrent measurements in P3HT:PCBM and PCDTBT:PCBM using a dispersive transport model.[167,168] The CT absorption may be broadened to a slightly larger value than E_0 by the convolution of the valence band and conduction band density of states and may also be broadened by electron-phonon coupling. However, we foresee no mechanism by which the CT absorption measured by PSR can have an exponential slope that is substantially steeper than the wider of the two band tails.

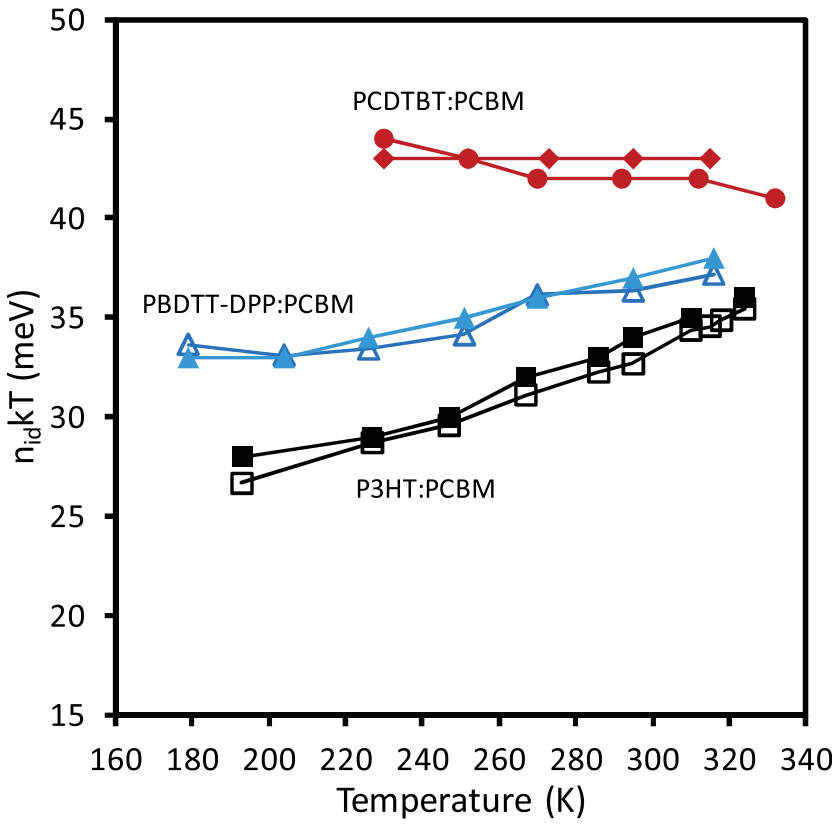

Figure 3.3: Measured values of $n_{id}kT$ for the three solar cells in Figure 3.5. The P3HT:PCBM and PBDTT-DPP:PCBM data show values obtained from the fit to Eq. (3.19) (filled symbols) and from Eq. (3.20) (open symbols). The PCDTBT:PCBM data is for two different samples using Eq. (3.19) (filled diamonds and circles).

Room temperature PSR data are shown for the three devices in Figure 3.4 and the temperature dependence of the exponential band-tail slope for P3HT:PCBM is shown in the inset. The arrows show the approximate energy of the CT band gap EG and there is a region of exponential absorption at lower energy. The room temperature PSR band-tail slopes are $E_0 = 32$, 27, and 47 meV, respectively, for P3HT:PCBM, PBDTT-DPP:PCBM and PCDTBT:PCBM. The PCDTBT: PCBM and PBDTT-DPP:PCBM PSR spectra have a clear change of slope at low absorption, suggesting the presence of other deep trap states, but P3HT:PCBM has a more extended exponential region. The band-tail slope of P3HT:PCBM shows a small temperature dependence of E_0, which is also comparable to the temperature dependence of $n_{id}kT$. The band tail state distribution may have some thermal broadening which can explain the observed weak temperature dependence of the slope.

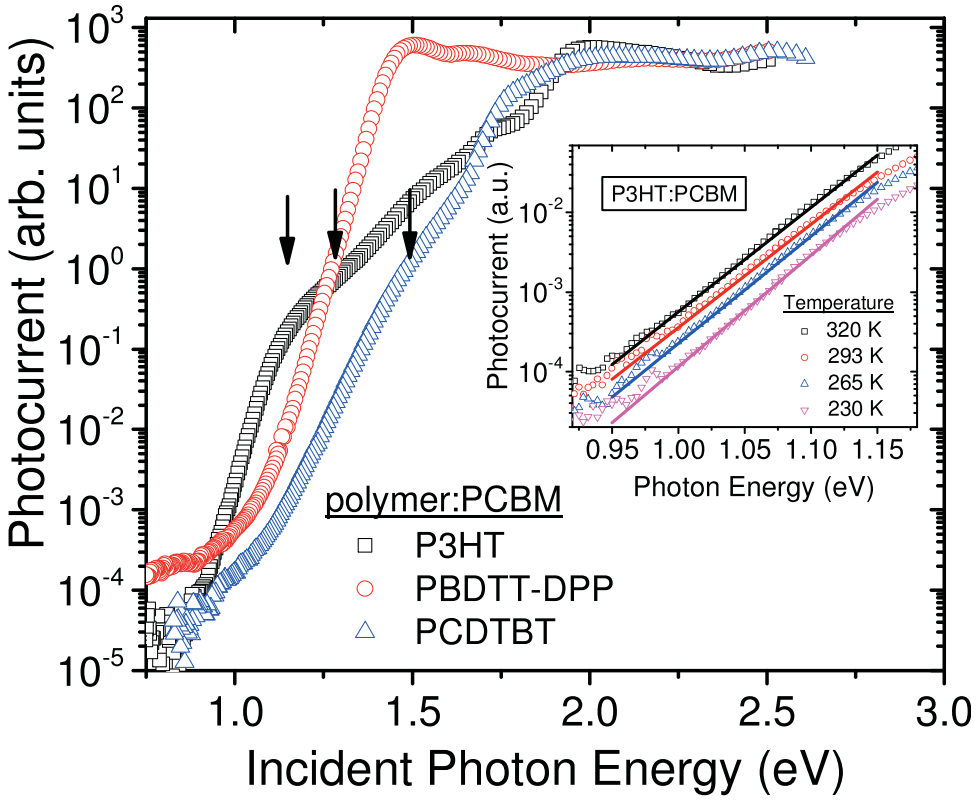

Figure 3.4: Photocurrent spectral response measurements for the three different solar cells. The arrows indicate the approximate location of the charge transfer band gap EG and the band-tail slope is measured from exponential region at lower energy. The inset shows the exponential region for P3HT:PCBM at different temperatures (data are offset vertically for clarity).

Figure 3.5 shows the complete fit of the SRH model Eq. (3.14) to the $J_D(V)$ data for the three solar cells, including the series and shunt resistance. The analysis is only valid up to the built-in potential, and this is the voltage range of the fit. The fit assumes that E_0 has a small linear temperature dependence, as indicated by the n_{id} data of Figure 3.3 and consistent with the PSR data of Figure 3.4, rather than using independent fit parameters of E_0 for each data set. Figure 3.6 compares the temperature dependence of the fit parameters for $E_0 = n_{id}kT$ from Eq. (3.14) to the measured E_0 from the PSR data. The fit values of E_0 for P3HT:PCBM increase from 31 meV to 36 meV across the temperature range which agrees closely with E_0 measured by PSR. These values are larger than the $n_{id}kT$ values obtained from the fit to the diode equation (Figure 3.3) by about 3 meV. The reason for this small difference is that the β prefactor to Eq. (3.14)

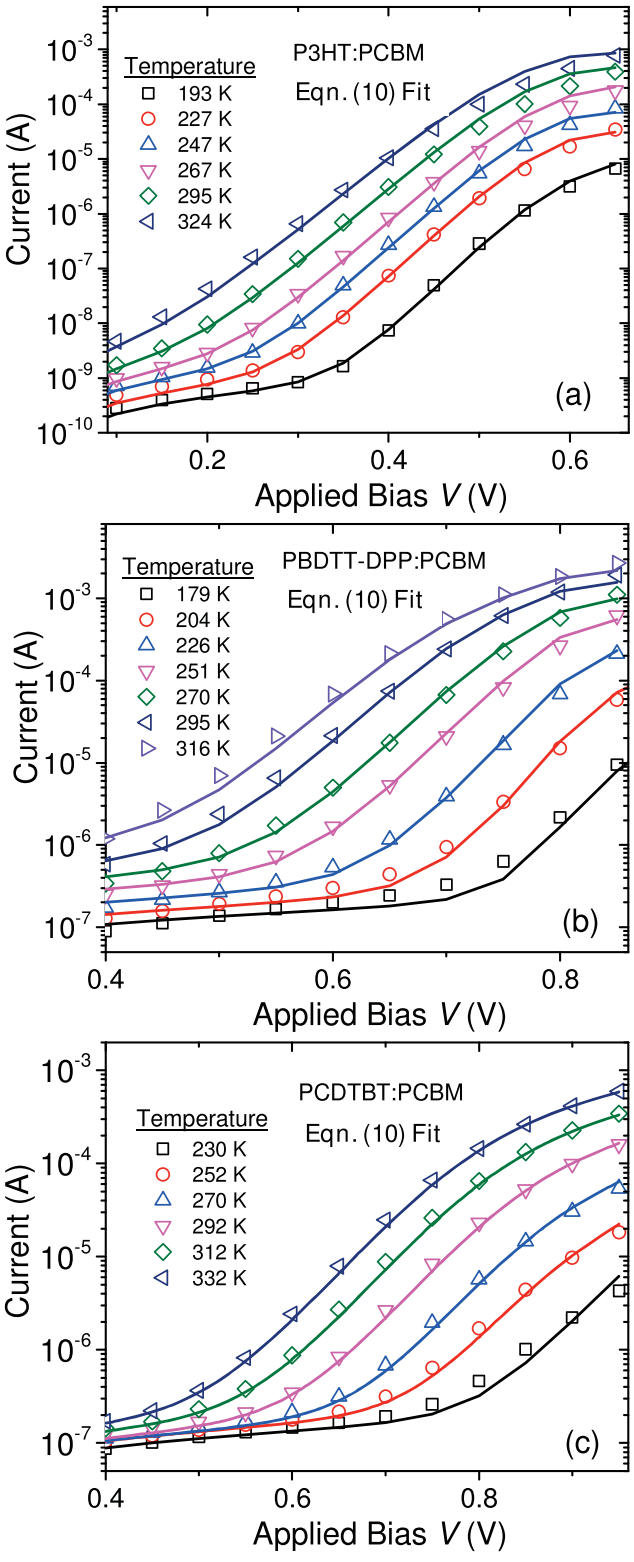

Figure 3.5: Dark current data from Figure 3.2 (points) and the fit to the SRH model Eq. 10 (lines) for the three types of solar cell (a) P3HT:PCBM (b) PBDTTDPP: PCBM (c) PCDTBT:PCBM.

contains terms with both T and V and hence slightly changes the slope of the exponential region compared to the diode equation. The data can also be fit slightly less well with a temperature-independent value of E_0. The PBDTT-DPP:PCBM data assume the same temperature dependence of E_0 as for the dark ideality factor, while the PCDTBT:PCBM is fitted with a constant E_0, as indicated by the data in Figure 3.3. The PCDTBT:PCBM band tail slope may have some temperature dependence,[155] but we chose to fit the data with the temperature dependence in Figure 3.3 for consistency and so as not to introduce another parameter. The fit values of E_0 are also larger than the $n_{id}kT$ values in Figure 3.3 by 2-3 meV for the same reason.

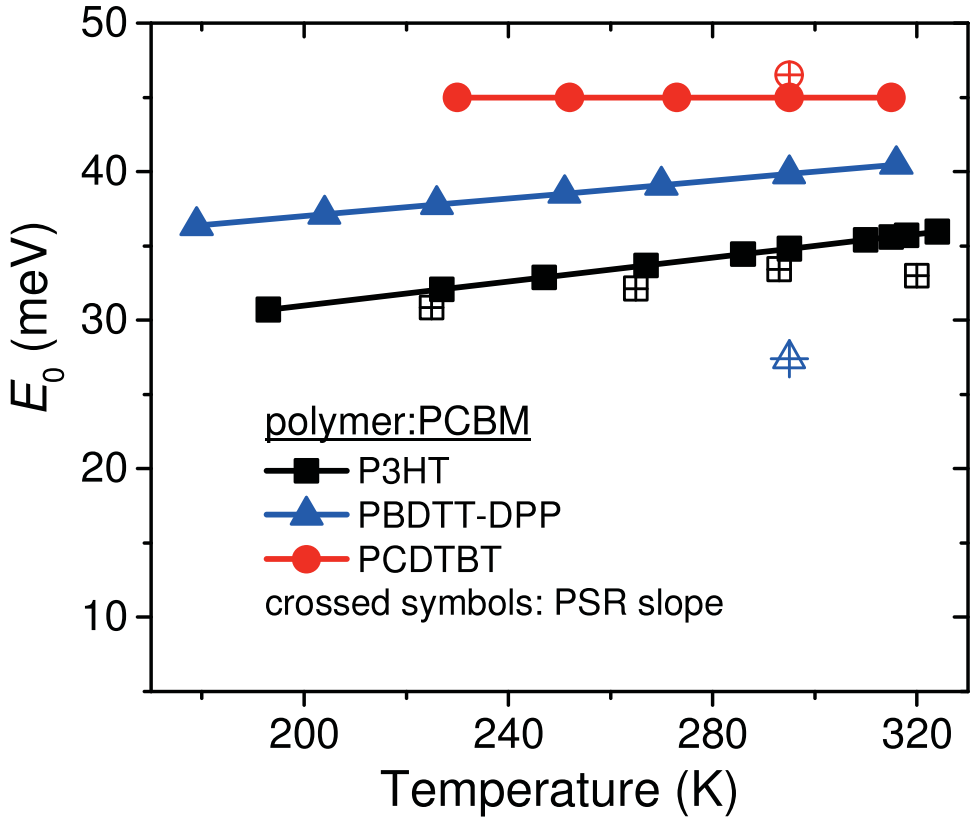

Figure 3.6: Plot of parameter values of $E_0 = n_{id}kT$ (filled points and lines) obtained from the Eq. (3.14) fit to the data in Figure 3.5, compared to the bandtail slope values measured by PSR (crossed open symbols) for the three solar cells.

3.4.3 Ideality Factor Measured from the Open-Circuit Voltage

The solar cell current can be defined as the sum of the dark current and the photocurrent J_{PC}, where J_{PC} is the difference in the measured current under light and dark conditions.[181] Since the current at

V_{OC} is zero, it follows that for an ideal exponential diode-dark current without shunt resistance that J_{PC} and V_{OC} are related by

$$V_{OC} = \frac{n_{id}kT}{q} \ln\left(\frac{J_{PC}(V_{OC})}{J_0} + 1\right) \tag{3.21}$$

$$\cong \text{constant} + \frac{n_{id}kT}{q} \ln\left(Gf(V_{OC})\right) \tag{3.22}$$

The second expression arises because $J_{PC} \gg J_0$ and the reverse bias photocurrent is linear in light intensity G when all the photo-generated charge is collected. The voltage dependent term denoted by $f(V)$ represents the voltage dependence of J_{PC} and reflects the shape of the cell fill factor and all non-ideal processes occurring in the cell.10 In a high fill factor cell, $f(V)$ is constant up to near the built-in potential, but in a low fill factor cell, $f(V)$ will change more rapidly. Hence, the light intensity of V_{OC} is an alternative measurement of the dark ideality factor, but with the benefit that the series resistance does not affect Eq. (3.21) because no external current flows.[157] The shunt resistance, however, does affect Eq. (3.21) and V_{OC} is given by $R_pGf(V_{OC})$ in the region dominated by the shunt resistance.

The open-circuit voltage as a function of incident light intensity is shown in Figure 3.7 for the same devices as for the dark current in Figure 3.2. The strong drop in V_{OC} at low light intensities in Figure 3.7 is due to the shunt resistance as described above. At high light intensity, the slope of V_{OC} vs. $\ln(G)$ flattens off because the $f(V_{OC})$ term in Eq. (3.21) decreases as V_{OC} increases. The photocurrent drops to zero (and changes sign) at the built-in potential so that $f(V_{BI}) = 0$ and therefore V_{OC} is limited to being less than V_{BI}. The flattening of V_{OC} at high light intensity may also have a small contribution from sample heating by the strong illumination because V_{OC} decreases at higher temperature. The built-in potential is indicated in Figure 3.7 and is measured by the voltage at which the cell photocurrent tends to zero, obtained by fitting the voltage dependence of the photocurrent to a simple recombination model.[158] The observed flattening off of V_{OC} at high illumination is consistent with the measured V_{BI} and is independent of the specific

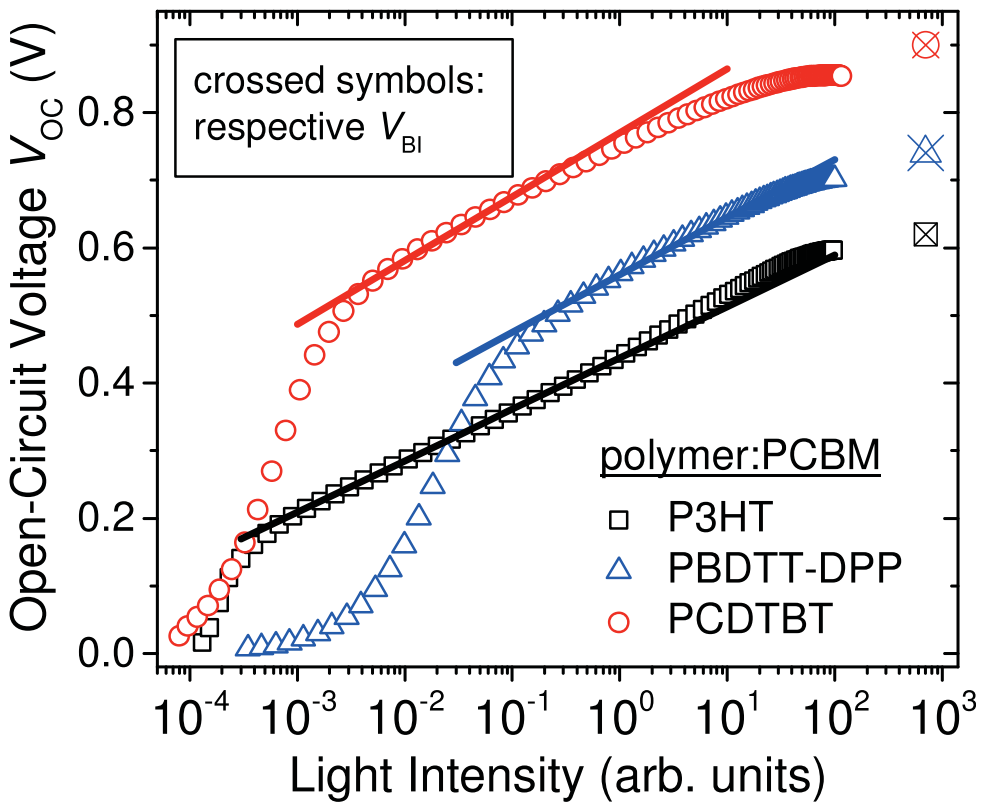

Figure 3.7: The dependence of V_{oc} on incident light intensity for the three different cells. The strong drop in V_{oc} at low light intensity arises from the shunt resistance. The solid lines are the slopes corresponding to the measured dark ideality factors.

recombination mechanism because in principle $f(V)$ can arise from any mechanism. Alternative descriptions of this effect based upon surface recombination dominating at high V_{oc} values have also been given in the literature.[157] The solid lines in Figure 3.7 are slopes corresponding to the measured room temperature darkcurrent ideality factor, adjusted vertically to match the V_{oc} data. The data show that the dark and light ideality factors agree well over much of the expected range. The P3HT:PCBM data show some curvature with an apparently larger ideality factor at high voltage, which is discussed further below. The decrease in V_{oc} due to the $f(V)$ factor is most evident in the PCDTBT:PCBM data.

3.5 Discussion

Figure 3.6 compares the $n_{id}kT$ values from the fit of the data to Eq. (3.14) with the measured E_0 data from PSR. The P3HT:PCBM and PCDTBT:PCBM data show almost perfect agreement with the fit values of $n_{id}kT$ within 2 meV of the measured band-tail slope. The data therefore show that Eq. (3.17) gives almost perfect agreement for P3HT:PCBM and PCDTBT:PCBM but is a less good fit for PBDTTDPP: PCBM where E_0 is 27 meV compared to $n_{id}kT$ of 39 meV at room temperature, which is discussed further below. In addition, the model agrees with data for hydrogenated amorphous silicon, since the predicted slope for $n_{id} \approx 1.5$ at room temperature is $E_0 \approx 38$ meV, which is in good agreement with the measured band tail slope and with the hole mobility dispersion parameter of $\sim$0.6.[182] The agreement with the data strongly indicates that the band tail recombination mechanism dominates in the corresponding materials.

The fits to the data in Figure 3.5 assume values of N_c and N_v of 10^{20} cm^{-3}, and adjusts V_{e0} and c_n. We assume an average value of V_{BI} based on the measured value at room temperature, although V_{BI} likely does vary with temperature.[183] The extracted value of V_{e0} is 0.11 V, 0.28 V, and 0.44 V for P3HT:PCBM, PBDTT-DPP:PCBM and PCDTBT:PCBM, respectively, and the value of c_n is 4×10^{-10} cm^3/s, 1.8×10^{-8} cm^3/s, and 7×10^{-7} cm^3/s for the three materials. Both parameters are sensitive to the temperature dependence of E_0, where reducing the temperature dependence of E_0 increases V_{e0}. The P3HT:PCBM value of V_{e0} is perhaps lower than expected but V_{e0} is itself probably temperature dependent, and the use of contact barrier heights of 0.1 eV or less have been used by others in drift-diffusion modeling to describe various aspects of these cells.[105,157,162] c_n is the product of the capture cross section and the thermal velocity and the fit values are consistent with an atomic scale cross-section of about 10^{-15}-10^{-14} cm^2 and a thermal velocity of $\sim 10^6$ cm/s. Given all the uncertainties in the values, we cannot deduce any parameter with accuracy, but the values are at least consistent with general expectations.

The observation of a significant difference between E_0 and $n_{id}kT$ for PBDTT-DPP:PCBM suggests that another mechanism may be involved, and we propose that this is the added contribution of deeper band-tail states. The PSR data of Figure 3.4 show a change of slope at about 1.1 eV, indicating that there is a substantial density of deep states. More significantly, this change of slope

occurs only about 0.2 eV below the CT band gap and so the broader band of deep states will intersect the hole qFE at relatively high applied voltage, which could therefore easily explain the relatively larger $n_{id}kT$. There is a similar change of slope in the PSR data of PCDTBT:PCBM, but this occurs further from the CT band gap and so will have less influence on the value of $n_{id}kT$ in the observable voltage range. PSR measurements in PCDTBT:PCBM and P3HT:PCBM find that these deep states increase in density as a result of prolonged illumination and they are attributed to defects resulting from C-H bond breaking.[159] It is not yet known if the deep states in pristine samples are of a similar type. A more detailed analysis is needed to calculate the effect on $n_{id}kT$ of these deeper states.

An increase of the ideality factor by the presence of a sufficiently high density of deep states is known from studies of x-ray and light-induced degradation of BHJ cells.[158,159] Figure 3.8 shows that the ideality factor in PCDTBT:PCBM increases from $\sim$1.7 to above 3 as the density of induced deep states increases as a result of prolonged exposure to light[158] and there is a similar increase in P3HT:PCBM.[159] The relative deep state density is evaluated from the solar cell current-voltage characteristics using a charge collection model.[155] Some BHJ cells, notably MEHPPV:PCBM have an ideality factor that is independent of temperature and closer to unity.9 These properties indicate that a different recombination mechanism dominates, which could be geminate recombination or recombination at a contact. We emphasize that several different recombination mechanisms are possible in BHJ cells and the dominant process will depend on the specific material and the device structure.

The measured ideality factor can also be influenced by extrinsic effects. Some forms of contact resistance associated with ambient degradation have an exponential currentvoltage relation and lead to an apparent increase in the ideality factor.[173] In a

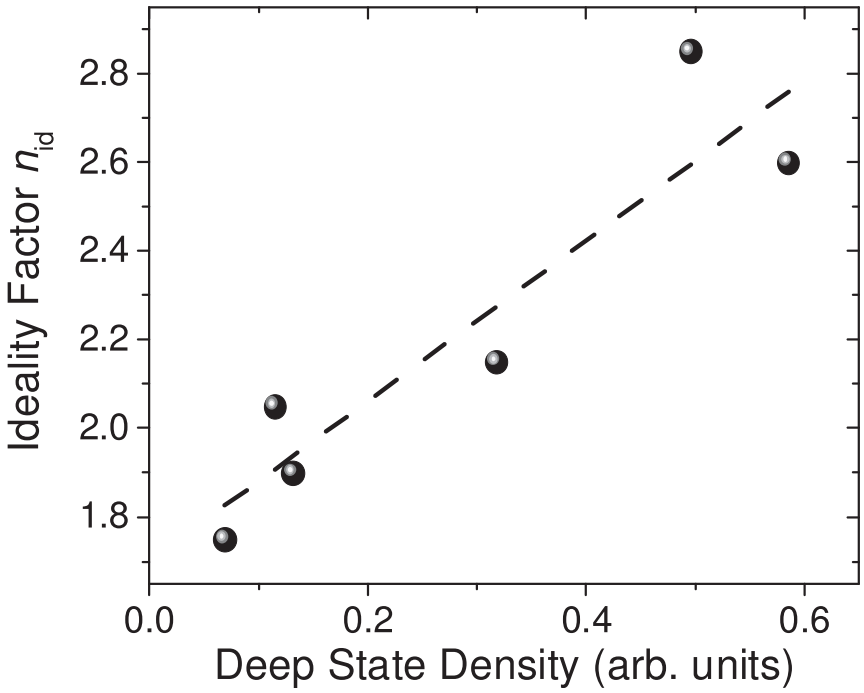

Figure 3.8: Increase of the ideality factor in PCDTBT:PCBM with deep state density induced by prolonged illumination. The data are re-plotted from Ref. 158.

similar regard, the differences in the dark and light ideality factor commonly observed in polymer:fullerene solar cells can also be easily caused by errors in interpretation due to resistive-type effects.[154,157] The data in Figure 3.7 indicate that the measured ideality factors are essentially identical in the dark and under illumination. Equation (3.22) shows that the dark and illuminated ideality factors must be the same apart from the $f(V)$ term. The agreement does not imply that the recombination mechanisms in the dark and under illumination are the same but only that $f(V)$ is relatively constant over the range of voltages measured. Hence cells with high fill factor will show the same ideality factor, while those with low fill factor will exhibit a difference due to the change in $f(V)$. There is, however, a strong expectation and ample evidence that the recombination mechanisms are the same in the dark and under illumination. The cell fill factor reflects the recombination under illumination and decreases with both an increase in band-tail slope and an increase in deep state density and is correlated with the changes in dark ideality factor.[158,159]

3.5.1 Validity of the model

The analysis that leads to Eq. (3.14) assumes that the quasi-Fermi energy is flat across the cell and that the bands are linear. In terms of the SRH equation, (Eq. (3.2)) one important condition for validity of the model is that the thermal excitation rate between the band tail and HOMO transport energy is large enough to maintain the flat qFE. When the electron traps are sufficiently far from the LUMO band that there is little thermal excitation back to the LUMO, the SRH equation can be expressed as,

$$R = c_n n N_t \left[\frac{1}{1 + \exp\left(-\frac{E_t - E_f}{kT}\right) + \frac{c_n n}{c_p p}} \right] \tag{3.23}$$

where E_t is the trap energy. This equation corresponds to the assumed model apart from the $c_n n / c_p p$ term when summed over the distribution of band-tail states. The first two terms in the denominator in brackets are the Fermi-Dirac function, which is the assumed trap occupancy function. Hence the model is valid provided that $c_n n / c_p p < 1$.

This condition for validity of the model is easily met when the applied voltage is close to the built-in potential when $p \approx n$, and is increasingly hard to meet at lower voltages when $p \approx n$ and the model is only valid when $c_n \ll c_p$. There are, however, good reasons why $c_n \ll c_p$ in a BHJ solar cell. First, the electron is making a transition from the fullerene to the polymer, which involves a tunneling term of the form $\exp(2R/R_0)$ where R is the separation of the electron from the hole band tail state and R_0 is the electron wave-function penetration into the polymer. Not much is known about the parameters R or R_0, but the exponential term can easily reduce the capture rate by a few orders of magnitude. The hole capture transition is higher because the band-tail states are in the polymer and no tunneling by holes is involved. Second, the electron transition is across a substantial fraction of the interface band gap energy, while the hole transition to the band-tail state is over a much smaller energy. In general, the transition rate decreases as the energy difference between the initial and final state increases. Hence there is good reason to expect that $c_n \ll c_p$ and that the model is valid over a reasonable voltage range. Additionally, there is precedent in the literature for using highly asymmetric recombination coefficients when modeling the optoelectronic properties of these

devices.[133,135,157,176,184] Eventually, at a low enough applied voltage, p is so much smaller than n that the model will break down. However, the exponential region of the dark current only extends 0.2-0.3 V below the built-in potential for PBDTT-DPP:PCBM and PCDTBT:PCBM, because of the presence of the shunt resistance and thus the model should be valid over this range. The P3HT:PCBM cell data cover a larger voltage range and hence the model may lose validity at the lower voltage region of the data. Possibly this effect accounts for the small temperature dependence of $n_{id}kT$ in Figure 3.3 and for the curvature in the light intensity dependence of V_{oc} seen in Figure 3.7 for P3HT:PCBM, which suggests a decrease in the ideality factor at low light intensity and low voltage.

The SRH model does not require a linear band-edge profile, as was assumed to derive Eq. (3.14). A curved band edge, for example, arising from space charge, only changes the integral in Eq. (3.11) because this term contains all the spatial dependence. Hence, the functional form of the dark current would be the same and only the pre-factor would change, and this term only contains terms linear in V and T. For all the devices used herein, however, we measured the amount of dark charge (free plus trapped) residing in the active layer under dark unbiased conditions using the charge extraction by linearly increasing voltage (CELIV) technique and found that in all cases the devices had an undetectable dark-carrier charge density ($<\sim 10^{14-15}$ cm^{-3}). The low dark carrier concentration in combination with the low dielectric constants and thin active layers ($\sim$100 nm) suggest that the Debye length is greater than the device thickness, and therefore the linear band assumption is valid.

3.5.2 Verification with numerical drift-diffusion modeling

The analytical model does not consider transport but assumes that carriers can diffuse readily enough across the device to refill traps vacated by recombination events. Hence our model assumes that the opposing drift and diffusion components are much larger than the total current.[164,165] The flat quasi-Fermi energy approximation breaks down when charge transport cannot replenish traps sufficiently quickly, making the hole quasi-Fermi energy bend upward near the cathode contact, which forces recombination to shift toward the anode. For this and general verification reasons, we performed full numerical drift-diffusion modeling to confirm that the model and its associate assumptions are reasonable. The tailstate model outlined in Figure 3.1(a) was implemented in the

SCAPS simulation program, which has been used previously to model polymer:fullerene solar cells.[185] We only considered the polymer HOMO band tail for consistency with the analytic model and because we found that the implementation of a narrower PCBM LUMO band tail had little effect on the properties of interest.

The SCAPS simulator models recombination with the SRH formalism and takes into account band-tail trapped charge in the Poisson equation but does not allow it to contribute to the current. Thus, the SCAPS program implements a transport-energy model where the input drift mobility represents that of a mobile carrier and not the smaller effective value that is often measured in experiments. For this reason, we used a free hole mobility of 1×10^{-2} cm^2/V-s, which is similar to what others have used when implementing such a model for polymer:fullerene solar cells and in good agreement with experimentally measured band mobilities.[176,184,186,187] Because fullerene band tails were ignored, we used an effective mobility of 10^{-4} cm^2/V-s for electrons to take into account that there are LUMO band-tail trap states. However, the magnitude of the electron mobility had little influence on the simulation results. The effective band gap in the model is the interface gap between the polymer HOMO and the fullerene LUMO transport energies, which is about 1.1 eV for P3HT:PCBM.

Simulated dark J-V-T curves using the parameters in Table 3.1 are shown in Figure 3.9(a) and agree well with the experimental P3HT:PCBM data from Figure 3.1(a). The parameters outlined in Table 3.1 are for the case of $T = 295$ K; however, only c_n and the series and shunt resistances were varied slightly over the temperature range in order to fit the data. In general, we found that only the band-tail characteristic energy and the magnitude of the asymmetry of the capture coefficients affected the dark ideality factor in the simulations, which is consistent with our discussions of the analytic model above. A smaller E_0 and/or capture coefficient asymmetry resulted in a steeper slope and therefore lower ideality factor.

The recombination profile at $T = 295$ K and $V = 0.3$ V, in Figure 3.9(b) confirms that recombination is largest nearer to the cathode contact and therefore in good agreement with the predictions of the analytic model. The reason why the recombination profile does not have a maximum at the cathode, as predicted by our simple analytic model, is due to the presence of a finite hole diffusion length and a non-zero $c_n n / c_p p$ term in the SRH occupation function, as

Table 3.1: Summary of parameters used in the drift-diffusion simulation. The device thickness was 220 nm and the relative dielectric constant was 3.7. The series (5-7.5 Ω-cm^2) and shunt (3-20 MΩ-cm^2) resistances were tuned to fit the relevant *J-V* regimes.

Contact Barriers (eV)	Free Hole Mobility (cm^2/V-s)	Electron Mobility (cm^2/V-s)	N_C,N_V (cm^{-3})	E_g (eV)	Total N_t (cm^{-3})	Hole Capture Cross-Section (cm^2)	Electron Capture Cross-Section (cm^2)	E_0 (meV)	Thermal Velocities (cm/s)
0.2	1×10^{-2}	1×10^{-4}	2×10^{20}	1.1	1×10^{19}	5×10^{-14}	1.5×10^{-17}	38	10^6

discussed above. Another factor influencing the temperature dependence of the ideality factor is the decrease in the diffusion constant with decreasing temperature, which will cause the hole qFE to bend upward near the cathode contact and thus force recombination toward the center of the active layer. Despite these details, Figure 3.9 confirms that the basic approximations made in our model are reasonable. The magnitude of the capture coefficients in the simulations should not be taken as necessarily accurate because they primarily influence the magnitude of the current, but significantly less so the shape, and many other factors of unknown magnitude also influence the magnitude of the current. In addition, the simulation is an effective medium model and does not capture many details of the mechanism and device structure. For example, the electron capture cross-section is an average over transitions to band-tail states that are spatially distributed at various distances from the interface with transition rates that must vary widely. The local anisotropy of transport in the polymer is also not represented in the model.

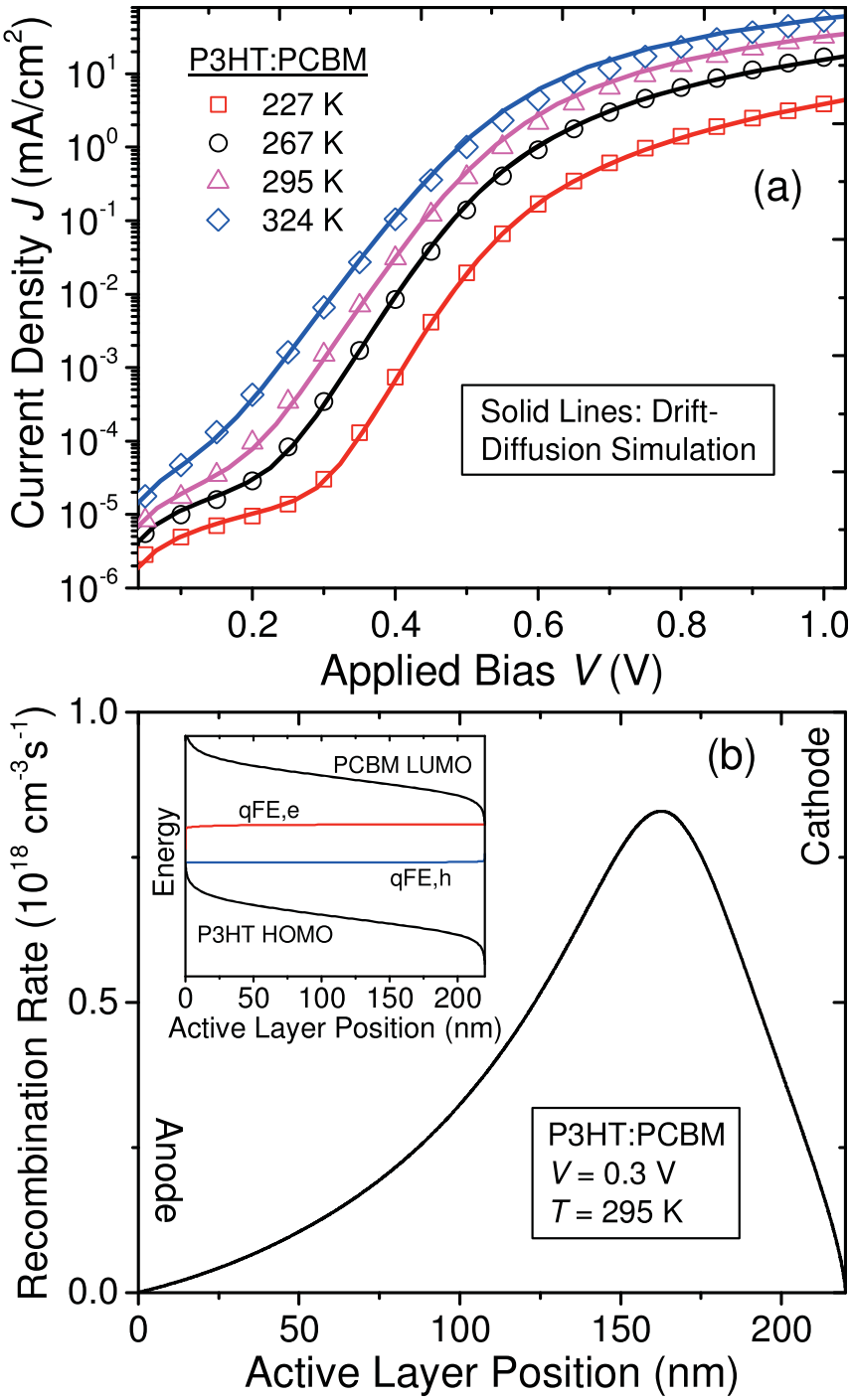

Figure 3.9: (a) Experimental *J-V-T* data for the P3HT:PCBM cell from Figure 3.2(a) along with the drift-diffusion simulation results (lines). (b) The recombination rate as a function of position in the active layer corresponding to the simulation in (a) at 295 K and 0.3 V applied bias. The recombination rate has a maximum nearer to the cathode contact. Inset: the associate band diagram with quasi-Fermi energies.

3.6 Summary and Conclusions

A Shockley-Read-Hall analysis to describe the dark forward bias diode current for the case of recombination in an exponential band tail results in the expression for the ideality factor $n_{id} = E_0/kT$, providing a direct link between the dark current and the band-tail slope when band-tail recombination dominates. In two of the three polymers studied and in amorphous silicon, there is excellent agreement between the ideality factor and the measured band tail slope confirming that band tail recombination is the dominant mechanism. In the P3HT:PCBM system, we were able to self-consistently reproduce the measured room temperature ideality factor with both detailed drift-diffusion simulations and our analytical model. The PBDTT-DPP:PCBM cell, on the other hand, has a larger ideality factor than expected from the measured band-tail slope and there is evidence of additional deep states that contribute to a second recombination channel. Other recombination mechanisms can also lead to a different ideality factor from that predicted by the band tail recombination model.

The light intensity dependence of the open-circuit voltage gives an alternative measurement of the dark ideality factor. The dark and light measurements give the same result provided that the voltage dependence of the cell photocurrent is taken into account.

Based on the evidence for recombination through band tail and deep states, further improvement in the organic solar cell efficiency requires materials with a steeper band-tail slope and the ability to suppress the light-induced creation of mid-gap states. Gains in the cell efficiency arise in two ways: a reduction in dark current and an increase in fill factor. Both factors depend exponentially on the band-tail slope, so small changes can make a large difference in the cell efficiency. The band tails reflect the disorder and indicate that more ordered materials are needed. It is interesting to note that the effective mobility of polymer thin film transistors (TFT) has recently increased to about 5 cm^2/V-s as a result of the introduction of new materials,[188] while the polymer mobility in solar cells is still much smaller. The difference must relate at least partially to a higher degree of molecular ordering in the TFT. If the same level of structural order could be achieved in the cells as in the TFTs, then perhaps the cell efficiency would be substantially increased.

CHAPTER 4

Theory of Current Transients in Planar Semiconductor Devices: Insights and Applications to Organic Solar Cells

4.1 Introduction

Planar semiconductor diodes form the backbone of important technologies such as solid-state lighting and photovoltaic energy conversion. The relatively simple physics associated with these one-dimensional devices also makes them ideal for studying the properties of emerging functional materials.[24, 83, 136, 189–193] For instance, in the fields of dye-sensitized solar cells and organic photovoltaics (OPVs),[136, 194, 195] substantial insights on recombination and charge transport have been gained by examining photocurrent, photovoltage, and charge-extraction transients of planar diode devices.[33, 89, 91, 94, 95, 97, 137, 150, 176, 196–201] In terms of specific analysis, examination of the temporal decay of photocurrent transients has been used to measure the charge-transport properties of organic semiconductors,[99, 167, 202] while the integral of these transients has been taken to quantify initial amounts of photogenerated charge.[86, 203, 204] Additionally, charge-extraction transients have been routinely used to probe semiconductor recombination kinetics, average doping densities, and carrier mobilities.[11, 90, 138, 205–207]

Despite these and countless other studies, the physics of current transients in planar optoelectronic devices is often overlooked or presumed to be obvious. Because such measurements are ultimately a major determinant of benchmark material properties, it is especially important that their physics be thoroughly understood both conceptually and analytically. Thus, in this paper, we present a thorough analytical analysis of current transients in planar diode-like semiconductor devices. Although our reference point comes from the field of OPVs, the equations we present are general and apply to any planar semiconductor device, so long as the transients are not dominated

by external RC effects.

Our approach is based on a consideration of the average charge densities within the semiconductor layer. Although some information is lost by averaging, this is not particularly restrictive because, experimentally, one often only has access to spatially-averaged values of the carrier concentrations. After deriving an expression for the total measured current, we then present equations describing the subtle but highly important charge on the electrodes as well as the time integral of a current-density transient for the purpose of assessing the initial amount of free charge in the active layer. We find that non-intuitive displacement current effects have led to misinterpretations of charge-extraction measurements, particularly in the organic solar cell literature. As examples, we apply our new formalism to a variety of transient current experiments commonly used to characterize the active layers of semiconductor diodes, including time-of-flight (ToF),[208,209] transient photocurrent,[99,167,210–212] and photoinduced charge extraction by linearly increasing voltage (photo-CELIV) measurements.[213–216] In the context of the original CELIV framework, our new, generalized formalism reveals a common misinterpretation of CELIV integrals that results in an error in the estimation of the initial free carrier concentration by at least a factor of two.[214,217,218] The existence of such misunderstandings and their increasing prevalence in solar cell research underlines the importance of the general framework described in this work. Finally, in order to visualize our formalism and verify that it is built into common drift-diffusion solvers, we numerically simulate a photo-CELIV trace and compare the total current calculated to that predicted by our analytic equations. As expected, the two approaches yield precisely the same result, confirming that our formalism is a simple, physically correct, and general way to think about current transients in planar devices.

4.2 Derivation of a General Current-Density Equation for 1-D Planar Semiconductor Diodes

4.2.1 Contributions to the Total Measured Current

To analytically analyze current transients in semiconductor devices, we begin by considering a planar diode structure at uniform temperature that is well-described by simple 1-D electrodynamics.

The relevant equations for the electric current are therefore:

$$\frac{dn}{dt} = G - R + G_e^D - R_e^D + G_e^A - R_e^A + \frac{1}{q}\frac{dJ_n}{dx} \tag{4.1}$$

$$\frac{dp}{dt} = G - R + G_h^D - R_h^D + G_h^A - R_h^A - \frac{1}{q}\frac{dJ_p}{dx} \tag{4.2}$$

$$J_D = \varepsilon\frac{dE}{dt} \tag{4.3}$$

$$J_{\text{tot}} = J_n + J_p + J_D, \tag{4.4}$$

where n, p are the mobile electron and hole concentrations, respectively, G is the generation rate of mobile-carrier pairs, R is the recombination rate of mobile-carrier pairs, $G_{e,h}^{D,A}$ are the generation rates of mobile carriers from localized donor- and acceptor-type trap sites, $R_{e,h}^{D,A}$ are the recombination rates of mobile charge into localized donor- and acceptor-type trap sites, E is the electric field, ε is the semiconductor permittivity, q is the absolute value of the electron charge, $J_{n,p}$ are the electric current due to mobile electrons and holes, J_D is Maxwell's displacement current, and J_{tot} is the experimentally measured total electric current at a given time and position in the device. Physically, Eqs. (4.1) and (4.2) account for the continuity of free carriers and simply add or subtract the contributions of both bulk and trap-mediated recombination/generation to the free carrier populations.

Our goal is to use the above equations as a starting point to obtain a more insightful and experimentally-relevant expression for J_{tot} (Eq. (4.4)) in terms of the average generation and recombination processes and the average carrier concentrations. In this regard, it is highly important to note that J_{tot} does not vary spatially within the device (see Supplemental Material in Appendix C for derivation), which means that the (average) total current anywhere within the active layer is equal to the total current everywhere at a given time.

Our sign convention is chosen such that recombination current is positive and generation current is negative, as is commonly used when reporting experimental (photo)diode currents. Furthermore, it is important to distinguish between the generation and recombination of mobile carrier pairs (G,R), which are shared terms in the continuity equations, and the individual generation and

recombination rates of mobile carriers through immobile trap sites ($G_{e,h}^{D,A}$,$R_{e,h}^{D,A}$), which are not shared because an oppositely-charged mobile carrier is not necessarily created or destroyed simultaneously. Traditionally, the $G_{e,h}^{D,A} - R_{e,h}^{D,A}$ terms in Eqs. (4.1) and (4.2) are treated as a net recombination rate within the Shockley-Read-Hall (SRH) formalism,[151,219] but such a treatment is not necessary for the derivation at hand.

4.2.2 Mobile-Carrier Currents

To develop a new expression for J_{tot}, we start by integrating Eqs. (4.1) and (4.2) across the device thickness to spatially average the continuity equations:

$$J_n(d) = qd\frac{d\bar{n}}{dt} - qd\langle G-R\rangle - qd(\langle G_e^D - R_e^D\rangle + \langle G_e^A - R_e^A\rangle) + J_n(0) \tag{4.5}$$

$$J_p(0) = qd\frac{d\bar{p}}{dt} - qd\langle G-R\rangle - qd(\langle G_h^D - R_h^D\rangle + \langle G_h^A - R_h^A\rangle) + J_p(d) \tag{4.6}$$

where $\bar{n}d = \int_0^d n(x)\,dx$ and $\bar{p}d = \int_0^d p(x)\,dx$ are the average carrier concentrations in the active layer, d is the semiconductor active-layer thickness, q is the elementary charge, and $\langle G-R\rangle$ and $\langle G_{e,h}^{D,A} - R_{e,h}^{D,A}\rangle$ are the spatially averaged differences in generation and recombination over the entire active-layer thickness. Figure 4.1 schematically illustrates the formalism described above on a semiconductor energy band diagram. Eqs. (4.5) and (4.6) have the advantage of removing the spatial derivative of the free-carrier current densities and replacing them with the averaged quantities and processes of interest. The fact that the current densities are evaluated at the contacts is acceptable because the quantity of interest, J_{tot}, is constant at all positions throughout the active layer.

4.2.3 The Displacement Current

In order to complete the expression for J_{tot} (Eq. (4.4)), we must also derive expressions for the displacement current J_D (Eq. (4.3)) at either of the contacts ($x = 0$ and/or d) that are decoupled from each other. We note that simply integrating Gauss's law, $dE/dx = \rho/\varepsilon$, and combining with the displacement current (Eq. (4.3)) will not suffice because $J_D(0)$ and $J_D(d)$ would be coupled. To ultimately decouple $J_D(0)$ and $J_D(d)$, we must use the general 1-D solution of Gauss's law for a plane

of charge[220] in order to relate the electric field at the contacts to the average carrier concentrations within the active layer:

$$E(0) = -\frac{qd}{2\varepsilon}(\bar{p} - \bar{n} + \bar{N}_D^+ - \bar{N}_A^-) + \frac{\sigma_{\text{EL}}}{2\varepsilon} \tag{4.7}$$

$$E(d) = \frac{qd}{2\varepsilon}(\bar{p} - \bar{n} + \bar{N}_D^+ - \bar{N}_A^-) + \frac{\sigma_{\text{EL}}}{2\varepsilon} \tag{4.8}$$

where $\bar{N}_{D,A}^{+,-}$ are the average number density of immobile ionized trap sites within the active layer, which we consider as localized electron states that can either be neutral when filled (N_D) or neutral when empty (N_A), and are only singly charged. We define $\sigma_{\text{EL}} = \sigma_0 - \sigma_d$ to represent the areal charge on the metal electrodes, with $\sigma_{0,d}$ being the areal charge densities on the left and right metal contacts, respectively (Figure 4.1). The charge densities $\sigma_{0,d}$ can be either positive, negative, or zero, and we use their difference, σ_{EL}, for the rest of the paper because it is directly proportional to the total electric field contribution from the charge on the metal electrodes. Additional considerations regarding the charge on the electrodes are presented in Section II F. below and in the Supporting Material (SM). We note, though, that the electric field at the contacts is dependent only on the average charge within the active layer and not on its specific distribution, which is a unique consequence of the simple physics of charged 1-D planes.[220] Equations (4.7) and (4.8) are also the origin of the factor of 1/2 that will carry on throughout this derivation—another consequence of the physics of charged 1-D planes.[220]

With the primary electric field contributions in hand, we can now simply apply Eq. (4.3) to Eqs. (4.7) and (4.8) to obtain the decoupled displacement current at each of the contacts:

$$J_D(0) = \frac{qd}{2}\left(\frac{d\bar{n}}{dt} - \frac{d\bar{p}}{dt}\right) + \frac{qd}{2}\left(\frac{d\bar{N}_A^-}{dt} - \frac{d\bar{N}_D^+}{dt}\right) + \frac{1}{2}\frac{d\sigma_{\text{EL}}}{dt} \tag{4.9}$$

$$J_D(d) = \frac{qd}{2}\left(\frac{d\bar{p}}{dt} - \frac{d\bar{n}}{dt}\right) + \frac{qd}{2}\left(\frac{d\bar{N}_D^+}{dt} - \frac{d\bar{N}_A^-}{dt}\right) + \frac{1}{2}\frac{d\sigma_{\text{EL}}}{dt}. \tag{4.10}$$

As a check of validity, the difference in the displacement current at the two contacts according to Eqs. (4.9) and (4.10) is proportional to the time rate of change of the charge density within the semiconductor layer, which is expected from a simple integration of Gauss's law. Just like the

electric fields, these simple expressions for the displacement current at the contacts depend only on the average internal charge density and not on the charge-density profile—a consequence of the simple physics of planar geometries.

We would now like to substitute Eqs. (4.9) and (4.10) along with Eqs. (4.5) and (4.6) into Eq. (4.4) in order to obtain the total measured current density (J_{tot}) at the contacts and therefore everywhere. However, in order to simplify the final result, we first derive relationships between $\bar{N}_{D,A}^{+,-}$ and the kinetic processes that connect them, $G_{e,h}^{D,A}$ and $R_{e,h}^{D,A}$. Fortunately, this is done straightforwardly by summing the generation and recombination events that create and annihilate ionized trap sites, leading to the following kinetic equations:

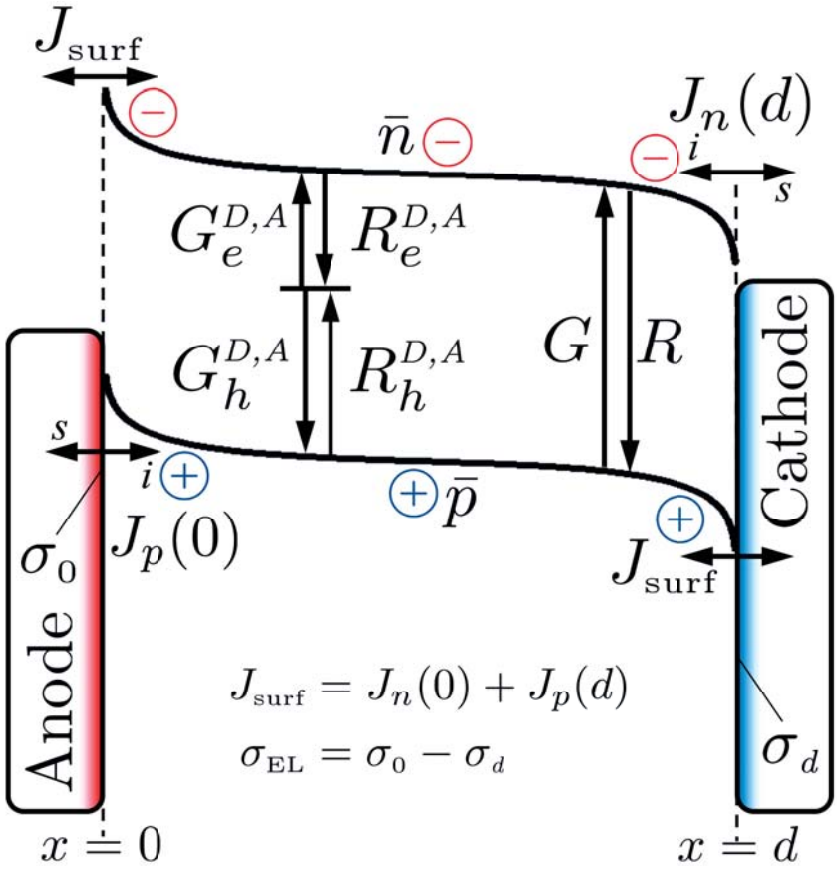

Figure 4.1: A schematic band diagram illustrating the device model used in this derivation in forward (positive) bias. The semiconductor (photoactive) layer is sandwiched between metal contacts at $x = 0$ and $x = d$. The i and s scripts on the J_n (electron current) and J_p (hole current) arrows stand for injection and sweep out, respectively. The average carrier densities are $\bar{n}$ for electrons and $\bar{p}$ for holes. The generation and recombination rates of electron-hole pairs, G and R, are distinct from the rates of freeing and trapping carriers from traps, $G_{e,h}^{D,A}$ and $R_{e,h}^{D,A}$. J_{surf} takes into account the 'surface' current that does not effectively make a transition though the semiconductor energy gap. Note that only the relative heights of the anode/cathode depictions are meant to be part of the implicit energy scale.

$$\frac{d\bar{N}_D^+}{dt} = \langle G_e^D - R_e^D \rangle + \langle R_h^D - G_h^D \rangle \tag{4.11}$$

$$\frac{d\bar{N}_A^-}{dt} = \langle R_e^A - G_e^A \rangle + \langle G_h^A - R_h^A \rangle. \tag{4.12}$$

As noted above, these equations only consider singly ionized states.

4.2.4 The Total Measured Current

We can now combine all of the relevant relations obtained above to produce a more insightful expression for the total measured electric current density in terms of the averaged quantities of interest. We do this by combining Eqs. (4.5) and (4.6) with Eqs. (4.9-4.12) at each contact to obtain an expression for J_{tot} (Eq. (4.4)) as a function of time:

$$J_{\text{tot}} = \frac{qd}{2}\left(\frac{d\bar{p}}{dt} + \frac{d\bar{n}}{dt} + \sum \langle R_{e,h}^{D,A} - G_{e,h}^{D,A} \rangle\right) + qd\langle R - G \rangle + \frac{1}{2}\frac{d\sigma_{\text{EL}}}{dt} + J_{\text{surf}}, \tag{4.13}$$

where the summation term in Eq. (4.13) covers all subscript combinations displayed in Eqs. (4.5) and (4.6), and the other terms are discussed in detail below.

Eq. (4.13) is the first of two primary theoretical results of this paper. Its simple form—only dependent upon average charge densities and kinetic processes—is a direct consequence of the straightforward physics of charged planes. Eq. (4.13) and the preceding analysis provide both a simple conceptual framework for generally thinking about current transients in planar devices as well as reveal non-trivial aspects of these measurements, such as the prefactor of one-half in front of the first term. This general but non-intuitive factor is independent of the carrier distributions and spatial generation/recombination profiles and arises from the combination of Gauss's law and the displacement current for planar 1-D electrodynamic systems (Eqs. (4.7)-(4.10)). The factor of one-half means that uniformly injecting or extracting only electrons or holes, for example, results in a measured current proportional to just half of the rate of change in average hole concentration. It also means that current measured by vacating traps, like that in thermally-stimulated currents, I-DLTS, or even charge-extraction experiments is only half due to mobile charge carriers if sweep-out

causes negligible changes in the carrier concentrations.[204,205,221–225] Thus, if this factor of one-half that results from displacement current effects is not properly accounted for, the deduced amount of charge extracted in various experiments will be off by at least a factor of two. Although this may not be a significant correction for many applications, it at least serves as a lesson that the interpretation of current transients is not necessarily trivial.

Despite the fact that the factor of one-half in Eq. (4.13) is generally ignored, it is clearly necessary from a conceptual standpoint. Consider the case where mobile carriers are photogenerated within the semiconductor layer with negligible recombination, extraction current, leakage current, or changes in the electrode charge. In such a scenario, the spatially integrated generation rate equals the rate of change of the average concentrations of both carriers, $\langle G \rangle = d\bar{n}/dt = d\bar{p}/dt$, and thus in Eq. (4.13) the measured current sums to zero. This makes intuitive sense because no current should be measured if mobile carriers are generated uniformly in a hypothetical semiconductor device with no built-in potential or recombination. Such a simple situation could not be understood without the factor of one-half in Eq. (4.13).

It is also worth noting that even if the change in electrode charge ($d\sigma_{\text{EL}}/dt$), generation, recombination, and leakage current (J_{surf}) are negligible, the average carrier concentrations can still change implicitly by charge carrier flow through the 'correct' contact (i.e., extraction by 'sweep out' and filling by injection for a diode; see Figure 4.1),[12,99] which are critical aspects of any solar cell or LED. Indeed Eq. (4.13) could be optionally re-written as $J_{\text{tot}} = J_{i,s} + J_{\text{EL}} + J_{\text{sur}}$, where $J_{i,s}$ is composed of the first two terms of Eq. (4.13) and embodies the net injection or sweep out (extraction) of carriers into or out of the semiconductor material, and J_{EL}, the third term in Eq. (4.13), represents the current density due to changes in the electrode charge density (see Eq. (4.15), discussed below), and the last term, J_{surf}, takes into account the 'surface' current that does not effectively make a transition though the semiconductor energy gap.

4.2.5 The Surface Recombination Current, J_{surf}

As just alluded to, the J_{surf} term in Eq. (4.13) accounts for current that effectively traverses the active layer without making a transition though the semiconductor energy gap. Here J_{surf} is mathematically defined as $J_{\text{surf}} = J_n(0) + J_p(d)$. For a diode, J_{surf} is typically dubbed surface

recombination and includes the net electron extraction/injection at the hole-selective contact (anode) and net hole extraction/injection at the electron-selective contact (cathode, see Fig. 4.1). In other words, positive J_{surf} corresponds to net carrier extraction at the wrong contact(s) while negative J_{surf} corresponds to net carrier injection at the wrong contact(s). The J_{surf} term is often referred to as 'shunt' or 'leakage' current in diodes, LEDs, and solar cells, and herein we use all of these terms interchangeably. In addition to Ohmic-like leakage,[226] the implied surface recombination that underlies J_{surf} is expected in OPV diodes to have an exponential voltage dependence with low ideality factor and therefore will be important at higher biases/charge densities.[103,157,227] In single-carrier devices, J_{surf} is often analyzed from the standpoint of space-charge limited current.[228]

4.2.6 Areal Charge Densities on the Contacts

A highly important aspect of Eq. (4.13) is that the seemingly benign $d\sigma_{\text{EL}}/dt$ term can often significantly contribute to the total measured current. To better understand this term, here we discuss the physical attributes of the device that determine σ_{EL}.

The free-carrier density of the metal electrodes is typically sufficiently high such that the electric field is zero inside them at all times.[220] Under this reasonable (but not always true[229]) limit, the total areal charge summed over both electrodes must be equal and opposite to the total charge within the active layer, or $\sigma_0 + \sigma_d = -qd(\bar{p} - \bar{n} + \bar{N}_D^+ - \bar{N}_A^-)$. A related consequence is that the surface charge is directly proportional to the electric field immediately outside the surface, or $\sigma_0 = \varepsilon E(0)$ and $\sigma_d = -\varepsilon E(d)$,[220] where the sign of $\sigma_{0,d}$ depends on the sign of the charge. These relations will be used below in conjunction with drift-diffusion calculations to determine σ_{EL} at various times during a simulated solar cell photo-CELIV transient.

One can conceptually imagine the σ_{EL} term as a variable quantity that is used to supply enough electric field to meet the imposed voltage conditions. As derived in the SM, σ_{EL} is only a function of the space-charge distribution within the device and the electric potential drop across the active layer ($V = -\int_0^d E\,dx$) according to

$$\sigma_{\text{EL}} = \bar{\rho}d - \frac{2}{d}\int_0^d \int_0^x \rho(\acute{x})\,d\acute{x}\,dx - \frac{2\varepsilon V}{d} \tag{4.14}$$

$$J_{\text{EL}} = \frac{d}{2}\frac{d\bar{\rho}}{dt} - \frac{1}{d}\int_0^d \int_0^x \frac{d\rho(\acute{x})}{dt} d\acute{x}\, dx - \frac{\varepsilon}{d}\frac{dV}{dt}, \tag{4.15}$$

where $\rho(x) = q[p(x) - n(x) + N_D^+(x) - N_A^-(x)]$, $\acute{x}$ is a dummy variable for spatial integration, $2J_{\text{EL}} = d\sigma_{\text{EL}}/dt$, and $\bar{\rho}d = \int_0^d \rho(x)\, dx$.

Eqs. (4.14) and (4.15) show that $d\sigma_{\text{EL}}/dt$ is non-zero only if the applied bias or the spatial distribution of net charge are changing with time. We strongly emphasize that V in Eq. (4.14) and all other equations herein is just the electric potential difference across the active layer and not the total potential difference (V_{tot}). The total potential difference in a diode often includes an additional built-in (diffusion, composition, etc.) potential (V_{BI}) that is nominally constant with light intensity and applied bias.[79] Since V_{BI} is usually well-approximated as a constant, the electric potential and total potential are related by $V(t) = V_{\text{tot}}(t) - V_{\text{BI}}$, and the conclusions made herein are essentially unchanged.

Equations (4.14) and (4.15) also tell us something about the measured device capacitance. This is recognized by the fact that the voltage derivative of Eq. (4.14) is related to the electrode capacitance, though one must also account for the charge stored in the active layer ('chemical capacitance') when considering the total measured capacitance of a diode.[230–232] Interestingly, though, Eq. (4.15) reduces to the classical parallel-plate capacitor current, $C_g \cdot dV/dt$, where $C_g = \varepsilon/d$ if the internal space-charge distribution is not changing in time, independent of the space-charge distribution. In other words, Eq. (4.15) implies that the effective device geometric capacitance is independent of any static space-charge profile, only deviating from its classical value of ε/d when the internal space-charge distribution is changing in time. Unfortunately, since the difference in electric potential between the contacts depends on the specific space-charge distribution, it is not possible to determine a more simple relationship between the effective geometric capacitance, the charge on the electrodes, and the potential difference across the device beyond what is presented in Eqs. (4.14) and (4.15). Additionally, as an aside, the σ_{EL} term can be eliminated to yield a generalized relation between the electric-field profile $E(x)$, the electric-potential difference across the device V, and the internal space-charge/dielectric profile $\rho(x)/\varepsilon(x)$ (see SM Eq. (S12)).

4.2.7 Integrating the Total Measured Current

The factor of one-half in Eq. (4.13) is relevant to experiments on diodes because Eq. (4.13) is often experimentally integrated over an extraction-current transient in order to estimate the initial average steady-state carrier concentration in such devices.[33,90,92,93,95,97,233] When integrating Eq. (4.13) over a current transient and multiplying by $1/qd$, we find that the apparent initial carrier concentration ($\Delta\bar{n}_{\text{meas}}$) is

$$\Delta\bar{n}_{\text{meas}} = \frac{1}{2}(\Delta\bar{n} + \Delta\bar{p}) + \frac{\Delta\sigma_{\text{EL}}}{2qd} + \int_0^{t_{\text{tr}}} \left(\frac{J_{\text{sur}}}{qd} + \frac{1}{2}\sum \langle R_{e,h}^{D,A} - G_{e,h}^{D,A} \rangle + \langle R - G \rangle \right) dt, \tag{4.16}$$

where the difference terms are negative for an extraction current transient. These terms are given by, for example, $\Delta\bar{n} = \bar{n}(t_{\text{tr}}) - \bar{n}(0)$, evaluated at the start ($t = 0$) and finish ($t = t_{\text{tr}}$) of the transient. The left hand side of Eq. (4.16) is given by $qd\Delta\bar{n}_{\text{meas}} = \int_0^{t_{\text{tr}}} J_{\text{tot}}(t)\, dt$ and is the apparent amount of charge extracted or injected from integration of the (experimental) current transient.

Eq. (4.16) is the other primary theoretical result of this paper because integrated extraction-current transients are widely used, particularly in the organic solar cell community, to measure average steady-state carrier concentrations.[87,89,90,92,95,196,234] To our knowledge, however, a formalism describing such integrals has not been previously presented. Equation (4.16) provides significant physical insight into the most common methods of experimentally determining the average carrier densities in diode-based devices, as it details all of the apparent sources of charge present in a 1-D (extraction) current transient.[87,137,233] Notably, the factor of one-half in the first term of Eq. (4.13) persists, which as we discuss further below has resulted in errors in the estimation of the average charge density when such experiments were performed on organic solar cell devices.

Examples of common methods that rely heavily on integrating current transients include the charge extraction by linearly increasing voltage (CELIV),[213] charge extraction (CE),[90,200] and time-delayed collection field (TDCF) techniques.[203] Although these methods allow experimenters to estimate the total average carrier concentrations relative to a short-circuit or quasi-depleted state, they have the downside of having to correct for the change in charge on the electrodes ($\Delta\sigma_{\text{EL}}$) at the beginning and end of the transient. Equations (4.14) and (4.16) clarify this previously nebulous correction. In particular, Eq. (4.14) reveals that $\Delta\sigma_{\text{EL}}$ is only a function of the geometric

capacitance (C_g), the change in applied bias (ΔV), and the change in the internal charge-density profile ($\Delta\rho(x)$) from the beginning and end of the transient. In many polymer:fullerene BHJ OPVs, researchers have found that consideration of only the voltage conditions and the geometric capacitance (the last term in Eq. (4.14)) is sufficient to account for $\Delta\sigma_{\text{EL}}$ in their charge-extraction measurements.[87,88,90,93,97,133] The success of this correction implies that the OPV devices in these experiments experienced negligible changes in the internal space-charge distribution between the beginning and ending of the extraction transient. Since most BHJ OPVs are thin, have low dielectric constants, and are weakly- or un-doped, this suggests that these devices are largely space-charge free over the operational voltage regime (i.e., have a linear band structure). This conclusion is not obvious, however, without the help of Eqs. (4.14) and (4.16).

Finally, it is common to approximate the initial amount of photogenerated charge in organic photovoltaic devices by integrating the a transient photocurrent (TPC) taken at a constant DC bias.[33,93,97] This approach typically relies on a quick laser flash to photogenerate mobile charge, which due to the built-in potential and/or externally-applied bias results in a current transient. This transient is then integrated over time to estimate the initial amount of photogenerated charge. Equation (4.13) shows that if the bias is held constant ($\Delta\sigma_{\text{EL}} = 0$) and generation, recombination, and leakage current can be ignored (or corrected for), then the integral of the photocurrent decay is actually equal to half the sum of the average initial photogenerated charge carrier densities. Since photogeneration typically gives $\Delta n = \Delta p$, the integral of a photocurrent transient without generation, recombination, or leakage current gives an apparent initial excess carrier concentration of $\Delta\bar{n}_{\text{meas}} = \Delta\bar{n} = \Delta\bar{p}$. We note that these considerations are independent of the generation profile or initial carrier concentration distributions.

4.3 Analytical Applications of the Model: Implications for Materials Characterization

4.3.1 The Time-of-Flight Experiment

A classic approach to measuring the charge-transport properties of materials is via a time-of-flight (ToF) or transient photoconductivity experiment.[99,167,208–210,235,236] Although ToF techniques are well documented, discussing the ToF conceptual model in terms of Eqs. (4.13) and (4.15) is insightful and illustrative of the different possible sources of current in such measurements/models. We note that we do not consider aspects of trap-limited dispersive transport here, but rather emphasize that the basic physics of such measurements must first be fully understood before new/unique physical effects can be identified. Moreover, this discussion demonstrates how readily a simple physical picture can be translated into a theoretically measured current transient using the equations presented above and in the SM.

In the ToF experiment, a planar device is used and the semiconducting material of interest is made thick so that a laser flash photogenerates an approximately planar carrier packet at one side of the device. During the measurement, a constant applied bias and/or built-in potential is used to drive the carrier plane across the sample. Theoretically, in terms of Eqs. (4.14) and (4.15), this situation corresponds to a space-charge profile of $\rho(x) = \sigma_{\text{gen}}\delta(x - x_\sigma(t))$, where δ is the Dirac delta function, σ_{gen} is the charge density of the drifting plane, and $x_\sigma(t)$ is the spatial position of the plane of charge. Since $dV/dt = 0$ and V is dependent on $x_\sigma(t)$, a continuous supply of charge must be given to the electrodes in order to keep the voltage constant as the carrier plain drifts across the sample. Thus, by inspection of Eq. (4.13), the only source of current in the ToF model arises from changes in electrode charge. The current transient is readily derived by substituting $\rho(x) = \sigma_{\text{gen}}\delta(x - x_\sigma(t))$ into Eq. (4.15):

$$J_{\text{tot}} = J_{\text{EL}} = \frac{\sigma_{\text{gen}}}{d}\frac{dx_\sigma(t)}{dt} = q\bar{p}\mu E_{\text{EL}}, \tag{4.17}$$

where μ is the mobility of the carrier plane, E_{EL} is the electric field supplied by the electrode charge (see SM Eq. (S10)), and $\bar{p} = \sigma_{\text{gen}}/qd$ is the spatially-averaged carrier concentration, assumed here

to arise from a plane of positive charge originating at $x = 0$. Since the total current is rigorously constant everywhere (see the SM), the ToF transient also can be rewritten as just the average drift current flowing within the device (RHS of Eq. (4.17)). The solution of Eq. (4.17) can be readily obtained with the aid of Eq. (S10) upon substituting $\rho(x) = \sigma_{\text{gen}}\delta(x - x_\sigma(t))$, giving the following differential equation and subsequent expression for the ToF current transient:

$$\frac{dx_\sigma(t)}{dt} = \mu E_{\text{EL}} = \frac{x_\sigma(t)}{\tau} - \frac{d}{2\tau} - \frac{\mu V}{d} \tag{4.18}$$

$$J_{\text{ToF}} = -\left(\frac{qd\bar{p}}{\tau} + \frac{q\bar{p}\mu V}{d}\right) e^{\frac{t}{\tau}}, \tag{4.19}$$

where here $\tau = \varepsilon / q\bar{p}\mu$ is the dielectric relaxation time of the semiconductor with excess conductive charge $\bar{p}$, V is assumed to be negative, and the carrier plane starts at $x = 0$. Thus, for large values of τ and high magnitudes of V, the value of J_{ToF} is, as expected, approximately constant in time and equal to $q\bar{p}\mu V/d$ due to an approximately constant velocity of the drifting plane of charge.

In short, this demonstrates that Eqs. (4.13), (4.14), and (S10) readily capture all the essential features and fine details of the classic ToF experiment, illustrating how a simple physical picture (a plane of charge moving across a device) results in an actual measured current transient (Eq. (4.19)). This example thus illustrates how simple current transient models in planar optoelectronic devices readily fit within the general relations derived in this work.

4.3.2 Determination of the Average Carrier Concentration with CELIV

As a more detailed example of the utility of Eqs. (4.13), (4.14), and (4.16) when applied to charge-extraction techniques that vary the applied bias, in this Section we re-examine the assumptions underlying the CELIV framework for measuring charge densities in solar cell devices. The original analytical model describing CELIV transients by Juska *et al.*[213] considered a unipolar device with flat-band contacts and no generation, recombination, or leakage current. This model also ignores diffusion current, considering only a slab of uniform-density charge drifting under the influence of an electric field (Figure 4.2a). Lorrmann *et al.*[214] and Sandberg *et al.*[237] later presented an excellent analysis of the mathematical implications of this CELIV model using the same original assumptions

and equations as Juska *et al.*:[213]

$$J_{\text{tot}} = \frac{U_{\text{R}}\varepsilon}{d} + nq\left(1 - \frac{l(t)}{d}\right)\frac{dl(t)}{dt} \tag{4.20}$$

$$\frac{dl(t)}{dt} = \frac{\mu U_{\text{R}} t}{d} - \frac{nq\mu}{2\varepsilon d} l(t)^2, \tag{4.21}$$

where U_{R} is the voltage ramp rate, d the film thickness, n is the uniform unipolar free-carrier density, $l(t)$ is the time-dependent extraction depth (i.e., depletion width), μ is the unipolar carrier mobility, ε the semiconductor permittivity, and J_{tot} the total measured current density. The properties of $l(t)$ are: $l(0) = w$, $dl(0)/dt = 0$, $0 \leq l(t) \leq d$, and $l(t_{\text{tr}}) = d$ where t_{tr} is the time taken to extract all the mobile carriers within the active layer. Schottky junctions under the full-depletion assumption are well approximated by this model through a finite initial steady-state depletion width, w (Figure 4.2a).[237]

In examining how this model is used in the literature, we find that the integral of Eq. (4.20) is often misinterpreted because of the factor of one-half in the first terms of Eqs. (4.13) and (4.16) due to improper accounting of $\Delta\sigma_{\text{EL}}$. Although this factor of one-half was recently noticed by Sandberg *et al.*[237] for the CELIV model described above, the origin of this term was not understood. The issue arises from attributing the second term in Eq. (4.20) solely to mobile carriers.[238] Under this seductive but incorrect assumption, subtracting the time independent $U_{\text{R}}\varepsilon/d$ term and integrating (shaded area in Figure 4.2b) yields the presumed total number of free-carriers extracted and thus the initial carrier density.[216,218]

If this were true, however, then integrating the second term of Eq. (4.20) from $t = 0$ to t_{tr} and multiplying by $1/qd$ should give the actual initial carrier concentration n. Instead, we find that:

$$\bar{n}_{\text{meas,CELIV}} = \frac{n}{d}\int_0^{t_{\text{tr}}} \left(1 - \frac{l(t)}{d}\right)\frac{dl(t)}{dt}dt \tag{4.22}$$

$$= \frac{n}{2}\left(1 - \frac{l(0)}{d}\right)^2 \tag{4.23}$$

$$= \frac{\bar{n}}{2}\left(1 - \frac{w}{d}\right), \tag{4.24}$$

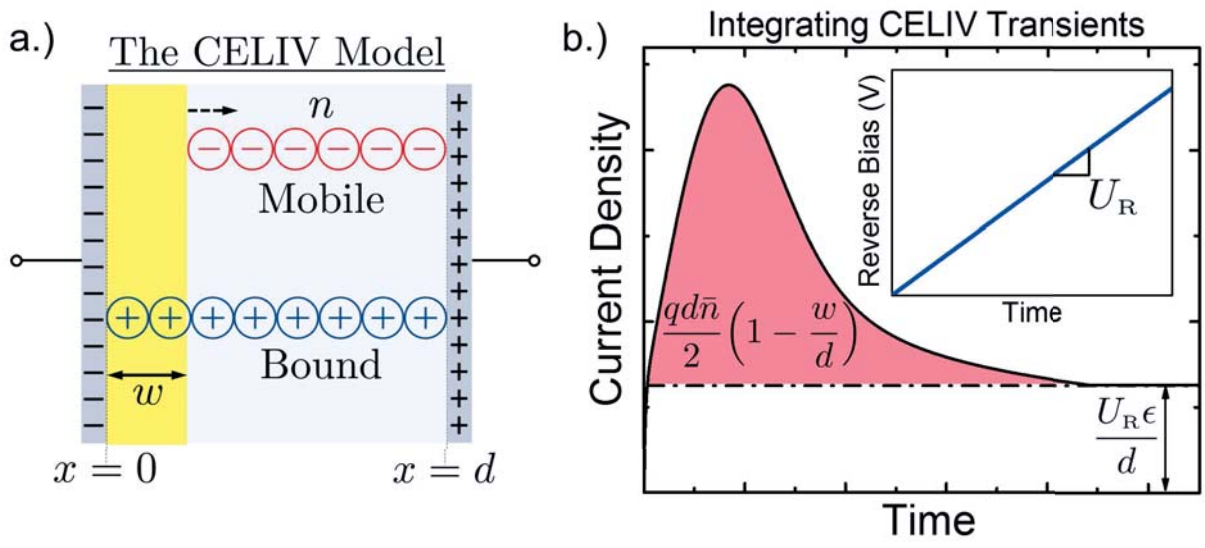

Figure 4.2: a.) Schematic representation of the CELIV model device under consideration. A uniform block of free charge with local density *n* and average density *n*(1 - *w*/*d*) is swept out under a linearly changing reverse bias pulse (inset of b.)). Here *w* denotes the steady-state initial depletion width. b.) An Example CELIV current transient showing the typical portion of the curve that is integrated to yield the initial uniform free-carrier density (*n*). Non-intuitively, the shaded region is at most proportional to half of the initial average free-charge density and even further reduced if *w* is non-zero.

where $dq\bar{n}_{\text{meas,CELIV}} = \int_0^{t_{\text{tr}}} (J(t) - U_{\text{R}}\varepsilon/d)\, dt$ is the apparent initial carrier concentration in the Juska *et al.*[213] model obtained by integrating the CELIV transient with $U_{\text{R}}\varepsilon/d$ subtracted away and $l(0) = w$ as the initial steady-state depletion width.[237] Thus, we see that integrating a CELIV transient in this model over the total evacuation time, t_{tr}, gives at most half of the actual mobile charges extracted, which is in exact agreement with Eq. (4.16) under the same assumptions.

In addition to this factor of $1/2$ reduction, Eq. (4.24) also shows that there is another reduction of the apparent initial average free-charge density by an additional factor of $1 - w/d$. Inspection of Eq. (4.16) readily reveals that this is due to electrode-charge effects. Indeed, Eq. (4.16) indicates that if there is an initial steady-state depletion width, $w > 0$, then the initial charge on the electrodes ($\sigma_{\text{EL}}(t = 0)$) will be finite due to the initial presence of space charge. Thus, the $\Delta\sigma_{\text{EL}}$ correction in Eq. (4.24) will be altered from the case where $w = 0$ since both cases end in an identical fully-depleted state. This additional reduction due to $\Delta\sigma_{\text{EL}}$ is generally nontrivial since in real devices the steady-state space-charge profile can take on shapes more complex than the simple rectangular version assumed by the CELIV model. Overall, though, these previously nebulous aspects of current

transients are decoupled and made obvious by Eqs. (4.13), (4.14), and (4.16), thus highlighting the conceptual utility of our formalism. Overall, Eq. (4.16) readily corrects a common misinterpretation of CELIV transients and explains why, for example, Lorrmann *et al*.[214] concluded that a substantial fraction of the mobile charge within the active layer was not extracted during CELIV even after long extraction times ($\sim$1 ms).

It is worth noting that none of the above analysis includes RC time constant effects,[239] which inevitably makes interpretation of the current transients more complicated. However, we have found through numerical simulations that when RC effects are included at reasonable levels ($\tau_{RC} \approx 300$ ns), the conclusions we have reached for low-mobility materials are not altered. Moreover, RC effects should mostly influence the temporal shape of the current transient, leaving the integral (Eq. (4.16)) largely unaffected.

4.4 Understanding the Formalism Via Time-Dependent Drift-Diffusion Modeling: CELIV Revisited

Lastly, to better understand each of the terms underlying the total current in Eq. (4.13) and the analysis in the previous Section, we performed time-dependent drift-diffusion numerical modeling to simulate a photo-CELIV measurement. In the following, we demonstrate that Eq. (4.13) is compatible with detailed numerical drift-diffusion simulations, verifying that we have obtained a physically correct expression for the total current.

The drift-diffusion approach involves solving the continuity equations (Eqs. (4.1) and (4.2)) along with the Poisson equation to determine the individual carrier concentrations and the electric field during the simulation. To explicitly solve these equations, the approach assumes that the current densities follow the drift-diffusion form

$$J_n = qn\mu_n E + \mu_n kT\frac{dn}{dx} \tag{4.25}$$

$$J_p = qp\mu_p E - \mu_p kT\frac{dp}{dx} \tag{4.26}$$

where μ_n and μ_p refer to the mobility of electrons and holes, respectively, and kT is the thermal energy. We have previously performed steady-state drift-diffusion calculations to model OPV devices using homemade code,[240] and we employ the same approach here only extended into the time domain (see the SM for a detailed description of our drift-diffusion computational approach). In this study, the time dependence is accounted for by solving the continuity equations and employing an implicit method to iterate forward in time. Recombination is assumed to take the simple reduced Langevin form ($R = q\gamma np(\mu_n + \mu_p)/\varepsilon$; see Table 4.1),[186,202,241] and the generation profile is taken from a transfer-matrix calculation using experimentally available optical constants for the different layers.[54,55] The device parameters for our simulations are presented in Table 4.1, and are loosely designed to be representative of those of polymer-based solar cell using P3HT and PCBM.[240,242] We chose to simulate an organic solar cell photo-CELIV transient because photo-CELIV is a common method for studying low-mobility semiconductors and the technique involves many of the physical processes that our analytical model aims to capture: generation, recombination, and a time-varying applied voltage. The $\langle R_{e,h}^{D,A} - G_{e,h}^{D,A} \rangle$ term is the only term in Eq. (4.13) not accounted for in this simulation, and was therefore assumed to be zero.

We simulated the photo-CELIV experiment by first performing a steady-state calculation to verify that the dark J-V characteristics of the device were reasonable. Then, for the transient, our virtual device was initially held in the dark at an applied bias equal to the built-in potential, V_{BI} (Table 4.1). Next, these steady-state conditions were perturbed by a brief pulse of illumination to produce excess carriers. After this pulse, the photogeneration of carriers was set to zero and, after an additional short period of time (5 μs), a linear reverse bias voltage ramp was applied to sweep out any remaining photogenerated charge.

To visualize Eq. (4.13), we explicitly calculated each term during the simulated photo-CELIV process and compared their sum to the total current calculated from the drift-diffusion simulation (Figure 4.3). We plot in Figure 4.3 the negative of the total current ($-J_{\text{tot}}$) calculated by each approach since $-J_{\text{tot}}$ is what is typically reported in the literature for CELIV transients.[207,215,243–246] Because the drift-diffusion simulations use a different starting formalism than Eq. (4.13), the fact that the two results agree precisely verifies the legitimacy and generality of our derivation. Furthermore, as also highlighted in the ToF Section, this shows that Eq. (4.13) and Eqs. (4.25) and (4.26)

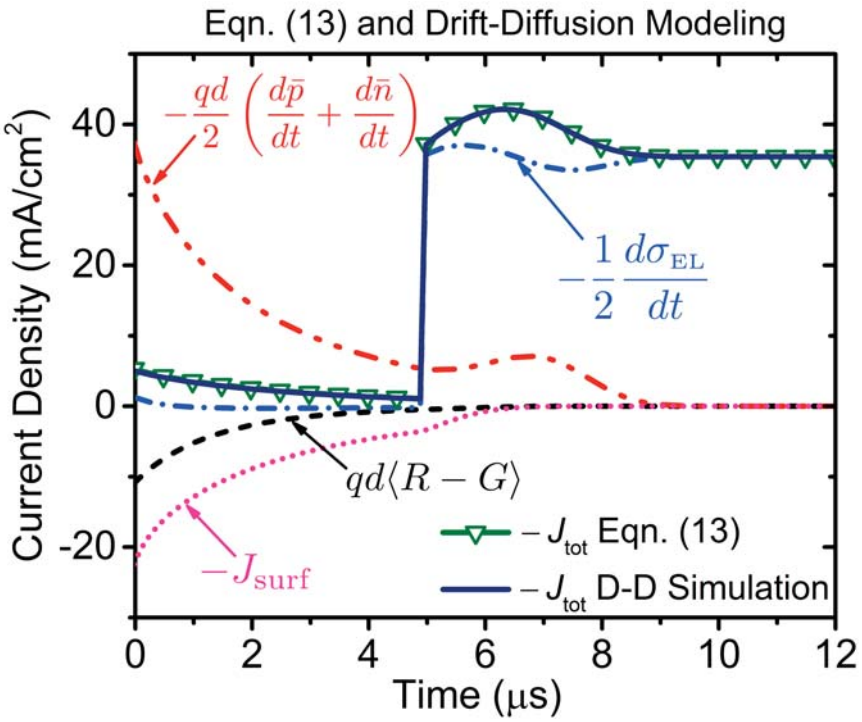

Figure 4.3: The various current contributions from Eq. (4.13) determined from numerical simulations and the negative of their sum, -J_{tot} (upside down open triangles). Note that here the reverse bias extraction current is plotted as positive. The simulated CELIV ramp conditions are 0.1 V/μs starting at an initial forward bias of 0.6 V. The total current density from the simulation is also shown (solid blue line). The simulated total current density and the summed current density from Eq. (4.13) lie on top of each other, showing their precise quantitative agreement. We note that trapping was not included in the numerical model and thus was assumed to be zero.

can be combined to examine the materials-related aspects of these transients.

In addition to the negative of the total current, Figure 4.3 also shows the negative of each component of Eq. (4.13). The current due to the changing electrode charge runs in the opposite direction for this case because CELIV involves a reverse-bias voltage ramp. The carrier concentrations decrease in time due to recombination, sweep-out/diffusion, and surface recombination current, and therefore the derivative of the average carrier concentrations are also negative. Since generation only takes place initially and is set to zero afterwards, only recombination contributes to the $qd\langle R-G\rangle$ term in Eq. (4.13), which registers as a positive current density in our sign convention.

Finally, it is worth noting that the J_{surf} term is rather large and positive in the initial part of the transient in Figure 4.3, corresponding to net carrier extraction at the 'wrong' contacts. The reason for such a large value of this current density is that the cell is initially held at a forward bias

Table 4.1: Parameters used in the drift-diffusion photo-CELIV simulation; the values chosen are designed to roughly simulate an organic photovoltaic device

Parameter	Symbol	Value
Electron,Hole Mobility	μ_n,μ_p	1×10^{-4} cm^2/V–s
Active Layer Thickness	d	100 nm
Relative Permittivity	ε_r	3.5
Injection Barriers	ϕ_n, ϕ_p	0.3 eV
Langevin Reduction Factor	γ	0.1
Built-in Voltage	V_{BI}	0.6 V
Effective Density of States	$N_{\mathrm{C}}, N_{\mathrm{V}}$	1×10^{20} cm^{-3}
Temperature	T	298 K
Band Gap	E_g	1.2 eV

equal to the built-in potential until the start of the CELIV ramp. At this applied bias, the built-in electric field is entirely canceled, and thus a significant amount of excess carriers get collected at the 'wrong' contact by way of diffusion. Real, well-working, devices are designed to avoid this problem by having higher built-in potentials and/or blocking layers to prevent extraction of carriers by the 'wrong' contact.

All in all, Figure 4.3 verifies that our formalism provides another level of insight into current transient measurements that is fully consistent with detailed time-domain numerical drift-diffusion modeling. The benefit of our approach, though, is that it pairs the generality of a full numerical calculation with the physical insight of a analytical model. With these tools at hand, researchers can now understand any current transient measurement in terms of a simple set of discrete physical processes.

4.5 Conclusions

In summary, we have derived a generalized equation for describing current transients in planar optoelectronic devices at uniform temperature. Our results detail all the possible sources of current using only fundamental physical equations and spatially-averaged values of the quantities/processes of interest. Integrating our generalized current-density equation provides further insight on how

to interpret the apparent charge extracted from transient current measurements, including how to account for changes in charge on the electrodes. One unexpected result from this analysis is a factor of one-half reduction in the apparent extracted charge due to non-intuitive displacement current effects. We have shown how this factor of one-half, along with an improper accounting of the electrode charge, has lead to misinterpretations of charge-extraction transients in the organic solar cell literature. We further demonstrated how readily a simple physical picture—like that of the classic CELIV and ToF models—can be translated into an expression for the total measured current density as a function of time using our set of simple generalized equations. Finally, we have shown that the derived relations are effectively built into time-domain drift-diffusion numerical solvers, thus verifying the correctness of our approach while demonstrating a new avenue for understanding current transients in 1-D optoelectronic devices.

CHAPTER 5

Comparing Matched Polymer:Fullerene Solar Cells Made by Solution-Sequential Processing and Traditional Blend Casting: Nanoscale Structure and Device Performance

5.1 Introduction

Photovoltaics based on mixtures of semiconducting polymers and functionalized fullerenes have attracted significant interest as low-cost solar energy harvesters.[136] Improvements in device architecture and polymer design have yielded single-junction power conversion efficiencies (PCEs) above 9%,[84] and tandem-cell efficiencies over 10%.[247–249] The ability to achieve high PCEs with these materials is predicated on forming a nanoscale polymer-fullerene network, known as a bulk heterojunction (BHJ), that must simultaneously dissociate excitons, transport separated mobile charges, and suppress recombination of excess photogenerated carriers.[94,133] An extensively studied approach for creating such networks is the blend-casting (BC) method, wherein the polymer and fullerene are dissolved together in solution and then cast into a thin film. This approach is highly sensitive to processing conditions and to material properties because it relies on (poorly understood) spontaneous nanoscale phase separation to create the desired donor-acceptor network morphology.[250] Thus, even though the BC approach is simple and amenable to extensive optimization, it introduces irreversible interdependencies between material properties, processing, and morphology that limit control over BHJ network formation and thus also device performance.[195] Additionally, with the BC approach, it is difficult to determine if an optimized morphology is kinetically trapped and unstable or near a reasonable thermodynamic minimum and suitable for long-term solar energy harvesting.

Recently, we presented an alternative to the BC method that involves sequential deposition of the polymer and fullerene layers from semi-orthogonal solvents.[251,252] This solution sequential-processing (SqP) route involves interdiffusing the acceptor molecule into a pre-cast donor underlayer. Although it involves two processing steps for the active layer instead of one, the SqP method is advantageous for making a BHJ compared to the BC method because it affords more control over the polymerfullerene network formation and still preserves device efficiency and the ease of solution-based fabrication.[253–255] A schematic illustrating the methodology behind these two processing routes is presented in Figure 5.1. Though initially misunderstood,[251] it is now generally accepted that extensive mixing of the donor and acceptor components

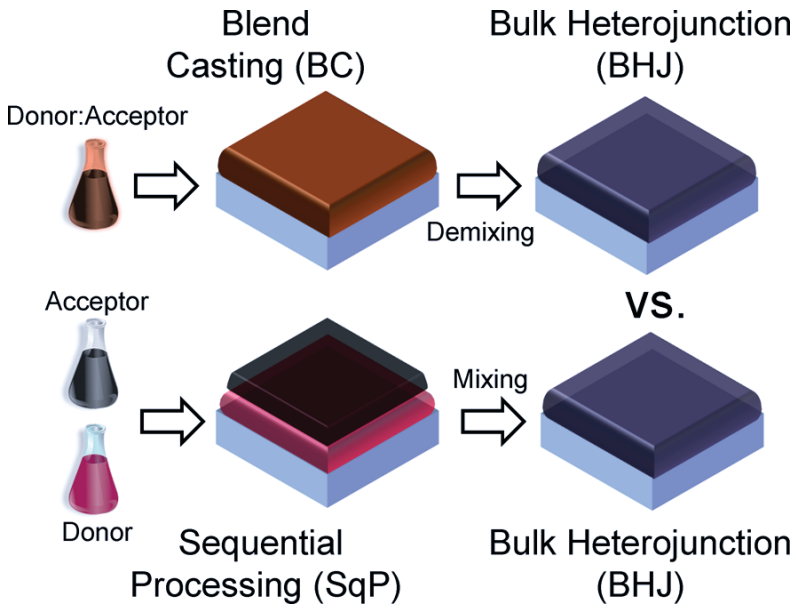

Figure 5.1: Active-layer BHJ formation approaches for the SqP and traditional BC methods. The SqP method creates a BHJ network by interdiffusion of the acceptor into a host donor matrix, whereas the traditional BC approach relies upon spontaneous nanoscale phase separation. The questions we aim to address here are: is the final BHJ structure from the two methods the same, or not, and what implications does the respective processing route have for device performance?

must occur for optimal SqP device performance.[255–263] These interdiffusion processes in SqP result from selective swelling of the amorphous regions of the (donor) underlayer with the solvent used to deposit the acceptor overlayer material. Additionally, thermal diffusion from annealing also can be used to intermix the two components. The added versatility of this interdiffusion-based SqP approach has allowed researchers to better understand the underlying factors that give rise to

functional polymer:fullerene morphologies and to use techniques that are inapplicable or detrimental to the BC method.[216,259,262,264–271] For instance, the polymer layers in the SqP approach are amenable to cross-linking,[259,268] chemical doping,[272] nanopatterning,[270,273,274] polarization by chain alignment,[271] and controlled solution-based deposition using a gas-permeable cover layer,[269] whereas these treatments are typically harmful or non-beneficial to BC device performance.[43] Recently, the SqP approach has also surpassed the BC method in a comparison of overall device performance using different polymers paired with PCBM.[275,276]

Despite all of these advantages, there still has not been a stringent comparison of the nanoscale networks formed via SqP and BC to determine what differences, if any, exist between them. One of the main reasons for this lack of comparison is that the polymer:fullerene film composition in the SqP processing route is not accurately known because the components are deposited separately instead of from a pre-mixed solution. To the best of our knowledge, only approximate, indirect estimates of the SqP film composition have been made using a variety of methods, including solid-film UV-visible absorption spectroscopy,[277] photoluminescence (PL) quenching,[257] neutron reflectivity,[255] and time-resolved microwave conductivity (TRMC).[258] Since all of this previous work is only approximate, the overall morphology/processing/performance relationships are not well known for SqP active layers, so equivalent head-to-head comparisons of the two approaches summarized in Figure 5.1 have not been carried out to date.

In this article, we present a rigorous comparison of the nanoscale morphological and photovoltaic properties of composition- and thickness-matched SqP and BC bulk heterojunction solar cells made from active layers composed of poly(3-hexylthiophene-2,5-diyl) (P3HT) and [6,6]-phenyl C_{61}-butyric acid methyl ester (PCBM). To do this, we first developed a new method for accurately determining the overall SqP film composition, and then used this method to produce composition- and thickness-matched BC and SqP layers. When examining these thickness- and composition-matched BC and SqP P3HT:PCBM solar cells, we find that the optimal SqP active-layer composition is between 44 and 50% PCBM by mass. This is more PCBM-rich than expected based on our previous work,[258,277] and lies in the same optimal regime as BC P3HT:PCBM films.[23] Furthermore, structural characterization shows that SqP films have a higher degree of both polymer and fullerene molecular ordering than equivalent BC films, and that the SqP P3HT:PCBM films are blended on a

slightly finer scale than the matched BHJs produced by BC. Despite these differences in molecular crystallinity and nanoscale BHJ morphology, matched SqP and BC films have remarkably similar electronic and photovoltaic properties in small-scale devices. However, when we compare matched films in larger active area devices, the SqP route yields higher device performance and significantly better reproducibility due to enhanced film quality. Overall, even when matched as closely as possible, SqP and BC produce different nanoscale BHJ architectures; however, these different architectures lead to similar device performance (in small active areas), showing that polymer-based BHJ photovoltaics can tolerate a fair range of nm-scale structures.

5.2 Method for Determining the Composition of Polymer:Fullerene Films

Experimental details for the standard, well-established, techniques used in this work can be found in Appendix D. Here we detail only our original method for obtaining the composition of SqP active layers.

SqP films were made by casting a PCBM overlayer dissolved in dichloromethane (DCM) on top of a pre-deposited 130 nm 5 nm thick P3HT underlayer cast from *o*-dichlorobenzene (ODCB). Since the amount of PCBM deposited onto the P3HT film is unknown, the total mass ratio of P3HT to PCBM in the final film is also not known. Although it may seem safe to assume that UV-visible absorption measurements on thin-film samples easily can be used to calculate solid-state film compositions, in fact the polymer extinction coefficients can vary significantly with the crystallinity of the polymer, and a myriad of other effects can also affect solid-film absorbance measurements (e.g., scattering, interference, reflectivity, etc.). As a result, the composition cannot be accurately determined from solid-state optical absorption, as will be revealed in detail below.

Instead of using solid-film absorbance measurements, our approach for determining an active-layer's stoichiometry involves re-dissolving the film after casting/processing and fitting the resulting dilute-solution absorption spectrum to a linear combination of the individual-component spectra (Figure 5.2a and inset to Figure 5.2b). Procedurally, we first remove the outer edges of the film with a razor, leaving only the area where solar cells are fabricated. We scratch away the outer edge of the films as a precautionary measure because by eye this region looks different, and it has no relevance

to the questions at hand. Once the edges are removed, the active layer is then re-dissolved in ODCB and transferred to a 1-mm thick cuvette. Even after thermal annealing, we found that P3HT:PCBM films readily dissolve in ODCB. We carried out the redissolving/washing step at least 3-4 times for each film in order to fully remove all material from the surface of the substrate. If the substrate was insufficiently cleaned, the compositions determined for BC films appeared anomalously rich in PCBM by roughly 10% by mass. We suspect that the anomalously rich PCBM compositions arising from insufficient cleaning are due to the higher propensity for P3HT to remain on the substrate rather than enter solution upon redissolving. Fortunately, this issue can be easily avoided by simply washing away the entirety of the film. The final solutions typically had peak optical densities in the range of 0.1-0.2 and concentrations on the order of 0.05 mg/ml for each component.

Figure 5.2a shows the solution-phase absorption spectrum of a redissolved 1:0.8 P3HT:PBCM mass ratio BC film (black circles), along with a fit (blue curve) of the absorption to the sum of the individual solution-phase components:

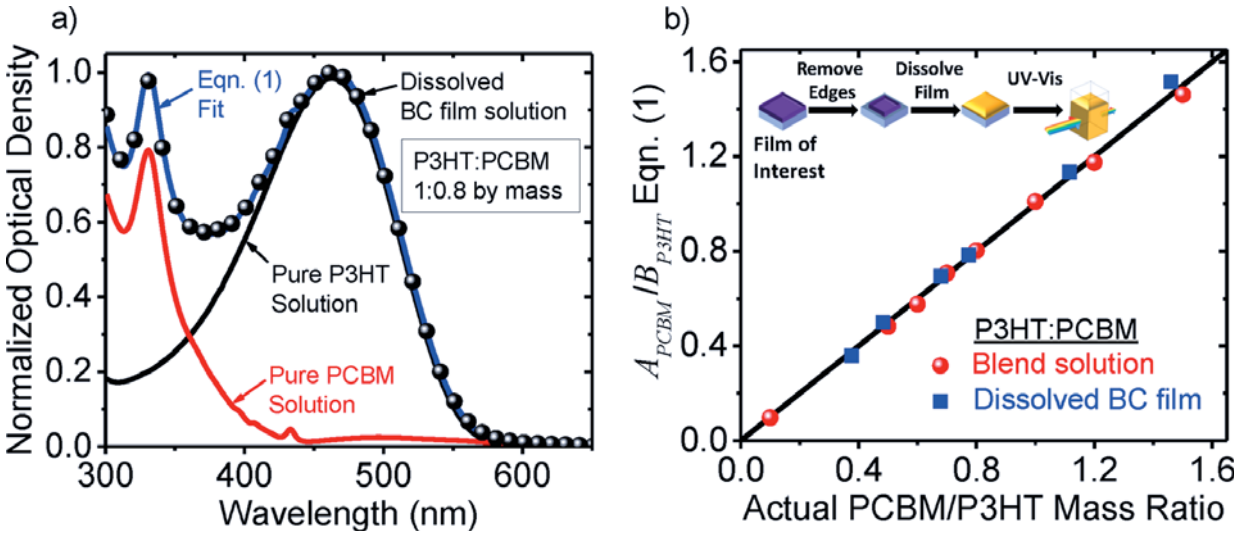

Figure 5.2: (a) Solution-phase absorption spectrum (blue curve) of a redissolved 1:0.8 P3HT:PCBM weight ratio BC film (obtained from the procedure shown in the inset of panel b), along with its fit to a linear combination of the pure solution-phase P3HT (black curve) and PCBM (red curve) components. (b) Test of this procedure on BC films and solutions with known composition. The fitted P3HT:PCBM mass ratio using Eq. (5.1) of BC solutions (red spheres) and redissolved BC films (blue squares) as a function of their actual mass ratio; the black line is a reference with slope 1 and intercept zero. Clearly, the solution UV-vis of a redissolved blend film can accurately recover the film's composition. Each point is the average of three substrates/solutions, and the error bars (one standard deviation) are smaller than the plotted symbols.

$$OD_{\text{Soln}}(\lambda) = A_{\text{PCBM}} \cdot OD_{\text{PCBM}}(\lambda) + B_{\text{P3HT}} \cdot OD_{\text{P3HT}}(\lambda) \tag{5.1}$$

where A_{PCBM} and B_{P3HT} are fitting coefficients representing the amount of each material, $OD_{\text{Soln}}(\lambda)$ is the measured optical density of the composite (dissolved-film) solution, $OD_{\text{PCBM}}(\lambda)$ is the normalized optical density of a dilute pure PCBM solution in ODCB (red curve), and OD_{P3HT} is the normalized optical density of a dilute pure P3HT solution in ODCB (black curve). We fit the entire solution spectrum to take advantage of the full spectral information and also to minimize/recognize any effects of impurities or aggregation. We found that the fits to Eq. (5.1) were excellent (Fig. 2a is typical) and unaffected by the use of different P3HT or PCBM material batches or extensive thermal annealing. Clearly this approach is general and can be extended to a wide range of soluble organic molecule combinations.

Since the dilute re-dissolved solutions faithfully follow Beer's law with invariant extinction coefficients, the ratio of the fitted coefficients $A_{\text{PCBM}}/B_{\text{P3HT}}$ is equal to the PCBM/P3HT mass ratio of the solution/redissolved film. To confirm this, Figure 5.2b plots the ratio of the Eqn. (5.1) fit coefficients for as-prepared dilute BC solutions (red circles) as a function of their actual PCBM/P3HT mass ratio. As expected, all points fall on a line of slope one and intercept zero. Figure 5.2b also plots the ratio of the Eqn. (5.1) fit coefficients obtained from a series of re-dissolved BC films (blue squares) as a function of their actual mass ratio, which falls on the same line of slope one and intercept zero, proving that a film's composition can be accurately determined by our method. We note that the dissolved BC film data in Figure 5.2 are averages over 3 separate substrates with standard deviations that are smaller than the symbol size, demonstrating that the method is highly reproducible.

5.3 Comparing the Active-Layer Composition and Morphology of Matched SqP and BC P3HT:PCBM Films

5.3.1 Revealing the SqP Film Composition

After establishing that our composition measurement technique was accurate and reproducible, we applied it to P3HT:PCBM SqP films processed over a range of conditions representative of what is employed in the literature.[251,261,262,267] Figure 5.3 shows SqP film compositions resulting from a series of active layers made by casting a PCBM overlayer from DCM with a variety of different concentrations and spin speeds on top of a pre-deposited 130 ± 5 nm thick P3HT underlayer (see Appendix D for more detailed experimental procedures). The results in Figure 5.3 show that SqP films are richer in PCBM than would be expected based upon our previous estimates.[258,277] When we fabricated photovoltaic devices out of these active layers, we found that the optimal device performance was achieved when the overlayer was spun from a 10 mg/mL PCBM solution in DCM at a spin speed of 419 rad/s (4000 RPM), which corresponded to film compositions with mass ratios between 1:0.8 and 1:1 P3HT:PCBM. We found that the run-to-run compositions we obtained were highly reproducible when using solutions of PCBM in DCM with concentrations less than 8 mg/mL, but that the commonly used 10 mg/mL concentration was too near the PCBM solubility limit and gave run-to-run results

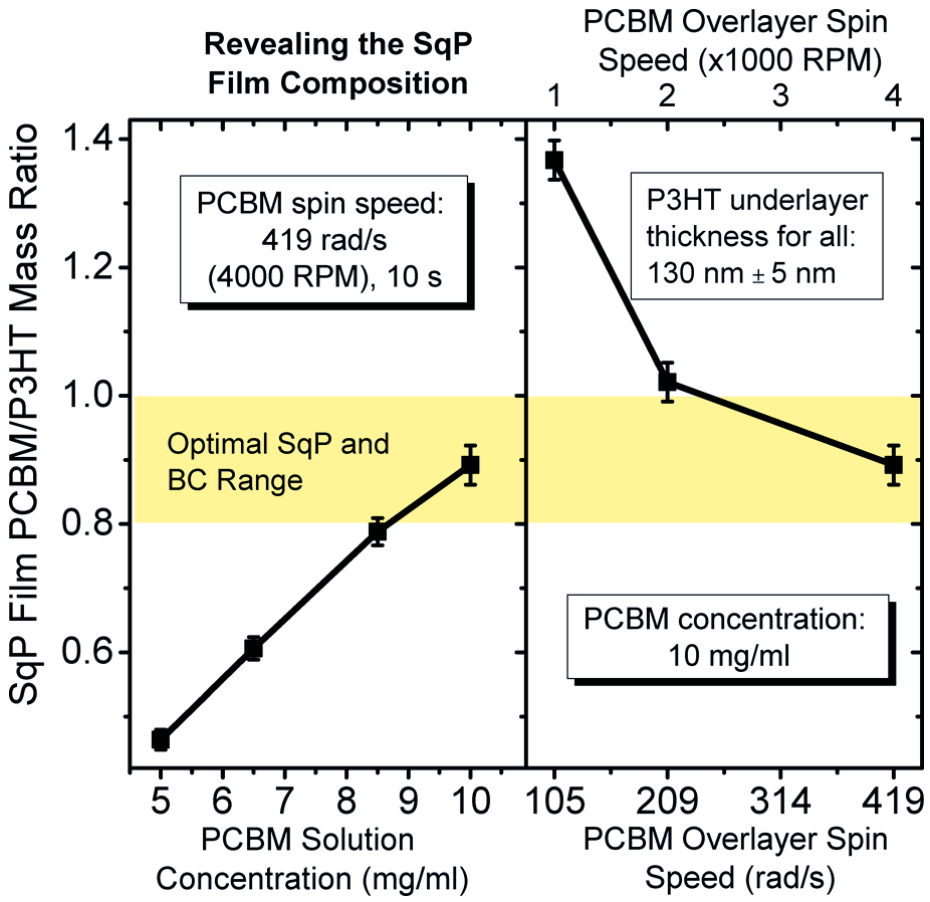

Figure 5.3: Composition of P3HT/PCBM SqP active layers as a function of the PCBM solution concentration in DCM and spin speed used to create the overlayer. In all cases the P3HT underlayer was 130 ± 5 nm thick. In this comparison, the optimal conditions for SqP solar cell performance (cf. Figure 5.7) are 10 mg/mL, 419 rad/s (4000 rpm), and 10 s. The optimal BC solar cell composition range is from Ref 23.

that varied between 1:0.8 and 1:1 P3HT:PCBM by mass for the same spin conditions. In a particular run, though, we found that a 10 mg/mL PCBM solution in DCM can give reproducible compositions (Figure 5.3 error bars). In comparing the results of Figure 5.3 to previously reported processing conditions for P3HT:PCBM SqP devices, we conclude that optimal P3HT:PCBM SqP active layers have a composition in the same range as their optimal BC counterparts (1:0.8 to 1:1 P3HT:PCBM mass ratio; yellow bar in Figure 5.3), which is surprising because it is not necessarily obvious that SqP should have the same optimal composition as BC.[23,251,278–280] Additionally, in the Appendix D Figure D.4 we show how a high enough PCBM content of ∼1:0.8 in SqP devices is necessary for device performance and that herein SqP active layers do not operate well at lower PCBM contents.[23]

Figure 5.3 further shows that the SqP film composition can be tuned over a wide range from 31% PCBM by mass (1:0.45 wt. ratio) to 58% PCBM by mass (1:1.37 wt. ratio) by simply changing the processing parameters for the PCBM overlayer (i.e. solution concentration and spin speed). This allows us to make better sense of the wide range of processing conditions in the literature for P3HT:PCBM SqP films.[255,257,259,261,262,272,278] Figure 5.3 suggests that when optimizing an SqP active layer for device performance, the PCBM solution concentration and deposition conditions are tuned for a given P3HT underlayer to achieve a composition that is approximately the same as the optimal composition for an equivalent BC film. Finally, we also note that compositions for processing-condition combinations not indicated in Figure 5.3 can be estimated from linear extrapolation from the data in Figure 5.3. This analysis can also be performed for previous SqP morphology studies where the overall composition was unknown.[255]

5.3.2 Morphology Differences of Matched SqP and BC P3HT:PCBM Films

Given that the optimal device processing conditions lead to SqP active layers with the same composition as that for optimal BC films, the next important question we ask is whether or not the two different processing routes produce the same nanoscale BHJ architecture. There have been claims that SqP simply provides a more complex route to the same BHJ structure as BC,[278,279] so it is important to determine if thickness- and composition-matched films produced via SqP and BC have the same morphology. To investigate this question, we fabricated a series of 1:0.8 P3HT:PCBM mass ratio active layers via SqP, determining the composition as above, and then made corresponding BC films with matching composition and thickness (see Appendix D for the detailed matching recipe). In the following analysis, when we refer to 'matched' BC and SqP films, we mean films with identical 1:0.8 composition ratios and identical thicknesses of

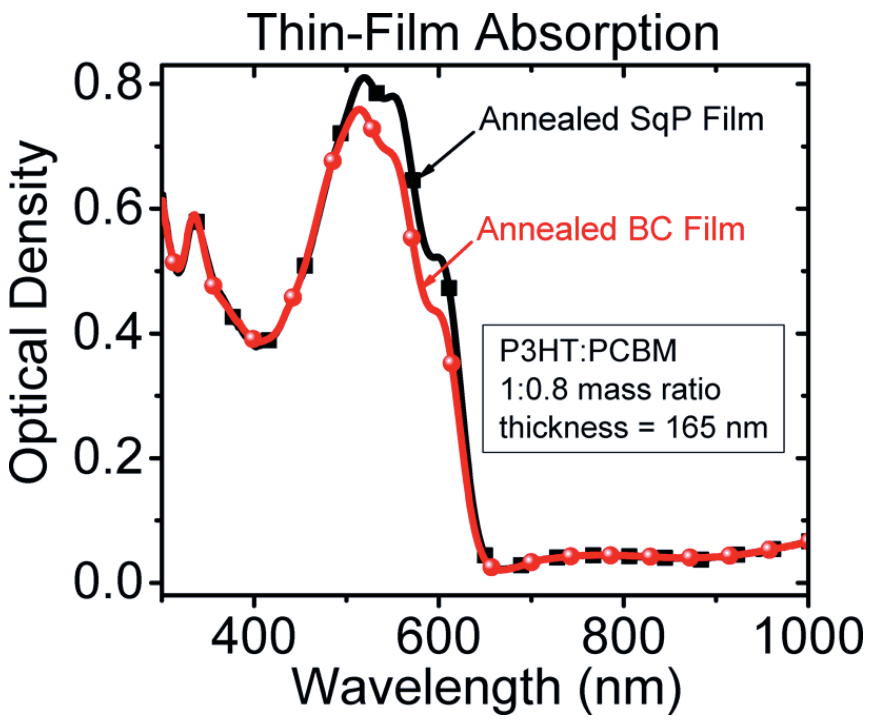

Figure 5.4: Solid-film absorbance 1:0.8 P3HT:PCBM weight ratio, 165 nm thick matched SqP and BC films that were thermally annealed for 20 m at 150 °C. The significant difference in absorbance is due to differences in P3HT crystallinity. The well-matched features in the near-IR region, due to thin-film interference, show that the two films indeed have similar thickness.

165 nm.

We begin by examining absorption spectra of matched films produced by the two different processing routes since the absorptive features of P3HT directly reflect its molecular ordering.[281] Figure 5.4 shows the thin-film absorbance of matched annealed P3HT:PCBM SqP and BC films prepared in the manner described in the Appendix D. When compared to the equivalent BC film, the P3HT:PCBM SqP film shows stronger absorbance in the region associated with aggregated P3HT as well as a different vibronic structure.[281] We note that when repeating this measurement, the absorbance of SqP films was more reproducible than the corresponding BC films because the absorption of BC films is highly sensitive to drying history, irrespective of thermal annealing (see Appendix D Figure D.1).[29] Although this sensitivity to drying is especially prevalent with P3HT-based BC films, aggregation-dependent absorption is a feature of many molecular materials that are of interest for SqP solar cells.[282] Thus, Fig. 4 provides the first evidence that SqP films are less sensitive to processing kinetics than BC films, showing that SqP can yield high-quality active

layers that are less affected by the details of the drying conditions.

Perhaps more importantly, as discussed above, Figure 5.4 also demonstrates that solid-film UV-vis absorbance cannot be used to obtain reliable composition estimates: the two films whose spectra are shown in Figure 5.4 have identical compositions and thickness but different absorbances. This is because the polymer absorption spectrum depends sensitively on its local environment (e.g., degree of (para)crystallinity, orientation, crystallite size, etc.). Additionally, solid-film absorption measurements are strongly affected by reflectivity, scattering, and thin-film interference,[283] so that there is no simple way to extract the composition. Thus, it is critical that our re-dissolving method be used if accurate and reproducible composition estimates are desired.

The differences in the spectra in Figure 5.4 also suggest that, in the present comparison, the P3HT in the SqP films is more crystalline than in matched, equivalently-processed BC films. The reason for this is that, in SqP, there is no PCBM to inhibit aggregation when the polymer film is cast. This is an important difference to consider when attempting to tailor a (polymer) underlayer for ideal network formation. The effect of annealing and interdiffusion on the SqP absorbance is presented in the Appendix D (Figure D.3), showing that the P3HT absorbance for SqP films is unchanged by incorporation of the PCBM. We note, however, that slow-drying of BC films can result in a similar polymer film absorbance and thus presumably similar levels of P3HT aggregation. For this work, however, we did not slow dry the BC films because we wanted to make the best head-to-head comparison with the SqP approach, which involves thermal annealing instead of slow drying. We note that our chosen post-processing conditions for BC P3HT:PCBM devices yield similar solar cell performance to devices made by slow drying.[284]

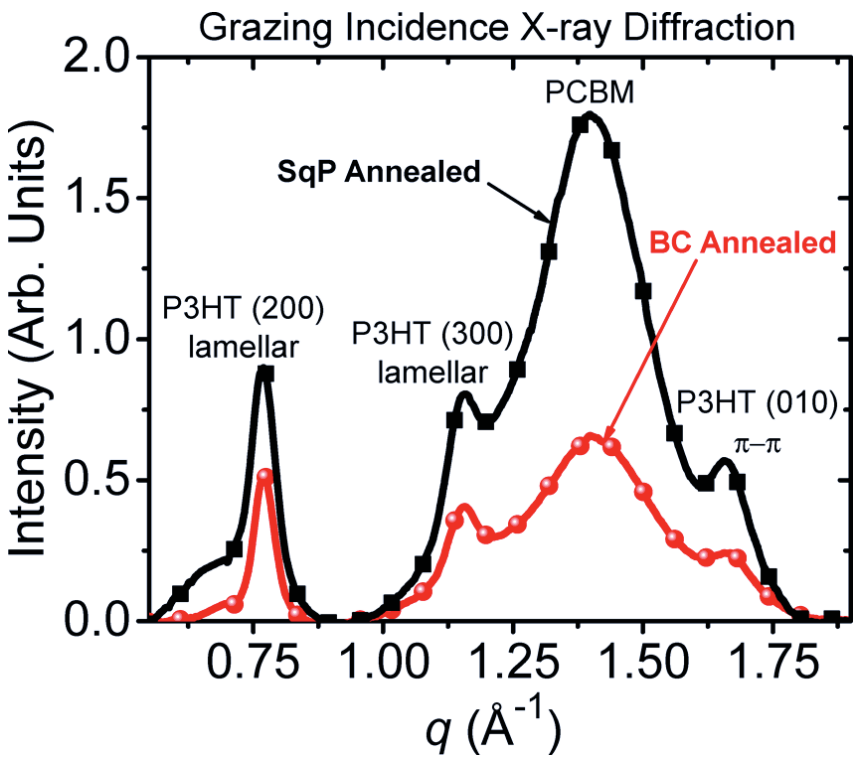

Figure 5.5: GIXD data of matched 1:0.8 P3HT:PCBM SqP and BC films after thermal annealing for 20 m at 150 °C, showing stronger diffraction in the SqP active layer. Each curve represents the integrated intensity at each *q* averaged over three separate films.

Although absorption spectroscopy can provide a general indication as to the relative crystallinity of P3HT in different film environments, it does not provide detailed information about the morphology of the polymer:fullerene networks in such films. Thus, we examined the structure of our matched annealed SqP and BC films using grazing-incidence x-ray diffraction (GIXD). Although we collected the diffraction in 2-D (Appendix D Figure D.7), Figure 5.5 shows the radially integrated data, which immediately provides a sense of the relative degree of crystallinity of the components in each of the matched films. We emphasize that this integrated data is representative of the differences in molecular order between SqP and BC films because the experiment was conducted on multiple samples that were rigorously thickness- and composition-matched and examined under identical beam-line conditions (see Appendix D for experimental details). Indeed, Figure 5.5 confirms the general conclusion we drew from Figure 5.4, showing not only that the P3HT but also the PCBM exhibits stronger diffraction in annealed SqP active layers. In particular, Figure 5.5 shows that both the P3HT lamellar and π-π stacking order is greater in SqP films. Further analysis of the P3HT

(100) (not shown) and (200) peaks, however, reveals that the full width half maximum (FWHM) of the diffraction peaks is slightly larger for SqP derived layers ($FWHM_{(100)} = 0.039$ Å^{-1} and $FWHM_{(200)} = 0.073$ Å^{-1}) than BC films ($FWHM_{(100)} = 0.035$ Å^{-1} and $FWHM_{(200)} = 0.053$ Å^{-1}), suggesting that despite increased order (which would likely decrease the FWHM), the SqP morphology perhaps produces smaller domain sizes, a conclusion we support with energy-filtered TEM tomography below. The stronger PCBM diffraction in SqP films observed in Fig. 5 could also be partly due to the presence of a pure, thin PCBM overlayer on top of the annealed SqP film, which would also be consistent with the XPS results below.

As briefly mentioned above, there are good reasons why P3HT:PCBM SqP active layers should have more ordered domains when compared to equivalent BC active layers. BC films rely on spontaneous nanoscale phase separation during film formation, which means that P3HT crystallization occurs in the presence of a significant amount of PCBM. This initial presence of PCBM will therefore play a significant role in determining the final P3HT morphology as the blend transitions from solution to solid film. With SqP P3HT:PCBM active layers, on the other hand, the neat P3HT underlayer is already formed and in the solid state when the PCBM is introduced. During interdiffusion into the polymer matrix, the PCBM primarily intercalates into the amorphous regions of the P3HT,[251] allowing the high initial crystallinity of the P3HT to remain intact throughout processing (Figure S3).[262,263] Thus, PCBM has a significantly reduced role in determining the overall morphology in the SqP approach as opposed to the BC approach.

Lastly, we performed energy-filtered transmission electron microscopy (EF-TEM) and tomography to examine the morphologies of our matched-annealed SqP and BC films (Figure 5.6). In EF-TEM, images of the specimen are formed using electrons that have lost a specific amount of energy. This imaging mode can be combined with electron tomography techniques to produce a three-dimensional reconstruction of the specimen from a series of two-dimensional EF-TEM projections. This technique has proven quite useful for P3HT:PCBM devices, where the contrast produced in conventional bright-field TEM imaging is much lower due to the similar electron scattering characteristics of the two constituent materials. Several groups have reported results using EF-TEM tomography to image the nanoscale morphology of P3HT:PCBM devices.[285–288] Our images were collected in a similar fashion to this previous work (see Appendix D section for

details regarding data acquisition and processing). Figure 5.6 displays the results of this procedure for the thickness- and composition-

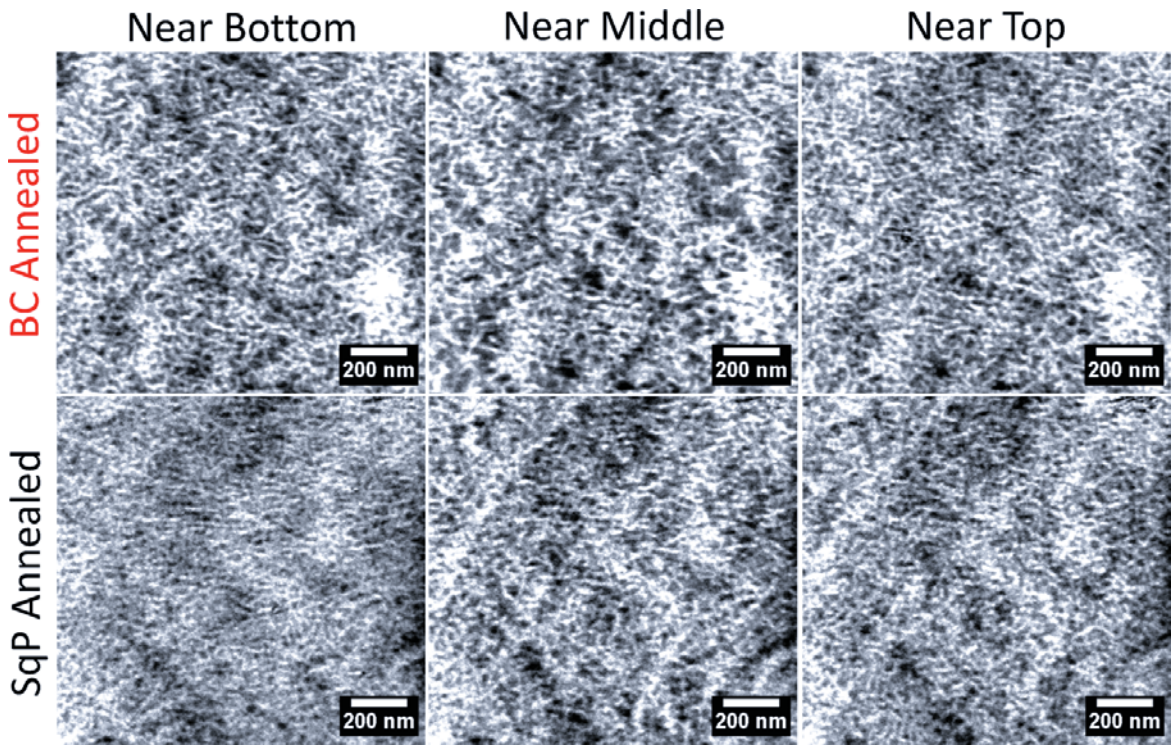

Figure 5.6: EF-TEM tomography slices of matched-annealed SqP and BC films showing the *x*-*y* plane (parallel to the substrate plane) for near the top (film/air interface), middle, and bottom (film/substrate interface) regions of the films (see Supporting Information for details on how the contrast was obtained). The SqP film has an overall finer nanometer-scale structure, especially in the region near the substrate; see text for details.

matched annealed SqP and BC active layers. In-plane slices extracted from near the top (film/air), middle, and bottom (film/PEDOT) sections of the EF-TEM tomograms show the vertical distribution of the P3HT-rich domains (bright) and PCBM-rich domains (dark). The most striking difference in morphology exists near the substrate interface, where it is clear that the SqP device has a much finer nm-scale structure (Figure 6).[289] Moving vertically through the film toward the top surface (film/air) shows that the matched SqP and BC films converge to a more similar morphology, though the SqP has consistently smaller overall domains and a finer structure (as also observed by GIXD, above). We note that EF-TEM is not surface sensitive, and thus the near-top images in Figure 6 are actually buried slightly below the top surfaces that were analyzed by XPS and CELIV.

We hypothesize that the fine structure of the SqP film morphology derives from the fact that

polymer-layer formation occurs in the absence of PCBM. When PCBM is present in large amounts, as in the BC case, it carves out significant volume during film formation. Upon annealing and polymer/fullerene separation, some of the blended volume becomes available for the P3HT to use in forming larger domains. In SqP, the polymer matrix is already in the solid state, and thus it is likely that the interdiffusion of PCBM does not significantly alter its fine structure. Hence, in the BC case, the initial presence of PCBM plays a more significant role in determining the polymer morphology.

Although there are structure differences in Figure 5.6, given the significantly different processing routes used (Figure 5.1), it is somewhat surprising that the two BHJ networks are so generally similar. This suggests that for the P3HT:PCBM materials combination, formation of a BHJ network on this length scale can be achieved by multiple processing routes. With blend casting, it is generally difficult to assess whether any given morphology is kinetically trapped or is a structure near a thermodynamic minimum. Thus, alternative processing routes, such as the SqP approach, may prove useful in screening for functional multicomponent molecular systems that form thermodynamically favorable and nanoscale networks.[191]

To summarize our morphological studies, as-cast SqP films have a top surface that is almost entirely PCBM, but thermal annealing allows nearly all of this PCBM to intersperse into the P3HT underlayer, creating a well-ordered nanoscale BHJ network whose top surface is somewhat enriched in PCBM when compared to an equivalent BC film. Moreover, our comparison of matched films using GIXD and TEM shows that the morphology obtained by the traditional BC approach has larger and less ordered material domains when compared to the SqP morphology, although both BHJs have structure on similar length scales.

5.3.3 Top-Surface Composition of Matched P3HT:PCBM Films

In addition to the overall crystallinity of the components of a BHJ, photovoltaic performance can also depend on the degree of vertical phase separation; i.e., the composition distribution of the components in the direction normal to the plane of the film.[290,291] Since SqP films (prior to thermal annealing) start with most of the fullerene on top, one might expect that the degree of vertical phase separation could be different in films produced via SqP and BC. To determine if there actually is

any difference, we measured the top and bottom surface compositions of our matched annealed SqP and BHJ active layers using x-ray photoelectron spectroscopy (XPS).

For P3HT:PCBM blend films, XPS can provide an estimate of the average surface composition by measuring the sulfur-to-carbon (S/C) ratio since the PCBM component does not contain sulfur.[292–294] By fitting the sulfur 2p and the carbon 1s spectral lines (see Appendix D for experimental and analysis details), we found that the top (film/air) surface of annealed SqP films is slightly richer in PCBM when compared to annealed BC films (see Table 5.2, below). A statistical t-test for the annealed top-surface data gives a significance level of $p = 0.106$, indicating with a reasonable degree of confidence that the surface composition is indeed slightly different, with the SqP film having marginally more fullerene on the top surface than the BC sample. The S/C ratio of the as-cast SqP films, on the other hand, is smaller than the annealed layer's S/C ratio by more than an order of magnitude (Table 5.2). This confirms that the top surface of as-cast SqP P3HT/PCBM films are covered by PCBM with only a very small fraction of P3HT, in agreement with previously published XPS and neutron reflectivity experiments.[255,256] Interestingly, the bottom surface of both SqP and BC films are significantly enriched in fullerene (Table 5.2), but there is no statistically significant difference in S/C ratio for annealed films. Thus, our XPS results indicate that a difference between matched-annealed P3HT:PCBM SqP and BC films is that annealed SqP films are slightly richer in PCBM at the top surface, a remnant of the initial SqP as-cast quasi-bilayer structure.

As a way to better understand how differences in surface composition can affect device characteristics, we measured the equilibrium dark doping density of our matched BC and SqP films using the CELIV technique.[213] In CELIV, a linear reverse-bias voltage ramp is applied to a device and the resulting current is monitored. Most of the measured signal in this experiment results from displacement current, since the device acts as a capacitor, but if there are any mobile carriers present due to doping, CELIV can easily and accurately measure their presence. Integrating the CELIV transients (Appendix D Figure D.5) after subtracting the displacement current gives the results that are summarized below in Table 5.2. We find that there is indeed a correlation between the average doping density measured by CELIV and the top-surface PCBM content determined by the XPS S/C ratio. Specifically, the as-cast SqP films have a substantial number of carriers in the dark at zero bias, whereas annealed SqP devices have ≈ 7 less and annealed BC films have an undetectable number

of dark carriers. To explain these results, we hypothesize that the Ca cathode is doping PCBM at or around the top interface (the device structure is ITO/PEDOT:PSS/P3HT:PCBM/Ca/Al). This is consistent with other studies,[295–297] and provides further verification that annealed SqP films have somewhat more PCBM on their top surface than equivalent BCs. Moreover, this shows that CELIV can be used as a simple and sensitive tool for examining the relative amount of fullerene material at the metal/active-layer contact. We note that hole doping of the P3HT from chemical contaminants cannot be responsible for the CELIV signals because all the materials were made using P3HT from the same batch and all the solutions underwent identical processing. In the next section, we explore how these morphological vertical composition differences affect the performance of photovoltaic devices.

5.4 Comparing the Device Physics of Matched SqP and BC P3HT:PCBM Photovoltaic Devices

5.4.1 The Solar Cell Performance of Matched BC and SqP P3HT:PCBM Films

Now that we understand the similarities and differences in the nm-scale morphology of thickness- and composition-matched BC and SqP films, we turn to photovoltaic devices based on these films. The details of how the devices were fabricated are described in the Appendix D. Figure 5.7 and Table 5.1 compare the average photovoltaic performance of matched 1:0.8 mass ratio P3HT:PCBM SqP and BC active layers in standard ITO(150 nm)/PEDOT:PSS(35 nm)/Active-Layer(165 nm)/Ca(10 nm)/Al(70 nm) devices under AM1.5 illumination. The data show that annealed SqP devices are more efficient than the corresponding matched annealed BC devices due to higher short-circuit current densities (J_{sc}) and fill factors (FF). The larger J_{sc} for SqP devices is almost certainly due to stronger P3HT absorption (Figure 5.4), and the higher fill factor is likely due to a better-ordered network (Figure 5.5) and higher shunt resistance (Table 5.2). For completeness, in Figure D.2 we also compare the performance of SqP and slow-dried BC active-layer devices, which have more crystalline P3HT and thus more similar device efficiencies.

A major reason for the excellent performance of the larger area SqP active layers in Figure

Table 5.1: Photovoltaic Performance of Composition and Thickness Matched SqP and BC Solar Cells.[a]

Active Layer	Active Area (mm^2)	V_{OC} (V)	J_{SC} (mA/cm^2)	Fill Factor (%)	Efficiency (%)
annealed SqP	7.2	610 ± 8	8.3 ± 0.4	66 ± 1	3.4 ± 0.2
annealed BC	7.2	622 ± 6	7.6 ± 0.5	61 ± 3	2.9 ± 0.3
as-cast SqP	7.2	429 ± 25	4.2 ± 0.3	44 ± 4	0.8 ± 0.1
annealed SqP	34	580 ± 10	8.3 ± 0.5	52 ± 3	2.5 ± 0.2
annealed BC	34	590 ± 10	8.7 ± 1.7	39 ± 7	2.0 ± 0.4

[a]Each value for 7.2 mm^2 active area devices is averaged over ~30 solar cells made on multiple substrates over multiple device fabrication runs. Each value for 34 mm^2 active area devices was averaged over 8 solar cells. Values after the $\pm$ represent one standard deviation.

5.7b is the overall film quality, which is significantly better than that resulting from traditional BC processing. This visual observation does not readily manifest itself in the performance of small-area devices (Figure 5.7a), but does become apparent in larger-area cells (Figure 5.7b). The error bars in Figure 5.7b represent one standard deviation for at

least 8 independent large-area devices. Thus, Figure 5.7b and Table 5.1 clearly demonstrate that the SqP fabrication approach is more amenable to scaling than the traditional BC method, as the large-area SqP devices are both more efficient and significantly more reproducible. We are presently working on developing new fullerene casting solvents that will make SqP more conducive to printing techniques, which will allow the inherently better film quality and more scalable morphology to be fully exploited. The reason for these differences in film quality arise from the radically different means by which the donor:acceptor BHJ network is created (Figure 5.1). Sequential processing is not influenced by film-drying kinetics or co-solubility requirements, but instead relies on how well an acceptor molecule (PCBM here) can intercalate into a semi-crystalline polymer network. Blend-casting, on the other hand, is more difficult to control because it requires molecularly co-dissolved solutions that, upon casting, must spontaneously yield the ideal amount of nanoscale phase separation. This type of spontaneous phase-separation process is not well understood, and more importantly, is inherently ultra-sensitive to processing conditions (e.g., deposition conditions, film drying kinetics, use of solvent additives, etc.), which is why optimizing the BC film morphology still relies heavily on

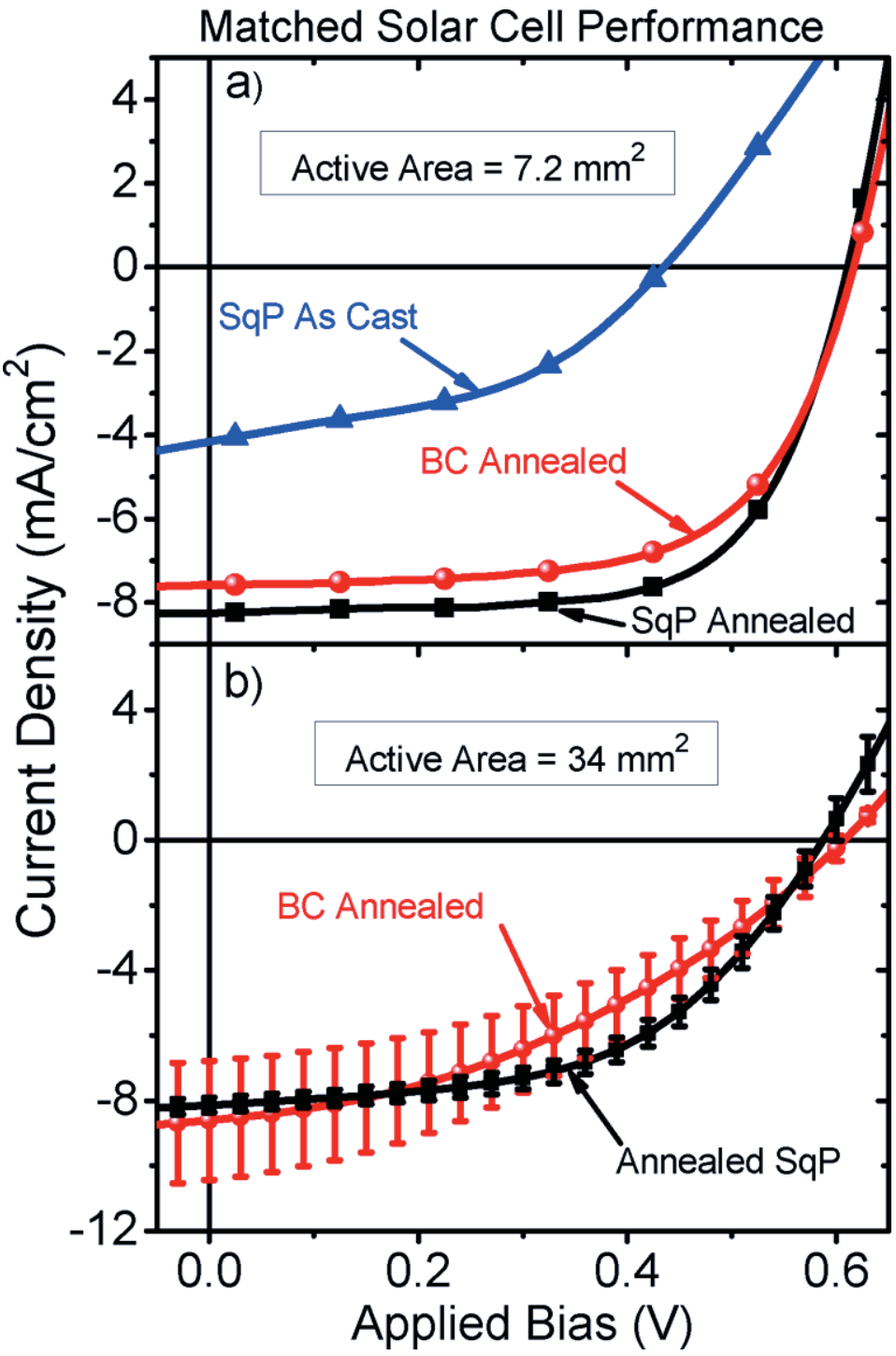

Figure 5.7: (a) Comparison of SqP vs BC device performance in the standard ITO/PEDOT:PSS/active-layer/Ca/Al device structure. (b) Larger-area device performance of matched SqP and BC solar cells. The enhanced film quality of SqP devices results in better scalability when compared to traditional BC as well as a lower overall device shunt resistance. The error bars in (b) represent one standard deviation obtained from averaging over eight devices; the error bars for (a) are given in Figure 5.1. Other device parameters are summarized in Tables 1 and 2 (see also Figure 5.8).

trial-and-error.[298] Moreover, given the significant differences in BHJ formation, it is reassuring that the SqP method can reproduce and even surpass BC device performance for a set of molecules (i.e. P3HT and PCBM) that are considered to be ideally suited for BC processing.

Figure 5.7a and Table 5.1 also present the photovoltaic performance of matched as-cast SqP devices, which show far inferior performance to annealed versions of both SqP and BC cells.[251] It is well known that as-cast SqP films have more of a bilayer structure than an intermixed BHJ morphology, and that this structure gives significantly worse photovoltaic performance.[251,255,256] Since comparisons of as-cast and annealed SqP P3HT:PCBM solar cells have been examined in other work,[251,255,261,262] we relegate discussion of our as-cast SqP device performance to the Appendix D.

5.4.2 Steady-State Device Physics

To further understand how the differences in morphology explored above manifest in device behavior, we analyzed the open-circuit voltage (V_{oc}) as a function of light intensity (I) (Table 5.2 and Figure 5.8a) and the dark diode current density (J) as a function of applied voltage (V) (Table 5.2 and Figure 5.8b) for our matched BC and SqP devices. Our methods for obtaining the values in Table 5.2 are detailed in the Appendix D. Since one might expect the morphology differences to lead to differences in recombination process(es) occurring within the device, we focus in this section on the diode ideality factor (n_{id}).[97,134,135,157,299] The ideality factor derives from the slope of the linear region in a semi-logarithmic dark J-V or V_{oc} vs. I plot, and primarily reflects the dominant recombination mechanism occurring within the semiconductor active layer. Ideality factors are unitless and typically range from 1-2, though values outside this range are possible.[157,158] An ideality factor of one is consistent with more ideal band-to-band recombination processes, whereas an ideality factor of two is consistent with trap-assisted recombination through mid-gap states. The recombination processes that give rise to intermediate ideality factors between 1 and 2 are not readily evident and must be evaluated on a contextual basis, though these values are often closely tied to trap-assisted recombination.[135]

Table 5.2 shows that the ideality factors we extract for matched-annealed SqP and BC devices are

Table 5.2: Diode Characteristics of Composition and Thickness Matched SqP and BC Solar Cells.[a,b]

Active Layer	n_{id} (Dark J-V)	n_{id} (V_{OC} vs I)	R_{series} (Ω-cm^2)	R_{shunt} ($\times 10^5$ Ω-cm^2)	Avg. Dark Carrier Density (cm^{-3})	XPS S/C Ratio Film/Air ($\times 10^{-3}$)	XPS S/C Ratio Film/Glass ($\times 10^{-3}$)
annealed SqP	7.2	610 ± 8	8.3 ± 0.4	66 ± 1	3.4 ± 0.2	41 ± 7	12 ± 3
annealed BC	7.2	622 ± 6	7.6 ± 0.5	61 ± 3	2.9 ± 0.3	35 ± 4	17 ± 7
as-cast SqP	7.2	429 ± 25	4.2 ± 0.3	44 ± 4	0.8 ± 0.1	1.7 ± 0.3	–

[a]The diode characteristics are averaged over ~30 solar cells made on multiple substrates over multiple device fabrication runs. Values after the $\pm$ represent one standard deviation. [b]Device active area of 7.2 mm^2

identical whether evaluated from dark J-V curves or from V_{oc} vs. I. The reason for the discrepancy between n_{id}'s obtained from dark J-V and from V_{oc} vs. I analysis is the subject of some controversy and has been discussed in detail elsewhere.[154,157] As mentioned above, the non-unity ideality factors in Table 5.2 for both the BC and SqP devices are consistent with a significant amount of trap-assisted recombination, likely through a distribution of trap energies.[134,135,299] If the ideality factor is considered to be representative of bulk recombination processes, then our results surprisingly suggest that the dominant recombination mechanism(s) is(are) the same in matched-annealed SqP and BC films, despite the rather significant differences in overall crystallinity and more subtle differences in BHJ network morphology. Our results thus suggest that the interfacial density of states and recombination processes are very similar in optimized SqP and BC films and not as strongly correlated with domain size and molecular ordering as one might have expected. This conclusion is also consistent with our subgap EQE and transient measurements, discussed below.

Further analysis of the J-V curves in Figure 5.8 also allows us to extract the effective external series and shunt resistances of our matched BC and SqP devices (see Appendix D for analysis details). When we perform this analysis, also summarized in Table 5.2, we find that annealed SqP devices have a substantially higher shunt resistance than the BC devices, which can be readily observed in the low bias region of Figure 5.8b. This is likely another manifestation of the better film quality of annealed SqP devices, since macroscopic film defects facilitate leakage current. The effective series resistances for the matched BC and SqP annealed active layers, on the other hand, are identical, which indicates that the devices are well matched in terms of contact and interlayer properties. Further discussion of the as-cast SqP dark device data can be found in the Appendix D.

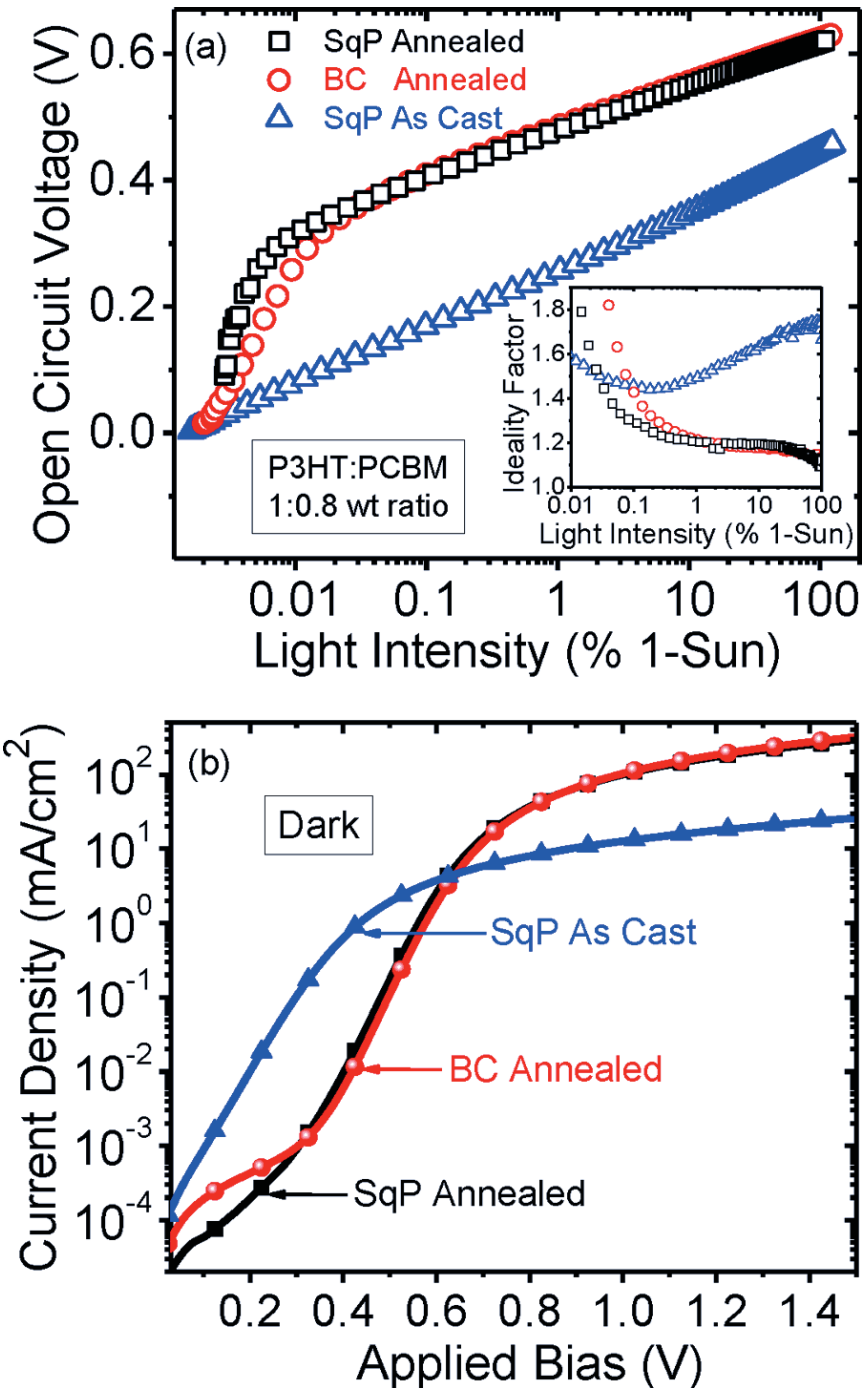

Figure 5.8: Photovoltaic behavior of matched, annealed BC (red cirlcles/curves), and as-cast (blue triangles/curves) and annealed (black squares/curves) SqP devices. (a) V_{oc} as a function of light intensity. The V_{oc} of annealed SqP devices rises faster at lower light intensity than that of BC devices because of a larger shunt resistance. Beyond the shunt-dominated regime, the annealed SqP V_{oc} almost uniformly tracks the annealed BC except for a $\sim$12 mV offset. The inset shows the differential ideality factor. (b) Dark *J-V* characteristics of 7.2 mm^2 active area devices. Clearly, the annealed SqP has significantly less leakage current than the annealed BC while the ascast SqP has both higher series resistance and lower shunt resistance.

5.4.3 Recombination Kinetics and Interfacial Density of States

Given that the *J-V* curves of matched-annealed SqP and BC devices (over small active areas) are so similar, the question is: do the morphology differences that result from the different processing routes make any noticeable difference in the device physics that is not evident from the *J-V* curves? To answer this question, we first used transient photovoltage (TPV) and transient photocurrent (TPC) techniques to study the recombination kinetics in our matched films. TPV measures the return-to-steady-state decay of the V_{oc} after a small light-pulse perturbation, while TPC examines the response of the J_{sc} to this same light pulse. TPV provides a good window into the recombination kinetics since at V_{oc} the excess perturbation charges must decay via recombination.[197] TPC, on the other hand, is dominated by carrier sweep-out and is therefore used to measure the amount of photogenerated charge caused by the perturbation pulse. TPC and TPV have been widely used in the organic solar cell community to determine excess-carrier recombination rates as a function of total average excess-carrier density (n).[87,88,90,95,150,196,300] The information obtained from TPC, TPV, and related techniques are highly relevant because the entire *J-V* curve at multiple light intensities can be reconstructed from the analysis.[90–94,150]

Figure 5.9 compares the average excess-carrier recombination properties of two annealed SqP (black squares) and two annealed BC (red circles) devices as derived from our TPC/TPV analysis (see Appendix D for details). As is typically found in polymer:fullerene BHJs, the carrier lifetime (τ) is observed to depend more strongly on the total average carrier concentration (n) than would be expected for the case of ideal
band-to-band recombination $(\tau \propto n^{-1})$.

The relationship that we observe ($\tau \propto n^{\gamma}$ where $\gamma > 1$) is consistent with a significant contribution by trap-assisted (Shockley-Read-Hall) recombination through a distribution of trap energies, which is also in agreement with our ideality factor analysis above.[97,134] Thus, Figure 5.9 shows that despite the modestly different nm-scale morphologies and significantly different molecular ordering, the SqP and BC processing routes yield devices that have essentially identical recombination kinetics as measured by TPC/TPV. This again suggests that while the nanoscale architecture of SqP and BC BHJ films is different, the recombination kinetics are not terribly sensitive to these structural

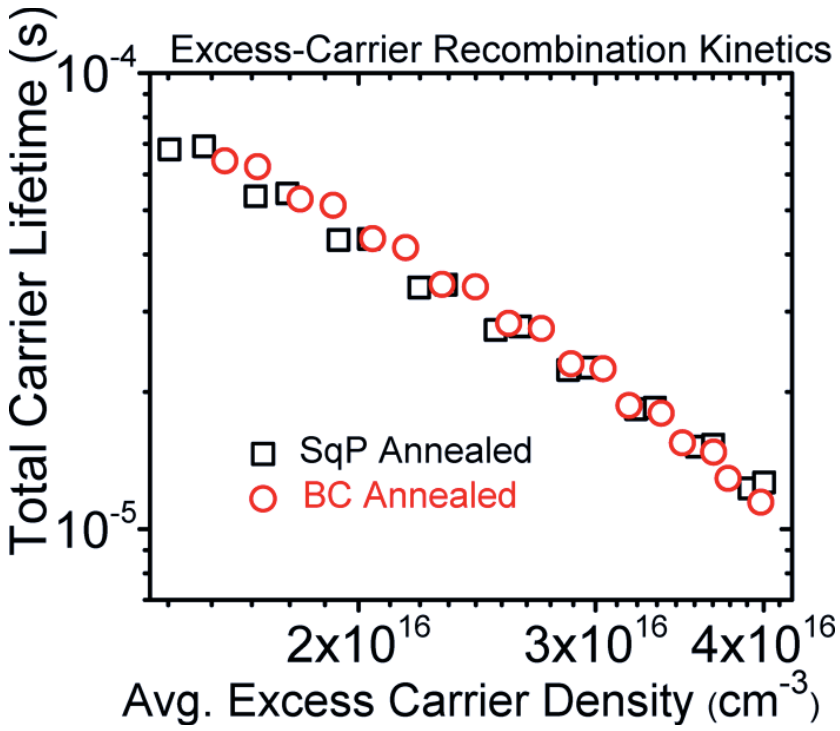

Figure 5.9: Total carrier lifetime plotted as a function of total (trapped plus free) average excess-carrier concentration relative to short circuit in the dark, as obtained from analysis of TPV and TPC measurements. The data for each active-layer type is composed of the results from two different solar cells. These recombination kinetics suggest that the interfacial electronic properties of matched annealed SqP (black squares) and BC (red circles) films is essentially identical, despite the differences in component crystallinity and BHJ architecture between them.

differences, but instead are likely dominated by interfacial structure and mixing at the boundary of P3HT and PCBM domains.

To further confirm these ideas, we directly measured the interfacial density of states distributions in these BHJ structures using subgap external quantum efficiency (EQE) measurements.[158] Subgap EQE details a solar cell's photoresponse to sub-energy-gap photoexcitation, and has previously been interpreted as reflecting the joint density of interfacial states in polymer:fullerene BHJs.[168] The lowest energy portion of the EQE spectrum in particular has been shown to correlate well with solar cell performance, dark diode characteristics, and intentionally introduced defects.[98, 168, 175, 299]

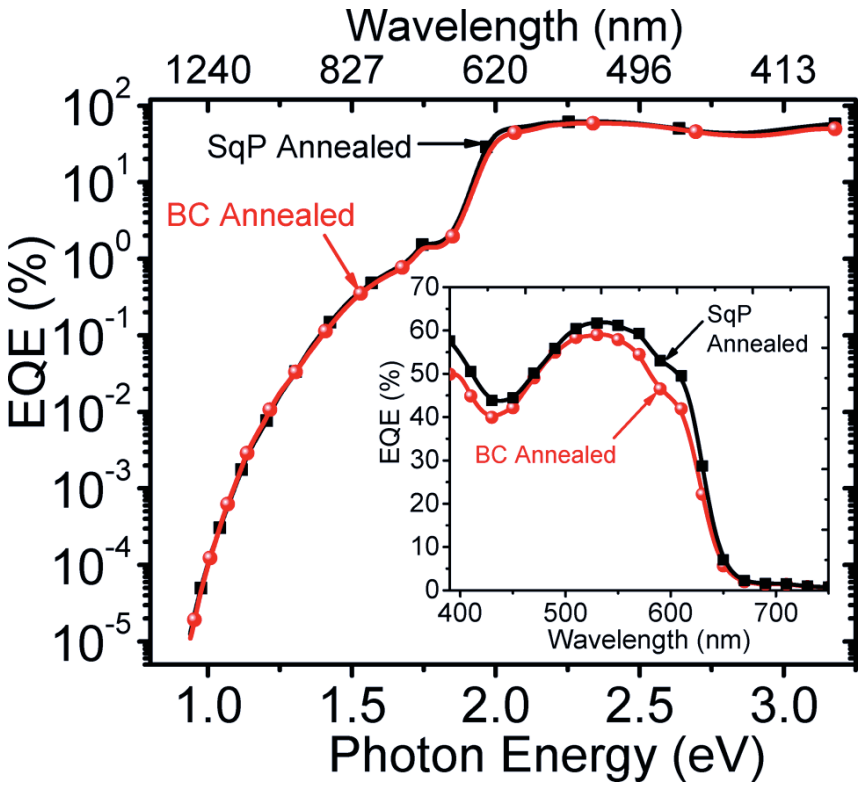

Figure 5.10: EQE spectra for matched annealed BC (red curves/circles) and SqP (black curves/circles) devices. The linear scale EQE (inset) is consistent with the differences in absorption in Figure 5.4. The subgap EQE signal involving interfacial transitions ($\lesssim$1.5 eV) is essentially identical for annealed SqP and BC devices.

Figure 5.10 shows the EQE of our matched annealed SqP (black curve/square) and BC (red curve/circles) devices. The differences in the above-gap EQE (Figure 10 inset) are consistent with the differences in absorption seen above in Figure 5.4; the higher EQE at $\approx$ 600 nm shows that the P3HT is more crystalline in the SqP case. When integrated against the AM 1.5G solar spectrum, the predicted J_{SC} values for these devices are 8.05 mA/cm^2 and 7.29 mA/cm^2 for the annealed SqP and annealed BC, respectively, in reasonable agreement with the measured J_{SC} values in Table 5.1. Interestingly, the subgap EQE signal involving interfacial transitions (below $\sim$1.5 eV) is nearly identical for annealed SqPs and BCs, again suggesting that the two routes yield essentially the same interfacial electronic properties despite the measured differences in morphology, molecular crystallinity, and doping. More specifically, these similarities indicate that, in these BHJs, the overall molecular ordering and nanoscale morphology is not necessarily directly coupled to the molecular structure at the heterojunction interfaces. Indeed, the interfacial properties for optimal P3HT:PCBM

appear to be highly robust, which is perhaps one reason why this materials combination consistently photogenerates mobile charges with high yield.

Taken together, Table 5.2 and Figures 5.7-5.10 jointly support the broad claim that, despite modestly different nm-scale morphologies and doping densities and significant differences in molecular ordering and crystallinity, the interfacial electronic processes in matched annealed SqP and BC photovoltaic devices are essentially identical.

5.5 Conclusions

In summary, we have presented an extensive comparison of the morphology and device performance/characteristics of thickness- and composition-matched P3HT:PCBM SqP and BC active layers. Since the composition of SqP active layers was not previously known to an accurate degree, we invented a novel method for obtaining the overall composition of a polymer/fullerene SqP film based on redissolving and analyzing the dilute-solution absorption spectrum. We showed that our solution-based method is both accurate and reproducible. When applying this technique, we found that the optimal composition of P3HT:PCBM SqP and BC active layers falls in the same range (44-50 % PCBM by mass). Despite the similarity in composition, annealed SqP active layers yield better device performance due to both enhanced absorption from more crystalline P3HT and superior film quality. The improved film quality of SqP active layers plays a major role in enhancing the performance of larger-area devices, which indicates that the SqP approach is more amenable to scaling than the traditional BC approach. GIXD, UV-vis absorption, and energy-filtered transmission electron tomography all show that annealed SqP active layers have a finer-scale blend morphology as well as more ordered polymer and fullerene domains when compared to equivalently-processed BC active layers. XPS analysis reveals a top interface for SqP films that is slightly richer in PCBM when compared to matched BC active layers, an observation also supported by CELIV measurements of PCBM doping at the cathode interface. Despite these clear morphological differences, measurements of the carrier recombination kinetics from TPC and TPV experiments and the distribution of interface states from subgap EQE measurements all indicate that the interfacial electronic processes occurring at P3HT:PCBM heterojunctions are

essentially identical for matched annealed SqP and BC active layers. This suggests that modest differences in network order do not make a large impact on the interfacial electronic processes, perhaps explaining why the BHJ morphology has worked so well despite the lack of processing control over its nm-scale architecture.

CHAPTER 6

Extensive Penetration of Evaporated Electrode Metals into Fullerene Films: Intercalated Metal Nanostructures and Influence on Device Architecture

6.1 Introduction

Polymer:fullerene bulk heterojunction (BHJ) organic photovoltaics (OPVs)[23,24,48,83,136,301] and perovskite-based solar cells[302–304] have attracted widespread interest as potential low-cost solar energy harvesters. Although much research has been directed toward the optoelectronic processes occurring within the cell's photoactive layer,[11,12,97,135,150,187,192,195,205,225,305–308] another critically important aspect of these devices is their mesoscopic structure. In OPVs, for example, it is desirable to have a vertical composition profile that is enriched in fullerene material at the electron-collecting contact to promote charge extraction out of the active layer and increase cathode selectivity.[18,22,118,211,216,240,262,275,290,291,309–311] Perovoskite-based solar cells also often use fullerene electron transport layers between the active layer and the cathode for the same reason.[312–315] For both types of devices, the correct energetic alignment and conductivity are important for achieving, as closely as possible, selective Ohmic contacts.[293,307,312,314,316–321]

Despite a significant amount of research on both OPVs and perovskite-based solar cells, somewhat less attention has been paid to the morphology of the electrode interfaces.[322,323] It is typically assumed that the deposition techniques (e.g., thermal evaporation, spin coating, etc.) used to create the device give clean interfaces with minimal ($\lesssim$ a few nm) interpenetration.[322] In particular, there is little work examining how commonly-used evaporated cathode metals, such as Ca or Al, specifically interact with the fullerene component of the active layer or electron transport layer. Understanding

the interaction of fullerene derivatives and metals is important because fullerenes strongly prefer the metal interface due to their high surface energy,[296,324–326] and previous work has shown that C_{60} strongly interacts with metals, undergoing charge transfer with essentially any metallic species to form fullerene:metal salts.[327–332]

It is well known, for example, that evaporated metals can penetrate through films of organic molecules that are only a few nm thick, allowing the creation of 'memistors' and other devices that originally were expected to behave as simple capacitors or tunnel junctions.[333,334] The nature of organic layer/metal contacts also has been studied in films of small molecules such as pentacene,[335–337] tris-8-hydroxyquinolinato-aluminum (Alq_3),[338,339] and diindenoperylene (DIP),[335,336,340,341] where it has been established that even though nearly all the metal remains on top of the organic layer, small amounts of evaporated metal can penetrate to the bottom of $\sim$60-nm thick films. A diffusion depth of $\sim$ 2 nm of Au atoms into the amorphous polystyrene film during the metal sputtering has also been reported previously.[342] It is also well known that evaporated metals can co-crystallize with C_{60}, forming fullerene:metal salts that can even be superconductors in certain cases.[327–332,343]

In this work, we show that evaporated electrode metals penetrate extensively—by many tens of nanometers—into films of both pure fullerene derivatives and the fullerene-rich portion of OPV active layers. By using a combination of capacitance measurements, cross-sectional transmission electron microscopy (X-TEM), and UV-visible spectroscopy on fullerene/evaporated metal layers in various device geometries, we find that commonly-used electrode metals, including Au, Al, Ag, and Ca, all readily penetrate entirely through thick fullerene-derivative layers, significantly altering both the optical and electrical properties of the devices. Our electrical measurements show that the effective electrical thickness of fullerene-based devices, as measured by their geometric capacitance, can easily change by 70 nm. This has important implications for device physics experiments (e.g., space-charge limited current and other carrier mobility measurements, whose analysis depends sensitively on knowing the (electrical) thickness of the device. For the particular case of Au evaporated onto as-cast sequentially-processed poly(3-hexylthiophene) (P3HT)/[6,6]-phenyl-C_{61}-butyric acid methyl ester (PCBM) quasi-bilayers,[201,251,344] we show that metal penetration results in the formation of $\sim$3-20-nm diameter nanoparticles (NPs) that are embedded throughout the

PCBM overlayer matrix (see Fig. 6.3, below). This not only indicates an exceptionally high penetration/diffusivity of the metal into the fullerene,[345,346] but also results in readily-measurable plasmonic effects from the NPs, which can alter the optical properties of the device. Since fullerene-rich top layers paired with evaporated metals such as Au, Ca, Ag, and Al are critical components of OPV and perovskite-based solar cells as well as transistors and other organic electronic devices,[27,29,216,347–356] the fact that metals can extensively penetrate into fullerene derivatives has important implications for the organic electronics research community.

6.2 Results and Discussion

6.2.0.1 Electrical Thickness of Fullerene Films Measured via Device Geometric Capacitance

Our initial evidence for the interpenetration of evaporated metals into fullerene-rich layers comes from simple electrical characterization experiments. We started by measuring the geometric capacitance (C_g) of standard planar fullerene-based devices with different active-layers using the charge extraction by linearly increasing voltage (CELIV) technique.[204,213,357] The CELIV approach for obtaining C_g is schematically shown in Fig. 6.1A, and involves using (if necessary) an initial steady-state reverse bias to fully deplete the active layer of any equilibrium free charge. The experiment is also run in the dark, which eliminates the presence of photogenerated carriers. The initial bias is followed by a linear reverse-bias ramp of the form $V(t) = U_R t + V_0$ where t is the time after the start of the ramp, V_0 is the initial steady-state reverse bias, and U_R is the ramp rate in V/s. For a typical parallel-plate capacitor, the current response to this voltage ramp is constant in time and directly related to C_g (Fig. 6.1A). Since the device is initially depleted and the voltage ramp is run in reverse bias, the device behaves essentially as a capacitor. It is thus straightforward to fit the CELIV current transients to an equivalent circuit model, described in Appendix E, in order to accurately extract C_g.

One of the reasons CELIV is particularly well-suited for measuring C_g is because it allows for easy decoupling of the geometric capacitance from other quantities, such as the equilibrium

doping density, series/shunt resistances, and the device's built-in potential.[237,238,358] The geometric capacitance is determined solely by the device's geometry, with $C_g = A\varepsilon_0\varepsilon/d$ for a simple single-layer capacitor, where A is the device area, ε_0 is the vacuum permittivity, ε is the dielectric constant of the material between the electrodes, and d is the electrical thickness of the device. Thus, we have chosen to focus on the device C_g because it provides an excellent indicator of metal penetration due to its high sensitivity to the active-layer dielectric constant and electrical thickness, both of which are strongly impacted by the incorporation of metal.

Our discovery of metal interpenetration took place when we were examining CELIV transients on OPV devices based on poly(3-hexylthiophene) (P3HT) and PCBM. We built numerous devices via solution sequential processing (SqP) of the active layer,[359,360] where the polymer layer is deposited first, in this case from *o*-dichlorobenzene (ODCB), and then the fullerene layer is deposited in a second step from a quasi-orthogonal solvent, in this case dichloromethane (DCM). We used the active layers as-cast without thermal or solvent annealing, which results in devices with a quasi-bilayer geometry: ITO/PEDOT:PSS/P3HT/PCBM/Metal.[255–257] Since the top of the active layer of these devices is rich in PCBM,[201,255–257] this provided a perfect opportunity to observe how evaporated metal electrodes interacted with fullerene-rich layers in sandwich-structure devices. Our experiments explored as-cast sequentially-processed devices with varying active layer compositions, thicknesses, and evaporated electrodes (see Table 6.1, below). In all cases, we directly measured the thickness of the active layer using profilometry, which has an accuracy of ± 5 nm. Figure 6.1B shows an example of the results, where the red circles are for a device with a pure 115-nm thick P3HT film as the active layer, and the blue squares are for a device with an active layer consisting of an identically-processed P3HT film with a $\sim$66-nm thick solution sequentially-processed PCBM overlayer. Surprisingly, even though the 181-nm thick sequentially-processed active layer is significantly thicker than the pure P3HT layer, the sequentially-processed device actually has a slightly higher capacitive current and thus, a slightly larger geometric capacitance.

To analyze the geometric capacitances of our devices obtained from CELIV, we calculated the C_g's for pure active layers from the parallel-plate capacitor relation: $C_g = A\varepsilon_0\varepsilon/d$, with typical values for P3HT layers ranging from $d_{P3HT} = 115 \pm 5$ nm, $A = 7.2 \pm 0.5$ mm^2 (we used this electrode area for all devices unless otherwise specified), and $\varepsilon_{P3HT} = 3 \pm 0.1$.[361] For the sequentially-processed

devices with fullerene overlayers, we assumed a bilayer parallel-plate geometry, where fullerene penetrates into the polymer film producing a mixed underlayer,[257] plus an essentially pure fullerene layer on top, resulting in:

$$C_g = \frac{A\varepsilon_0\varepsilon_{P3HT:PCBM}\varepsilon_{PCBM}}{d_{PCBM}\varepsilon_{P3HT:PCBM} + d_{P3HT:PCBM}\varepsilon_{PCBM}}, \tag{6.1}$$

where for the devices in Fig. 6.1B, $\varepsilon_{PCBM} = 3.9 \pm 0.1$,[361] and $d_{PCBM} = 66 \pm 5$ nm. Previous work using neutron reflectometry on as-cast sequentially-processed P3HT/PCBM active layers found that the P3HT-rich underlayer contains ~25-30 wt% PCBM and that the underlayer does not change appreciably in thickness.[255–257] Using this information and the effective medium approximation, we employed typical values of $d_{P3HT:PCBM} = 115 \pm 5$ nm and $\varepsilon_{P3HT:PCBM} = 3.25 \pm 0.1$ for the P3HT-rich underlayer. The uncertainties quoted here lead directly to those quoted for C_g in Table 6.1 using standard propagation of errors.[362]

A further statistical comparison of numerous devices processed identically to those shown in Fig. 6.1B reveals that pure P3HT devices of this thickness should have a C_g of 1.66 ± 0.08 nF, which is in good agreement with the measured value of 1.74 ± 0.09 nF. In contrast, the sequentially-processed quasi-bilayer has a predicted C_g of 1.25 ± 0.1 nF, which is well outside the error of the measured value. The fact that the measured C_g for the quasi-bilayer is significantly larger than expected indicates that the effective electrical thickness of the device is much thinner than anticipated, and in fact, this device has essentially the same thickness as the original P3HT underlayer (Table 6.1). The only simple explanation for this discrepancy between the measured and predicted C_g values is that in the quasi-bilayer samples, the evaporated Ca/Al electrode penetrates entirely through the PCBM-rich overlayer and only stops at the P3HT-rich interface, so that the quasi-bilayer C_g values become identical to those of the pure underlayer. Table 6.1 presents measured and predicted C_g values for a number of as-cast P3HT/PCBM SqP quasi-bilayer devices with different evaporated metal electrodes (Ca/Al, Ca, Al, Mg, Ag, Pt, K, Na and Au) and varying PCBM overlayer thicknesses, all of which exhibit discrepancies between the measured and predicted geometric capacitances that are consistent with significant metal penetration into the active layers. In particular, the C_g values in Table 6.1 indicate that Au, Al, and Ca electrodes penetrate entirely

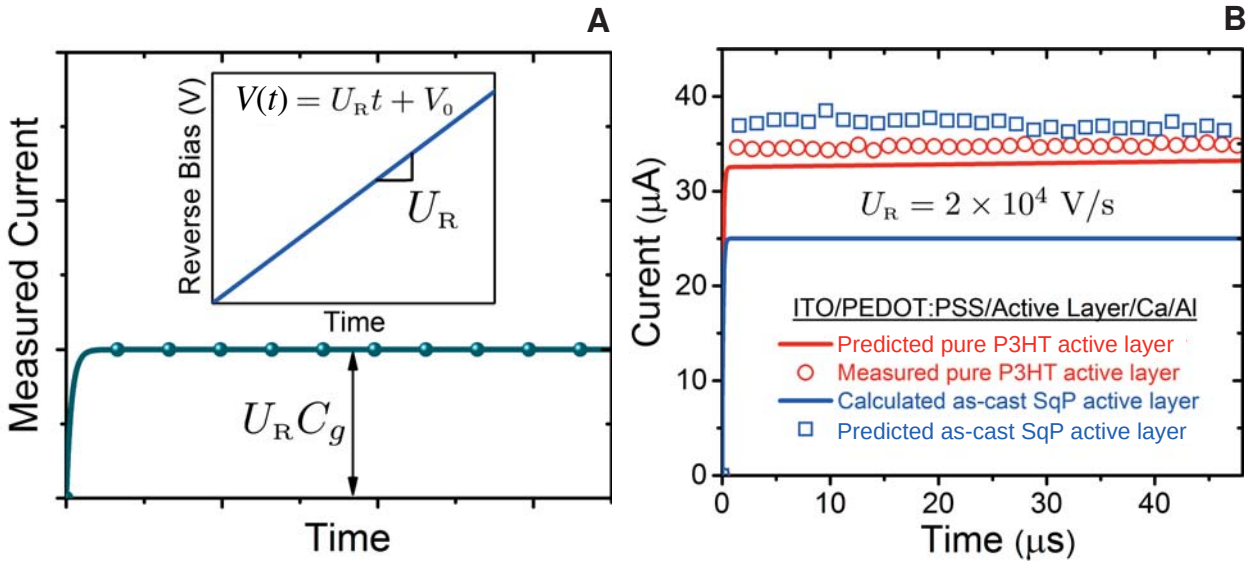

Figure 6.1: A) Schematic of how C_g is measured straightforwardly in the CELIV experiment. More details on the mathematical extraction of C_g from CELIV traces are given in the SI. B) Measured reverse-bias CELIV current transients of ITO/PEDOT:PSS/P3HT(115 nm)/PCBM(66 nm)/Ca/Al devices showing a distinct difference between the predicted (solid curves, from Eq. 6.1 using the measured layer thickness(es) and dielectric constant(s)) and measured C_g values (open symbols) when a PCBM-rich overlayer (sequentially-processed quasi-bilayer) is added on top of the P3HT and then exposed to the evaporated metal electrode. Note that V_0 = 0 for the pure P3HT capacitor (no equilibrium free charge), but a $V_0 = -3$ V was needed for the quasi-bilayer in order to ensure that the active layer was fully depleted.

through the fullerene-rich overlayer but not into the P3HT-rich underlayer, and that Ag, Mg, Pt, K, and Na can actually penetrate through the fullerene-rich overlayer and into the P3HT-rich underlayer as well (Table 6.1).

To evaluate how far the evaporated metal can penetrate through a fullerene-rich overlayer, we next analyzed the geometric capacitances of P3HT/PCBM quasi-bilayers as the thickness of the PCBM overlayer was varied. Figure 6.2A shows a strong divergence between the measured and predicted C_g values for P3HT/PCBM/Ca/Al devices when the PCBM overlayer is made successively thicker by increasing the PCBM concentration of the casting solution (at 4000 rpm, a 5 mg/mL solution of PCBM in DCM gives a 37-nm PCBM overlayer, a 10 mg/mL solution results in a 66-nm thick overlayer, and a 15 mg/mL near-saturated solution yields a 75-nm thick overlayer). For all these devices, it is particularly striking that the measured C_g remains constant and approximately equal to that of the pure P3HT underlayer despite the additional PCBM overlayer thickness. This is a strong indication that metal penetration can occur through PCBM overlayers of essentially any

thickness obtainable by spin-coating. We note that the slight increase in capacitance observed with fullerene incorporation in Figs. 6.2A and 6.1B (blue squares vs. red circles) likely results either from a small amount of the P3HT underlayer being washed away by the DCM fullerene-casting solvent or from an increase in the dielectric constant of the underlayer, as PCBM has a higher dielectric constant than P3HT and the SqP approach results in ~25-30 wt% intercalation of PCBM into the P3HT underlayer.[257]

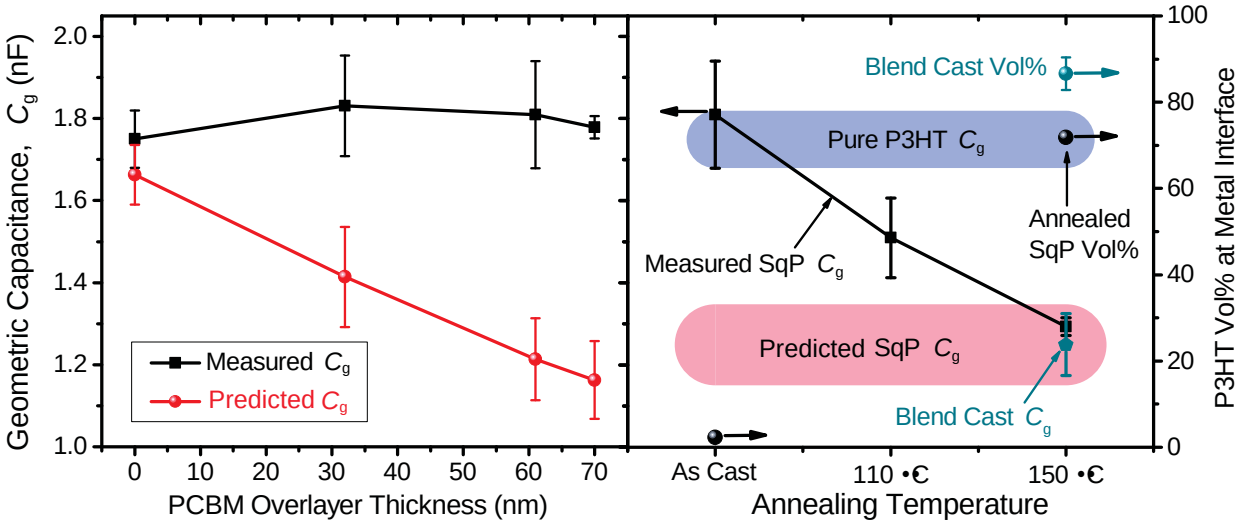

Figure 6.2: A) The measured and predicted geometric capacitances of P3HT/PCBM/Ca/Al sequentially-processed as-cast quasi-bilayer devices with different PCBM overlayer thicknesses. The divergence of the measured and predicted C_g values indicates metal interpenetration through the entire fullerene overlayer. B) The device geometric capacitance as a function of quasi-bilayer active-layer annealing temperature before metal deposition (black line; error bars one standard deviation). All devices were annealed for 20 min. The thick blue bar represents the measured pure P3HT underlayer geometric capacitance with ± one standard deviation uncertainty. The thick pink bar represents the predicted device C_g with uncertainty calculated using the measured active-layer thickness. Annealing as-cast quasi-bilayers intermixes the P3HT and PCBM, which causes the measured C_g to approach the predicted C_g due to blocking of the metal-penetration by the presence of P3HT at the top interface. The right vertical axis shows P3HT volume percent at the top surface (black spheres; obtained from XPS S/C analysis).[275] Traditional blend-cast devices (dark cyan symbols) also show no measurable metal penetration due to the presence of nearly pure P3HT at the top surface of the active layer (dark cyan sphere).

Table 6.1: Measured and Predicted Geometric Capacitance (C_g) based on the Measured Active-layer Thickness for Various Organic Semiconductor Diodes[a]

Active Layer	Evaporated Electrode[a]	Measured C_g (nF)	Calculated C_g (nF)	Measured Thickness[b] (nm)	C_g Thickness[c] (nm)
P3HT[d]	Ca/Al	1.74 ± 0.09	1.68 ± 0.08	115 ± 5	110 ± 6
P3HT	MoO_3	1.39 ± 0.01	1.39 ± 0.01	115 ± 5	115 ± 1
PCBM (80 nm)	Ca/Al	Shorted	3.11 ± 0.19	80 ± 5	-
PCBM (80 nm)	MoO_3	2.27 ± 0.01	2.30 ± 0.19	80 ± 5	79 ± 1
P3HT/PCBM (37 nm) SqP	Ca/Al	1.83 ± 0.12	1.41 ± 0.12	152 ± 5	111 ± 7
P3HT/PCBM (66 nm) SqP	Ca/Al	1.81 ± 0.13	1.21 ± 0.10	181 ± 5	115 ± 8
P3HT/PCBM (75 nm) SqP	Ca/Al	1.78 ± 0.03	1.16 ± 0.09	190 ± 5	118 ± 2
P3HT/PCBM, 150 °C SqP	Ca/Al	1.29 ± 0.02	1.25 ± 0.09	178 ± 5	171 ± 3
P3HT/PCBM, 110 °C SqP	Ca/Al	1.51 ± 0.09	1.29 ± 0.10	178 ± 5	147 ± 9
P3HT:PCBM, 150 °C BC	Ca/Al	1.25 ± 0.07	1.30 ± 0.04	173 ± 5	177 ± 10
P3HT/PCBM SqP	Ca (0.3 nm)/Ag	1.87 ± 0.16	1.21 ± 0.10	181 ± 5	112 ± 10
P3HT/PCBM SqP	Al	1.78 ± 0.19	1.21 ± 0.10	181 ± 5	117 ± 12
P3HT/PCBM SqP	Mg	2.40 ± 0.02	1.21 ± 0.10	181 ± 5	87 ± 9
P3HT/PCBM SqP	Au	2.01 ± 0.06	1.21 ± 0.10	181 ± 5	104 ± 3
P3HT/PCBM SqP	Ag	Shorted	1.21 ± 0.10	181 ± 5	-
P3HT/PCBM SqP	Pt[e]	Shorted	1.21 ± 0.10	181 ± 5	-
P3HT/PCBM SqP	Na (15 nm)/Ag	Shorted	1.21 ± 0.10	181 ± 5	-
P3HT/PCBM SqP	K (15 nm)/Ag	Shorted	1.21 ± 0.10	181 ± 5	-
P3HT/bis-PCBM SqP	Ca/Al	2.16 ± 0.20	1.21 ± 0.10	176 ± 5	97 ± 9
P3HT/ICBA[f] SqP	Ag	Shorted	< 1.21	> 181	-
P3HT/ICBA SqP	Ca (45 nm)	2.52	< 1.21	> 181	89
P3HT/ICBA SqP	Al	3.11	< 1.21	> 181	72
SiO_2 (270 nm)	Ca/Al	1.55 ± 0.01	1.55 ± 0.1	270[f]	270 ± 2
SiO_2 (285 nm)/PCBM (95 nm)	Ca/Al	1.35 ± 0.03	1.10 ± 0.1	380[g]	310 ± 3

[a] If not specified, the thickness for Ca is 10 nm, for Al is 70 nm, for Ag is 70 nm, for MoO_3 is 15 nm and for ZnO is 40 nm.;
[b] All thickness values are determined by profilometry;
[c] Calculated from measured C_g;
[d] P3HT C_g is sensitive to polymer batch and thermal annealing;
[e] *e*-beam deposited to 50 nm at less than 0.5 Å/s rate;
[f] The ICBA-based SqP devices were thicker than their PCBM counterparts but with indeterminate thickness due to surface roughness;
[g] SiO_2 contribution determined by spectroscopic ellipsometry and PCBM contribution determined by both profilometry and spectroscopic ellipsometry.

In addition to diodes built with pure P3HT active layers and P3HT/PCBM quasi-bilayers (as in Fig. 6.1B), we also fabricated devices with well-mixed P3HT:PCBM active layers using both traditional blend-casting and thermal annealing of the sequentially-processed quasi-bilayers. It is well known that annealing P3HT/PCBM quasi-bilayers results in rapid interdiffusion of the two components,[255–257,263] transforming the quasi-bilayer into a more well-mixed P3HT:PCBM bulk heterojunction film. Since the degree of mixing increases as the temperature is raised above 110 °C,[255] we expect annealing at temperatures above this threshold to significantly increase the amount of P3HT that resides at the top surface of the active layer. Figure 6.2B shows that the measured C_g of annealed P3HT/PCBM quasi-bilayers steadily decreases with increasing annealing temperature from 110 °C to 150 °C. Moreover, when the mixing becomes strong enough (annealing for 20 min at 150 °C) the measured C_g becomes, within error, equal to the predicted C_g based on the measured active-layer thickness. Also plotted in Fig. 6.2B is the C_g of a blend-cast P3HT:PCBM device that has the same total thickness and composition as the quasi-bilayer devices.[201] The C_g of this blend-cast device also shows no deviation between the measured and predicted C_g values.

All of these results suggest that even small amounts of P3HT at the top surface of the active layer can block metal penetration in the same way that a P3HT-rich underlayer stops metal interpenetration from completely shorting a quasi-bilayer device. To better quantify this effect, we measured the surface composition of these active layers using x-ray photoelectron spectroscopy (XPS). For the P3HT/PCBM system, the measured XPS sulfur/carbon ratio provides a direct measure of the amount of P3HT in the top few nm of the active layer.[201,275] The right vertical axis of Fig. 6.2B shows the volume percent of P3HT at the top surface of each of these samples as determined by XPS (see the SI for S/C calculation details). The data show that 150 °C-annealed quasi-bilayers and traditional blend-cast P3HT:PCBM active layers have $>$ 70 vol% P3HT at their top surfaces, while as-cast P3HT/PCBM quasi-bilayers only have $\sim$3 vol% P3HT at their surfaces. Clearly, Fig. 6.2B suggests that evaporated metal electrodes can easily penetrate through fullerene-rich layers but cannot penetrate through even a small amount of dilute conjugated polymer such as P3HT. Taken together, the C_g analysis in Figs. 6.1 and 6.2, and Table 6.1 lead to three major conclusions: first, that the device geometric capacitance is a reliable indicator of metal penetration; second, that the functional device structure is dramatically changed when an electrode metal is evaporated onto a

PCBM-rich layer; and third, that P3HT acts as a remarkably efficient blocker of metal penetration.

Since the presence of even small amounts of P3HT at the top surface can affect metal penetration, it makes sense to investigate the interaction of evaporated metals with pure fullerene films. Table 6.1 shows that when we fabricated diodes with a pure PCBM active layer (device structure ITO/PEDOT:PSS/PCBM/Ca/Al), the devices were always either shorted or too leaky to obtain reliable C_g values. This indicates that the evaporated electrode can effectively penetrate through the entire fullerene layer to make electrical contact with the bottom electrode, consistent with the quasi-bilayer results discussed above. To verify that there is nothing special about P3HT stopping metal interpenetration, Table 6.1 also summarizes results indicating metal penetration can be blocked by placing a thin insulating interlayer (e.g., 15 nm of MoO_3, which is typically used to fabricate 'inverted' devices[45,296]) on top of the fullerene layer; see also Fig. E.5 of the SI. This observation might be an important reason why inverted device architectures that utilize metal oxide buffer layers typically work better than their normal-structure counterparts for OPVs,[45,84,116] as metal interpenetration could easily be detrimental to solar cell performance. Finally, Table 6.1 also shows that we obtained identical C_g trends using other fullerene derivatives, including indene-C_{60} bisadduct (ICBA)[363] and bis-PCBM,[364,365] demonstrating that evaporated metal interpenetration is a general phenomenon for many fullerene derivatives.

As another way to investigate evaporated metal penetration into pure fullerene films, we also fabricated devices using doped-Si with a thick thermal oxide overlayer as the bottom electrode. Table 6.1 shows that when a Ca/Al top electrode is evaporated directly onto the thick SiO_2 thermal oxide layer, the measured C_g of the resulting device is in excellent agreement with the parallel-plate capacitor equation prediction: $C_g = A\varepsilon_0\varepsilon_{SiO_2}/d_{SiO_2} = 1.55$ nF, with $d_{SiO_2} = 270$ nm, $\varepsilon_{SiO_2} = 3.9$, and $A = 12.1$ mm^2. However, when 95 nm of PCBM (as measured by profilometry and spectroscopic ellipsometry) is spun on top of the SiO_2 overlayer, the measured C_g is just 1.35 nF (with the same Ca/Al top electrode), which is much larger than that predicted and only slightly smaller than that of the device built without PCBM. A simple analysis reveals that this C_g value accounts for only $\sim$25 nm of the PCBM layer, leaving $\sim$70 nm of PCBM thickness missing from the dielectric thickness. This demonstrates that the evaporated Au electrode has an effective electronic penetration depth of approximately 70 nm into the 95-nm thick PCBM film. This suggests that either the top 70 nm of

the fullerene layer has become a part of the electrode or that the dielectric constant of this portion of the film has become so high because of the amount of intercalated metal that it essentially has no measurable capacitance when placed in series with the effective ∼25 nm of 'pure' PCBM.

6.2.0.2 X-TEM Analysis of Metal Interpenetration in PCBM Films

With ample evidence in hand for metal penetration, the obvious question becomes: can we directly observe and measure the infiltrated metal distribution inside these fullerene layers? To address this question, we turn to cross-sectional transmission electron microscopy (X-TEM), where a focused-ion beam (FIB) is used to cut a thin section from an as-cast, sequentially-processed P3HT/PCBM quasi-bilayer device, and the resulting device cross-section is directly imaged with TEM.[251,252,267,278,279,322,366–368] To generate a sample for this process, we evaporated a Au top electrode onto an as-cast P3HT/PCBM quasi-bilayer active layer at a rate of only 0.1 Å/s, leading to an expected device architecture of glass/ITO (150 nm)/PEDOT:PSS (35 nm)/P3HT:PCBM (130 nm)/PCBM (45 nm)/Au (50 nm); here, as above, we expect the P3HT:PCBM underlayer to have ∼25-30 wt.% PCBM from the SqP.[257] When collecting this data, care was taken to limit electron beam exposure and any subsequent possible sample damage.[369–371] We note, however, that our primary interest in this work is the structure of the interpenetrated metal, which is robust to beam exposure. We chose to use gold as the evaporated top electrode material for three reasons: first, the capacitance measurements described above indicate that Au can penetrate up to ∼70 nm into fullerene-rich films; second, Au has excellent *Z*-contrast in comparison to the carbon-based P3HT/PCBM active-layer materials; and third, Au does not readily degrade or oxidize, making it robust to the necessary processing steps leading up to TEM imaging.

Figure 6.3A clearly shows that instead of the nominally fabricated glass/ITO/PEDOT:PSS/P3HT:PCBM/ PCBM/Au device structure, there is indeed readily-visible Au metal penetration into the PCBM overlayer. Further inspection suggests that a more accurate description of the actual device architecture is glass/ITO/PEDOT:PSS/P3HT:PCBM/PCBM:Au/Au, with clear distinct boundaries for each of these layers. We used high-angle annular dark-field (HAADF) scanning transmission electron microscopy (STEM), discussed below, and spot EDS

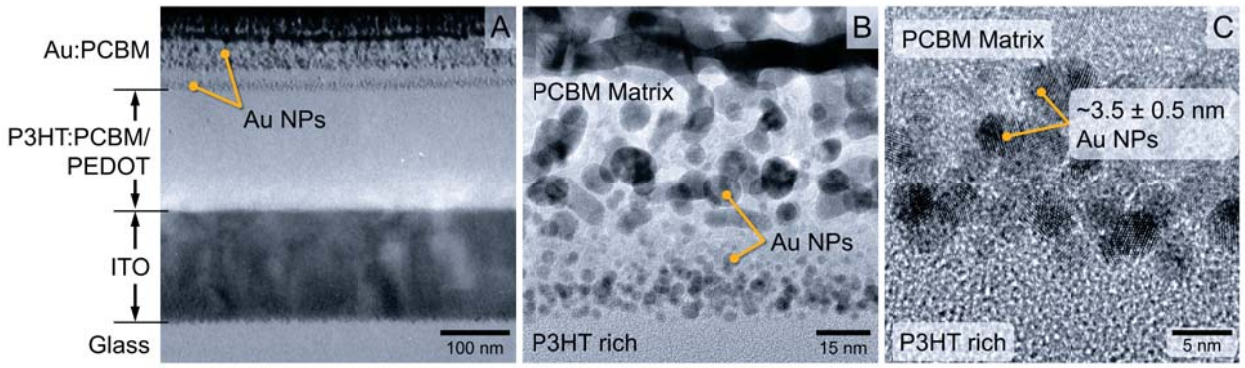

Figure 6.3: Bright field, cross-sectional TEM images of a glass/ITO/PEDOT:PSS/P3HT:PCBM-/PCBM:Au/Au as-cast, sequentially-processed quasi-bilayer device. A) A representative section of the entire device stack and each layer's persistence in the in-plane direction. B) Higher magnification view of the P3HT:PCBM/PCBM:Au/Au interfaces, showing the clear formation of metal nanoparticles resulting from the thermal evaporation of Au onto the PCBM-rich portion of the active layer. C) A further magnified view of the region just above the interface with the P3HT-rich underlayer, showing a layer of fairly monodisperse $\sim$3.5 $\pm$ 0.5 nm diameter Au nanocrystals.

spectra, shown in the SI, to verify the elemental composition in each region of the image. One of the most striking and unexpected features of Fig. 6.3A is a distinct layer of Au nanoparticles (NPs) that is visible $\sim$175 nm above the ITO/PEDOT:PSS interface. This distance is consistent with the nominal thickness of the P3HT-rich underlayer plus PEDOT:PSS interlayer, indicating that Au penetration proceeds all the way down to the P3HT-rich layer. This is certainly surprising given that P3HT has a lower mass density than PCBM,[372] but is in perfect agreement with the conclusions reached above from our C_g analysis. We hypothesize that the sulfur heteroatom in the polymer plays a role in stopping metal penetration, since gold, for example, has an otherwise high diffusivity in conjugated carbonaceous systems.[345,346] In the P3HT/Ca system, for instance, it has been shown that the Ca/S-heteroatom interaction is significant enough to even abstract the sulfur from P3HT.[373–375]

Figure 6.3B focuses on what should have been the P3HT/PCBM quasi-bilayer interface,[255–257] but instead is found to be a PCBM:Au-NP matrix in contact with the P3HT-rich underlayer. This image reveals that moving upwards from the P3HT-rich underlayer interface, there is first a dense region of small ($\sim$3.5-nm diameter) Au NPs located at and just above the interface, followed by a PCBM-rich region that contains very little Au, followed by a PCBM-rich layer that contains larger-sized ($\sim$10-20 nm diameter) Au particles. Figure 6.3C shows higher magnification of the

small Au NP layer just above the P3HT-rich interface, making clear that the spontaneously-formed Au NPs are highly crystalline (see also the selected-area electron diffraction pattern in Fig. E.4 of Appendix E). These particles are nominally spherical and fairly monodisperse in size with diameters in the range of 3.5 ± 0.5 nm. We believe that the P3HT-rich underlayer has much to do with both the metal NP formation and distribution. There likely is a small amount of P3HT in the PCBM-rich overlayer (since SqP does mix the polymer and fullerene components as indicated by the XPS data of Figure 6.2).[255,256] Given that P3HT interacts strongly with the penetrated metal, it is entirely possible that the few P3HT chains dissolved in the PCBM-rich overlayer act as nucleation sites for the penetrated Au to grow into NPs, leading to the observed nanostructure.

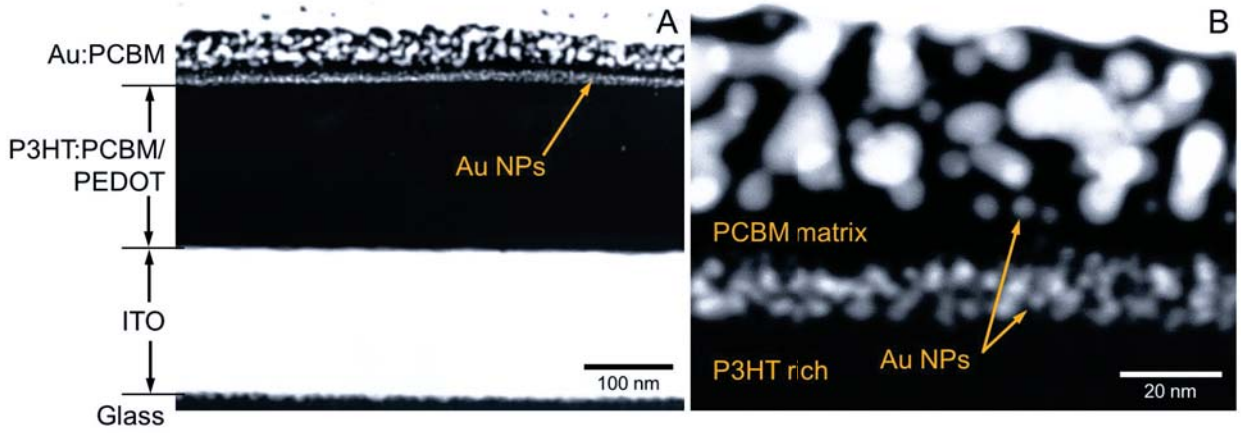

Figure 6.4: HAADF STEM images of the same device cross-section studied in Fig. 6.3. A) Lower magnification view, showing each distinct layer of the device as-labeled. B) Higher magnification view of the P3HT:PCBM/PCBM:Au/Au interface. The high contrast between the Au nanoparticles and the surrounding PCBM matrix indicates extensive phase separation of the metal and the organic materials.

6.2.0.3 HAADF X-TEM Analysis

To better visualize the compositional nanostructure studied in Fig. 6.3, we employed STEM HAADF imaging of these same device cross-sections. HAADF STEM is not influenced by diffraction effects and primarily reveals variations in atomic mass density (Z-contrast), making it ideal for examining the distribution of metallic Au in organic matrices. As expected, the HAADF images in Fig. 6.4 show sharp contrast between the carbon-rich and gold-rich regions of the Au:PCBM layer. Figure 6.4A shows the entire glass/ITO/PEDOT/P3HT:PCBM/PCBM:Au/Au layer stack,

confirming that the layered structure of each region persists throughout the in-plane direction. Notably, there are several Au NPs visible as small grey dots in the P3HT-rich layer, although it is not clear whether these particles diffused into the layer via interpenetration from above or were simply displaced during the FIB processing and are located on top of the cross-section. Figure 6.4A also better reveals the non-uniform Au:PCBM nanostructure seen in Fig. 6.3A, which consists of a dense region of small, ∼3.5-nm diameter gold NPs at the P3HT-rich interface, followed by a region devoid of Au, and then a thicker Au:PCBM matrix composed of large, semi-interconnected Au NPs (∼10-20 nm diameter). In Figure 6.4B, higher magnification HAADF imaging shows high contrast (i.e., a complete lack of gray-scale) between the particles and surrounding matrix, indicating essentially complete phase separation of Au in the PCBM-rich layer. The formation of discrete Au nanoparticles suggests that a significant contributor to the reduction of C_{g} – as discussed above – is the large increase in effective dielectric constant of the mixed metal:fullerene layer, which causes this layer to have no effective contribution to the overall device capacitance (Eq. (6.1) with $\varepsilon_{\mathrm{PCBM:Au}} \rightarrow \infty$).

Overall, Figs. 6.3 and 6.4 completely change our perception of what can happen when evaporated electrode metals are deposited onto layers rich in fullerene derivatives. The fact that electrode metals penetrate many tens of nm into fullerene-rich layers is not only unexpected, but also will clearly have a significant impact on device optoelectronic properties. For example, the fact that the effective active-layer thickness is reduced can impact device physics experiments that require accurate knowledge of the thickness (e.g., space-charge limited current, time-of-flight measurements, charge extraction, etc.),[138,167,197,335,337,358,376,377] and the excessive metal penetration will probably cause increased leakage current,,[226,354] exciton quenching,[355] produce alterations of the active-region energy band structure,[378,379] and likely also strongly affect device stability.[173,347,380–382]

6.2.0.4 Plasmonic Effects of Interpenetrated Nanoparticles

One particularly important impact, however, comes from the fact that interpenetrated metal need not be uniformly present in the fullerene layer, but instead can be phase-separated into NPs that are of exactly the size required for significant plasmonic effects (Figs. 6.3 and 6.4).[383–387] We show that

plasmonic effects can be readily measured in metal-interpenetrated fullerene films in Fig. 6.5. In this figure, we plot the normal-incidence absorbance of a glass/PCBM (55 nm) sample both before (black curve, squares) and after (red curve, circles) the evaporation of 3 nm of gold. The blue curve in the inset shows absorption difference expected if the 3-nm Au overlayer were planar, as calculated via a transfer-matrix approach using published optical constants.[55,66] Instead, the actual change in optical density upon Au evaporation is shown by the orange curve in the inset, which has a distinct peak at ∼620 nm. This peak is in the range one would expect for the collective plasmon resonance of inhomogeneously-distributed, interacting, Au nanoparticles.[388,389] Since the NPs formed in

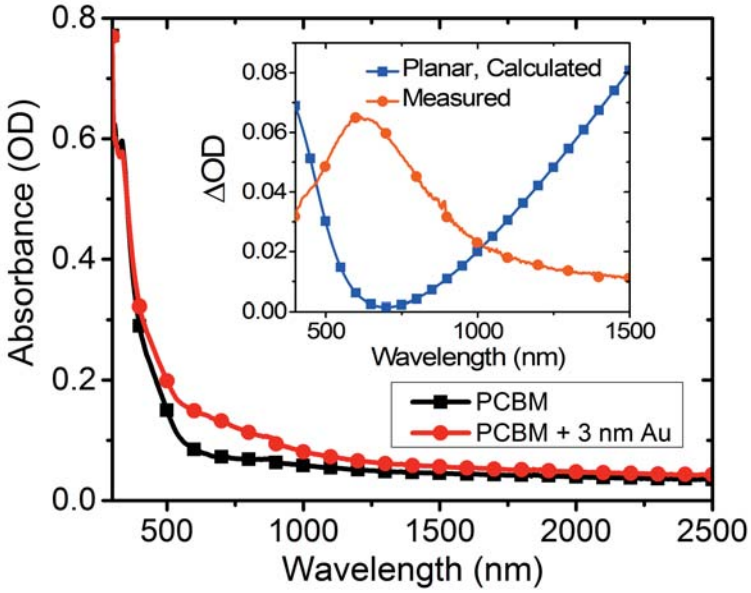

Figure 6.5: Normal-incidence optical density of a 55-nm PCBM layer on glass before (black curve, squares) and after (red curve, circles) thermal evaporation of 3 nm of Au. The red circles/curve in the inset shows the measured change in OD upon metal evaporation, while the blue squares/curve show the expected ΔOD (calculated using a transfer matrix approach with published optical constants)[55,66] if the Au formed a 3 nm overlayer on top of the PCBM film. The fact that the observed ΔOD peaks near 600 nm is consistent with the plasmon resonance of Au NPs that have formed within the fullerene layer.

fullerene films are obviously bare (i.e., they have no capping agents), there should be significant near-field coupling to the organic material around the NPs. This means that the presence of metal NPs must be accounted for when performing optical modeling of any devices with evaporated metal electrodes on fullerene-rich layers. Moreover, it is possible that with appropriate design this effect could be utilized to enhance, for example, the absorption of fullerenes such as $PC_{71}BM$ that are placed intentionally at the top surface of OPVs.[384,390]

6.3 Conclusions

In summary, we have shown that evaporated metal electrodes significantly penetrate into films of fullerene derivatives, having substantial implications for optoelectronic devices that involve metal/fullerene interfaces (e.g., OPVs, perovskite solar cells, thin-film transistor contacts, etc.). The most direct consequence is that the effective electrical thickness of fullerene-based devices, as measured by their geometric capacitance, is dramatically reduced due to the metal incorporation. For example, we showed using a model doped-Si/SiO_2/PCBM/Au device structure that there is $\sim$70 nm of effective Au penetration into a pure PCBM film. We also confirmed via C_g analysis that evaporated metal penetration into fullerene-rich films occurs with numerous fullerene derivative and evaporated metal combinations, so this is a general phenomenon that is not specific to materials such as Au and PCBM. Our X-TEM analysis shows that a striking and unexpected interpenetrated nanostructure is formed when an electrode metal is evaporated onto a fullerene-rich layer that is cast on top of polymer-rich underlayer. Instead of yielding a clean fullerene/metal interface, metal evaporation results in extensive penetration and metal nanoparticle formation throughout the fullerene-rich layer. Furthermore, the images and C_g analysis indicate that metal penetration is efficiently stopped by the presence of even small amounts of conjugated polymers such as P3HT or insulating materials such as MoO_3. In addition to all the implications for optoelectronic device physics experiments, this discovery opens up a number of possibilities in terms of interface and optical engineering with fullerene semiconductor materials.

6.4 Experimental Section

Fabrication of Diodes with Fullerene and Polymer/Fulllerene Active Layers: We used P3HT (Rieke Metals, Inc. Sepiolid P100, and PCBM (Nano-C®, 99.5% purity, used as received) materials for all devices. We found that the quality of the P3HT batch was important, since low molecular weight or regiorandom material tends to segregate to the top of sequentially-processed PCBM overlayers during casting of the fullerene, blocking metal penetration. We strongly recommend using highly regioregular P3HT that has also been double extracted by DCM,[251] lest the materials

intermix too much during PCBM casting resulting in P3HT blocking of the metal penetration.

All devices with polymer in the active layer were fabricated by first sequentially sonicating ITO-coated (150 nm, 20-25 $\Omega/\square$) glass substrates in acetone and isopropyl alcohol, respectively. We then dried the substrates and further cleaned them in a UV-ozone reactor for $\sim$20 min, which was immediately followed by the spin-coating of a $\sim$35 nm thick PEDOT:PSS (Clevios P VP AI 4083) layer onto the ITO-coated glass. The PEDOT-coated substrates were then thermally annealed at 150 °C for 15 min in order to drive off residual water. After PEDOT deposition and baking, we spin-coated the P3HT layer from an ODCB solution, always keeping the polymer concentration at 20 mg/ml. For sequentially-processed devices, we first spun the P3HT solution at 1000 RPM for 60 s, which resulted in fully dried P3HT films that were $\sim$115-130 nm thick. These P3HT films were then placed in an evacuated antechamber for at least one hour to remove any residual ODCB solvent. If placed under vacuum for an insufficient time, the ODCB remaining in the P3HT underlayer promoted intermixing of the P3HT with the PCBM overlayer, which substantially hindered metal penetration.

After the vacuum drying process, we deposited the PCBM layer from a DCM solution at 10 mg/ml concentration at 4000 RPM for 10 s. Different PCBM overlayer thicknesses were obtained by adjusting the PCBM concentration in DCM. For devices with pure PCBM as the active layer, the Si-based substrates described above were prepared in an identical manner to the ITO substrates and the PCBM layer was spun from a 10 mg/ml PCBM solution at 1000 RPM for 20 s. Finally, we deposited metal electrodes with an Ångstrom Engineering, Inc. evaporator at a pressure of $\leq 1\times10^{-6}$ torr. All initial metal layers were typically deposited at a rate of 0.1-0.5 Å/s to a thickness of 10 nm, and the subsequent layer was deposited at a rate of 1.5 Å/s to thicknesses of $\geq$ 40 nm. Before exposing the devices, $\sim$5-10 nm of material was typically evaporated onto the shutter to ensure layer purity. Film thicknesses were measured with a profilometer (Dektak).

For the devices with a structure of ITO/ZnO/Organic Semiconductor/MoO_3/Ag, the ZnO nanoparticle solution was synthesized following the method by Beek *et al.*[391] and then spun onto cleaned ITO substrates from chloroform to form a 40 nm ZnO layer, as confirmed by profilometry. These ZnO-coated substrates were then annealed at 150 °C in a nitrogen glovebox for 20 min. After the organic layer fabrication, a 15 nm MoO_3 layer was deposited on top of the organic layer at rates

below 0.5 Å/s, followed by a 70 nm Ag layer deposited at rates below 1.0 Å/s.

CELIV Experiment for Determination of C_g: For a description of the analytical CELIV analysis approach, we refer the reader to Appendix E and Ref. 201. Experimentally, we measured CELIV traces with a DS345 function generator paired with a Tektronix DPO 3014 150 MHz digital Oscilloscope.[201]

FIB Processing, Cross-Sectional TEM, and Sample Preparation: The as-cast P3HT/PCBM quasi-bilayer device made by SqP was imaged in a FEI Titan S/TEM operated at 300 kV. As described above, we were careful to limit any potential electron beam damage.[369–371] Our cross-sectional TEM samples were prepared using typical lift-out methods in an FEI Nova 600 Nanolab DualBeam Ga FIB system. Prior to milling, the surface was protected with a $\sim$2-μm thick layer of Pt deposited first by electron beam, then by ion beam. Side-by-side trenches were cut into the bulk substrate to create a $\sim$20 μm $\times$ 2 μm thin section, which was then partially milled from the substrate by a U-cut. Next, the detached end of the sample was attached to a nanomanipulator needle, the opposite end was milled completely out of the substrate, and the sample was glued with ion-beam-deposited Pt to a commercial Cu lift-out grid. The needle tip and excess Pt were cut out, and the sample was further thinned to electron transparency. The final thinning process was executed at the low-power conditions of 10-kV beam energy, 40 nm beam diameter, and 0.12-nA probe current.[288] The final step involved making a 2° wedge-shaped sample with thinner top and thicker bottom for structural integrity.

XPS for Determination of Surface Composition: Surface volume percent calculation details can be found in the SI,[275] while the experimental apparatus and approach is described in detail in Ref. 201.

Spectroscopic Ellipsometry for Layer Thickness: The organic layer thicknesses that were determined by spectroscopic ellipsometry were obtained by fitting the transparent region of the material to a thickness/Cauchy-dispersion model. All of these values were obtained from equivalently processed layers deposited on a Si/(1.8 nm SiO_2 native oxide) substrate. The thick SiO_2 thermal oxide values reported in the text and Table 6.1 were determined by fitting the entire $\tan(\Psi), \cos(\Delta)$ spectrum to the well-known optical constants of SiO_2 and Si (SOPRA *nk* library). A detailed

description of the experimental setup and procedures can be found elsewhere.[359]

APPENDIX A

EQE Setup Standard Operating Procedures (SOP)

A.1 Turning the Setup On

1.) Turn on Xe Lamp power supply.

2.) Turn on Xe Lamp.

3.) The power supply should read 300 W going to the lamp.

4.) Make sure that the LabVIEW program is *not* already running on the computer (if possible, close LabVIEW entirely before starting), and turn on the monochromator. The monochromator will make some noises; this is okay.

5.) Turn on the chopper. The frequency should read a stable 20-25 Hz.

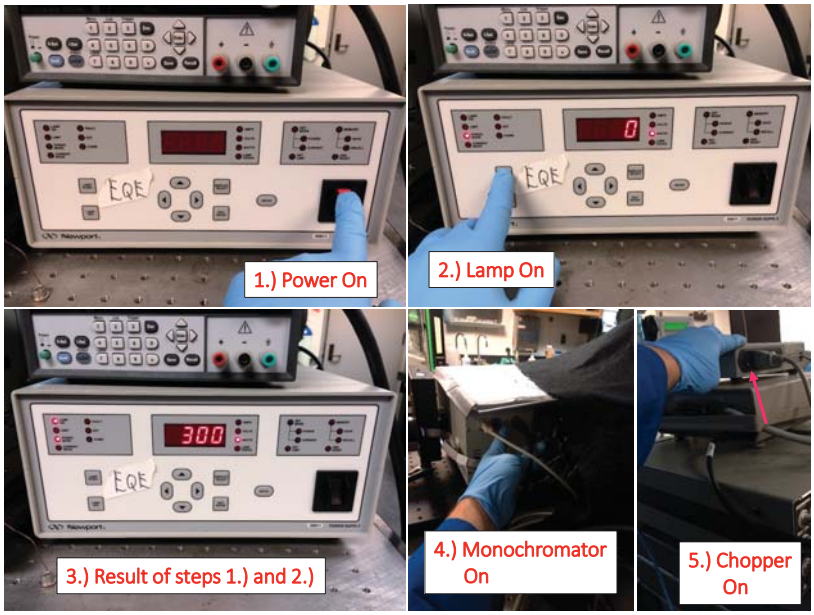

Figure A.1: Turning on the power supply, lamp, monochromator, and chopper.

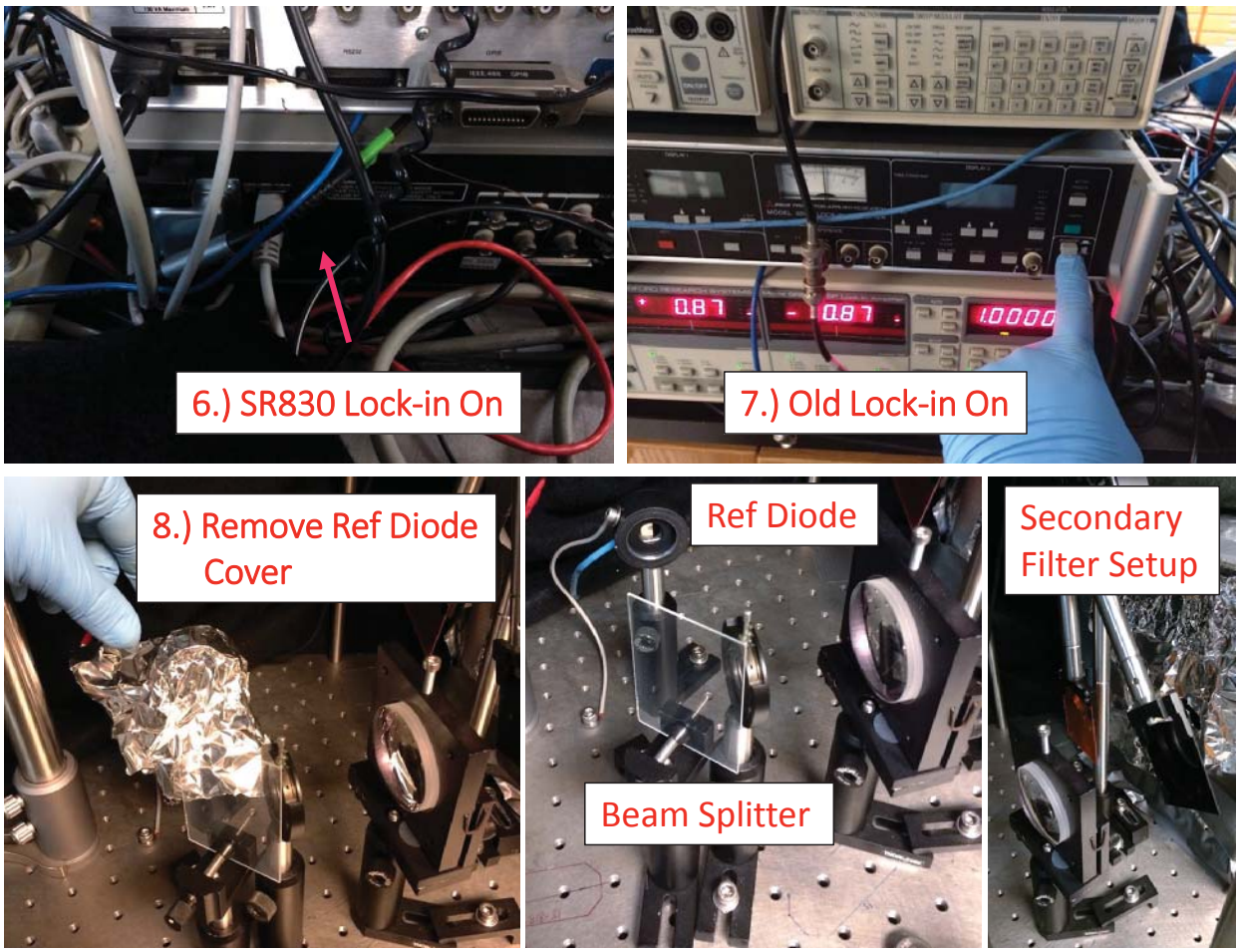

Figure A.2: Turning on the lock-ins, removing the ref diode cover slip.

6.) Turn on SR830 Lock-in.

7.) Turn on the old lock-in for the reference diode.

8.) Remove the reference diode dust-preventing cover slip (aluminum foil). The reference diode setup (old lock-in + beam splitter + ref diode) should never be altered, as it is only there for 'live' relative intensity monitoring. This portion of the apparatus is critical for obtaining an accurate representation of the absolute intensity of the light hitting the device-of-interest at the time of testing.

Note also the secondary filter setup. The beam should pass between the filters for wavelengths below 620 nm, through the orange filter for wavelengths between 620-780 nm, and through the black filter for wavelengths beyond 780 nm. The reason for this filter setup is to further purify the monochromatic light coming out of the monochromator and is especially necessary for sub-energy-gap measurements. The motor/control setup must be reset at the beginning of each EQE run (see below). This is not necessarily a time delay, though, as the lamp needs time to warm up anyway.

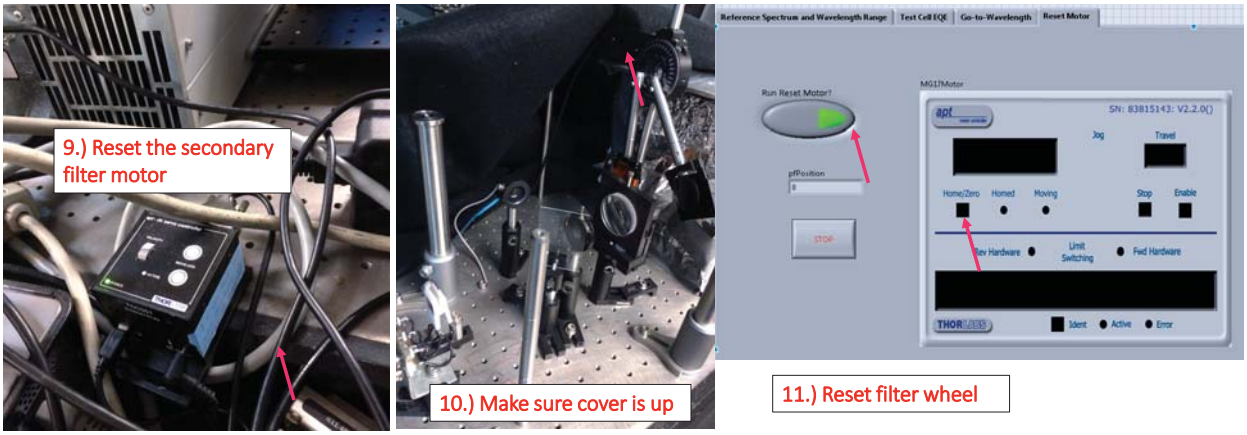

Figure A.3: Resetting the secondary filter wheel setup.

9.) Reset the filter wheel motor power supply by either plugging it in or unplugging and then plugging in again.

10.) Make sure that the black cover cloth is up off the filter setup. Resetting will result in the filter wheel going all the way up (filters pointing more towards the ceiling) and then going back down again to what is shown in the Figure A.3 middle image. The path must be unobstructed during this process..

A.2 Initializing and Getting Ready to Measure

11.) Open the main EQE program "EQE_V2.1" located on the desktop. Go to the reset motor tab (Figure A.3).

(a) Click the "Run Reset Motor?" button so that it turns green. Run the program.

(b) Once the initialization is done, click the "Home/Zero" button. After a few seconds, the filters should go up toward the ceiling and stop. The position should read 0.

(c) Click stop. Unclick the "Run Reset Motor?" button so that it is no longer green.

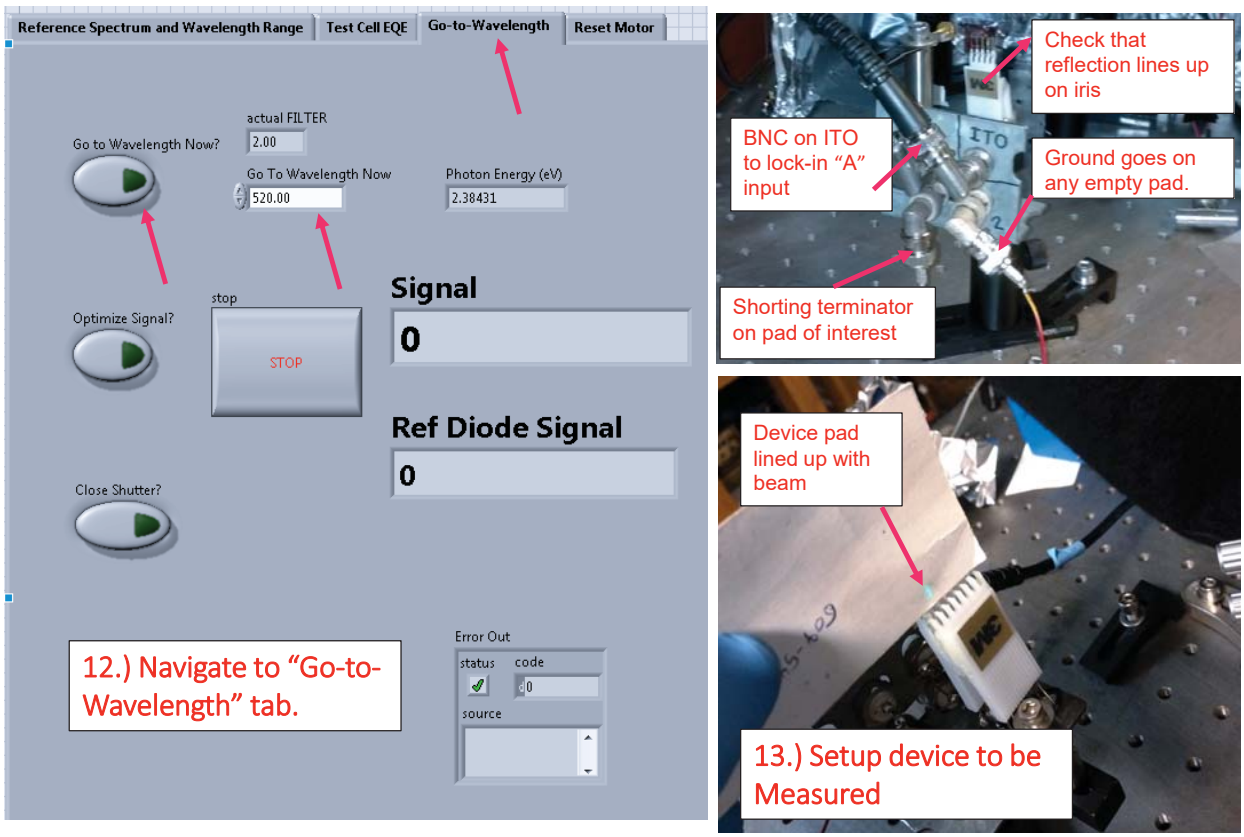

Figure A.4: Setting up the device to be measured.

12.) Navigate to the "Go to Wavelength" tab.

(a) Make sure that the "Go to Wavelength Now" input is at 520 nm. This is a good and bright wavelength for you to align your device with.

(b) Click the "Go to Wavelength Now?" button so that it turns green.

(c) Run the program. After a moment, the filter wheel should go down to be in the position shown in Figure A.3 middle image.

(d) After the program is done running (i.e., the background to the program has a square grid), uncheck the "Go to Wavelength Now" button so that it is no longer green.

13.) Setup and align the device to be measured as shown in the Figure A.4 images. Make sure that:

(a) The beam is well focused/aligned on the device/pad of interest.

(b) The reflection is going nominally straight back up the optical path (normal incidence).

Check the normal incidence by finding the reflection on the iris before the glass slide beam splitter.

(c) You remove dust from the pad with a cotton q-tip.

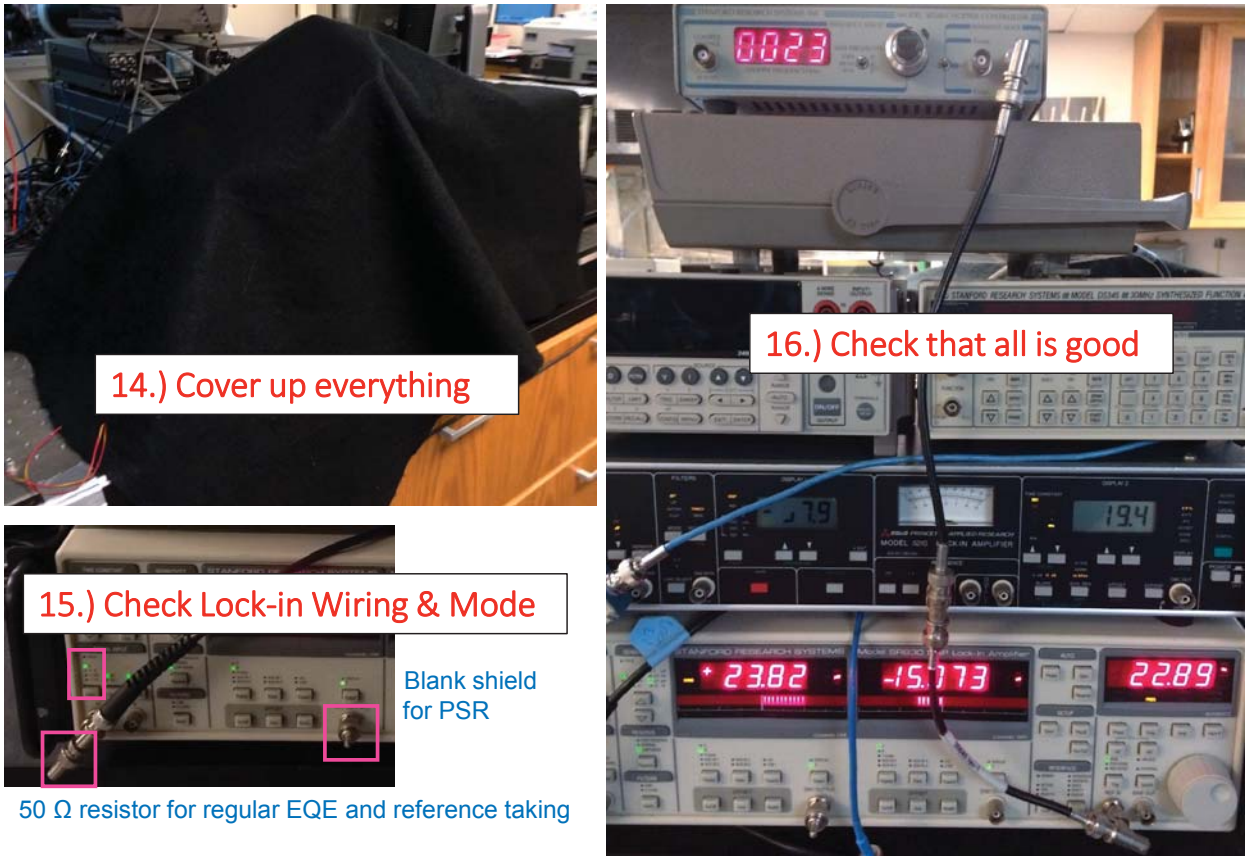

Figure A.5: Make sure that settings/signals are good to go.

14.) Cover up the entire setup for best signal/noise.

15.) Check that the SR830 lock-in is set up properly (it may be in PSR mode from last time). If doing PSR, follow directions on the prompt. If doing regular EQE or redoing a reference spectrum, make sure that:

(a) The 50 Ω resistor is on the t-connector at the "A" input and the black BNC cable is connected.

(b) The time constant is at 300 ms.

(c) The voltage scale is at 100 μV.

(d) The mode is "single ended voltage."

16.) You're almost ready to go. Check that all is well before running the measurement. Namely, the SR830 should have something like a 1-100 μV signal from your device or reference diode;

usually in the ballpark of 50 μV. The old lock-in should have a steady/stable signal. The chopper should read 20-25 Hz and the SR830 measured chopper frequency[1] (lower right number in Figure A.5) should agree.

17.) MAKE SURE TO GIVE THE LAMP A TOTAL OF AT LEAST $\sim$10 MIN TO WARM UP AFTER YOU'VE TURNED IT ON BEFORE RUNNING THE MEASUREMENT.

[1] A note about the chopper: it is located inside the cardboard box with aluminum foil around it. Sometimes if the box gets bumped, the chopper wheel can become impeeded and the frequency reading will become inaccurate/unstable. Also, I found that a low chopper frequency was necessary for the large area reference diodes to give a stable/accurate output.

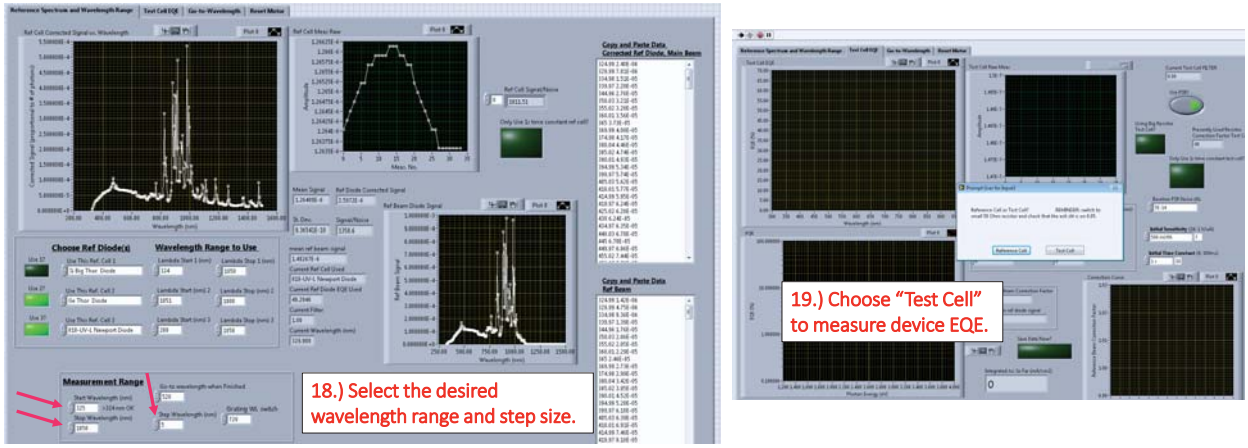

Figure A.6: Measuring an EQE.

A.3 Measuring a Device or Reference Spectrum

A.3.1 Measureing a Device: Regular EQE

18.) Go to the "Reference Spectrum and Wavelength Range" tab and set the wavelength to the desired range and step size.

19.) Go to the "Test Cell EQE" tab and run the program. Select "Test Cell" in the prompt.

20.) Stay and watch the first few EQE data points come in to make sure all is well. In particular, check that:

(a) The EQE values that are being measured are reasonable. I.e., they are not really high or unexpectedly low.

(b) The "Reference Beam Correction Factor" data that is also coming in should be close to 1 (no more that 0.15 away from 1). This correction factor should also look noisy and be larger for ∼325-345 nm light and then settle down to values closer to 1. After 1100 nm, the correction factor automatically goes to 1 because the reference diode looses its sensitivity after that.

(c) If the correction data is consistently greater than ∼8%, then you should probably re-run the reference (see below for how-to).

A.3.2 Measureing a Device: Subgap EQE

21.) This is easy and the same as regular EQE. The program will automatically prompt you when the signal gets too low and you need to "Switch to PSR mode" (PSR = Photocurrent Spectral Response).

22.) Follow the directions on the prompt and click ok. This will run and take awhile since it is a sensitive measurement.

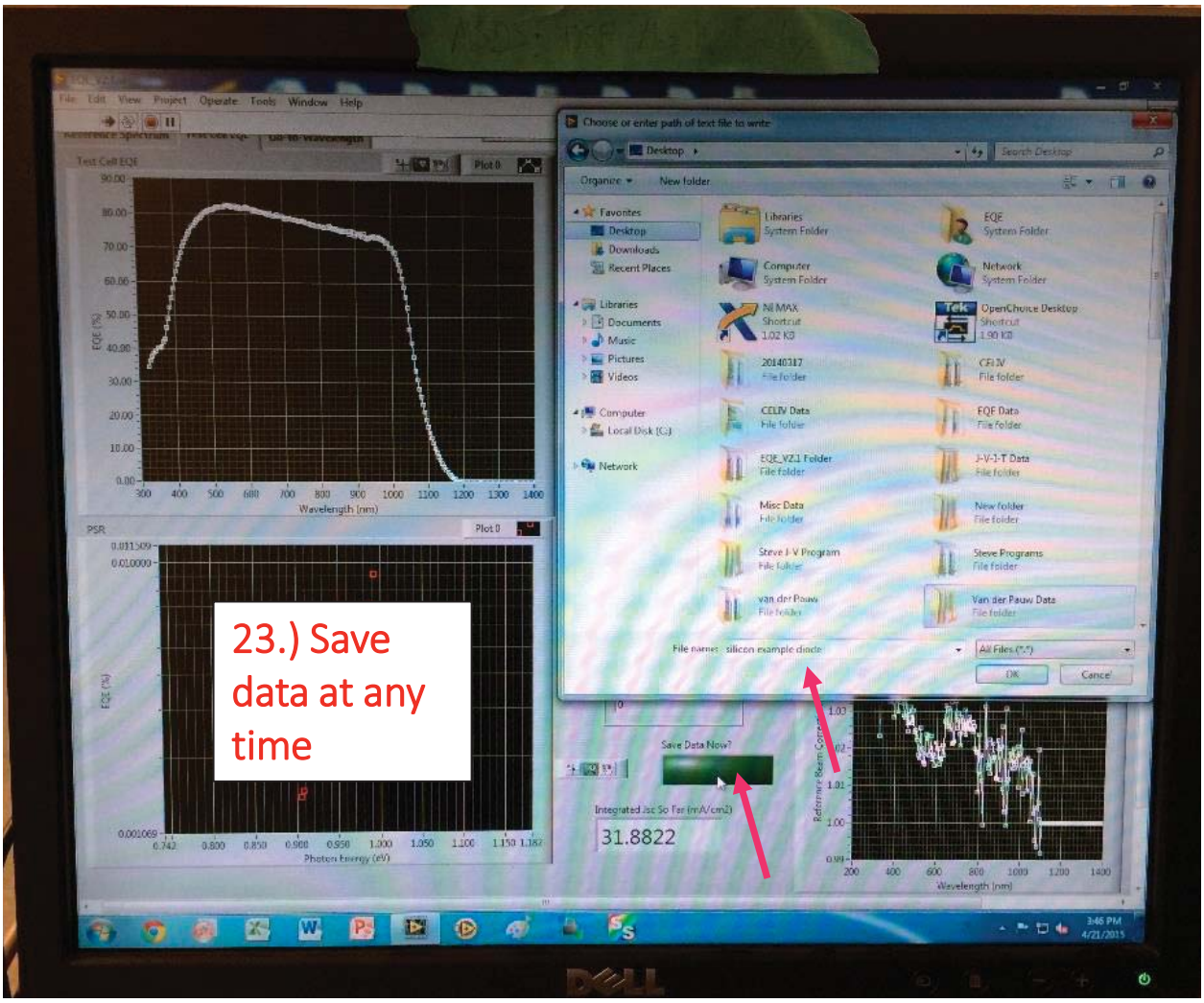

Figure A.7: Saving (subgap) EQE data.

A.3.3 Saving the Data

23.) To save the data at any time, just click the ”Save Data Now?” button.

24.) If the program reaches the final wavelength before you save the data, it will automatically prompt to save.

25.) Note that you can always right click a graph in LabVIEW and export the data to the clipboard or excel.

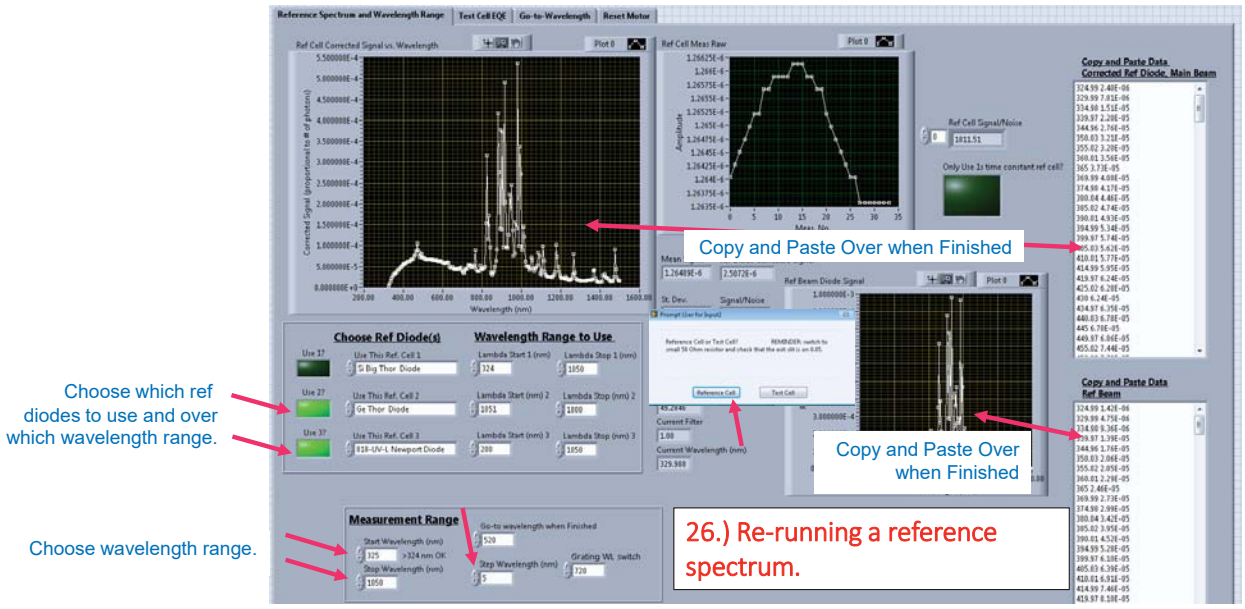

Figure A.8: Redoing a Reference Spectrum.

A.3.4 Measuring a Reference Spectrum

26.) Align the reference diode (found on the optical table or in the drawer under the EQE setup) in the beam similar to what is described for a device above. However, this time:

(a) Make sure the beam is as defocused as possible over the entire ref diode area. The reason for this is to take advantage of the entire area rather than saturate the device in one intense spot.

(b) Make sure that the reference diode BNC cable is plugged in at the SR830 lock-in.

(c) Make sure that there is a reasonable signal ∼30-60 μV at the SR830 lock-in when the wavelength is at 520 nm.

27.) Once aligned, go to the "Reference Spectrum and Wavelength Range" tab and set the wavelength to the desired range and step size. This is usually out to 1050 nm, since beyond this wavelength you have to 1.) switch to the Ge diode (found in drawer), which is annoying, 2.) not usually necessary because the near-IR portion of the spectrum is very stable and consistent, and 3.) this range you do not usually care if the reference spectrum is off by a few %.

In theory, you will never have to redo a reference spectrum. However, after hours of operation, the lamp will degrade and the correction factor will get too large and you will need to redo it. When calibrating from 325-1050 nm, use the Newport 818 diode. If calibrating beyond 1050 nm, you will be prompted to use the little Ge diode. For this you will need to remove the black filter *temporarily* from the secondary filter wheel so that you can align the beam onto the diode. Once aligned, of course, put the black filter back.

28.) Make sure the correct reference diodes and ranges are selected (this should not need changing).

29.) Run the program. Select ”Reference Cell” at the prompt. The program should run and start taking data.

30.) Once the data collection is complete, copy and paste the data from the graphs into their respective data columns as shown in Figure A.8. If your data range is only out to 1050 nm (as recommended), then just replace this portion of the data in the data column. To do this:

(a) Right click the big spectrum graph $\rightarrow$ go to the “Export” option $\rightarrow$ click “Export Data to Clipboard”. Paste this data over the relevant range into the relevant data column (see Figure A.8).

(b) Repeat this process for the little “Ref Beam Signal” plot.

(c) IMPORTANT: Once the new data is in, right click each data column $\rightarrow$ go to “Data Operations” $\rightarrow$ click “Make Current Value Default”. Do this for both data columns in Figure A.8.

(d) Save the program to store the reference spectrum changes.

APPENDIX B

Supporting Information for Chapter 2

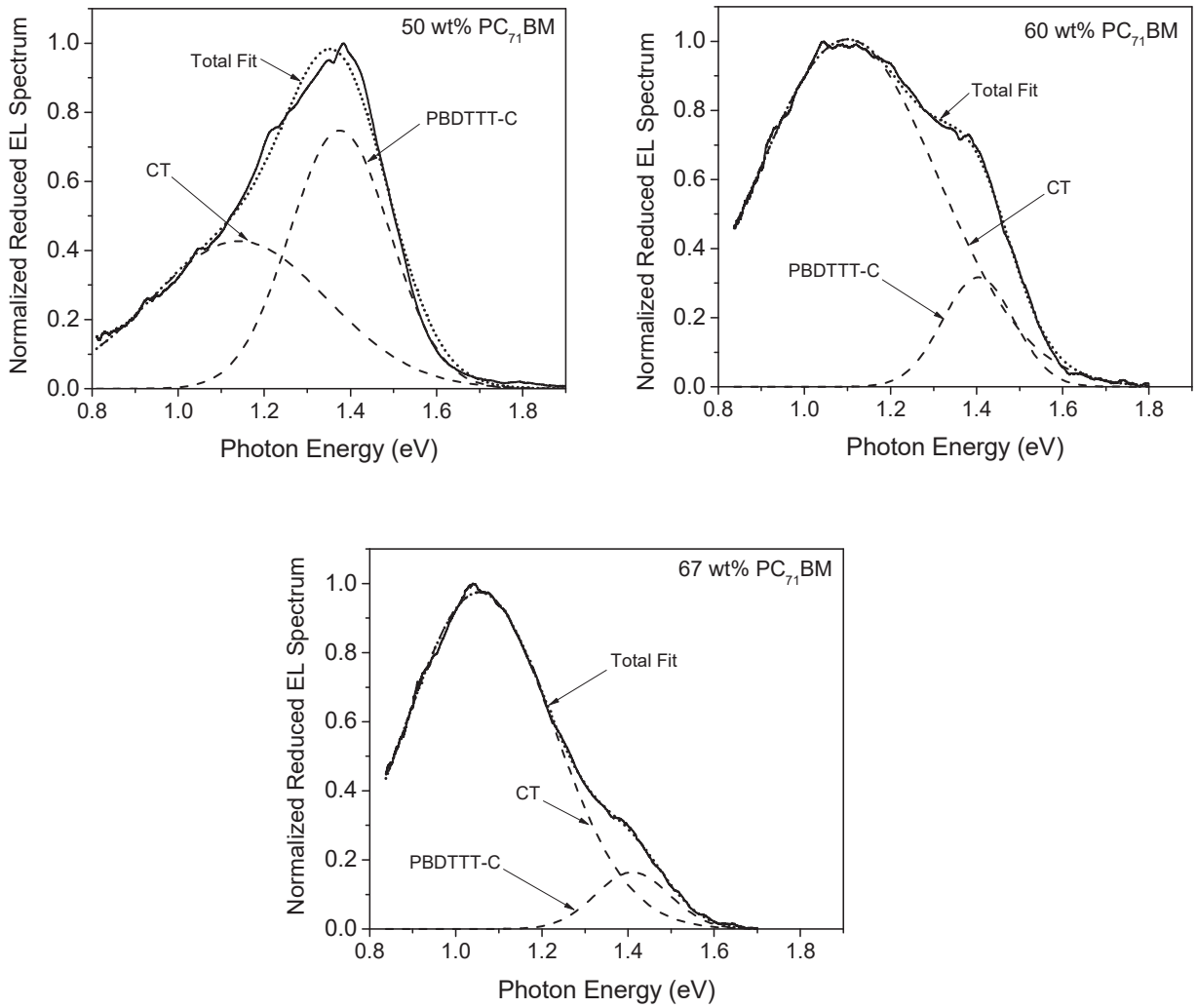

Figure B.1: Example fits of the EL spectra. All plots are for injections conditions of J = 160 mA/cm^2.

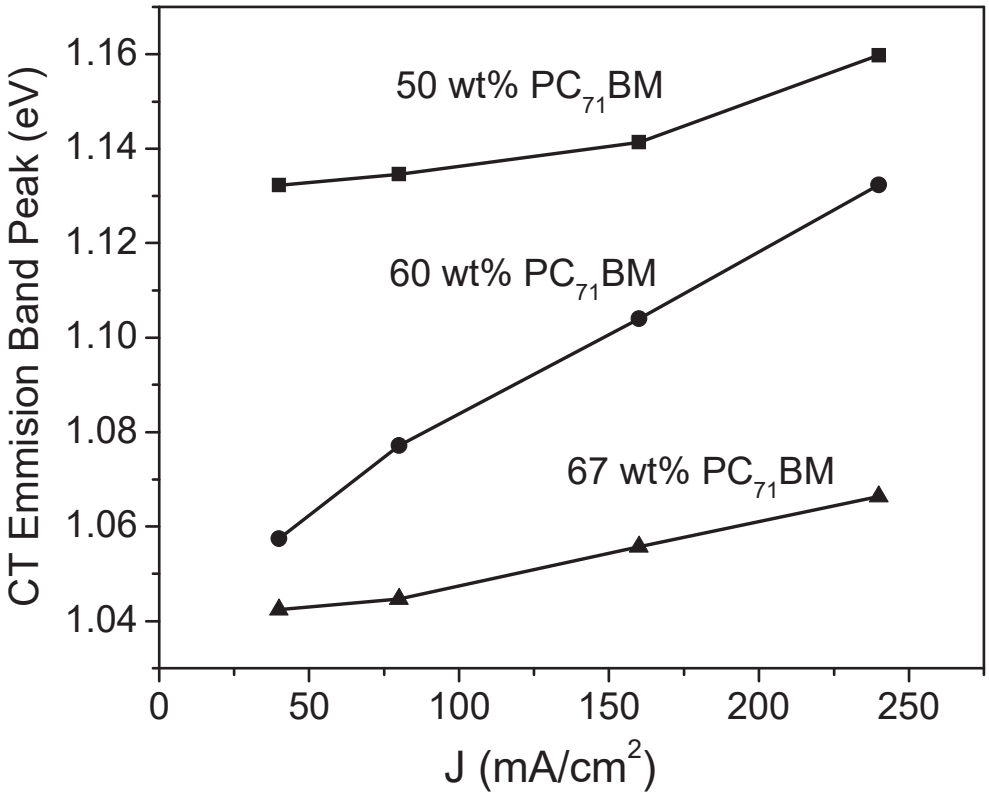

Figure B.2: The dependence of the CT emission band center of mass as a function of injection conditions.

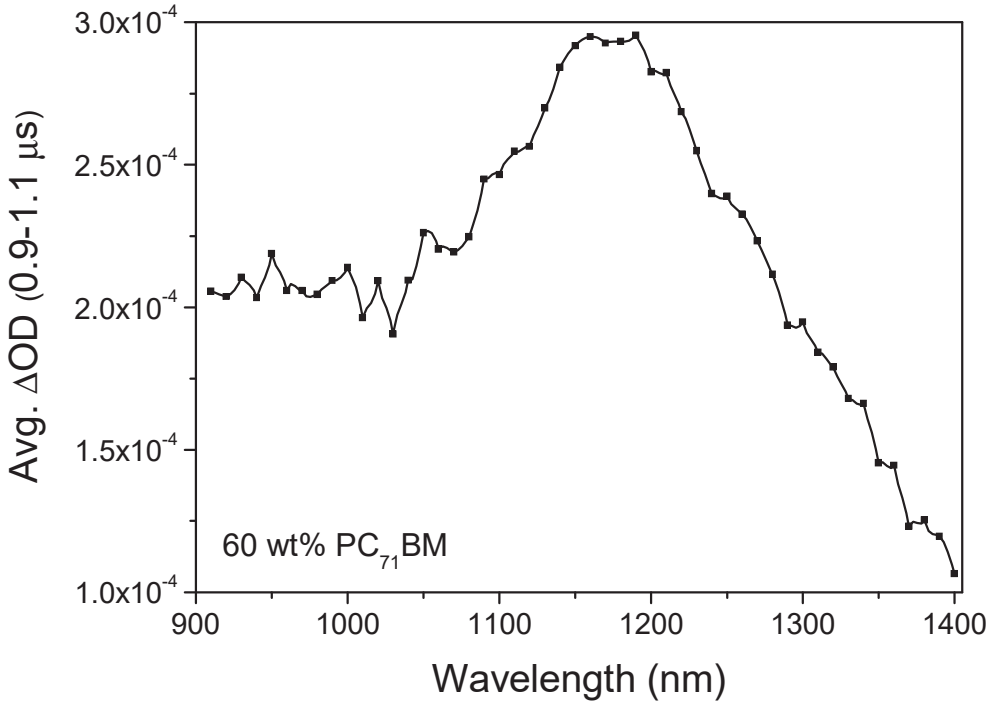

Figure B.3: Transient spectrum for the 60 wt% $PC_{71}BM$ blend around 1 μs showing relatively strong polaron absorption between 1150-1190 nm.

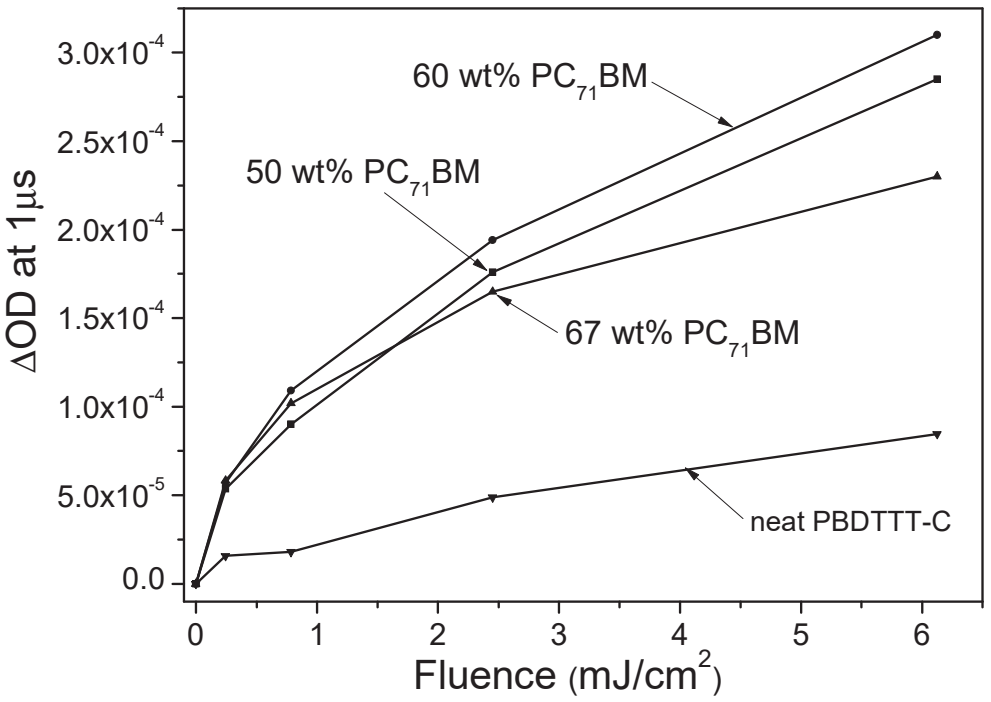

Figure B.4: Dependance of ΔOD signal at 1 μs on pump fluence. The pump wavelength was 650 nm and the probe was held at 1190 nm.

APPENDIX C

Supplemental Material for Chapter 4

C.1 Derivation of the Spatially Constant Total Current

In order to show that the total current is spatially constant, we must demonstrate that the spatial derivative of Eq. (4) in the main text is equal to zero:

$$\frac{dJ_{\text{tot}}}{dx} = \frac{dJ_n}{dx} + \frac{dJ_p}{dx} + \frac{dJ_D}{dx} = 0. \tag{C.1}$$

Fortunately, a straightforward rearrangment of the continuity equations (Eqs. (1) and (2) in the main text) gives two of the terms we need:

$$\frac{dJ_n}{dx} = q\frac{dn}{dt} - q(G-R) - q(G_e^D - R_e^D + G_e^A - R_e^A) \tag{C.2}$$

$$\frac{dJ_p}{dx} = -q\frac{dp}{dt} + q(G-R) + q(G_h^D - R_h^D + G_h^A - R_h^A). \tag{C.3}$$

We can then take the time derivative of Gauss' law and use the non-averaged (local) versions of Eqs. (11) and (12) in the main text to obtain the following expression for the spatial derivative of the displacement current:

$$\frac{dJ_D}{dx} = q\frac{dp}{dt} - q\frac{dn}{dt} + q(G_e^D - R_e^D + G_e^A - R_e^A) - q(G_h^D - R_h^D + G_h^A - R_h^A). \tag{C.4}$$

Clearly, the sum of the right-hand-sides of Eqs. (S2-4) is exactly zero, demonstrating that the total current is spatially constant at each instant in time, as discussed in the main text.

C.2 Relating the Charge on the Contacts to the Voltage

We can solve for the charge on the electrodes and thus σ_{EL} by recognizing that the electric field within the device can be written as:

$$E(x) = \frac{1}{2\varepsilon}\int_0^x \rho(\acute{x})d\acute{x} - \frac{1}{2\varepsilon}\int_x^d \rho(\acute{x})d\acute{x} + \frac{\sigma_{EL}}{2\varepsilon} \tag{C.5}$$

$$= \frac{1}{\varepsilon}\int_0^x \rho(\acute{x})d\acute{x} - \frac{\bar{\rho}d}{2\varepsilon} + \frac{\sigma_{EL}}{2\varepsilon} \tag{C.6}$$

$$\rho(x) = q[p(x) - n(x) + N_D^+(x) - N_A^-(x)], \tag{C.7}$$

where $E(x)$ is the electric field in the active layer, q is the electron charge, $\bar{\rho}d = \int_0^d \rho(x)\,dx$, and $\acute{x}$ is a dummy variable for spatial integration. Integrating Eq. (B2) from $x = 0$ to d gives the total electric potential drop ($V = -\int_0^d E\,dx$) across the active layer:

$$V = \frac{\bar{\rho}d^2}{2\varepsilon} - \frac{\sigma_{EL}d}{2\varepsilon} - \frac{1}{\varepsilon}\int_0^d\int_0^x \rho(\acute{x})d\acute{x}dx. \tag{C.8}$$

Eq. (C.8) provides the relationship between the electric field supplied by the electrode charge, the electric potential, and the space-charge distribution within the active layer. If desired, one can use Eq. (B4) with $\sigma_0 + \sigma_d = -\bar{\rho}d$ and $\sigma_{EL} = \sigma_0 - \sigma_d$ to solve for the charge on each electrode, σ_0 and σ_d, in terms of ρ and V. Solving for σ_{EL} then gives the following useful relations:

$$\sigma_{EL} = \bar{\rho}d - \frac{2\varepsilon V}{d} - \frac{2}{d}\int_0^d\int_0^x \rho(\acute{x})d\acute{x}dx \tag{C.9}$$

$$E_{EL} = \frac{\bar{\rho}d}{2\varepsilon} - \frac{V}{d} - \frac{1}{\varepsilon d}\int_0^d\int_0^x \rho(\acute{x})d\acute{x}dx \tag{C.10}$$

$$V_{EL} = \frac{\bar{\rho}d^2}{2\varepsilon} - V - \frac{1}{\varepsilon}\int_0^d\int_0^x \rho(\acute{x})d\acute{x}dx, \tag{C.11}$$

where V_{EL} is the electric potential drop due to the electrode charge, E_{EL} is the electric field supplied by the electrode charge, and $V = V_{\text{app}} - V_{\text{BI}}$ is the electric potential drop across the active layer. Also, here V_{app} is the applied bias and V_{BI} is the constant built-in potential due to, e.g., permanent asymmetric carrier concentrations at the contacts, compositional gradients, etc. Thus, from Eq. (C.9), $d\sigma_{\text{EL}}/dt$ is non-zero only if the space-charge density distribution $\rho(x)$ and/or the applied bias V_{app} are changing in time. If desired, σ_{EL} can be eliminated by combining Eqs. (C.8) and (C.6) to give the general equation

$$E(x) = \frac{1}{\varepsilon}\left(\int_0^x \rho(\acute{x})d\acute{x} - \frac{1}{d}\int_0^d\int_0^x \rho(\acute{x})d\acute{x}dx\right) - \frac{V}{d}, \tag{C.12}$$

where again V is the electric potential drop across the active layer, which is related by the total applied bias by $V = V_{\text{app}} - V_{\text{BI}}$. If the dielectric environment is inhomogeneous, then $\varepsilon \to \varepsilon(\acute{x})$ and is absorbed into the integrals of Eq. (C.12).

C.3 Drift Diffusion Model

The drift-diffusion model is a continuum approach that can be derived from the Boltzmann transport equation. The model states that the charge carrier current densities, $J_{n,p}$, can be expressed as (also see Eqs. (25) and (26) in the main text):

$$J_n = -qn\mu_n\nabla\psi + \mu_n kT\nabla n \tag{C.13}$$

$$J_p = -qp\mu_p\nabla\psi - \mu_p kT\nabla p \tag{C.14}$$

where n and p refer to electrons and holes, ψ is the electrostatic potential, q is the fundamental charge, $\mu_{n,p}$ are the electron and hole mobilities, k is the Boltzmann constant, and T is the temperature. The current densities have two components: a drift term, which arises from carriers moving in response to an electric field, and a diffusion term, which arises from the presence of carrier density gradients. In order to fully model an electronic device, one must solve the carrier continuity equations (also

Eqs. (1) and (2) in the main text):

$$\frac{\partial n}{\partial t} = \frac{1}{q}\nabla \cdot J_n + G - R \tag{C.15}$$

$$\frac{\partial p}{\partial t} = -\frac{1}{q}\nabla \cdot J_p + G - R \tag{C.16}$$

where G is the carrier generation rate and R is the carrier recombination rate. The continuity equations take account for all loss and gain mechanisms relevant to the device being modeled. Note that these equations, which were used in the numerical solver, do not include trapping and de-trapping terms like the more general continuity equations presented in the text. In any case, though, to relate the carrier densities to the electrostatic potential distribution, one must couple the above equations to the Poisson equation:

$$\nabla^2 \psi = \frac{q}{\varepsilon}(n - p + N_{\text{A}}^- - N_{\text{D}}^+) \tag{C.17}$$

where $\varepsilon = \varepsilon_0 \varepsilon_r$ and ε_0 and ε_r are the vacuum and relative permittivities, respectively, and N_{A}^- and N_{D}^+ are the localized charge densities as defined in the text. The set of equations (C.15)-(C.17) must be solved in order to fully simulated a device.[392]

C.4 Numerical methods and Solution Details

C.4.1 Boundary Conditions

The above Eqs. (C.15)-(C.17) represent a set of 3 second order partial differential equations with three independent variables (n, p and ψ). Thus we require six boundary conditions, two for each independent variable. For the charge carrier densities, we assume thermionic injection conditions at the electrode contacts, which are treated as Schottky contacts.[233,393] Under these conditions, the carrier densities at the contacts is assumed to be constant and is set to, for example,

$$n(0) = N_{\text{C}} \cdot \exp\left(-\frac{\Phi_{\text{B,anode}}}{kT}\right) \tag{C.18}$$

where $\Phi_{B,anode}$ is the height of the Schottky barrier at the anode contact and N_c is the effective density of states of the conduction band. An analogous expression is implemented at both contacts for both electrons and holes. As for the electrostatic potential, we assume that the total potential change through the device should be equal to the built-in potential of the device, which we set to 0.6 V.

C.4.2 Generation and Recombination

Two of the most important factors in device simulation—and of particular importance for OPV devices—are the generation and recombination terms in eqs (C.15) and (C.16). To ensure physically representative data for an OPV device, one must choose appropriate generation and recombination mechanisms. First, we assume that the spatial generation rate inside the device should follow the absorption profile of the active layer. Unfortunately, because of the arrangement of thin films within a typical OPV device, complex interference patterns arise that result in a complex absorption profile rather than a typical Beer's law type exponential decay. Thus, we use a transfer matrix formalism to calculate a generation ($G(x)$) profile that properly accounts for thin film interference patterns within the active layer.[54] We do not consider exciton dynamics and instead assume that an absorbed photon immediately generates a pair of free electrons and holes with a finite efficiency that is independent of, e.g., electric field. For recombination we assume Langevin-type bimolecular recombination statistics for which $R = qnp(\mu_n + \mu_p)/\varepsilon$. We don't consider any recombination with traps as this extra detail introduces significant complexity, and we are more focused on how the total measured current can be broken down into a several intuitive terms (Eq. (13) in the text) and to test the validity of the formalism.

C.4.3 Solution Scheme

Using our own in-house code, we implement the Gummel method, by which Eqs. (C.15)-(C.17) are decoupled and solved in an iterative manner. Using a finite difference scheme, we discretize the partial differential equations and solve for n, p and ψ on 1-D meshes. The discretization of the semiconductor equations results in a set of algebraic equation for every mesh point. Using

our own homemade MATLAB® code, we solve this set of algebraic equations by utilizing the open source, linear algebra C++ library Eigen. Once we have solved for these three independent variables, we may extract whatever information we wish (current densities, recombination rates, etc.) In particular, we are able to explicitly calculate the terms of Eq. (13) in the main text.

C.4.4 Transient Simulations

In order to model current transients, we must forgo the usual steady-state approximation ($\partial n/\partial t = \partial p/\partial t = 0$). Starting from a converged, steady-state solution for n, p, and ψ, we iterate the continuity equations forward in time. In order to improve numerical stability, we use an implicit method rather than an explicit approach to iterate through time steps.[392] A detailed outline of the exact method we used can be found in Ref. 392.

In order to simulate a typical photo-CELIV experiment, we begin with a steady-state solution for the device, without illumination, near its V_{oc}. We then generate an excess of free carriers by "turning on" the generation profile for a short time (0.1 μs). After some time has passed (5 μs), during which some carriers recombine, we sweep out the remaining carriers by applying a voltage ramp at the contacts. Voltage ramp that is linear with time, in keeping with normal CELIV operation. The continuity equations are iterated forward in time using an implicit method and the carrier densities and potential distribution recorded at every time step. The carrier densities and potential distribution are then used to calculate the current densities (Eqs. C.13 and C.14) and the time-dependent displacement current:

$$J_{D} = \varepsilon \frac{\partial E}{\partial t} = -\varepsilon \frac{\partial}{\partial t} \frac{\partial \psi}{\partial x} \tag{C.19}$$

The total measured current in the device is then just (Eq. (4) in main text):

$$J_{\mathrm{tot}} = J_n + J_p + J_{D} \tag{C.20}$$

This total measured current is then compared to the our new analytic expression for the total current(Eq. (13)). Because the three independent variables (n, p, and ψ) are recorded at all time

steps, it is trivial to calculate every term in Eq. (13) in the main text.

APPENDIX D

Supporting Information for Chapter 5

D.1 Sensitivity of Blend Cast Active Layers to Drying Conditions

Figure D.1 compares solid-film absorption profiles of two annealed BC P3HT:PCBM 1:0.8 active layers with different post-deposition drying times; the absorption spectra are normalized to the PCBM absorption peak at 336 nm. This plot shows that relating a P3HT:PCBM BHJ active layers composition to its solid-film absorbance is not accurate due in part to an irreversible sensitivity to the active-layer drying conditions. Even extensive annealing (20 min at 150 °C) does not make the fast dried (t_{dry} = 1.3 min) P3HT absorbance resemble that of the slow dried (tdry = 10 min). Solid-film absorption is also strongly affected by reflectivity, scattering, and thin-film interference, making it less suitable for determining film composition. All of these potential issues can be largely avoided by using the solution-phase we detail in this work.

Figure D.2 compares the performance of the annealed sequentially-processed (SqP) devices (same data as in the main paper) to BC active-layer devices that were processed in a different manner than presented in the main text. It is well known that slow drying P3HT:PCBM active layers is an alternative route to morphology optimization. Along these lines, Figure D.2 indicates that the SqP approach yields active layers that are functionally similar to slower-dried BC P3HT:PCBM films. Slow drying, however, is difficult to control precisely and results in even worse film quality, which makes it even less amenable to scale-up. We conclude that the SqP approach is ideal for both scale-up and achieving the maximum possible device performance.

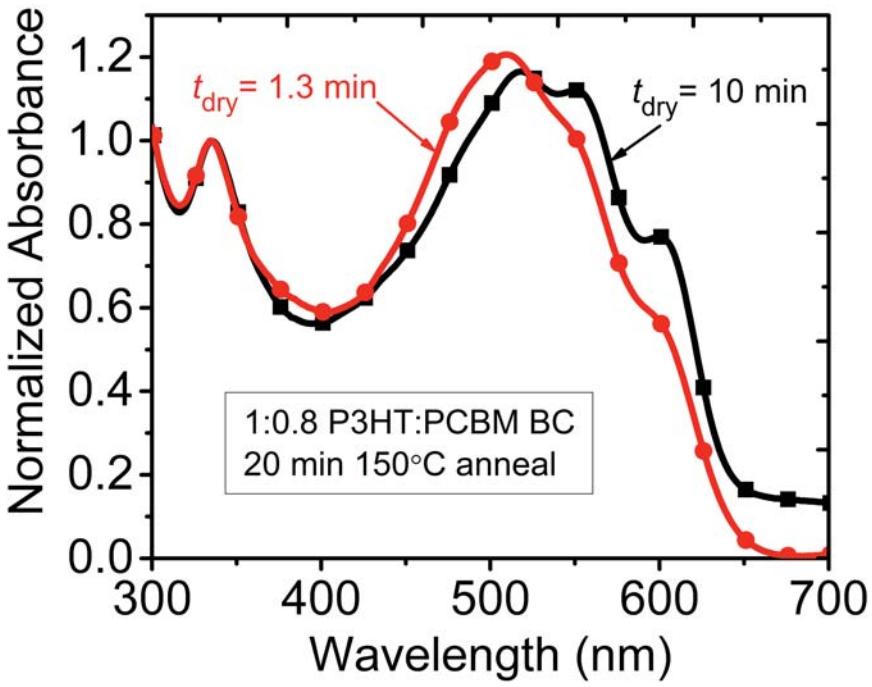

Figure D.1: An absorbance comparison of 1:0.8 P3HT:PCBM BC-processed active layers with different post-deposition drying times; both films subsequently were thermally annealed for 20 min at 150 °C. The data is normalized to the PCBM absorption peak at ∼336 nm. This plot shows that solid-film P3HT absorption, and hence crystallinity, is strongly and irreversibly a function of film drying time in the BHJ structure. Even after strong thermal annealing, the P3HT absorption for t_{dry} = 1.3 min does not reach the state or morphology that is present in the t_{dry} = 10 min case.

D.2 The Properties of As-Cast SqP Films

The following additional discussion and data are for composition- and thickness-matched as-cast P3HT:PCBM active layers. Figure D.3 comparing the solid-film absorption of an as-cast and thermally-annealed SqP, showing that P3HT absorption is unchanged following annealing for 20 min at 150 °C; the apparent absorption from PCBM is reduced upon interdiffusion into the P3HT film. The as-cast P3HT:PCBM SqP is known to have a quasi-bilayer structure with much of the PCBM on top of the P3HT film, but a notable mass fraction does infiltrate into the amorphous regions of the polymer underlayer due to swelling by the DCM solvent.

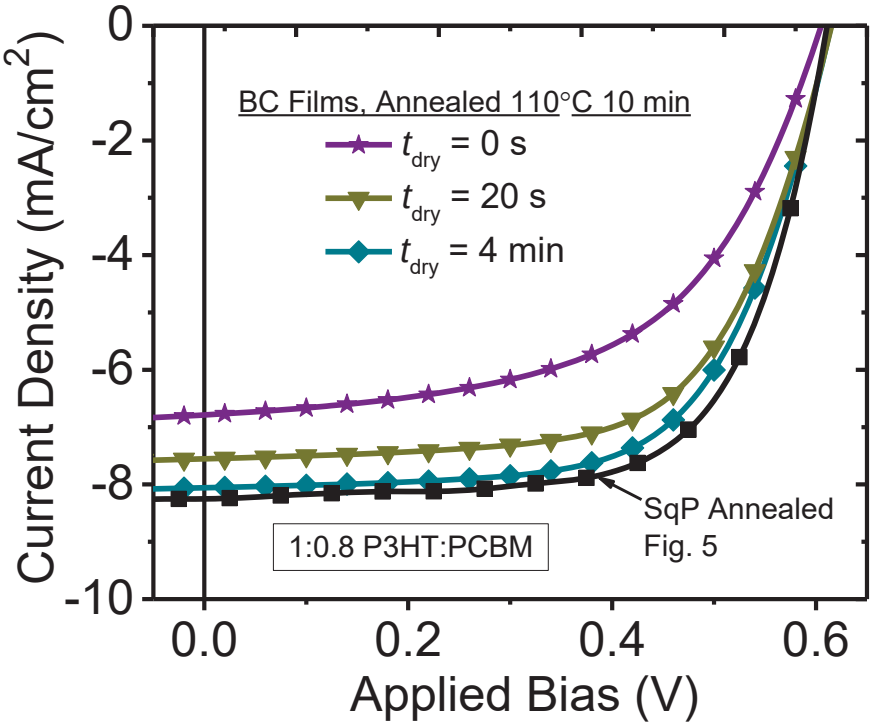

Figure D.2: An absorbance comparison of 1:0.8 P3HT:PCBM BC-processed active layers with different post-deposition drying times; both films subsequently were thermally annealed for 20 min at 150 °C. The data is normalized to the PCBM absorption peak at ∼336 nm. This plot shows that solid-film P3HT absorption, and hence crystallinity, is strongly and irreversibly a function of film drying time in the BHJ structure. Even after strong thermal annealing, the P3HT absorption for t_{dry} = 1.3 min does not reach the state or morphology that is present in the t_{dry} = 10 min case.

The reasons for the poor performance of the bilayer structure in Figure 5.7a and Figure 5.1 are multifold. First, the as-cast SqP devices have a significantly lower (J_{sc}) and and open-circuit voltage (V_{oc}) due to a lack of interfacial area for exciton splitting and charge photogeneration. Second, the amount of PCBM that does initially penetrate into the P3HT underlayer is not sufficient to create well-conducting pathways out toward the PCBM-rich overlayer. Thus, it is more difficult to extract photogenerated electrons out of the P3HT-rich underlayer in as-cast SqP devices, which results in a lower fill factor.

In addition to generally poorer performance, as-cast SqP solar cells also have significantly different ideality factors from annealed SqP and BC devices. The significantly larger dark ideality factor for as-cast SqP devices suggests that recombination takes place through more disordered interfacial states. The light ideality factor is more difficult

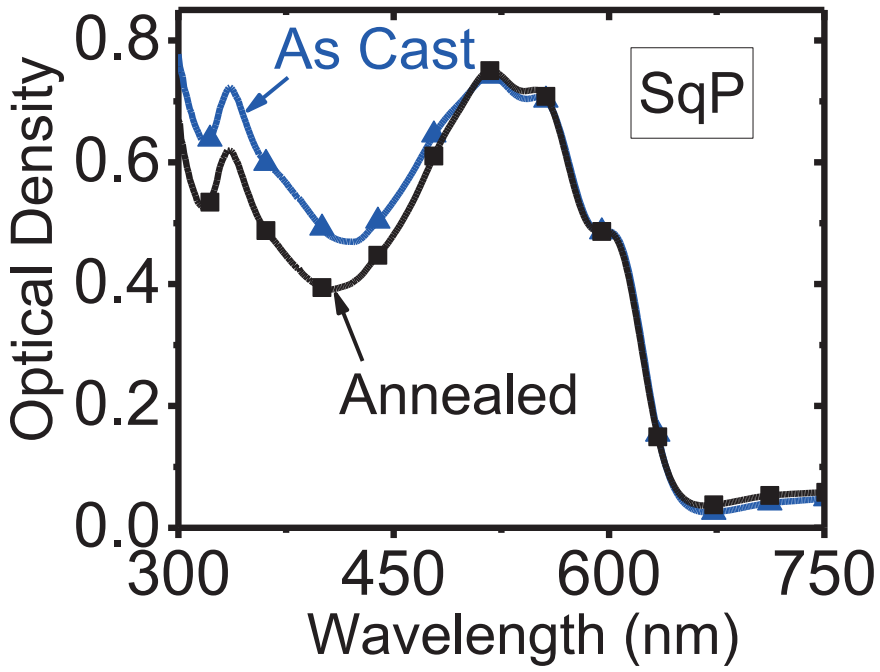

Figure D.3: Solid-film absorbance of as-cast and annealed SqP films at 150 °C for 20 min. The curves are representative of measurements taken over several as-cast and annealed films.

to determine, however, because the minimum differential nid from V_{oc} vs. I for the as-cast SqP film shown in Figure 5.6 would clearly continue decreasing with decreasing light intensity if it were not for an artificial increase due to the shunt resistance. A peculiar aspect of Figure 5.7 is that the ideality factor for as-cast SqP devices increases with light intensity whereas the other cells show a decrease, as is typically found in polymer:fullerene BHJs. It is difficult to assign a particular reason for this behavior, but it is clear that the device physics are entirely different in the as-cast more bilayer like SqPs.

As discussed in the main paper, the preference for PCBM to reside on the top surface of SqP active layers leads to an increased doping density in SqP devices relative to matched BC devices (Figure 5.2). Interestingly, the added conductivity caused by doping does not correlate with the effective series resistance, as also summarized in Figure 5.2 of the main text. Despite having a significant number of dark carriers, as-cast SqP devices have an effective series resistance that is over an order of magnitude higher than annealed SqP and BC cells, which are identical in spite of annealed SqP devices having slightly more doping. We suspect that the high Rseries in as-cast SqP cells is due to a lack of recombination sites that allow injected forward recombination current to

flow.

D.3 SqP Performance vs. Composition

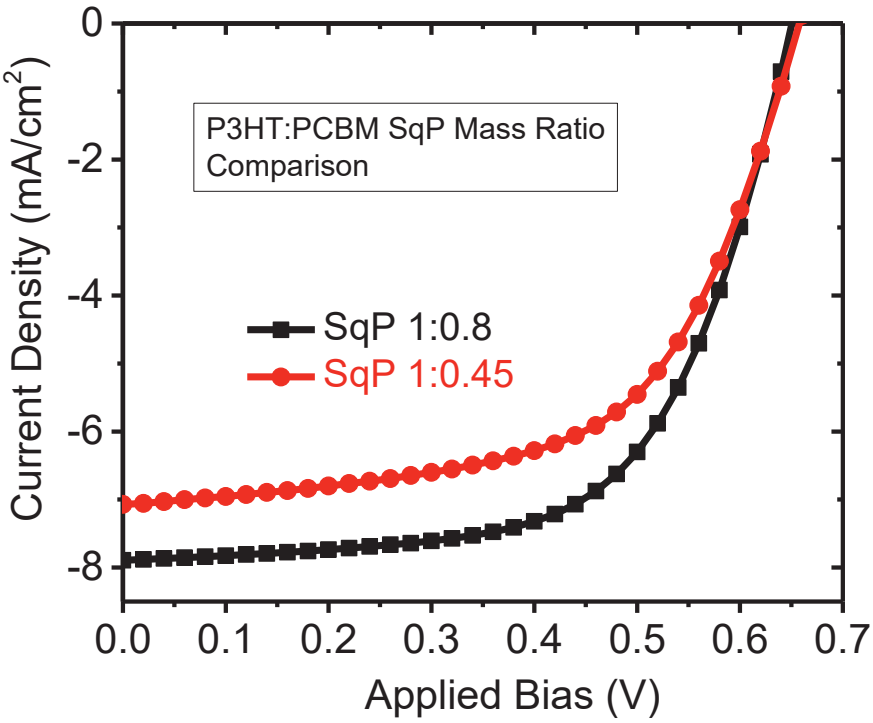

Figure D.4: Comparing SqP devices with different compositions showing that sufficient PCBM content is necessary for the SqP device performance.

Figure D.4 shows that SqP devices need an amount of PCBM that is similar to the optimal amount for BC conditions in order to operate efficiently. Insufficient PCBM gives poorer performance, in similar fashion to BC devices. In estimating the composition of devices in the literature and in looking at our own compositional dependence of device performance, we conclude that P3HT:PCBM SqP devices require similar amounts of PCBM as their BC counterparts.

D.4 CELIV Results

Figure D.5 shows the CELIV transients taken on the active-layers of interest from 0 V to -1.5 V applied bias in the dark. A flat line corresponds to ideal capacitor behavior whereas extraction peaks indicate the presence of an appreciable number of mobile carriers. Clearly, the BC films

behave most like an ideal capacitor devoid of free charges, while the SqP films show measurable amounts of mobile carriers due to doping. We postulate that the large amount of doping in the

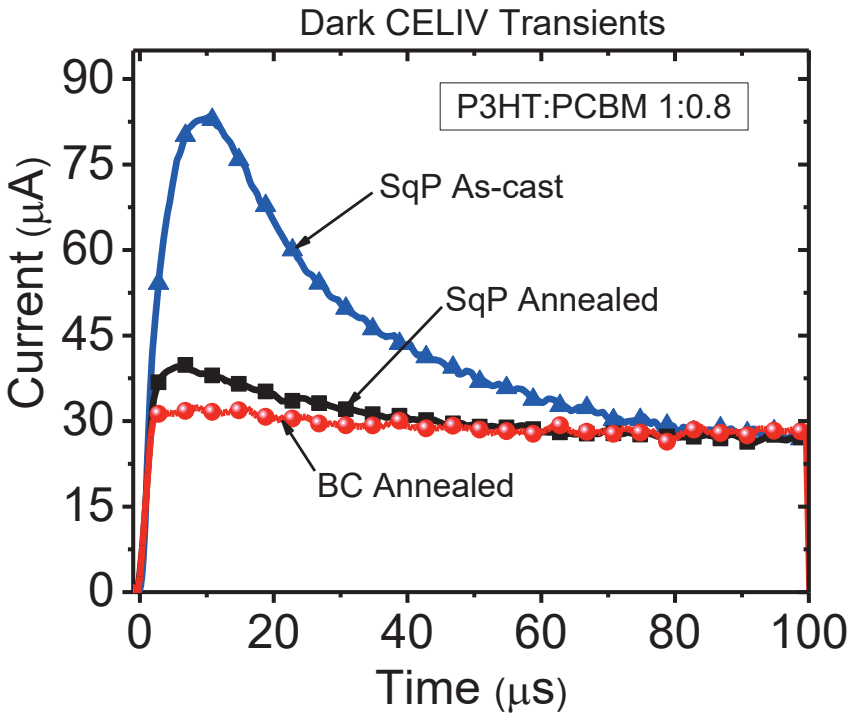

Figure D.5: Dark CELIV transients taken for each active-layer processing condition. A flat line corresponds to ideal capacitor behavior whereas peaks indicate the presence of an appreciable amount of doping. The as-cast SqP film clearly shows significant doping, while the annealed devices show significantly less. When corrected for the voltage ramp rate, all curves saturate at the same displacement current, indicating identical capacitances and therefore also thicknesses.

as-cast SqP film ($\sim 7 \times 10^{15}$ cm^{-3} when averaged over the entire active layer) is caused by the interaction between the calcium cathode and the excess PCBM on the top surface of the film. The solutions from which each active layer was made were exposed to identical conditions during processing and composed of materials from the same batches.

D.5 Experimental Details

D.5.1 Device Fabrication and J-V Characterization

We used the same P3HT (Rieke Metals, Inc. Sepiolid P200*, used as received) and PCBM (Nano-C, used as received) materials/batches for all BC and SqP devices. All devices were fabricated by first sequentially sonicating ITO (145 nm) coated glass substrates in acetone and isopropyl alcohol, respectively. We then dried the substrates and further cleaned them in a UV-ozone reactor for $\sim$20 min, which was immediately followed by the spin-coating of a $\sim$35 nm thick PEDOT:PSS (Clevios P VP AI 4083) layer onto the ITO-coated glass. The PEDOT-coated substrates were then thermally annealed at 120 °C for 15 min in order to drive off residual water. After PEDOT deposition and baking, we spin-coated the BHJ P3HT:PCBM active layers from an ODCB solution, always keeping the polymer concentration at 20 mg/ml. For composition and thickness matching, the BHJ spin-coating conditions were tuned to give a thickness nominally identical to the optimal SqP active-layer thickness ($\sim$165 nm, 121 rad/s (1160 RPM)), though the spin-coating time was kept constant at 40 s to minimize slow drying effects ($t_{\text{dry}} \approx$ 1 min - 2 min). For optimal SqP devices, we first spun the P3HT solution (20 mg/ml in ODCB) at 105 rad/s (1000 RPM) for 60 s, which resulted in a fully dried P3HT film that was $\sim$130 nm thick. These P3HT films were then placed in an evacuated antechamber for 20 min to remove any residual ODCB solvent. After this vacuum drying process, we deposited the PCBM layer from a DCM solution of the desired concentration at 419 rad/s (4,000 RPM) for 10 s unless otherwise stated. The subsequent structure was then thermally annealed for 20 min at 150 °C, resulting in a final film thickness of $\sim$165 nm. For consistency and comparison purposes, all BHJ structures were identically annealed at 150 °C for 20 min. Finally, we deposited Ca/Al electrodes

*Certain commercial equipment, instruments, or materials are identified in this paper in order to specify the experimental procedure adequately. Such identification is not intended to imply recommendation or endorsement by the National Institute of Standards and Technology, nor is it intended to imply that the materials or equipment identified are necessarily the best available for the purpose.

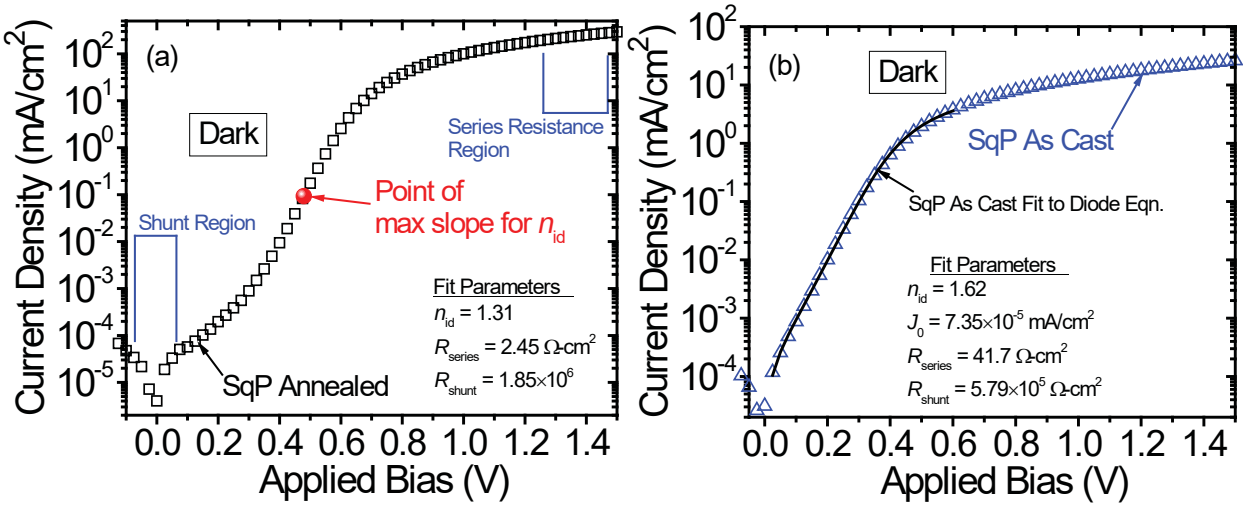

Figure D.6: Dark *J-V* curve fit and analysis examples. a.) shows how the dark parameters were determined for all annealed devices. We found that the simple method of finding the maximum slope in the exponential region yielded the same results as full fits to the diode equation. Therefore, we used the simpler and faster method of examining the maximum slope in the exponential region. b.) shows an example full fit to the diode equation for the as-cast sample. This was necessary because the series resistance was so large for as cast samples.

with an Angstrom Engineering, Inc. evaporator at a pressure of 1.3×10^{-4} Pa (1×10^{-6} Torr). The Ca layer was deposited at a rate of 0.05 nm/s to a thickness of 10 nm, and the Al layer was deposited at a rate of 0.15 nm/s to a thickness of 80 nm. Before exposing the devices, ∼10 nm of Ca was evaporated onto the shutter to ensure layer purity. The final device structure was ITO (150 nm)/PEDOT (∼35 nm)/Active Layer (∼165 nm)/Ca (10 nm)/Al (80 nm). Once the cells were complete, we tested the *J-V* characteristics using a Keithley 2400 sourcemeter and a Xe arc lamp light source with an AM 1.5G filter. The light source was calibrated to AM 1.5G intensity using a silicon photodiode with a KG-5 filter (Hamamatsu). Film thicknesses were measured with a profilometer (Dektak). We obtained the dark *J-V* ideality factors (n_{id}) in Table 5.2 of Chapter 5 from the maximum-slope in the exponential turn-on region in a semi-logarithmic plot for the annealed devices (see Ref. 157) and by full diode equation fits for the as-cast samples. Examples of these fits and analysis are shown in Figure D.6. The V_{oc} vs. light intensity (I) ideality factors were taken from the minimum plateau of the differential ideality factors shown the inset to Figure 5.6 of the main text. We estimated the series (R_{series}) and shunt (R_{shunt}) resistances from the inverse slope of the dark *J-V* curves at 1.5 V and 0 V applied bias, respectively (Figure D.6a). Finally, we measured the average dark carrier density from the relevant area under a charge extraction by

linearly increasing voltage (CELIV) pulse taken in the dark from 0 V to -1.5 V applied bias.

D.6 Active-Layer Composition Analysis by the Redissolving/UV-vis Technique

The following procedure for determining an active layers composition was performed on ITO/PEDOT/Active Layer substrates that were processed identically to that described above except without the evaporation of Ca/Al top electrodes. First, we removed the outer edge of the active layer with a razor blade, leaving only the center portion where the solar cells reside. We found that there can be an anomalous composition (rich in PCBM) on the very outer edge of the substrate in SqP processed films, which is likely due to surface tension effects influencing in the spin-coating deposition process. For this reason, a direct measurement of each films mass by, for example, a microgram-sensitive scale (e.g., Mettler AT20) will, at best, be off by the same amount. Additionally, a mass measurement does not take into account polymer lost due to the PCBM spin coating process.

After removing the outer edge, we cleaned the substrates with compressed inert gas and redissolved the active layer by dropping ODCB via a glass pipette directly onto the films surface, which typically results in instantaneous dissolution of the active layer, irrespective of annealing/processing conditions. We then drew off the dissolved active-layer solution with a clean glass pipette and placed it into a 1 mm thick quartz cuvette. We found it especially critical to execute this washing process at least 3-4 times so as to remove nearly all of the active-layer material on the substrate surface. In the present case, we observed that insufficient removal of the active layer film in the redissolving process resulted in film compositions with an anomalous $\sim$10% enrichment in PCBM. With complete washing, we found that there was not enough remaining material on the substrate for analysis of its relative composition. Finally, after transferring the dissolved active-layer solution, we vigorously shook the cuvette to yield a uniformly mixed and entirely dissolved solution with typical peak optical densities of $\sim$0.15-0.2. Our subsequent analysis of the solution UV-vis data is discussed in the main text.

D.7 XPS Experiments and Analysis

We performed XPS analysis on annealed glass/active-layer films using a Kratos Axis Ultra DLD with a monochromatic K radiation source. The bottom surface was analyzed by floating the films off the glass substrate in deionized water. We did not use PEDOT:PSS/glass substrates because PEDOT:PSS contains sulfur, which can therefore alter the measured S/C ratio. Previous measurements indicate that there is no difference in top surface S/C ratio when using silicon or glass/PEDOT:PSS substrates. In terms of XPS measurement details, a charge neutralizer filament was used to control charging of the sample, a 20 eV pass energy was used with a 0.05 eV step size, and scans were calibrated using the C 1s peak shifted to 284.8 eV. The integrated area of the peaks was found using the CasaXPS software, and atomic ratios were also found using this software. The atomic sensitivity factors used were from the Kratos library within the Casa software. In addition to the 0° XPS measurements described in Figure 5.2 and above, we also performed angle-resolved XPS at higher photoemission angles of 30° and 70° for better surface sensitivity. The 30° and 70° angles correspond to x-ray penetration depths of approximately 9 nm and 4 nm, respectively. We also found that there is a slight but consistent increase in the S/C ratio for all films measured at higher emission angles, but the overall results/conclusions for the systems studied herein are unchanged: annealed SqP has a higher average surface concentration of PCBM than an equivalent BC.

D.8 GIXD Experiments and Analysis

2D grazing incidence wide-angle X-ray diffraction (GIWAXS) experiments were performed at the Stanford Synchrotron Radiation Lightsource (SSRL) on beamline 11-3 using a wavelength of 0.9742 Å. The image in Fig. 5 in the main text corresponds to the integrated pattern of the data collected on a 2D image plate with the detector 400 mm from the sample center (Figure D.7). The beam spot was approximately 150 m wide and a helium chamber was utilized to reduce signal-to-noise. The data was analyzed using the WxDiff software package. The patterns shown in Figure 5.5 and Fig. S7 are results averaged from three separate film comparisons. In the main text we discuss the FWHM of the (100) peak for SqP and BC; we note that the crystallite size for these peaks obtained

by inserting the FWHM into the Scherrer equation, is 22.5 Å for SqP films and 25.1 Å for the BHJ films. This numbers represent more of a lower limit to the domain sizes since a significant amount of the FWHM comes from disorder within a domain rather than just the domain size.

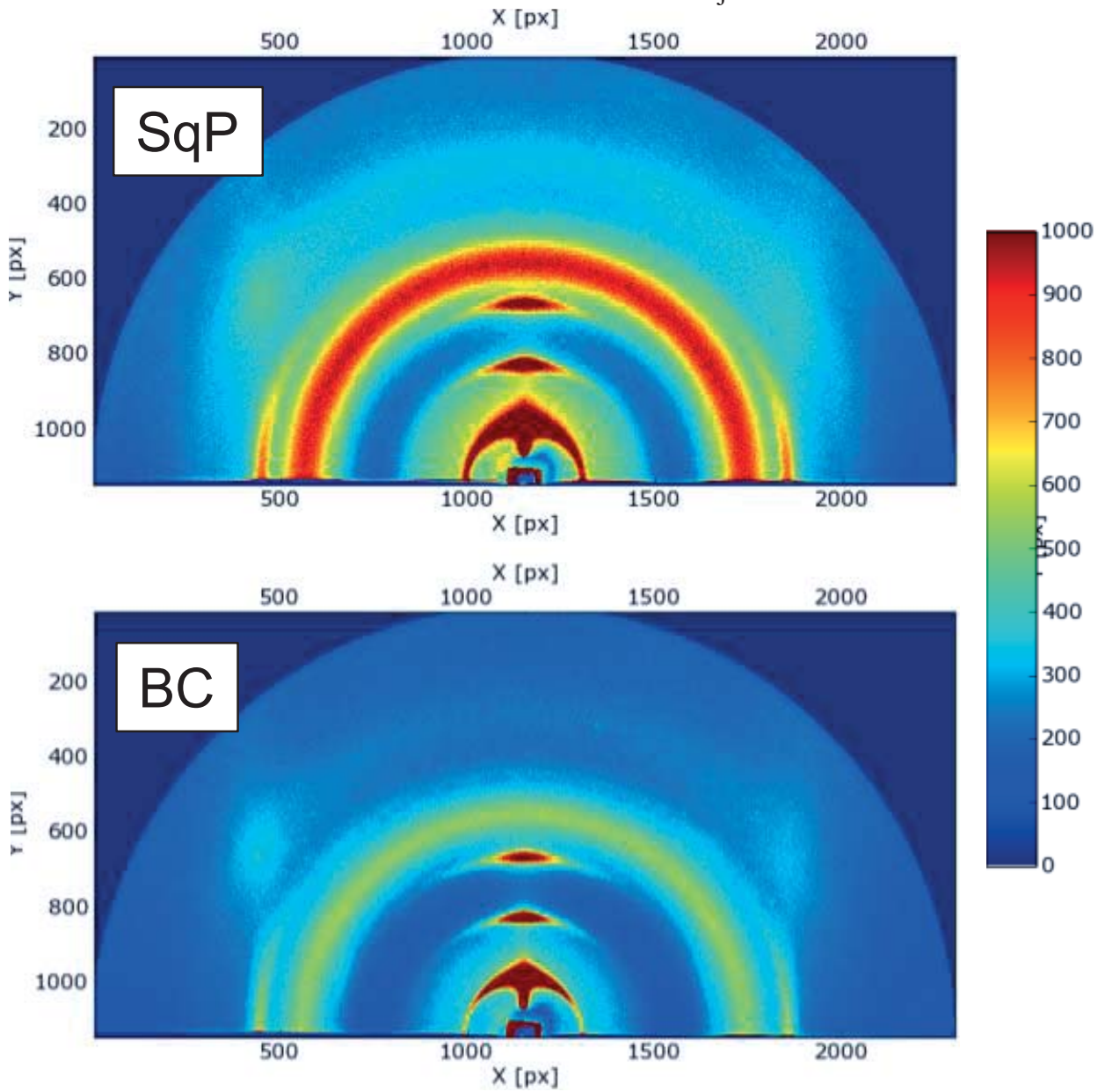

Figure D.7: 2-D GIWAXS diffraction patterns of matched-annealed 1:0.8 P3HT:PCBM SqP and BC fabricated films corresponding to the integrated data in Figure 5.5.

D.9 Transmission Electron Tomography Experiments

In terms of sample preparation, P3HT/PCBM/PEDOT:PSS SqP and BHJ thin films on Si substrates were floated on water and transferred to Cu TEM grids. 15 nm Au fiducial markers were then added to the top and bottom of the films and were allowed dried in air overnight. These thin films were analyzed via electron-energy loss (EELS) spectroscopy in an FEI Titan 80-300 TEM/STEM operating at 300 KV and equipped with a Gatan Model 865 Tridiem imaging energy filter. For electron tomography, a series of BF and EF-TEM images were simultaneously acquired at room temperature using a Fischione Instruments model 2020 high tilt tomography holder. Data was collected taken in 2 increments over a range of specimen tilts from $-60^{\circ} \leq \theta \leq 60^{\circ}$ using the FEI Xplore3D tomography acquisition software. At each value of specimen tilt, three EF-TEM images were acquired: a single zero-loss filtered BF image with the energy-selecting slit centered at 0 eV loss and a pair of plasmon-loss images with the slit centered at 19 eV and 29 eV, respectively. Acquisition was carried out at a magnification of 36,000X using a 5 eV wide energy-selecting slit, an integration time of 10 s, and 4X on chip binning. Offline, the BF image stacks were registered to a common tilt axis by multiple iterations of cross-correlation analysis and fiducial tracking using IMOD software. EF image stacks were generated by dividing the micrographs taken at an energy loss of 19 eV by the micrographs taken at an energy loss of 29 eV for each angle using imageJ software. The resulting EF ratio stacks were then registered to a common tilt axis by applying the translation vectors generated for the BF image series. The aligned EF image stacks were then reconstructed using 10 iterations of the the simultaneous iterative reconstructive technique (SIRT) as implemented in the Tomo3D software package.

D.10 Optoelectronic Analysis

EQE measurements were collected in a manner similar to that detailed elsewhere.[158] In short, the photocurrent from a chopped (211 Hz) monochromatic beam (Newport TLS-300X) was measured across a 0.1 k or 1 kΩ resistor using a SR830 lock-in amplifier. The 1 kΩ resistor (106 current amplification mode) was used when the signal across the 0.1 kΩ resistor reached less than 80 nV.

Because the currents are low, the voltage across the resistor and therefore also the device is small, which means that short-circuit conditions are well-maintained at all times. Multiple long wave pass filters (90% transmission cut-on at 345 nm, 605 nm, 850 nm, 1030 nm, and 1550 nm) were used during the measurement to remove high-energy light transmitted through the monochromator due to lower-order reflections. Each data point was taken from the amplitude (R) readout of the lock-in and averaged for 5 time constants. Below 1050 nm a Thor Labs FDS1010-CAL Si photodiode was used, while above 1050 nm a Thor Labs FDG05-CAL Ge photodiode was used. We note that in the EQE spectra presented in the main text, the noise appears to be similar for all the curves; this is because the same reference spectrum was used for every EQE calculation so that the reference noise is manifest in the same manner for all the devices measured. TPC and TPV transients were taken on a Tektronix DPO 3014 150 MHz oscilloscope in the 20 MHz bandwidth mode for noise reduction. For TPC, the oscilloscope input impedance was set to 50 Ω, while for TPV the input impedance was set to 1 MΩ. We employed a dye-Nitrogen laser for excitation adjusted to give small V_{oc} perturbations of $< 10\%$ of the baseline V_{oc}. The background light intensity was modulated with a Helieon 1200 lm white light LED module driven by a Keithley 2200-20-5 DC power supply. To evaluate the carrier densities, we used the TPC/TPV data to obtain a differential capacitance, which was then interpolated to zero V_{oc} and integrated to the desired V_{oc} in order to obtain $V_{oc}(n)$.[89] To obtain the total carrier lifetimes, we fit the TPV decays to a single exponential and derived the total carrier lifetime according to the approach detailed in Ref. 92.

APPENDIX E

Supporting Information for Chapter 6

E.1 CELIV: Circuit Modeling of Depleted Devices for Determination of C_g

We modeled depleted CELIV curves with the equivalent circuit depicted in Figure E.1. The solution to the differential equation for the current flowing through the circuit in Figure E.1 when applying a CELIV ramp of the form $V(t) = U_R t + V_0$ where t is the time after the start of the ramp, V_0 is the initial steady-state reverse bias, and U_R is the ramp rate in V/s is given by

$$I = I_0 \left(1 - e^{-\frac{t}{\tau}}\right) + \frac{U_R t + V_0}{R_p + R_s} \tag{E.1}$$

$$\tau = \frac{C_g R_p R_s}{R_p + R_s} \tag{E.2}$$

$$I_0 = \frac{C_g U_R}{\left(1 + \frac{R_s}{R_p}\right)^2} \tag{E.3}$$

Interestingly, with finite series (R_s) and shunt (R_p) resistances, the apparent displacement current (I_0) is reduced from its classical magnitude ($C_g U_R$) by a factor of $(1 + R_s/R_p)^{-2}$, though this reduction is typically quite small since usually $R_p \gg R_s$. In the main text, all values of C_g were derived from fits to Eq. (E.1).

It is also worth noting that surface roughness can increase C_g beyond what would be expected from the simple parallel-plate capacitor equation;[394] however, our films typically exhibited exquisite smoothness (< 10 nm^2 RMS surface roughness as measured by profilometry), which is consistent with the values previously reported in the literature.[216,251] Furthermore, if PCBM film or overlayer quality were affecting our calculated C_g values, then the addition of just 15 nm of MoO_3 would not yield the observed perfect capacitor with a C_g value that is consistent with the simple parallel-plate

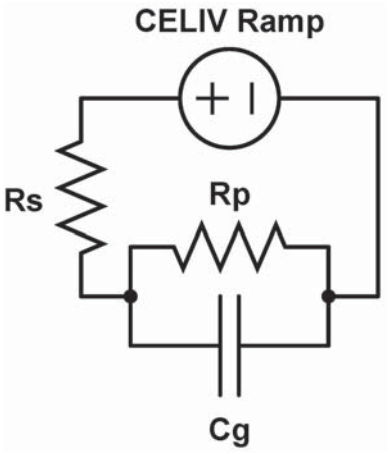

Figure E.1: The equivalent circuit for modeling depleted (no doping) dark CELIV curves. The current for this circuit/voltage-ramp combination are given by Eqs. (E.1-E.3).

capacitor analysis (SI Figure E.5 and Table 1 in the main text).

In addition to changes in C_g, we also observed a significant amount of apparent doping with CELIV in the as-cast sequentially-processed P3HT-based devices that also exhibited significant metal penetration (e.g., the SiO_2, intermixed P3HT:PCBM, MoO_3, and pure P3HT devices showed no apparent doping). The effect was similar to or greater than what we have reported previously ($\gtrsim 10^{16}$ cm^{-3} apparent doping concentration).[201] Since this effect was only observed in the as-cast P3HT-based quasi-bilayer structures and is not universal, we will address the details of why doping often accompanies metal penetration in future work. Regardless of their origin, however, the presence of these excess of dark carriers in certain cases is yet another way that metal penetration into fullerene layers can significantly alter the device physics.

E.2 XPS Analysis: Calculating Surface Composition from Measured C/S Ratios

For P3HT- and PCBM-based samples, the volume fraction of P3HT near the top surface was obtained from the following equations:[275]

$$n_{\mathrm{PCBM}} = \frac{\frac{C}{S}(\mathrm{BC\ or\ SqP}) - \frac{C}{S}(\mathrm{Pure\ P3HT})}{72} \tag{E.4}$$

$$\text{P3HT Weight \%} = \frac{n_{\text{P3HT}} \times M_{\text{P3HT}}}{n_{\text{P3HT}} \times M_{\text{P3HT}} + n_{\text{PCBM}} \times M_{\text{PCBM}}} \times 100\% \tag{E.5}$$

$$\text{P3HT Volume \%} = \frac{\frac{\text{P3HT Weight \%}}{\text{P3HT Physical Density}}}{\frac{\text{P3HT Weight \%}}{\text{P3HT Physical Density}} + \frac{\text{PCBM Weight \%}}{\text{PCBM Physical Density}}} \times 100\% \tag{E.6}$$

The C/S in the equations above is the average carbon (1s) to sulfur (2p) ratio obtained directly in the XPS experiment. The average values and standard deviations (see main text) were calculated based on at least two measurements at different spots on the same sample film.

E.3 Au HAADF EDS and Diffraction Analysis

In this section we present additional HAADF images, EDS, and XRD data in order to verify the labeling scheme used in Figure 3 of the main text. Figure E.2 show the spot EDS spectra for Figure 4 in the main text, confirming the labeling and conclusions regarding the overall device structure. Figure E.3 shows the spot EDS spectra for the higher magnification images of Figure 4 in the main text, again confirming the labeling and conclusions regarding the nature of the nanoparticle formation. Finally, Figure E.4 and Table E.1 confirm that the Au nanoparticles are highly crystalline. It is likely that the P3HT underlayer has much to do with this final nanostructure, as others have analyzed with X-TEM a similar P3HT/PCBM bilayer-like structure fabricated by lamination, but found no metal infiltration.[288] We suspect that in the case of Ref. S6, residual PDMS from the lamination process blocked the penetration of the sputtered Au:Pd overlayer.

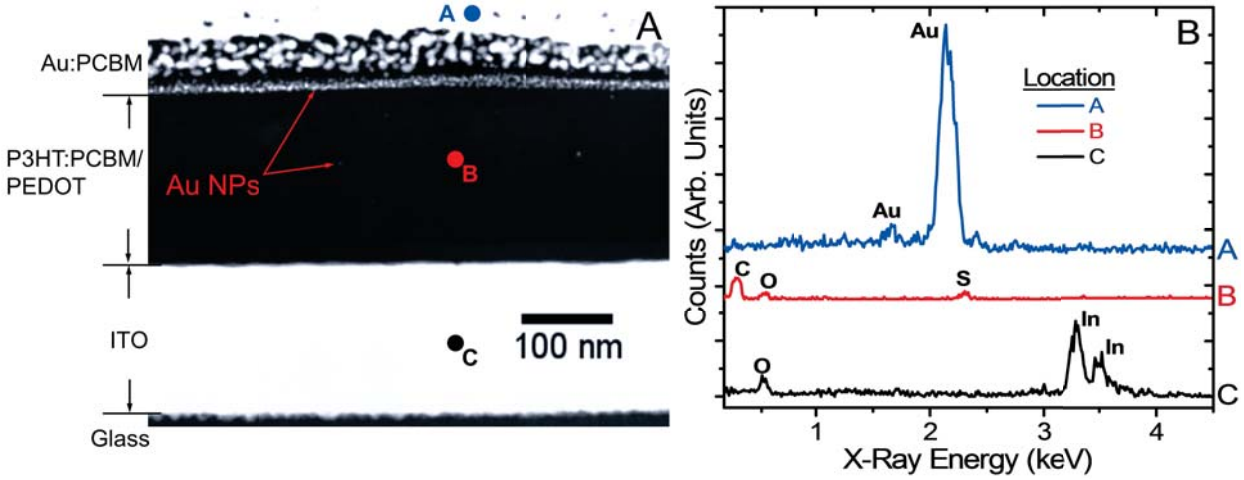

Figure E.2: A) Lower-magnification HAADF on an ITO/PEDOT/P3HT/PCBM/Au device. From the EDS plot in panel B), location C is clearly ITO, as it is composed of essentially entirely of In and O (Sn is not accessible in this energy region). Although location B is clearly composed mainly of P3HT due to the large C and small S signals, we do not have enough information from this data to determine the amount of intercalated PCBM at this location. Location A is the pure gold overlayer before intermixing with PCBM. Some Au NPs are present in/on the P3HT layer, but it is unclear whether their presence is an artifact from the FIB processing or results from penetration of the evaporated metal; see main text.

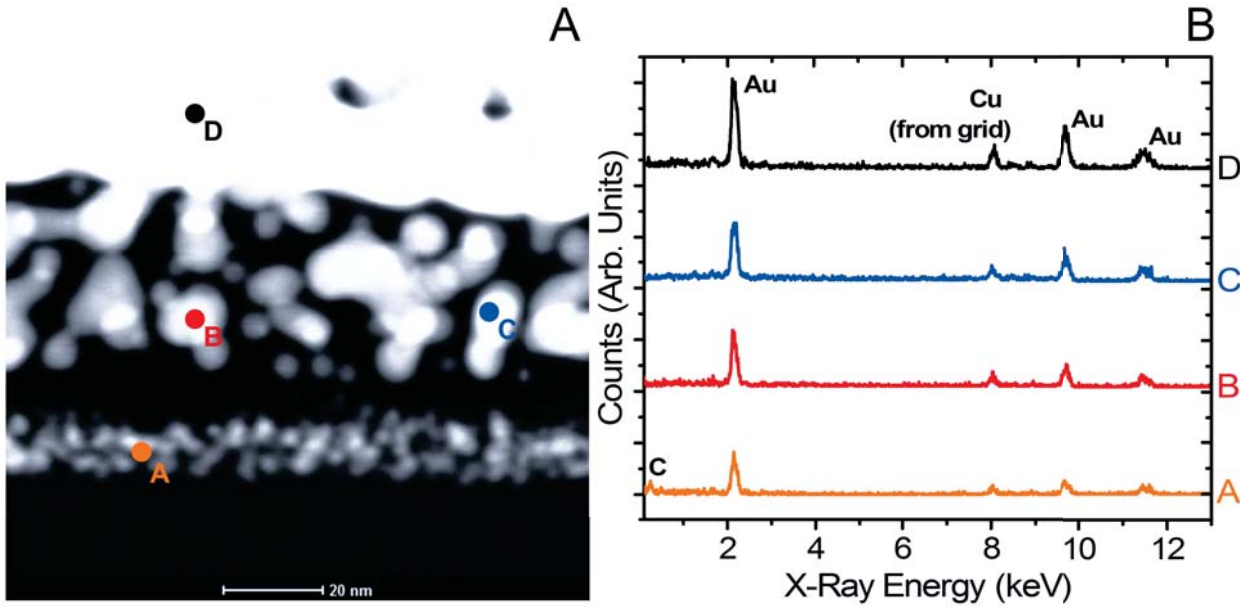

Figure E.3: A) Higher-magnification HAADF on the same ITO/PEDOT/P3HT/PCBM/Au device studied in Fig. S2, revealing that the composition of the nanoparticle domains (points A-C) are essentially pure Au. Point D, which is in the pure Au overlayer, is the same as point A in Fig. S2.

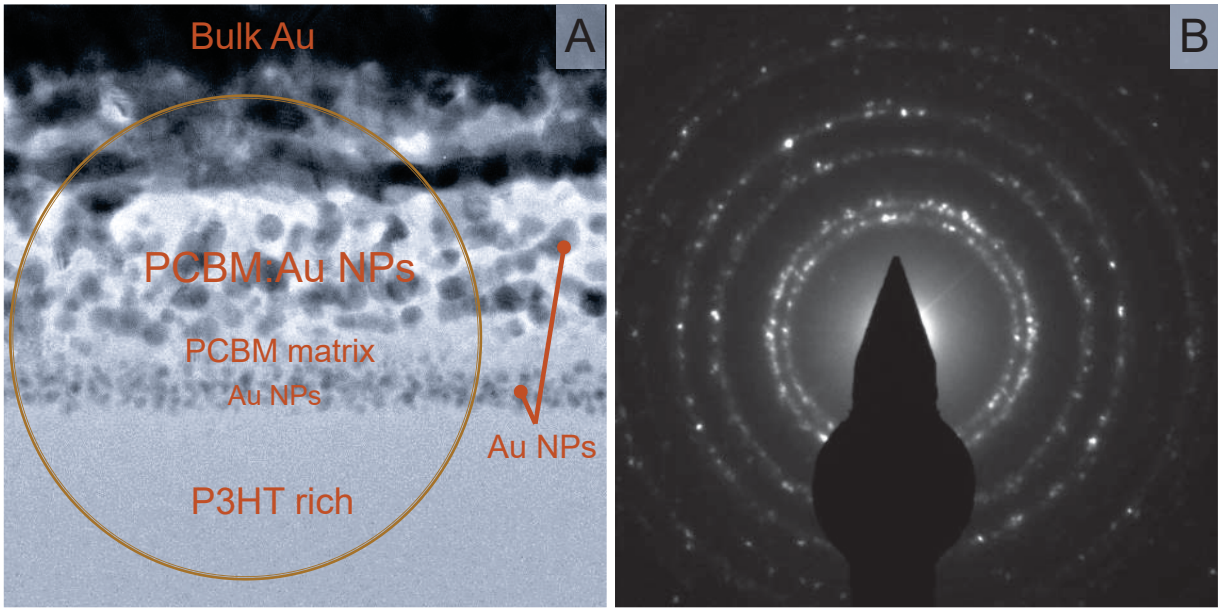

Figure E.4: A) Bright field TEM image of the same PEDOT/P3HT/PCBM/Au device studied in Figs. S2 and S3. The gold-circled area indicates where the electron diffraction pattern shown in panel B) was taken. B) Diffraction pattern obtained from the gold-circled region indicated in A). The measured d-spacing values are in excellent agreement with that of crystalline Au (Table E.1).

Table E.1: Selected Area Electron Diffraction (SAED) Results from Figure E.4B

$d_{measured}$ (Å)	d_{Au} (Å)[a]	Au hkl	Error (%)
2.325	2.355	111	1.28
2.065	2.039	200	1.27
1.461	1.442	220	1.31
1.211	1.230	311	1.55

[a]Refer to literature Au d-spacing (JCPDF #040784);

E.4 Metal Penetration with Different Evaporated Electrodes

Figure E.5 shows that when a MoO_3 blocking layer is inserted in between the fullerene layer and the evaporated metal essentially all leakage current or device shorting is shut off. This suggests that non-metallic interlayers are effective blockers of metal penetration into fullerene-rich films, and could be another reason why inverted devices often have better performance than their normal-structured counterparts.

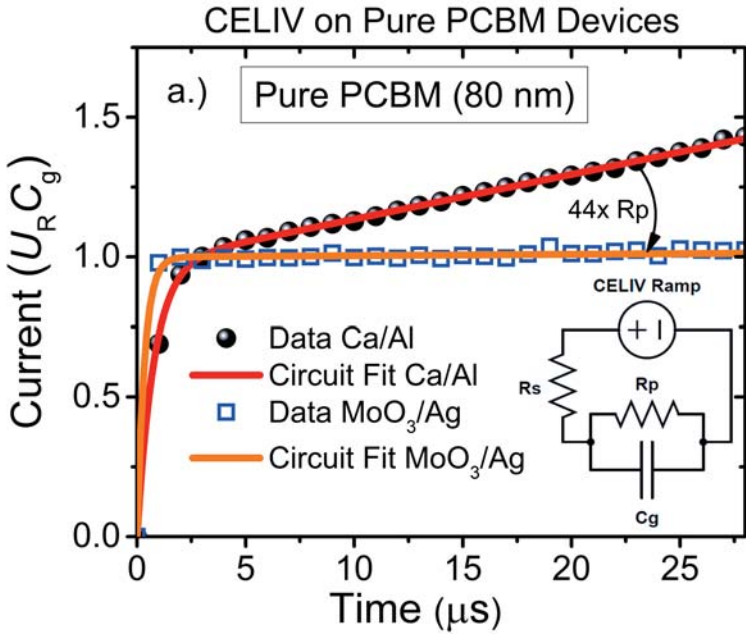

Figure E.5: Dark CELIV traces of ITO/PEDOT/PCBM (80 nm)/Cathode devices showing that when Ca/Al is used as the cathode, severe leakage is observed. However, when MoO_3/Ag is used as the cathode, the device behaves like an ideal capacitor.

REFERENCES

[1] J. A. Turner, "A Realizable Renewable Energy Future," *Science*, vol. 285, pp. 687–689, 1999.

[2] M. Z. Jacobson and M. A. Delucchi, "A Path to Sustainable Energy by 2030," *Sci. Am.*, vol. 301, no. 5, pp. 58–65, 2009.

[3] A. C. Mayer, S. R. Scully, B. E. Hardin, M. W. Rowell, and M. D. McGehee, "Polymer-based solar cells," *Mater. Today*, vol. 10, no. 11, pp. 28–33, 2007.

[4] A. A. Zakhidov, K. Inoue, R. Ulbricht, P. C. Madakasira, W. M. Sampson, L. Sergey, J. Gutierrez, and J. Ferraris, "Temperature and time dependence of heat treatment of RR-P3HT/PCBM solar cell," *Synth. Met. Met.*, vol. 154, no. 1-3, pp. 41–44, 2005.

[5] J. Peet, A. J. Heeger, and G. C. Bazan, ""Plastic" Solar Cells: Self-Assembly of Bulk Heterojunction Nanomaterials by Spontaneous Phase Separation," *Acc. Chem. Res.*, vol. 42, no. 11, pp. 1700–1708, 2009.

[6] C. J. Brabec and J. R. Durrant, "Solution-processed organic solar cells," *MRS Bull.*, vol. 33, no. 7, pp. 670–675, 2008.

[7] V. Shrotriya, G. Li, Y. Yao, T. Moriarty, K. Emery, and Y. Yang, "Accurate measurement and characterization of organic solar cells," *Adv. Funct. Mater.*, vol. 16, no. 15, pp. 2016–2023, 2006.

[8] D. J. Wehenkel, K. H. Hendriks, M. M. Wienk, R. a.J. Janssen, and R. a.J. Janssen, "The effect of bias light on the spectral responsivity of organic solar cells," *Org. Electron.*, vol. 13, pp. 3284–3290, 2012.

[9] T. Kirchartz, J. Mattheis, and U. Rau, "Detailed balance theory of excitonic and bulk heterojunction solar cells," *Phys. Rev. B*, vol. 78, no. 23, p. 13, 2008.

[10] W. Shockley and H. J. Queisser, "Detailed balance limit of efficiency of pn junction solar cells," *J. Appl. Phys.*, vol. 32, no. 3, pp. 510–519, 1961.

[11] C. M. Proctor, M. Kuik, and T.-Q. Nguyen, "Charge carrier recombination in organic solar cells," *Prog. Polym. Sci.*, vol. 38, pp. 1941–1960, 2013.

[12] S. R. Cowan, N. Banerji, W. L. Leong, A. J. Heeger, and G. Dennler, "Charge Formation, Recombination, and Sweep-Out Dynamics in Organic Solar Cells," *Adv. Funct. Mater.*, vol. 22, pp. 1116–1128, 2012.

[13] U. Rau and T. Kirchartz, "On the thermodynamics of light trapping in solar cells.," *Nat. Mater.*, vol. 13, no. 2, pp. 103–104, 2014.

[14] R. A. J. Janssen and J. Nelson, "Factors Limiting Device Efficiency in Organic Photovoltaics," *Adv. Mater.*, vol. 25, pp. 1847–1858, 2013.

[15] J.-L. Brédas, D. Beljonne, V. Coropceanu, J. Cornil, and J. L. Bredas, "Charge-transfer and energy-transfer processes in pi-conjugated oligomers and polymers: A molecular picture," *Chem. Rev.*, vol. 104, pp. 4971–5003, 2004.

[16] B. J. M. Szarko, J. Guo, Y. Liang, B. Lee, B. S. Rolczynski, J. Strzalka, T. Xu, S. Loser, J. Tobin, L. Yu, L. X. Chen, J. M. Szarko, and T. J. Marks, "When Function Follows Form: Effects of Donor Copolymer Side Chains on Film Morphology and BHJ Solar Cell Performance," *Adv. Mater.*, vol. 22, no. 48, pp. 5468–5472, 2010.

[17] R. A. J. Janssen, J. C. Hummelen, N. S. Saricifti, and N. S. Sariciftci, "Polymer-fullerene bulk heterojunction solar cells," *MRS Bull.*, vol. 30, no. 1, pp. 33–36, 2005.

[18] R. Po, C. Carbonera, A. Bernardi, and N. Camaioni, "The role of buffer layers in polymer solar cells," *Energy Environ. Sci.*, vol. 4, no. 2, p. 285, 2011.

[19] S. C. Price, A. C. Stuart, L. Yang, H. Zhou, and W. You, "Fluorine substituted conjugated polymer of medium band gap yields 7% efficiency in polymer-fullerene solar cells.," *J. Am. Chem. Soc.*, vol. 133, pp. 4625–31, 2011.

[20] H. Zhou, L. Yang, A. C. Stuart, S. C. Price, S. Liu, and W. You, "Development of Fluorinated Benzothiadiazole as a Structural Unit for a Polymer Solar Cell of 7 % Efficiency," *Angew. Chemie Int. Ed.*, vol. 50, no. 13, pp. 2995–2998, 2011.

[21] Y. Y. Liang, Z. Xu, J. B. Xia, S.-T. T. Tsai, Y. Wu, G. Li, C. Ray, and L. P. Yu, "For the Bright Future-Bulk Heterojunction Polymer Solar Cells with Power Conversion Efficiency of 7.4%," *Adv. Mater.*, vol. 22, no. 20, pp. E135–+, 2010.

[22] Y. Liu, J. Zhao, Z. Li, C. Mu, W. Ma, H. Hu, K. Jiang, H. Lin, H. Ade, and H. Yan, "Aggregation and morphology control enables multiple cases of high-efficiency polymer solar cells.," *Nat. Commun.*, vol. 5, p. 5293, 2014.

[23] M. T. Dang, L. Hirsch, G. Wantz, B. Minh, and T. Dang, "P3HT:PCBM, Best Seller in Polymer Photovoltaic Research," *Adv. Mater.*, vol. 23, no. 31, pp. 3597–3602, 2011.

[24] G. Dennler, M. C. Scharber, and C. J. Brabec, "Polymer-Fullerene Bulk-Heterojunction Solar Cells," *Adv. Mater.*, vol. 21, no. 13, pp. 1323–1338, 2009.

[25] W. L. Ma, C. Y. Yang, and A. J. Heeger, "Spatial Fourier-transform analysis of the morphology of bulk heterojunction materials used in "plastic" solar cells," *Adv. Mater.*, vol. 19, no. 10, pp. 1387–+, 2007.

[26] W. L. Ma, A. Gopinathan, and A. J. Heeger, "Nanostructure of the interpenetrating networks in poly(3-hexylthiophene)/fullerene bulk heterojunction materials: Implications for charge transport," *Adv. Mater.*, vol. 19, no. 21, pp. 3656–+, 2007.

[27] W. L. Ma, C. Y. Yang, X. Gong, K. Lee, and A. J. Heeger, "Thermally stable, efficient polymer solar cells with nanoscale control of the interpenetrating network morphology," *Adv. Funct. Mater.*, vol. 15, no. 10, pp. 1617–1622, 2005.

[28] M. Morana, H. Azimi, G. Dennler, H. J. Egelhaaf, M. Scharber, K. Forberich, J. Hauch, R. Gaudiana, D. Waller, Z. H. Zhu, K. Hingerl, S. S. van Bavel, J. Loos, and C. J. Brabec, "Nanomorphology and Charge Generation in Bulk Heterojunctions Based on Low-Bandgap Dithiophene Polymers with Different Bridging Atoms," *Adv. Funct. Mater.*, vol. 20, no. 7, pp. 1180–1188, 2010.

[29] G. Li, V. Shrotriya, J. S. Huang, Y. Yao, T. Moriarty, K. Emery, and Y. Yang, "High-efficiency solution processable polymer photovoltaic cells by self-organization of polymer blends," *Nat. Mater.*, vol. 4, pp. 864–868, 2005.

[30] V. D. Mihailetchi, H. X. Xie, B. de Boer, L. M. Popescu, J. C. Hummelen, P. W. M. Blom, and L. J. A. Koster, "Origin of the enhanced performance in poly(3-hexylthiophene): 6,6 -phenyl C-61-butyric acid methyl ester solar cells upon slow drying of the active layer," *Appl. Phys. Lett.*, vol. 89, p. 12107, 2006.

[31] B. Watts, W. J. Belcher, L. Thomsen, H. Ade, and P. C. Dastoor, "A Quantitative Study of PCBM Diffusion during Annealing of P3HT:PCBM Blend Films," *Macromolecules*, vol. 42, pp. 8392–8397, 2009.

[32] M. Shin, H. Kim, J. Park, S. Nam, K. Heo, M. Ree, C.-S. Ha, and Y. Kim, "Abrupt Morphology Change upon Thermal Annealing in Poly(3-Hexylthiophene)/Soluble Fullerene Blend Films for Polymer Solar Cells," *Adv. Funct. Mater.*, vol. 20, no. 5, pp. 748–754, 2010.

[33] D. Credgington, R. Hamilton, P. Atienzar, J. Nelson, and J. R. Durrant, "Non-Geminate Recombination as the Primary Determinant of Open-Circuit Voltage in Polythiophene:Fullerene Blend Solar Cells: an Analysis of the Influence of Device Processing Conditions," *Adv. Funct. Mater.*, vol. 21, no. 14, pp. 2744–2753, 2011.

[34] R. Hamilton, C. G. Shuttle, B. O. Regan, T. C. Hammant, and J. Nelson, "Recombination in annealed and non-annealed polythiophene / fullerene solar cells : transient photovoltage studies versus numerical modelling," pp. 3–5.

[35] M. Al-Ibrahim, O. Ambacher, S. Sensfuss, and G. Gobsch, "Effects of solvent and annealing on the improved performance of solar cells based on poly(3-hexylthiophene): Fullerene," *Appl. Phys. Lett.*, vol. 86, no. 20, p. 3, 2005.

[36] S. Khodabakhsh, B. M. Sanderson, J. Nelson, and T. S. Jones, "Using self-assembling dipole molecules to improve charge collection in molecular solar cells," *Adv. Funct. Mater.*, vol. 16, no. 1, pp. 95–100, 2006.

[37] A. C. Arias, M. Granstrom, D. S. Thomas, K. Petritsch, and R. H. Friend, "Doped conducting-polymer-semiconducting-polymer interfaces: Their use in organic photovoltaic devices," *Phys. Rev. B*, vol. 60, no. 3, pp. 1854–1860, 1999.

[38] F. L. Zhang, A. Gadisa, O. Inganas, M. Svensson, and M. R. Andersson, "Influence of buffer layers on the performance of polymer solar cells," *Appl. Phys. Lett.*, vol. 84, no. 19, pp. 3906–3908, 2004.

[39] K. Zilberberg, J. Meyer, and T. Riedl, "Solution processed metal-oxides for organic electronic devices," *J. Mater. Chem. C*, vol. 1, no. 32, pp. 4796–4815, 2013.

[40] T. Kuwabara, T. Nakayama, K. Uozumi, T. Yamaguchi, and K. Takahashi, "Highly durable inverted-type organic solar cell using amorphous titanium oxide as electron collection electrode inserted between ITO and organic layer," *Sol. Energy Mater. Sol. Cells*, vol. 92, no. 11, pp. 1476–1482, 2008.

[41] S. K. Hau, H.-l. Yip, N. S. Baek, J. Zou, K. O. Malley, A. K. Y. Jen, Y. Hin-Lap, B. Nam Seob, Z. Jingyu, and K. O psila Malley, "Air-stable inverted flexible polymer solar cells using zinc oxide nanoparticles as an electron selective layer," *Appl. Phys. Lett.*, pp. 253301–253303, 2008.

[42] P. P. Boix, J. Ajuria, I. Etxebarria, R. Pacios, G. Garcia-Belmonte, and J. Bisquert, "Role of ZnO Electron-Selective Layers in Regular and Inverted Bulk Heterojunction Solar Cells," *J. Phys. Chem. Lett.*, vol. 2, no. 5, pp. 407–411, 2011.

[43] X. Han, Z. Wu, and B. Sun, "Enhanced performance of inverted organic solar cell by a solution-based fluorinated acceptor doped P3HT:PCBM layer," *Org. Electron.*, vol. 14, pp. 1116–1121, 2013.

[44] C. E. Small, S. Chen, J. Subbiah, C. M. Amb, S.-W. Tsang, T.-h. Lai, J. R. Reynolds, and F. So, "High-efficiency inverted dithienogermole-thienopyrrolodione-based polymer solar cells," *Nat. Photonics*, vol. 6, no. 2, pp. 115–120, 2012.

[45] G. Li, C. W. Chu, V. Shrotriya, J. Huang, and Y. Yang, "Efficient inverted polymer solar cells," *Appl. Phys. Lett.*, vol. 88, no. 25, p. 3, 2006.

[46] T. Ameri, G. Dennler, C. Waldauf, P. Denk, K. Forberich, M. C. Scharber, C. J. Brabec, and K. Hingerl, "Realization, characterization, and optical modeling of inverted bulk-heterojunction organic solar cells," *J. Appl. Phys.*, vol. 103, no. 8, p. 6, 2008.

[47] V. D. Mihailetchi, H. X. Xie, B. de Boer, L. J. A. Koster, and P. W. M. Blom, "Charge transport and photocurrent generation in poly (3-hexylthiophene): Methanofullerene bulk-heterojunction solar cells," *Adv. Funct. Mater.*, vol. 16, no. 5, pp. 699–708, 2006.

[48] P. W. M. Blom, V. D. Mihailetchi, L. J. A. Koster, and D. E. Markov, "Device physics of polymer : fullerene bulk heterojunction solar cells," *Adv. Mater.*, vol. 19, no. 12, pp. 1551–1566, 2007.

[49] S. F. Alvarado, P. F. Seidler, D. G. Lidzey, and D. D. C. Bradley, "Direct determination of the exciton binding energy of conjugated polymers using a scanning tunneling microscope," *Phys. Rev. Lett.*, vol. 81, no. 5, pp. 1082–1085, 1998.

[50] J. J. M. Halls, J. Cornil, D. A. dos Santos, R. Silbey, D. H. Hwang, A. B. Holmes, J. L. Bredas, and R. H. Friend, "Charge- and energy-transfer processes at polymer/polymer interfaces: A joint experimental and theoretical study," *Phys. Rev. B*, vol. 60, no. 8, pp. 5721–5727, 1999.

[51] C. J. Brabec, N. S. Sariciftci, and J. C. Hummelen, "Plastic solar cells," *Adv. Funct. Mater.*, vol. 11, no. 1, pp. 15–26, 2001.

[52] G. Yu, J. Gao, J. C. Hummelen, F. Wudl, and A. J. Heeger, "Polymer Photovoltaic Cells - Enhanced Efficiencies Via a Network of Internal Donor-Acceptor Heterojunctions," *Science (80-.).*, vol. 270, no. 5243, pp. 1789–1791, 1995.

[53] J. J. M. Halls, K. Pichler, R. H. Friend, S. C. Moratti, and A. B. Holmes, "Exciton diffusion and dissociation in a poly(p-phenylenevinylene)/C-60 heterojunction photovoltaic cell," *Appl. Phys. Lett.*, vol. 68, no. 22, pp. 3120–3122, 1996.

[54] L. A. A. Pettersson, L. S. Roman, and O. Inganas, "Modeling photocurrent action spectra of photovoltaic devices based on organic thin films," *J. Appl. Phys.*, vol. 86, no. 1, pp. 487–496, 1999.

[55] G. F. Burkhard, E. T. Hoke, M. D. McGehee, and B. G. F. Burkhard, "Accounting for interference, scattering, and electrode absorption to make accurate internal quantum efficiency measurements in organic and other thin solar cells.," *Adv. Mater.*, vol. 22, pp. 3293–3297, 2010.

[56] E. Centurioni, "Generalized matrix method for calculation of internal light energy flux in mixed coherent and incoherent multilayers," *Appl. Opt.*, vol. 44, no. 35, p. 7532, 2005.

[57] T. Essinger-Hileman, "Transfer matrix for treating stratified media including birefringent crystals," *Appl. Opt.*, vol. 52, pp. 212–8, 2013.

[58] B. Harbecke, "Coherent and incoherent reflection and transmission of multilayer structures," *Appl. Phys. B*, vol. 170, pp. 165–170, 1986.

[59] S. Jung, K.-Y. Kim, Y.-I. Lee, J.-H. Youn, H.-T. Moon, J. Jang, and J. Kim, "Optical Modeling and Analysis of Organic Solar Cells with Coherent Multilayers and Incoherent Glass Substrate Using Generalized Transfer Matrix Method," *Jpn. J. Appl. Phys.*, vol. 50, p. 122301, 2011.

[60] K. Kang, S. Lee, and J. Kim, "Effect of an Incoherent Glass Substrate on the Absorption Efficiency of Organic Solar Cells at Oblique Incidence Analyzed by the Transfer Matrix Method with a Glass," *Jpn. J. Appl. Phys.*, vol. 052301, 2013.

[61] C. C. Katsidis and D. I. Siapkas, "General transfer-matrix method for optical multilayer systems with coherent , partially coherent , and incoherent interference," *Appl. Opt.*, vol. 41, no. 9, pp. 3978–3987, 2002.

[62] J.-H. Kim, S.-Y. Jung, and I.-K. Jeong, "Optical Modeling for Polarization-dependent Optical Power Dissipation of Thin-film Organic Solar Cells at Oblique Incidence," *J. Opt. Soc. Korea*, vol. 16, pp. 6–12, 2012.

[63] S. Lee, I. Jeong, H. P. Kim, S. Y. Hwang, T. J. Kim, Y. D. Kim, J. Jang, and J. Kim, "Effect of incidence angle and polarization on the optimized layer structure of organic solar cells," *Sol. Energy Mater. Sol. Cells*, vol. 118, pp. 9–17, 2013.

[64] A. Meyer and H. Ade, "The effect of angle of incidence on the optical field distribution within thin film organic solar cells," *J. Appl. Phys.*, vol. 106, no. 11, p. 113101, 2009.

[65] C. L. Mitsas and D. I. Siapkas, "Generalized matrix method for analysis of coherent and incoherent reflectance and surfaces, interfaces, and finite substrates," *Appl. Opt.*, vol. 34, no. 10, pp. 1678–1683, 1995.

[66] P. Peumans, A. Yakimov, and S. R. Forrest, "Small molecular weight organic thin-film photodetectors and solar cells," *J. Appl. Phys.*, vol. 93, no. 7, p. 3693, 2003.

[67] M. C. Troparevsky, A. S. Sabau, A. R. Lupini, and Z. Zhang, "Transfer-matrix formalism for the calculation of optical response in multilayer systems: from coherent to incoherent interference.," *Opt. Express*, vol. 18, pp. 24715–24721, 2010.

[68] M. Young, C. J. Traverse, R. Pandey, M. C. Barr, and R. R. Lunt, "Angle dependence of transparent photovoltaics in conventional and optically inverted configurations," *Appl. Phys. Lett.*, vol. 103, no. 13, p. 133304, 2013.

[69] J. Y. Kim, S. H. Kim, H. H. Lee, K. Lee, W. L. Ma, X. Gong, and A. J. Heeger, "New architecture for high-efficiency polymer photovoltaic cells using solution-based titanium oxide as an optical spacer," *Adv. Mater.*, vol. 18, no. 5, pp. 572–576, 2006.

[70] S. B. Dkhil, D. Duché, M. Gaceur, A. K. Thakur, F. B. Aboura, L. Escoubas, J.-J. Simon, A. Guerrero, J. Bisquert, G. Garcia-Belmonte, Q. Bao, M. Fahlman, C. Videlot-Ackermann, O. Margeat, and J. Ackermann, "Interplay of Optical, Morphological, and Electronic Effects of ZnO Optical Spacers in Highly Efficient Polymer Solar Cells," *Adv. Energy Mater.*, vol. 4, p. 1400805, 2014.

[71] A. Hadipour, B. de Boer, and P. W. M. Blom, "Solution-processed organic tandem solar cells with embedded optical spacers," *J. Appl. Phys.*, vol. 102, no. 7, p. 74506, 2007.

[72] J. K. Lee, N. E. Coates, S. Cho, N. S. Cho, D. Moses, G. C. Bazan, K. Lee, and A. J. Heeger, "Efficacy of TiOx optical spacer in bulk-heterojunction solar cells processed with 1,8-octanedithiol," *Appl. Phys. Lett.*, vol. 92, no. 24, p. 3, 2008.

[73] A. Roy, S. H. Park, S. Cowan, M. H. Tong, S. N. Cho, K. Lee, and A. J. Heeger, "Titanium suboxide as an optical spacer in polymer solar cells," *Appl. Phys. Lett.*, vol. 95, no. 1, p. 3, 2009.

[74] B. V. Andersson, D. M. Huang, A. J. Moule, and O. Inganas, "An optical spacer is no panacea for light collection in organic solar cells," *Appl. Phys. Lett.*, vol. 94, no. 4, p. 043302, 2009.

[75] B. Tremolet De Villers and B. J. Schwartz, "Destruction of amplified spontaneous emission via chemical doping at low-work-function metal/conjugated polymer interfaces," *Appl. Phys. Lett.*, vol. 90, p. 091106, 2007.

[76] Y. Roichman and N. Tessler, "Generalized Einstein relation for disordered semiconductor-simplications for device performance," *Appl. Phys. Lett.*, vol. 80, no. 11, pp. 1948–1950, 2002.

[77] G. A. H. Wetzelaer, L. J. A. Koster, and P. W. M. Blom, "Validity of the Einstein Relation in Disordered Organic Semiconductors," *Phys. Rev. Lett.*, vol. 107, no. 6.

[78] S. J. Fonash, *Solar Cell Device Physics*. 2010.

[79] J. Bisquert and G. Garcia-Belmonte, "On Voltage, Photovoltage, and Photocurrent in Bulk Heterojunction Organic Solar Cells," *J. Phys. Chem. Lett.*, vol. 2, no. 15, pp. 1950–1964, 2011.

[80] P. Wurfel and U. Wurfel, *Physics of solar cells : from basic principles to advanced concepts*. Weinheim: Wiley-VCH, 2nd, updat ed., 2009.

[81] G. Li, R. Zhu, and Y. Yang, "Polymer solar cells," *Nat. Photonics*, vol. 6, no. 3, pp. 153–161, 2012.

[82] T. Chu, J. Lu, and S. Beaupré, "Bulk heterojunction solar cells using thieno pyrrole-4, 6-dione and dithieno silole copolymer with a power conversion efficiency of 7.3%," *J. . . .*, vol. 133, pp. 4250–4253, 2011.

[83] J. Nelson, "Polymer: fullerene bulk heterojunction solar cells," *Mater. Today*, vol. 14, pp. 462–470, 2011.

[84] Z. He, C. Zhong, S. Su, M. Xu, H. Wu, and Y. Cao, "Enhanced power-conversion efficiency in polymer solar cells using an inverted device structure," *Nat. Photonics*, vol. 6, no. 9, pp. 591–595, 2012.

[85] S. R. Cowan, A. Roy, and A. J. Heeger, "Recombination in polymer-fullerene bulk heterojunction solar cells," *Phys. Rev. B*, vol. 82, no. 24, p. 245207, 2010.

[86] R. A. Street, S. Cowan, and A. J. Heeger, "Experimental test for geminate recombination applied to organic solar cells," *Phys. Rev. B*, vol. 82, p. 121301(R), 2010.

[87] C. G. Shuttle, A. Maurano, R. Hamilton, B. O'Regan, J. C. de Mello, and J. R. Durrant, "Charge extraction analysis of charge carrier densities in a polythiophene/fullerene solar cell: Analysis of the origin of the device dark current," *Appl. Phys. Lett.*, vol. 93, no. 18, p. 183501, 2008.

[88] C. G. Shuttle, B. O'Regan, A. M. Ballantyne, J. Nelson, D. D. C. Bradley, and J. R. Durrant, "Bimolecular recombination losses in polythiophene: Fullerene solar cells," *Phys. Rev. B*, vol. 78, p. 113201, 2008.

[89] C. G. Shuttle, B. O'Regan, A. M. Ballantyne, J. Nelson, D. D. C. Bradley, J. de Mello, and J. R. Durrant, "Experimental determination of the rate law for charge carrier decay in a polythiophene: Fullerene solar cell," *Appl. Phys. Lett.*, vol. 92, p. 093311, 2008.

[90] C. G. Shuttle, R. Hamilton, B. C. O'Regan, J. Nelson, and J. R. Durrant, "Charge-density-based analysis of the current-voltage response of polythiophene/fullerene photovoltaic devices," *Proc. Natl. Acad. Sci. U. S. A.*, vol. 107, pp. 16448–16452, 2010.

[91] G. F. A. Dibb, T. Kirchartz, D. Credgington, J. R. Durrant, and J. Nelson, "Analysis of the Relationship between Linearity of Corrected Photocurrent and the Order of Recombination in Organic Solar Cells," *J. Phys. Chem. Lett.*, vol. 2, no. 19, pp. 2407–2411, 2011.

[92] A. Maurano, C. G. Shuttle, R. Hamilton, A. M. Ballantyne, J. Nelson, W. Zhang, M. Heeney, and J. R. Durrant, "Transient Optoelectronic Analysis of Charge Carrier Losses in a Selenophene/Fullerene Blend Solar Cell," *J. Phys. Chem. C*, vol. 115, no. 13, pp. 5947–5957, 2011.

[93] D. Credgington, F. C. Jamieson, B. Walker, T.-Q. Nguyen, and J. R. Durrant, "Quantification of Geminate and Non-Geminate Recombination Losses within a Solution-Processed Small-Molecule Bulk Heterojunction Solar Cell," *Adv. Mater.*, vol. 24, pp. 2135–2141, 2012.

[94] G. F. A. Dibb, F. C. Jamieson, A. Maurano, J. Nelson, and J. R. Durrant, "Limits on the Fill Factor in Organic Photovoltaics: Distinguishing Nongeminate and Geminate Recombination Mechanisms," *J. Phys. Chem. Lett.*, vol. 4, no. 5, pp. 803–808, 2013.

[95] A. Maurano, R. Hamilton, C. G. Shuttle, A. M. Ballantyne, J. Nelson, B. O'Regan, W. M. Zhang, I. McCulloch, H. Azimi, M. Morana, C. J. Brabec, and J. R. Durrant, "Recombination Dynamics as a Key Determinant of Open Circuit Voltage in Organic Bulk Heterojunction Solar Cells: A Comparison of Four Different Donor Polymers," *Adv. Mater.*, vol. 22, no. 44, pp. 4987–4992, 2010.

[96] J. Nelson, *The physics of solar cells*. London: Imperial College Press ; Distributed by World Scientific Pub. Co., 2004.

[97] D. Credgington and J. R. Durrant, "Insights from Transient Optoelectronic Analyses on the Open-Circuit Voltage of Organic Solar Cells," *J. Phys. Chem. Lett.*, vol. 3, pp. 1465–1478, 2012.

[98] R. A. Street, D. Davies, P. P. Khlyabich, B. Burkhart, and B. C. Thompson, "Origin of the Tunable Open-Circuit Voltage in Ternary Blend Bulk Heterojunction Organic Solar Cells," *J. Am. Chem. Soc.*, vol. 135, no. 3, pp. 986–989, 2013.

[99] S. R. Cowan, R. A. Street, C. Shinuk, and A. J. Heeger, "Transient photoconductivity in polymer bulk heterojunction solar cells: Competition between sweep-out and recombination," *Phys. Rev. B*, vol. 83, p. 035205, 2011.

[100] W. L. Leong, S. R. Cowan, and A. J. Heeger, "Differential Resistance Analysis of Charge Carrier Losses in Organic Bulk Heterojunction Solar Cells: Observing the Transition from Bimolecular to Trap-Assisted Recombination and Quantifying the Order of Recombination," *Adv. Energy Mater.*, vol. 1, no. 4, pp. 517–522, 2011.

[101] M. Mingebach, S. Walter, V. Dyakonov, and C. Deibel, "Direct and charge transfer state mediated photogeneration in polymer–fullerene bulk heterojunction solar cells," *Appl. Phys. Lett.*, vol. 100, no. 19, p. 193302, 2012.

[102] L. J. A. Koster, V. D. Mihailetchi, and P. W. M. Blom, "Bimolecular recombination in polymer/fullerene bulk heterojunction solar cells," *Appl. Phys. Lett.*, vol. 88, no. 5, p. 52104, 2006.

[103] T. Kirchartz, B. E. Pieters, K. Taretto, and U. Rau, "Mobility dependent efficiencies of organic bulk heterojunction solar cells: Surface recombination and charge transfer state distribution," *Phys. Rev. B*, vol. 80, p. 035334, 2009.

[104] C. Deibel, A. Baumann, and V. Dyakonov, "Polaron recombination in pristine and annealed bulk heterojunction solar cells," *Appl. Phys. Lett.*, vol. 93, p. 163303, 2008.

[105] D. Rauh, C. Deibel, and V. Dyakonov, "Charge Density Dependent Nongeminate Recombination in Organic Bulk Heterojunction Solar Cells," *Adv. Funct. Mater.*, vol. 22, no. 16, pp. 3371–3377, 2012.

[106] J. H. Hou, H.-Y. Y. Chen, S. Q. Zhang, R. I. Chen, Y. Yang, Y. Wu, and G. Li, "Synthesis of a Low Band Gap Polymer and Its Application in Highly Efficient Polymer Solar Cells," *J. Am. Chem. Soc.*, vol. 131, no. 43, pp. 15586–15587, 2009.

[107] F. Piersimoni, S. Chambon, K. Vandewal, R. Mens, T. Boonen, A. Gadisa, M. Izquierdo, S. Filippone, B. Ruttens, J. DHaen, N. Martin, L. Lutsen, D. Vanderzande, P. Adriaensens, J. V. Manca, J. D'Haen, N. Martin, L. Lutsen, D. Vanderzande, P. Adriaensens, and J. V. Manca, "Influence of Fullerene Ordering on the Energy of the Charge-Transfer State and Open-Circuit Voltage in Polymer:Fullerene Solar Cells," *J. Phys. Chem. C*, vol. 115, pp. 10873–10880, 2011.

[108] K. Vandewal, A. Gadisa, W. D. Oosterbaan, S. Bertho, F. Banishoeib, I. Van Severen, L. Lutsen, T. J. Cleij, D. Vanderzande, and J. V. Manca, "The relation between open-circuit voltage and the onset of photocurrent generation by charge-transfer absorption in polymer: Fullerene bulk heterojunction solar cells," *Adv. Funct. Mater.*, vol. 18, no. 14, pp. 2064–2070, 2008.

[109] K. Vandewal, K. Tvingstedt, A. Gadisa, O. Inganas, and J. V. Manca, "Relating the open-circuit voltage to interface molecular properties of donor:acceptor bulk heterojunction solar cells," *Phys. Rev. B*, vol. 81, no. 12, p. 125204, 2010.

[110] K. Tvingstedt, K. Vandewal, A. Gadisa, F. L. Zhang, J. Manca, and O. Inganas, "Electroluminescence from Charge Transfer States in Polymer Solar Cells," *J. Am. Chem. Soc.*, vol. 131, no. 33, pp. 11819–11824, 2009.

[111] V. D. D. Mihailetchi, L. J. A. J. A. Koster, P. W. M. W. M. Blom, C. Melzer, B. deBoer, J. K. J. vanDuren, R. A. J. A. J. Janssen, B. de Boer, J. K. J. van Duren, and R. A. J. A. J. Janssen, "Compositional Dependence of the Performance of Poly(p-phenylene vinylene):Methanofullerene Bulk-Heterojunction Solar Cells," *Adv. Funct. Mater.*, vol. 15, no. 5, pp. 795–801, 2005.

[112] D. Veldman, O. Ipek, S. C. J. Meskers, J. Sweelssen, M. M. Koetse, S. C. Veenstra, J. M. Kroon, S. S. van Bavel, J. Loos, R. A. J. Janssen, S. S. van Bavel, J. Loos, and R. A. J.

Janssen, "Compositional and Electric Field Dependence of the Dissociation of Charge Transfer Excitons in Alternating Polyfluorene Copolymer/Fullerene Blends," *J. Am. Chem. Soc.*, vol. 130, no. 24, pp. 7721–7735, 2008.

[113] F. C. Jamieson, E. B. Domingo, T. McCarthy-Ward, M. Heeney, N. Stingelin, J. R. Durrant, C. Sci, and B. Domingo, "Fullerene crystallisation as a key driver of charge separation in polymer/fullerene bulk heterojunction solar cells," *Chem. Sci.*, vol. 3, no. 2, p. 485, 2012.

[114] H.-Y. Chen, J. Hou, S. Zhang, Y. Liang, G. Yang, Y. Yang, L. Yu, Y. Wu, and G. Li, "Polymer solar cells with enhanced open-circuit voltage and efficiency," *Nat. Photonics*, vol. 3, no. 11, pp. 649–653, 2009.

[115] Z. Tan, W. Zhang, Z. Zhang, D. Qian, Y. Huang, J. Hou, and Y. Li, "High-Performance Inverted Polymer Solar Cells with Solution-Processed Titanium Chelate as Electron-Collecting Layer on ITO Electrode," *Adv. Mater.*, vol. 24, no. 11, pp. 1476–1481, 2012.

[116] J. You, C.-C. Chen, L. Dou, S. Murase, H.-S. Duan, S. A. Hawks, T. Xu, H. J. Son, L. Yu, G. Li, and Y. Yang, "Metal Oxide Nanoparticles as an Electron-Transport Layer in High-Performance and Stable Inverted Polymer Solar Cells," *Adv. Mater.*, vol. 24, no. 38, pp. 5267–5272, 2012.

[117] Y. He, C. Chen, E. Richard, L. Dou, Y. Wu, G. Li, and Y. Yang, "Novel fullerene acceptors: synthesis and application in low band gap polymer solar cells," *J. Mater. Chem.*, vol. 22, no. 26, pp. 13391–13394, 2012.

[118] Y. Zhou, C. Fuentes-Hernandez, J. Shim, J. Meyer, A. J. Giordano, H. Li, P. Winget, T. Papadopoulos, H. Cheun, J. Kim, M. Fenoll, A. Dindar, W. Haske, E. Najafabadi, T. M. Khan, H. Sojoudi, S. Barlow, S. Graham, J.-L. Brédas, S. R. Marder, A. Kahn, and B. Kippelen, "A Universal Method to Produce Low-Work Function Electrodes for Organic Electronics," *Science (80-.).*, vol. 336, no. 6079, pp. 327–332, 2012.

[119] J. H. Seo, D.-H. Kim, S.-H. Kwon, M. Song, M.-S. Choi, S. Y. Ryu, H. W. Lee, Y. C. Park, J.-D. Kwon, K.-S. Nam, Y. Jeong, J.-W. Kang, and C. S. Kim, "High Efficiency Inorganic/Organic Hybrid Tandem Solar Cells," *Adv. Mater.*, pp. n/a–n/a, 2012.

[120] Y. Liang, Y. Wu, D. Feng, S.-t. Tsai, H.-j. Son, G. Li, and L. Yu, "Development of New Semiconducting Polymers for High Performance Solar Cells," *J. Am. Chem. Soc.*, vol. 131, no. 1, pp. 56–57, 2008.

[121] Y. Y. Liang, D. Q. Feng, Y. Wu, S.-T. T. Tsai, G. Li, C. Ray, and L. P. Yu, "Highly Efficient Solar Cell Polymers Developed via Fine-Tuning of Structural and Electronic Properties," *J. Am. Chem. Soc.*, vol. 131, no. 22, pp. 7792–7799, 2009.

[122] Z. C. He, C. M. Zhong, X. Huang, W.-Y. Y. Wong, H. B. Wu, L. W. Chen, S. J. Su, and Y. Cao, "Simultaneous Enhancement of Open-Circuit Voltage, Short-Circuit Current Density, and Fill Factor in Polymer Solar Cells," *Adv. Mater.*, vol. 23, no. 40, pp. 4636–4643, 2011.

[123] J. Guo, Y. Liang, J. Szarko, B. Lee, H. J. Son, B. S. Rolczynski, L. Yu, and L. X. Chen, "Structure, Dynamics, and Power Conversion Efficiency Correlations in a New Low Bandgap Polymer: PCBM Solar Cell," *J. Phys. Chem. B*, vol. 114, no. 2, pp. 742–748, 2010.

[124] M. R. Hammond, R. J. Kline, A. A. Herzing, L. J. Richter, D. S. Germack, H.-W. Ro, C. L. Soles, D. a. Fischer, T. Xu, L. Yu, M. F. Toney, and D. M. DeLongchamp, "Molecular Order in High-Efficiency Polymer/Fullerene Bulk Heterojunction Solar Cells," *ACS Nano*, vol. 5, pp. 8248–8257, 2011.

[125] B. A. Collins, Z. Li, J. R. Tumbleston, E. Gann, C. R. McNeill, and H. Ade, "Absolute Measurement of Domain Composition and Nanoscale Size Distribution Explains Performance in PTB7:PC71BM Solar Cells," *Adv. Energy Mater.*, vol. 3, no. 1, pp. 65–74, 2012.

[126] W. Chen, T. Xu, F. He, W. Wang, C. Wang, J. Strzalka, Y. Liu, J. Wen, D. J. Miller, J. Chen, O. K. Hong, O. L. Yu, S. B. Darling, K. Hong, and L. Yu, "Hierarchical Nanomorphologies Promote Exciton Dissociation in Polymer/Fullerene Bulk Heterojunction Solar Cells," *Nano Lett.*, vol. 11, no. 9, pp. 3707–3713, 2011.

[127] S. Albrecht, S. Schafer, I. Lange, S. Yilmaz, I. Dumsch, S. Allard, U. Scherf, A. Hertwig, and D. Neher, "Light management in PCPDTBT:PC70BM solar cells: A comparison of standard and inverted device structures," *Org. Electron.*, vol. 13, no. 4, pp. 615–622, 2012.

[128] A. Hadipour, D. Cheyns, P. Heremans, and B. P. Rand, "Electrode Considerations for the Optical Enhancement of Organic Bulk Heterojunction Solar Cells," *Adv. Energy Mater.*, vol. 1, no. 5, pp. 930–935, 2011.

[129] J. E. Parmer, A. C. Mayer, B. E. Hardin, S. R. Scully, M. D. McGehee, M. Heeney, and I. McCulloch, "Organic bulk heterojunction solar cells using poly(2,5-bis(3-tetradecyllthiophen-2-yl)thieno[3,2,-b]thiophene)," *Appl. Phys. Lett.*, vol. 92, no. 11, p. 3, 2008.

[130] A. P. Yuen, J. S. Preston, A. M. Hor, R. Klenkler, E. Q. B. Macabebe, E. E. van Dyk, and R. O. Loutfy, "Blend composition study of poly(3,3"'-didodecylquaterthiophene)/[6,6]-phenyl C-61 butyric acid methyl ester solution processed organic solar cells," *J. Appl. Phys.*, vol. 105, no. 1, p. 3, 2009.

[131] M. C. Scharber, N. A. Schultz, N. S. Sariciftci, and C. J. Brabec, "Optical- and photocurrent-detected magnetic resonance studies on conjugated polymer/fullerene composites," *Phys. Rev. B*, vol. 67, no. 8, 2003.

[132] T. Kirchartz and U. Rau, "Detailed balance and reciprocity in solar cells," *Phys. Status Solidi*, vol. 205, pp. 2737–2751, 2008.

[133] T. Kirchartz and J. Nelson, "Meaning of reaction orders in polymer:fullerene solar cells," *Phys. Rev. B*, vol. 86, no. 16, p. 165201, 2012.

[134] A. Foertig, J. Rauh, V. Dyakonov, and C. Deibel, "Shockley equation parameters of P3HT:PCBM solar cells determined by transient techniques," *Phys. Rev. B*, vol. 86, no. 11, p. 115302, 2012.

[135] T. Kirchartz, B. E. Pieters, J. Kirkpatrick, U. Rau, and J. Nelson, "Recombination via tail states in polythiophene: fullerene solar cells," *Phys. Rev. B*, vol. 83, no. 11, p. 115209, 2011.

[136] C. Deibel and V. Dyakonov, "Polymer-fullerene bulk heterojunction solar cells," *Reports Prog. Phys.*, vol. 73, p. 096401, 2010.

[137] C. G. Shuttle, R. Hamilton, J. Nelson, B. C. O'Regan, and J. R. Durrant, "Measurement of Charge-Density Dependence of Carrier Mobility in an Organic Semiconductor Blend," *Adv. Funct. Mater.*, vol. 20, no. 5, pp. 698–702, 2010.

[138] T. Kirchartz, T. Agostinelli, M. Campoy-Quiles, W. Gong, and J. Nelson, "Understanding the Thickness-Dependent Performance of Organic Bulk Heterojunction Solar Cells: The Influence of Mobility, Lifetime, and Space Charge," *J. Phys. Chem. Lett.*, vol. 3, no. 23, pp. 3470–3475, 2012.

[139] W. Gong, M. A. Faist, N. J. Ekins-Daukes, Z. Xu, D. D. C. Bradley, J. Nelson, and T. Kirchartz, "Influence of energetic disorder on electroluminescence emission in polymer:fullerene solar cells," *Phys. Rev. B*, vol. 86, no. 2, p. 24201, 2012.

[140] M. A. Faist, T. Kirchartz, W. Gong, R. S. Ashraf, I. McCulloch, J. C. de Mello, N. J. Ekins-Daukes, D. D. C. Bradley, and J. Nelson, "Competition between the Charge Transfer State and the Singlet States of Donor or Acceptor Limiting the Efficiency in Polymer:Fullerene Solar Cells," *J. Am. Chem. Soc.*, vol. 134, no. 1, pp. 685–692, 2012.

[141] E. T. Hoke, K. Vandewal, J. A. Bartelt, W. R. Mateker, J. D. Douglas, R. Noriega, K. R. Graham, J. M. J. Fréchet, A. Salleo, and M. D. McGehee, "Recombination in Polymer:Fullerene Solar Cells with Open-Circuit Voltages Approaching and Exceeding 1.0 V," *Adv. Energy Mater.*, vol. 3, no. 2, pp. 220–230, 2012.

[142] D. Di Nuzzo, G.-J. A. H. Wetzelaer, R. K. M. Bouwer, V. S. Gevaerts, S. C. J. Meskers, J. C. Hummelen, P. W. M. Blom, and R. A. J. Janssen, "Simultaneous Open-Circuit Voltage Enhancement and Short-Circuit Current Loss in Polymer: Fullerene Solar Cells Correlated by Reduced Quantum Efficiency for Photoinduced Electron Transfer," *Adv. Energy Mater.*, pp. n/a–n/a, 2012.

[143] D. Veldman, S. C. J. Meskers, and R. a. J. Janssen, "The Energy of Charge-Transfer States in Electron Donor-Acceptor Blends: Insight into the Energy Losses in Organic Solar Cells," *Adv. Funct. Mater.*, vol. 19, pp. 1939–1948, 2009.

[144] C. Risko, M. D. McGehee, J.-L. Bredas, and J.-L. Brédas, "A quantum-chemical perspective into low optical-gap polymers for highly-efficient organic solar cells," *Chem. Sci.*, vol. 2, no. 7, pp. 1200–1218, 2011.

[145] T. Agostinelli, S. Lilliu, J. G. Labram, M. Campoy-Quiles, M. Hampton, E. Pires, J. Rawle, O. Bikondoa, D. D. C. Bradley, T. D. Anthopoulos, J. Nelson, and J. E. Macdonald, "Real-Time Investigation of Crystallization and Phase-Segregation Dynamics in P3HT:PCBM Solar Cells During Thermal Annealing," *Adv. Funct. Mater.*, vol. 21, pp. 1701–1708, May 2011.

[146] J. M. Szarko, J. Guo, B. S. Rolczynski, and L. X. Chen, "Current trends in the optimization of low band gap polymers in bulk heterojunction photovoltaic devices," *J. Mater. Chem.*, vol. 21, no. 22, pp. 7849–7857, 2011.

[147] X. Guo, N. Zhou, S. J. Lou, J. Smith, D. B. Tice, J. W. Hennek, R. Ponce Ortiz, J. T. Lopez Navarrete, S. Li, J. Strzalka, L. X. Chen, R. P. H. Chang, A. Facchetti, and T. J. Marks, "Polymer solar cells with enhanced fill factors," *Nat. Photonics*, vol. 7, pp. 825–833, 2013.

[148] J. You, L. Dou, K. Yoshimura, T. Kato, K. Ohya, T. Moriarty, K. Emery, C.-C. Chen, J. Gao, G. Li, and Y. Yang, "A polymer tandem solar cell with 10.6% power conversion efficiency," *Nat. Commun.*, vol. 4, 2013.

[149] L. Dou, J. You, Z. Hong, Z. Xu, G. Li, R. A. Street, and Y. Yang, "25th Anniversary Article: A Decade of Organic/Polymeric Photovoltaic Research," *Adv. Mater.*, vol. 25, pp. 6642–6671, 2013.

[150] S. A. Hawks, F. Deledalle, J. Yao, D. G. Rebois, G. Li, J. Nelson, Y. Yang, T. Kirchartz, and J. R. Durrant, "Relating Recombination, Density of States, and Device Performance in an Efficient Polymer:Fullerene Organic Solar Cell Blend," *Adv. Energy Mater.*, vol. 3, pp. 1201–1209, 2013.

[151] R. N. Hall, "Electron-hole recombination in germanium," *Phys. Rev.*, vol. 87, p. 387, 1952.

[152] W. Shockley and W. T. Read Jr, "Statistics of the recombinations of holes and electrons," *Phys. Rev.*, vol. 87, no. 46, pp. 835–842, 1952.

[153] C.-T. Sah, R. N. Noyce, and W. Shockley, "Carrier generation and recombination in pn junctions and pn junction characteristics," *Proc. IRE*, vol. 45, no. 9, pp. 1228–1243, 1957.

[154] G. a. H. Wetzelaer, M. Kuik, M. Lenes, and P. W. M. Blom, "Origin of the dark-current ideality factor in polymer:fullerene bulk heterojunction solar cells," *Appl. Phys. Lett.*, vol. 99, no. 15, p. 153506, 2011.

[155] R. A. Street and M. Schoendorf, "Interface state recombination in organic solar cells," *Phys. Rev. B*, vol. 81, no. 20, p. 205307, 2010.

[156] L. J. A. Koster, V. D. Mihailetchi, R. Ramaker, and P. W. M. Blom, "Light intensity dependence of open-circuit voltage of polymer:fullerene solar cells," *Appl. Phys. Lett.*, vol. 86, no. 12, p. 123509, 2005.

[157] T. Kirchartz, F. Deledalle, P. S. Tuladhar, J. R. Durrant, and J. Nelson, "On the differences between dark and light ideality factor in polymer:Fullerene solar cells," *J. Phys. Chem. Lett.*, vol. 4, pp. 2371–2376, 2013.

[158] R. A. Street, A. Krakaris, and S. R. Cowan, "Recombination Through Different Types of Localized States in Organic Solar Cells," *Adv. Funct. Mater.*, vol. 22, no. 21, pp. 4608–4619, 2012.

[159] R. A. Street, J. E. Northrup, and B. S. Krusor, "Radiation induced recombination centers in organic solar cells," *Phys. Rev. B*, vol. 85, p. 205211, May 2012.

[160] C. Deibel, A. Wagenpfahl, and V. Dyakonov, "Influence of charge carrier mobility on the performance of organic solar cells," *Phys. Status Solidi-Rapid Res. Lett.*, vol. 2, no. 4, pp. 175–177, 2008.

[161] F. Gao, J. Wang, J. C. Blakesley, I. Hwang, Z. Li, and N. C. Greenham, "Quantifying loss mechanisms in polymer:Fullerene photovoltaic devices," *Adv. Energy Mater.*, vol. 2, no. 8, pp. 956–961, 2012.

[162] C. Hyun Kim, O. Yaghmazadeh, Y. Bonnassieux, and G. Horowitz, "Modeling the low-voltage regime of organic diodes: Origin of the ideality factor," *J. Appl. Phys.*, vol. 110, no. 9, p. 93722, 2011.

[163] L. J. A. Koster, E. C. P. Smits, V. D. Mihailetchi, and P. W. M. Blom, "Device model for the operation of polymer/fullerene bulk heterojunction solar cells," *Phys. Rev. B*, vol. 72, no. 8, p. 9, 2005.

[164] N. C. Giebink, B. E. Lassiter, G. P. Wiederrecht, M. R. Wasielewski, and S. R. Forrest, "Ideal diode equation for organic heterojunctions. I. Derivation and application," *Phys. Rev. B*, vol. 82, no. 15, p. 155305, 2010.

[165] N. C. Giebink, B. E. Lassiter, G. P. Wiederrecht, M. R. Wasielewski, and S. R. Forrest, "Ideal diode equation for organic heterojunctions. II. The role of polaron pair recombination," *Phys. Rev. B*, vol. 82, no. 15, p. 155306, 2010.

[166] C. van Berkel, M. J. Powell, A. R. Franklin, I. D. French, C. van Berkel, M. J. Powell, A. R. Franklin, and I. D. French, "Quality factor in a-Si:H nip and pin diodes," *J. Appl. Phys.*, vol. 73, no. 10, pp. 5264–5268, 1993.

[167] R. A. Street, K. W. Song, J. E. Northrup, and S. Cowan, "Photoconductivity measurements of the electronic structure of organic solar cells," *Phys. Rev. B*, vol. 83, no. 16, p. 165207, 2011.

[168] R. A. Street, "Localized state distribution and its effect on recombination in organic solar cells," *Phys. Rev. B*, vol. 84, no. 7, p. 75208, 2011.

[169] J. C. Blakesley and D. Neher, "Relationship between energetic disorder and open-circuit voltage in bulk heterojunction organic solar cells," *Phys. Rev. B*, vol. 84, p. 12, 2011.

[170] L. Tzabari and N. Tessler, "ShockleyReadHall recombination in P3HT:PCBM solar cells as observed under ultralow light intensities," *J. Appl. Phys.*, vol. 109, no. 6, p. 064501, 2011.

[171] L. Dou, J. Gao, E. Richard, J. You, C. C. Chen, K. C. Cha, Y. He, G. Li, and Y. Yang, "Systematic investigation of benzodithiophene- and diketopyrrolopyrrole-based low-bandgap polymers designed for single junction and tandem polymer solar cells," *J. Am. Chem. Soc.*, vol. 134, no. 24, pp. 10071–10079, 2012.

[172] S. Cho, N. Coates, J. S. Moon, S. H. Park, A. Roy, S. Beaupre, D. Moses, M. Leclerc, K. Lee, A. J. Heeger, and S. Beaupré, "Bulk heterojunction solar cells with internal quantum efficiency approaching 100%," *Nat. Photonics*, vol. 3, pp. 297–302, 2009.

[173] R. A. Street, P. P. Khlyabich, and B. C. Thompson, "Electrical characterization of organic solar cell contact degradation resulting from ambient exposure," *Org. Electron.*, vol. 14, pp. 2932–2939, 2013.

[174] D. M. Stevens, J. C. Speros, M. a. Hillmyer, and C. D. Frisbie, "Relationship between Diode Saturation Current and Open Circuit Voltage in Poly(3-alkylthiophene) Solar Cells as a Function of Device Architecture, Processing Conditions, and Alkyl Side Chain Length," *J. Phys. Chem. C*, vol. 115, pp. 20806–20816, 2011.

[175] L. Goris, A. Poruba, L. Hod'ákova, M. Vaněček, K. Haenen, M. Nesládek, P. Wagner, D. Vanderzande, L. De Schepper, and J. V. Manca, "Observation of the subgap optical absorption in polymer-fullerene blend solar cells," *Appl. Phys. Lett.*, vol. 88, no. 5, p. 52113, 2006.

[176] R. C. I. MacKenzie, C. G. Shuttle, M. L. Chabinyc, and J. Nelson, "Extracting Microscopic Device Parameters from Transient Photocurrent Measurements of P3HT:PCBM Solar Cells," *Adv. Energy Mater.*, vol. 2, no. 6, pp. 662–669, 2012.

[177] J. Bhattacharya, R. W. Mayer, M. Samiee, and V. L. Dalal, "Photo-induced changes in fundamental properties of organic solar cells," *Appl. Phys. Lett.*, vol. 100, p. 193501, 2012.

[178] M. Vaněček, J. Kočka, a. Poruba, and a. Fejfar, "Direct measurement of the deep defect density in thin amorphous silicon films with the "absolute" constant photocurrent method," *J. Appl. Phys.*, vol. 78, no. 10, pp. 6203–6210, 1995.

[179] N. M. Jackson, W. B. and Amer, "Direct measurement of gap-state absorption in hydrogenated amorphous silicon by photothermal defection spectroscopy," *Phys. Rev. B*, vol. 25, no. 8, pp. 5559–5562, 1982.

[180] N. F. Mott and E. A. Davis, *Electronic processes in non-crystalline materials*. Oxford New York: Clarendon Press ; Oxford University Press, 2d ed., 1979.

[181] R. A. Street, K. W. Song, and S. Cowan, "Influence of series resistance on the photocurrent analysis of organic solar cells," *Org. Electron.*, vol. 12, pp. 244–248, 2011.

[182] R. A. Street, *Hydrogenated amorphous silicon*. Cambridge University Press, 2005.

[183] M. Kemerink, J. M. Kramer, H. H. P. Gommans, and R. a. J. Janssen, "Temperature-dependent built-in potential in organic semiconductor devices," *Appl. Phys. Lett.*, vol. 88, no. 19, p. 192108, 2006.

[184] R. C. I. MacKenzie, T. Kirchartz, G. F. A. Dibb, and J. Nelson, "Modeling Nongeminate Recombination in P3HT:PCBM Solar Cells," *J. Phys. Chem. C*, vol. 115, no. 19, pp. 9806–9813, 2011.

[185] T. Kirchartz, W. Gong, S. A. Hawks, T. Agostinelli, R. C. I. Mackenzie, Y. Yang, and J. Nelson, "Sensitivity of the Mott-Schottky Analysis in Organic Solar Cells," *J. Phys. Chem. C*, vol. 116, no. 14, pp. 7672–7680, 2012.

[186] M. P. Eng, P. R. F. Barnes, and J. R. Durrant, "Concentration-Dependent Hole Mobility and Recombination Coefficient in Bulk Heterojunctions Determined from Transient Absorption Spectroscopy," *J. Phys. Chem. Lett.*, vol. 1, no. 20, pp. 3096–3100, 2010.

[187] J. C. Aguirre, C. Arntsen, S. Hernandez, R. Huber, A. M. Nardes, M. Halim, D. Kilbride, Y. Rubin, S. H. Tolbert, N. Kopidakis, B. J. Schwartz, and D. Neuhauser, "Understanding Local and Macroscopic Electron Mobilities in the Fullerene Network of Conjugated Polymer-based Solar Cells: Time-Resolved Microwave Conductivity and Theory," *Adv. Funct. Mater.*, vol. 24, pp. 784–792, 2014.

[188] J. Li, Y. Zhao, H. S. Tan, Y. Guo, C.-A. Di, G. Yu, Y. Liu, M. Lin, S. H. Lim, Y. Zhou, H. Su, and B. S. Ong, "A stable solution-processed polymer semiconductor with record high-mobility for printed transistors," *Sci. Rep.*, vol. 2, pp. 1–9, 2012.

[189] S. M. Sze and K. K. Ng, *Physics of semiconductor devices*. Hoboken, N.J.: Wiley-Interscience, 3rd ed., 2007.

[190] H. J. Snaith, "Perovskites: the emergence of a new era for low-cost, high-efficiency solar cells," *J. Phys. Chem. Lett.*, vol. 4, pp. 3623–3630, 2013.

[191] M. Liu, M. B. Johnston, and H. J. Snaith, "Efficient planar heterojunction perovskite solar cells by vapour deposition.," *Nature*, vol. 501, pp. 395–398, 2013.

[192] A. Mei, X. Li, L. Liu, Z. Ku, T. Liu, Y. Rong, M. Xu, M. Hu, J. Chen, Y. Yang, M. Gratzel, and H. Han, "A hole-conductor-free, fully printable mesoscopic perovskite solar cell with high stability," *Science (80-.).*, vol. 345, pp. 295–298, 2014.

[193] M. M. Lee, J. Teuscher, T. Miyasaka, T. N. Murakami, and H. J. Snaith, "Efficient hybrid solar cells based on meso-superstructured organometal halide perovskites.," *Science (80-.).*, vol. 338, pp. 643–647, 2012.

[194] C. J. Brabec, S. Gowrisanker, J. J. M. Halls, D. Laird, S. Jia, and S. P. Williams, "Polymer-Fullerene Bulk-Heterojunction Solar Cells," *Adv. Mater.*, vol. 22, no. 34, pp. 3839–3856, 2010.

[195] C. J. Brabec, M. Heeney, I. McCulloch, and J. Nelson, "Influence of blend microstructure on bulk heterojunction organic photovoltaic performance.," *Chem. Soc. Rev.*, vol. 40, pp. 1185–99, 2011.

[196] R. Hamilton, C. G. Shuttle, B. O'Regan, T. C. Hammant, J. Nelson, and J. R. Durrant, "Recombination in Annealed and Nonannealed Polythiophene/Fullerene Solar Cells: Transient Photovoltage Studies versus Numerical Modeling," *J. Phys. Chem. Lett.*, vol. 1, no. 9, pp. 1432–1436, 2010.

[197] F. Deledalle, P. Shakya Tuladhar, J. Nelson, J. R. Durrant, and T. Kirchartz, "Understanding the Apparent Charge Density Dependence of Mobility and Lifetime in Organic Bulk Heterojunction Solar Cells," *J. Phys. Chem. C*, vol. 118, pp. 8837–8842, May 2014.

[198] B. C. O'Regan and F. Lenzmann, "Charge Transport and Recombination in a Nanoscale Interpenetrating Network of n-Type and p-Type Semiconductors: Transient Photocurrent and Photovoltage Studies of TiO2/Dye/CuSCN Photovoltaic Cells," *J. Phys. Chem. B*, vol. 108, no. 14, pp. 4342–4350, 2004.

[199] B. C. O'Regan, S. Scully, A. C. Mayer, E. Palomares, and J. Durrant, "The Effect of Al2O3 Barrier Layers in TiO2/Dye/CuSCN Photovoltaic Cells Explored by Recombination and DOS Characterization Using Transient Photovoltage Measurements," *J. Phys. Chem. B*, vol. 109, no. 10, pp. 4616–4623, 2005.

[200] B. C. O'Regan, J. R. Durrant, P. M. Sommeling, and N. J. Bakker, "Influence of the TiCl4 Treatment on Nanocrystalline TiO2 Films in Dye-Sensitized Solar Cells. 2. Charge Density, Band Edge Shifts, and Quantification of Recombination Losses at Short Circuit," *J. Phys. Chem. C*, vol. 111, no. 37, pp. 14001–14010, 2007.

[201] S. A. Hawks, J. C. Aguirre, L. T. Schelhas, R. J. Thompson, R. C. Huber, A. S. Ferreira, G. Zhang, A. A. Herzing, S. H. Tolbert, and B. J. Schwartz, "Comparing Matched Polymer:Fullerene Solar Cells Made by Solution-Sequential Processing and Traditional Blend Casting: Nanoscale Structure and Device Performance," *J. Phys. Chem. C*, vol. 118, no. 31, pp. 17413–17425, 2014.

[202] A. Pivrikas, N. S. Sariciftci, G. Juška, and R. Österbacka, "A review of charge transport and recombination in polymer/fullerene organic solar cells," *Prog. Photovoltaics*, vol. 15, no. 8, pp. 677–696, 2007.

[203] S. Albrecht, W. Schindler, J. Kurpiers, J. Kniepert, J. C. Blakesley, I. Dumsch, S. Allard, K. Fostiropoulos, U. Scherf, and D. Neher, "On the Field Dependence of Free Charge Carrier Generation and Recombination in Blends of PCPDTBT/PC70BM: Influence of Solvent Additives," *J. Phys. Chem. Lett.*, vol. 3, no. 5, pp. 640–645, 2012.

[204] S. Bange, M. Schubert, and D. Neher, "Charge mobility determination by current extraction under linear increasing voltages: Case of nonequilibrium charges and field-dependent mobilities," *Phys. Rev. B*, vol. 81, no. 3, p. 035209, 2010.

[205] S. A. Hawks, G. Li, Y. Yang, and R. A. Street, "Band tail recombination in polymer:fullerene organic solar cells," *J. Appl. Phys.*, vol. 116, p. 074503, 2014.

[206] D. Di Nuzzo, S. van Reenen, R. A. J. Janssen, M. Kemerink, and S. C. J. Meskers, "Evidence for space-charge-limited conduction in organic photovoltaic cells at open-circuit conditions," *Phys. Rev. B*, vol. 87, p. 85207, 2013.

[207] R. Hanfland, M. A. Fischer, W. Brutting, U. Wurfel, and R. C. I. MacKenzie, "The physical meaning of charge extraction by linearly increasing voltage transients from organic solar cells," *Appl. Phys. Lett.*, vol. 103, no. 6, p. 063904, 2013.

[208] A. J. Morfa, A. M. Nardes, S. E. Shaheen, N. Kopidakis, and J. van de Lagemaat, "Time-of-Flight Studies of Electron-Collection Kinetics in Polymer:Fullerene Bulk-Heterojunction Solar Cells," *Adv. Funct. Mater.*, vol. 21, pp. 2580–2586, 2011.

[209] G. Juška, K. Arlauskas, R. Österbacka, and H. Stubb, "Time-of-flight measurements in thin films of regioregular poly(3-hexyl thiophene)," *Synth. Met.*, vol. 109, pp. 173–176, 2000.

[210] R. A. Street, "Measurements of depletion layers in hydrogenated amorphous silicon," *Phys. Rev. B*, vol. 27, pp. 4924–4932, 1983.

[211] B. J. Tremolet de Villers, R. C. I. MacKenzie, J. J. Jasieniak, N. D. Treat, and M. L. Chabinyc, "Linking Vertical Bulk-Heterojunction Composition and Transient Photocurrent Dynamics in Organic Solar Cells with Solution-Processed MoOx Contact Layers," *Adv. Energy Mater.*, vol. 4, p. 1301290, 2014.

[212] Z. Li, G. Lakhwani, N. C. Greenham, and C. R. McNeill, "Voltage-dependent photocurrent transients of PTB7:PC70BM solar cells: Experiment and numerical simulation," *J. Appl. Phys.*, vol. 114, p. 34502, 2013.

[213] G. Juška, K. Arlauskas, M. Viliunas, and J. Kocka, "Extraction current transients: new method of study of charge transport in microcrystalline silicon," *Phys. Rev. Lett.*, vol. 84, pp. 4946–9, May 2000.

[214] J. Lorrmann, B. H. Badada, O. Inganas, V. Dyakonov, and C. Deibel, "Charge carrier extraction by linearly increasing voltage: Analytic framework and ambipolar transients," *J. Appl. Phys.*, vol. 108, no. 11, p. 113705, 2010.

[215] A. J. Mozer, N. S. Sariciftci, L. Lutsen, D. Vanderzande, R. Osterbacka, M. Westerling, and G. Juska, "Charge transport and recombination in bulk heterojunction solar cells studied by the photoinduced charge extraction in linearly increasing voltage technique," *Appl. Phys. Lett.*, vol. 86, no. 11, p. 112104, 2005.

[216] B. T. D. Villers, C. J. Tassone, S. H. Tolbert, and B. J. Schwartz, "Improving the Reproducibility of P3HT:PCBM Solar Cells by Controlling the PCBM/Cathode Interface," *J. Phys. Chem. C*, vol. 113, pp. 18978–18982, 2009.

[217] G. Juška, N. Nekrašas, K. Genevičius, J. Stuchlik, and J. Kočka, "Relaxation of photoexited charge carrier concentration and mobility in μc-Si:H," *Thin Solid Films*, vol. 451-452, pp. 290–293, 2004.

[218] N. Nekrašas, K. Genevičius, M. Vilinas, and G. Juška, "Features of current transients of photogenerated charge carriers, extracted by linearly increased voltage," *Chem. Phys.*, vol. 404, pp. 56–59, 2012.

[219] W. Shockleyt, "Junctions and P-N Junction Characteristics * D-," vol. 1, 1956.

[220] D. J. Griffiths, *Introduction to Electrodynamics*. Upper Saddle River, N.J.: Pearson, 3 ed., 1999.

[221] K. Kawano, J. Sakai, M. Yahiro, and C. Adachi, "Effect of solvent on fabrication of active layers in organic solar cells based on poly(3-hexylthiophene) and fullerene derivatives," *Sol. Energy Mater. Sol. Cells*, vol. 93, pp. 514–518, 2009.

[222] J. A. Carr and S. Chaudhary, "The identification, characterization and mitigation of defect states in organic photovoltaic devices: a review and outlook," *Energy Environ. Sci.*, vol. 6, no. 12, p. 3414, 2013.

[223] S. Neugebauer, J. Rauh, C. Deibel, and V. Dyakonov, "Investigation of electronic trap states in organic photovoltaic materials by current-based deep level transient spectroscopy," *Appl. Phys. Lett.*, vol. 100, no. 26, p. 263304, 2012.

[224] J. Schafferhans, C. Deibel, and V. Dyakonov, "Electronic Trap States in Methanofullerenes," *Adv. Energy Mater.*, vol. 1, pp. 655–660, 2011.

[225] R. A. Street, S. A. Hawks, P. P. Khlyabich, G. Li, B. J. Schwartz, B. C. Thompson, and Y. Yang, "Electronic Structure and Transition Energies in Polymer-Fullerene Bulk Heterojunctions," *J. Phys. Chem. C*, vol. 118, pp. 21873–21883, 2014.

[226] S. Dongaonkar, J. D. Servaites, G. M. Ford, S. Loser, J. Moore, R. M. Gelfand, H. Mohseni, H. W. Hillhouse, R. Agrawal, M. a. Ratner, T. J. Marks, M. S. Lundstrom, and M. A. Alam, "Universality of non-Ohmic shunt leakage in thin-film solar cells," *J. Appl. Phys.*, vol. 108, no. 12, p. 124509, 2010.

[227] A. Wagenpfahl, C. Deibel, and V. Dyakonov, "Organic Solar Cell Efficiencies Under the Aspect of Reduced Surface Recombination Velocities," *IEEE J. Sel. Top. Quantum Electron.*, vol. 16, no. 6, pp. 1759–1763, 2010.

[228] J. C. Blakesley, F. A. Castro, W. Kylberg, G. F. A. Dibb, C. Arantes, R. Valaski, M. Cremona, J.-S. J. S. Kim, and J.-S. J. S. Kim, "Towards reliable charge-mobility benchmark measurements for organic semiconductors," *Org. Electron.*, vol. 15, pp. 1263–1272, 2014.

[229] W. Regan, S. Byrnes, W. Gannett, O. Ergen, O. Vazquez-Mena, F. Wang, and A. Zettl, "Screening-Engineered Field-Effect Solar Cells," *Nano Lett.*, vol. 12, pp. 4300–4304, 2012.

[230] T. Walter, R. Herberholz, C. Müller, and H. W. Schock, "Determination of defect distributions from admittance measurements and application to Cu (In ,Ga)Se2 based heterojunctions," *J. Appl. Phys.*, vol. 80, no. 8, pp. 4411–4420, 1996.

[231] J. Bisquert, "Chemical capacitance of nanostructured semiconductors: its origin and significance for nanocomposite solar cells," *Phys. Chem. Chem. Phys.*, vol. 5, no. 24, pp. 5360–5364, 2003.

[232] I. Mora-Seró, J. Bisquert, F. Fabregat-Santiago, G. Garcia-Belmonte, G. Zoppi, K. Durose, Y. Proskuryakov, I. Oja, A. Belaidi, T. Dittrich, R. Tena-Zaera, A. Katty, C. Lévy-Clément, V. Barrioz, and S. J. C. Irvine, "Implications of the negative capacitance observed at forward bias in nanocomposite and polycrystalline solar cells.," *Nano Lett.*, vol. 6, pp. 640–650, 2006.

[233] O. J. Sandberg, M. Nyman, and R. Österbacka, "Effect of Contacts in Organic Bulk Heterojunction Solar Cells," *Phys. Rev. Appl.*, vol. 1, p. 024003, 2014.

[234] D. Credgington and Y. Kim, "Analysis of recombination losses in a pentacene/C60 organic bilayer solar cell," *J. Phys. Chem. Lett.*, vol. 2, pp. 2759–2763, 2011.

[235] S. A. Choulis, J. Nelson, Y. Kim, D. Poplavskyy, T. Kreouzis, J. R. Durrant, and D. D. C. Bradley, "Investigation of transport properties in polymer/fullerene blends using time-of-flight photocurrent measurements," *Appl. Phys. Lett.*, vol. 83, no. 18, p. 3812, 2003.

[236] H. Scher and E. W. E. Montroll, "Anomalous transit-time dispersion in amorphous solids," *Phys. Rev. B*, vol. 12, pp. 2455–2477, 1975.

[237] O. J. Sandberg, M. Nyman, and R. Österbacka, "Direct determination of doping concentration and built-in voltage from extraction current transients," *Org. Electron.*, vol. 15, pp. 3413–3420, 2014.

[238] A. Armin, G. Juška, B. W. Philippa, P. L. Burn, P. Meredith, R. D. White, and A. Pivrikas, "Doping-Induced Screening of the Built-in-Field in Organic Solar Cells: Effect on Charge Transport and Recombination," *Adv. Energy Mater.*, vol. 3, pp. 321–327, 2013.

[239] S. W. Kettlitz, J. Mescher, N. S. Christ, M. Nintz, S. Valouch, A. Colsmann, and U. Lemmer, "Eliminating RC-Effects in Transient Photocurrent Measurements on Organic Photodiodes," *IEEE Photon. Tech. Lett.*, vol. 25, no. 7, pp. 682–685, 2013.

[240] B. Y. Finck and B. J. Schwartz, "Understanding the origin of the S-curve in conjugated polymer/fullerene photovoltaics from drift-diffusion simulations," *Appl. Phys. Lett.*, vol. 103, no. 5, p. 053306, 2013.

[241] G. Juška, N. Nekrašas, V. Valentinavičius, P. Meredith, and A. Pivrikas, "Extraction of photogenerated charge carriers by linearly increasing voltage in the case of Langevin recombination," *Phys. Rev. B*, vol. 84, p. 155202, 2011.

[242] C. Deibel and A. Wagenpfahl, "Comment on Interface state recombination in organic solar cells," *Phys. Rev. B*, vol. 82, p. 207301, 2010.

[243] C. Deibel, A. Baumann, A. Wagenpfahl, and V. Dyakonov, "Polaron recombination in pristine and annealed bulk heterojunction solar cells," *Synth. Met.*, vol. 159, no. 21-22, pp. 2345–2347, 2009.

[244] A. Mozer, G. Dennler, N. Sariciftci, M. Westerling, A. Pivrikas, R. Österbacka, and G. Juška, "Time-dependent mobility and recombination of the photoinduced charge carriers in conjugated polymer/fullerene bulk heterojunction solar cells," *Phys. Rev. B*, vol. 72, p. 35217, 2005.

[245] M. T. Neukom, N. A. Reinke, K. A. Brossi, and B. Ruhstaller, "Transient Photocurrent Response of Organic Bulk Heterojunction Solar Cells," *Proc. SPIE - Int. Soc. Opt. Eng.*, vol. 7722, p. 77220V, 2010.

[246] A. Seemann, T. Sauermann, C. Lungenschmied, O. Armbruster, S. Bauer, H.-J. Egelhaaf, and J. Hauch, "Reversible and irreversible degradation of organic solar cell performance by oxygen," *Sol. Energy*, vol. 85, pp. 1238–1249, 2011.

[247] J. You, C.-C. Chen, Z. Hong, K. Yoshimura, K. Ohya, R. Xu, S. Ye, J. Gao, G. Li, and Y. Yang, "10.2% Power Conversion Efficiency Polymer Tandem Solar Cells Consisting of Two Identical Sub-Cells," *Adv. Mater.*, p. DOI: 10.1002/adma.201300964, 2013.

[248] J. You, Z. Hong, Y. M. Yang, Q. Chen, M. Cai, T.-b. Song, C.-c. Chen, S. Lu, Y. Liu, H. Zhou, and Y. M. Yang, "Low-temperature solution-processed perovskite solar cells with high efficiency and flexibility," *ACS Nano*, vol. 8, no. 2, pp. 1674–1680, 2014.

[249] C.-C. Chen, W.-H. Chang, K. Yoshimura, K. Ohya, J. You, J. Gao, Z. Hong, and Y. Yang, "An Efficient Triple-Junction Polymer Solar Cell Having a Power Conversion Efficiency Exceeding 11%," *Adv. Mater.*, vol. 26, pp. 5670–5677, 2014.

[250] B. A. Collins, J. R. Tumbleston, and H. Ade, "Miscibility, Crystallinity, and Phase Development in P3HT/PCBM Solar Cells: Toward an Enlightened Understanding of Device Morphology and Stability," *J. Phys. Chem. Lett.*, vol. 2, no. 24, pp. 3135–3145, 2011.

[251] A. L. Ayzner, C. J. Tassone, S. H. Tolbert, and B. J. Schwartz, "Reappraising the Need for Bulk Heterojunctions in Polymer-Fullerene Photovoltaics: The Role of Carrier Transport in All-Solution-Processed P3HT/PCBM Bilayer Solar Cells," *J. Phys. Chem. C*, vol. 113, pp. 20050–20060, 2009.

[252] D. H. Wang, H. K. Lee, D.-G. Choi, J. H. Park, and O. O. Park, "Solution-processable polymer solar cells from a poly(3-hexylthiophene)/ 6,6 -phenyl C-61-butyric acidmethyl ester concentration graded bilayers," *Appl. Phys. Lett.*, vol. 95, no. 4, 2009.

[253] L. Hui, Z. Zhi-Guo, L. YongFang, W. Jizheng, H. Li, Z.-G. Zhang, Y. Li, and J. Wang, "Tunable open-circuit voltage in ternary organic solar cells," *Appl. Phys. Lett.*, vol. 101, no. 16, pp. 163302 (5 pp.)–163302 (5 pp.), 2012.

[254] D. H. Kim, J. Mei, A. L. Ayzner, K. Schmidt, G. Giri, A. L. Appleton, M. F. Toney, and Z. Bao, "Sequentially solution-processed, nanostructured polymer photovoltaics using selective solvents," *Energy Environ. Sci.*, 2014.

[255] K. H. Lee, Y. Zhang, P. L. Burn, I. R. Gentle, M. James, A. Nelson, and P. Meredith, "Correlation of diffusion and performance in sequentially processed P3HT/PCBM heterojunction films by time-resolved neutron reflectometry," *J. Mater. Chem. C*, vol. 1, no. 14, pp. 2593–2598, 2013.

[256] K. H. Lee, P. E. Schwenn, A. R. G. Smith, H. Cavaye, P. E. Shaw, M. James, K. B. Krueger, I. R. Gentle, P. Meredith, and P. L. Burn, "Morphology of All-Solution-Processed "Bilayer" Organic Solar Cells," *Adv. Mater.*, vol. 23, pp. 766–770, 2011.

[257] C. W. Rochester, S. A. Mauger, and A. J. Moule, "Investigating the Morphology of Polymer/Fullerene Layers Coated Using Orthogonal Solvents," *J. Phys. Chem. C*, vol. 116, no. 13, pp. 7287–7292, 2012.

[258] A. M. Nardes, A. L. Ayzner, S. R. Hammond, A. J. Ferguson, B. J. Schwartz, and N. Kopidakis, "Photoinduced Charge Carrier Generation and Decay in Sequentially Deposited Polymer/Fullerene Layers: Bulk Heterojunction vs Planar Interface," *J. Phys. Chem. C*, vol. 116, no. 13, pp. 7293–7305, 2012.

[259] T. Chen, M. Aljada, P. E. Shaw, K. H. Lee, H. Cavaye, M. N. Balfour, R. J. Borthwick, M. James, P. L. Burn, I. R. Gentle, P. Meredith, and C. Tao, "Controlling Hierarchy in Solution-processed Polymer Solar Cells Based on Crosslinked P3HT," *Adv. Energy Mater.*, vol. 3, pp. 105–112, 2013.

[260] B. A. Collins, E. Gann, L. Guignard, X. He, C. R. McNeill, and H. Ade, "Molecular Miscibility of Polymer-Fullerene Blends," *J. Phys. Chem. Lett.*, vol. 1, no. 21, pp. 3160–3166, 2010.

[261] A. Gadisa, J. R. Tumbleston, D.-H. Ko, M. Aryal, R. Lopez, and E. T. Samulski, "The role of solvent and morphology on miscibility of methanofullerene and poly(3-hexylthiophene)," *Thin Solid Films*, vol. 520, no. 16, pp. 5466–5471, 2012.

[262] A. Loiudice, A. Rizzo, G. Latini, C. Nobile, M. de Giorgi, and G. Gigli, "Graded vertical phase separation of donor/acceptor species for polymer solar cells," *Sol. Energy Mater. Sol. Cells*, vol. 100, pp. 147–152, May 2012.

[263] N. D. Treat, M. A. Brady, G. Smith, M. F. Toney, E. J. Kramer, C. J. Hawker, and M. L. Chabinyc, "Interdiffusion of PCBM and P3HT Reveals Miscibility in a Photovoltaically Active Blend," *Adv. Energy Mater.*, vol. 1, no. 1, pp. 82–89, 2011.

[264] V. Vohra, K. Higashimine, T. Murakami, and H. Murata, "Addition of regiorandom poly(3-hexylthiophene) to solution processed poly(3-hexylthiophene): 6,6 -phenyl-C61-butyric acid methyl ester graded bilayers to tune the vertical concentration gradient," *Appl. Phys. Lett.*, vol. 101, no. 17, pp. 1–4, 2012.

[265] V. Vohra, G. Arrighetti, L. Barba, K. Higashimine, W. Porzio, and H. Murata, "Enhanced Vertical Concentration Gradient in Rubbed P3HT:PCBM Graded Bilayer Solar Cells," *J. Phys. Chem. Lett.*, vol. 3, pp. 1820–1823, 2012.

[266] V. Vohra, K. Higashimine, S. Tsuzaki, K. Ohdaira, and H. Murata, "Formation of vertical concentration gradients in poly(3-hexylthiophene-2,5-diyl): Phenyl-C61-butyric acid methyl ester-graded bilayer solar cells," *Thin Solid Films*, vol. 554, pp. 41–45, 2014.

[267] D. H. Wang, J. S. Moon, J. Seifter, J. Jo, J. H. Park, O. O. Park, and A. J. Heeger, "Sequential processing: control of nanomorphology in bulk heterojunction solar cells.," *Nano Lett.*, vol. 11, pp. 3163–3168, 2011.

[268] B. Liu, R.-Q. Png, L.-H. Zhao, L.-L. Chua, R. H. Friend, and P. K. H. Ho, "High internal quantum efficiency in fullerene solar cells based on crosslinked polymer donor networks," *Nat. Commun.*, vol. 3, p. 1321, 2012.

[269] H. J. Park, J. Y. Lee, T. Lee, and L. J. Guo, "Advanced Heterojunction Structure of Polymer Photovoltaic Cell Generating High Photocurrent with Internal Quantum Efficiency Approaching 100%," *Adv. Energy Mater.*, vol. 3, p. DOI: 10.1002/aenm.201300245, 2013.

[270] H. Y. Yang, N. S. Kang, J.-M. Hong, Y.-W. Song, T. W. Kim, and J. A. Lim, "Efficient bilayer heterojunction polymer solar cells with bumpy donor-acceptor interface formed by facile polymer blend," *Org. Electron.*, vol. 13, pp. 2688–2695, 2012.

[271] R. Zhu, A. Kumar, and Y. Yang, "Polarizing Organic Photovoltaics," *Adv. Mater.*, vol. 23, pp. 4193–4198, 2011.

[272] A. Loiudice, A. Rizzo, M. Biasiucci, and G. Gigli, "Bulk Heterojunction versus Diffused Bilayer: The Role of Device Geometry in Solution p-Doped Polymer-Based Solar Cells," *J. Phys. Chem. Lett.*, vol. 3, no. 14, pp. 1908–1915, 2012.

[273] T. Kim, S. J. Yang, S. K. Kim, H. S. Choi, and C. R. Park, "Preparation of PCDTBT nanofibers with a diameter of 20 nm and their application to air-processed organic solar cells.," *Nanoscale*, vol. 6, pp. 2847–2854, 2014.

[274] J. Y. Oh, T. I. Lee, W. S. Jang, S. S. Chae, J. H. Park, H. W. Lee, J.-M. Myoung, and H. K. Baik, "Mass production of a 3D non-woven nanofabric with crystalline P3HT nanofibrils for organic solar cells," *Energy Environ. Sci.*, vol. 6, no. 3, p. 910, 2013.

[275] P. Cheng, J. Hou, Y. Li, and X. Zhan, "Layer-by-Layer Solution-Processed Low-Bandgap Polymer-PC61BM Solar Cells with High Efficiency," *Adv. Energy Mater.*, vol. 4, p. 1301349, 2014.

[276] B. Yang, Y. Yuan, and J. Huang, "Reduced Bimolecular Charge Recombination Loss in Thermally Annealed Bilayer Heterojunction Photovoltaic Devices with Large External Quantum Efficiency and Fill Factor," *J. Phys. Chem. C*, vol. 118, no. 10, pp. 5196–5202, 2014.

[277] A. L. Ayzner, S. C. Doan, B. Tremolet de Villers, B. J. Schwartz, and B. T. de Villers, "Ultrafast Studies of Exciton Migration and Polaron Formation in Sequentially Solution-Processed Conjugated Polymer/Fullerene Quasi-Bilayer Photovoltaics," *J. Phys. Chem. Lett.*, vol. 3, pp. 2281–2287, 2012.

[278] D. H. Wang, J. K. Kim, O. O. Park, and J. H. Park, "Analysis of surface morphological changes in organic photovoltaic devices: bilayer versus bulk-heterojunction," *Energy Environ. Sci.*, vol. 4, no. 4, pp. 1434–1439, 2011.

[279] J. S. Moon, C. J. Takacs, Y. Sun, and A. J. Heeger, "Spontaneous Formation of Bulk Heterojunction Nanostructures: Multiple Routes to Equivalent Morphologies," *Nano Lett.*, vol. 11, pp. 1036–1039, 2011.

[280] C. Müller, T. A. M. Ferenczi, M. Campoy-Quiles, J. M. Frost, D. D. C. Bradley, P. Smith, N. Stingelin-stutzmann, and J. Nelson, "Binary Organic Photovoltaic Blends: A Simple Rationale for Optimum Compositions," *Adv. Mater.*, vol. 20, no. 18, pp. 3510–3515, 2008.

[281] J. Clark, C. Silva, R. Friend, and F. Spano, "Role of Intermolecular Coupling in the Photophysics of Disordered Organic Semiconductors: Aggregate Emission in Regioregular Polythiophene," *Phys. Rev. Lett.*, vol. 98, p. 206406, May 2007.

[282] Y. Lin, L. Ma, Y. Li, Y. Liu, D. Zhu, and X. Zhan, "Small-Molecule Solar Cells with Fill Factors up to 0.75 via a Layer-by-Layer Solution Process," *Adv. Energy Mater.*, vol. 4, 2014.

[283] A. J. Moule and K. Meerholz, "Interference method for the determination of the complex refractive index of thin polymer layers," *Appl. Phys. Lett.*, vol. 91, no. 6, p. 61901, 2007.

[284] X. N. Yang, J. Loos, S. C. Veenstra, W. J. H. Verhees, M. M. Wienk, J. M. Kroon, M. A. J. Michels, and R. A. J. Janssen, "Nanoscale morphology of high-performance polymer solar cells," *Nano Lett.*, vol. 5, no. 4, pp. 579–583, 2005.

[285] A. a. Herzing, L. J. Richter, and I. M. Anderson, "3D Nanoscale Characterization of Thin-Film Organic Photovoltaic Device Structures via Spectroscopic Contrast in the TEM 1," *J. Phys. Chem. C*, vol. 114, pp. 17501–17508, 2010.

[286] L. F. Drummy, R. J. Davis, D. L. Moore, M. Durstock, R. A. Vaia, and J. W. P. Hsu, "Molecular-Scale and Nanoscale Morphology of P3HT:PCBM Bulk Heterojunctions: Energy-Filtered TEM and Low-Dose HREM," *Chem. Mater.*, vol. 23, no. 3, pp. 907–912, 2011.

[287] M. Pfannmöller, H. Flügge, G. Benner, I. Wacker, C. Sommer, M. Hanselmann, S. Schmale, H. Schmidt, F. A. Hamprecht, T. Rabe, W. Kowalsky, and R. R. Schröder, "Visualizing a Homogeneous Blend in Bulk Heterojunction Polymer Solar Cells by Analytical Electron Microscopy," *Nano Lett.*, vol. 11, no. 8, pp. 3099–3107, 2011.

[288] A. A. Herzing, H. W. Ro, C. L. Soles, and D. M. DeLongchamp, "Visualization of Phase Evolution in Model Organic Photovoltaic Structures via Energy-Filtered Transmission Electron Microscopy," *ACS Nano*, vol. 7, no. 9, pp. 7937–7944, 2013.

[289] V. S. Gevaerts, L. J. A. Koster, M. M. Wienk, and R. A. J. Janssen, "Discriminating between Bilayer and Bulk Heterojunction Polymer: Fullerene Solar Cells Using the External Quantum Efficiency," *ACS Appl. Mater. Interfaces*, vol. 3, no. 9, pp. 3252–3255, 2011.

[290] Y. V. Y. Vaynzof, D. Kabra, L. H. Zhao, L. L. Chua, U. Steiner, and R. H. Friend, "Surface-Directed Spinodal Decomposition in Poly 3-hexylthiophene and C(61)-Butyric Acid Methyl Ester Blends," *ACS Nano*, vol. 5, no. 1, pp. 329–336, 2011.

[291] M. Campoy-Quiles, T. Ferenczi, T. Agostinelli, P. G. Etchegoin, Y. Kim, T. D. Anthopoulos, P. N. Stavrinou, D. D. C. Bradley, and J. Nelson, "Morphology evolution via self-organization and lateral and vertical diffusion in polymer: fullerene solar cell blends," *Nat. Mater.*, vol. 7, no. 2, pp. 158–164, 2008.

[292] C. P. Chen, T. C. Tien, B. T. Ko, Y. D. Chen, and C. Ting, "Energy Level Alignment at the Anode of Poly(3-hexylthiophene)/Fullerene-Based Solar Cells," *ACS Appl. Mater. Interfaces*, vol. 1, no. 4, pp. 741–745, 2009.

[293] E. L. Ratcliff, A. Garcia, S. a. Paniagua, S. R. Cowan, A. J. Giordano, D. S. Ginley, S. R. Marder, J. J. Berry, and D. C. Olson, "Investigating the Influence of Interfacial Contact Properties on Open Circuit Voltages in Organic Photovoltaic Performance: Work Function Versus Selectivity," *Adv. Energy Mater.*, vol. 3, pp. 647–656, May 2013.

[294] A. Orimo, K. Masuda, S. Honda, H. Benten, S. Ito, H. Ohkita, and H. Tsuji, "Surface segregation at the aluminum interface of poly(3-hexylthiophene)/fullerene solar cells," *Appl. Phys. Lett.*, vol. 96, no. 4, p. 43305, 2010.

[295] T. Kirchartz, "Influence of diffusion on space-charge-limited current measurements in organic semiconductors.," *Beilstein J. Nanotechnol.*, vol. 4, pp. 180–8, 2013.

[296] S. A. Mauger, L. Chang, S. Friedrich, C. W. Rochester, D. M. Huang, P. Wang, and A. J. Moulé, "Self-Assembly of Selective Interfaces in Organic Photovoltaics," *Adv. Funct. Mater.*, vol. 23, pp. 1935–1946, 2013.

[297] A. J. Parnell, A. D. F. Dunbar, A. J. Pearson, P. A. Staniec, A. J. C. Dennison, H. Hamamatsu, M. W. A. Skoda, D. G. Lidzey, and R. A. L. Jones, "Depletion of PCBM at the Cathode Interface in P3HT/PCBM Thin Films as Quantified via Neutron Reflectivity Measurements," *Adv. Mater.*, vol. 22, pp. 2444–2447, 2010.

[298] A. J. Heeger, "25th anniversary article: Bulk heterojunction solar cells: understanding the mechanism of operation," *Adv. Mater.*, vol. 26, pp. 10–27, 2014.

[299] R. A. Street, "Reply to Comment on Interface state recombination in organic solar cells ," *Phys. Rev. B*, vol. 82, p. 207302, 2010.

[300] C. G. Shuttle, "Recombination dynamics in polythiophene : fullerene solar cells," no. , 2008.

[301] N. E. Jackson, B. M. Savoie, T. J. Marks, L. X. Chen, and M. a. Ratner, "The Next Breakthrough for Organic Photovoltaics?," *J. Phys. Chem. Lett.*, vol. 6, pp. 77–84, 2015.

[302] M. Grätzel, "The light and shade of perovskite solar cells," *Nat. Mater.*, vol. 13, no. 9, pp. 838–842, 2014.

[303] T.-b. Song, Q. Chen, H.-P. Zhou, C. Jiang, H.-H. Wang, Y. Yang, Y. Liu, J. You, and Y. Yang, "Perovskite solar cells: film formation and properties," *J. Mater. Chem. A*, vol. 3, pp. 9032–9050, 2015.

[304] H.-S. Kim, S. H. Im, and N.-G. Park, "Organolead Halide Perovskite: New Horizons in Solar Cell Research," *J. Phys. Chem. C*, vol. 118, pp. 5615–5625, 2014.

[305] G. Garcia-Belmonte, P. P. Boix, J. Bisquert, M. Sessolo, and H. J. Bolink, "Simultaneous determination of carrier lifetime and electron density-of-states in P3HT:PCBM organic solar cells under illumination by impedance spectroscopy," *Sol. Energy Mater. Sol. Cells*, vol. 94, no. 2, pp. 366–375, 2010.

[306] K. Vandewal, S. Albrecht, E. T. Hoke, K. R. Graham, J. Widmer, J. D. Douglas, M. Schubert, W. R. Mateker, J. T. Bloking, G. F. Burkhard, A. Sellinger, J. M. J. Fréchet, A. Amassian, M. K. Riede, M. D. McGehee, D. Neher, and A. Salleo, "Efficient charge generation by relaxed charge-transfer states at organic interfaces.," *Nat. Mater.*, vol. 13, pp. 63–8, 2014.

[307] N. J. Jeon, J. H. Noh, W. S. Yang, Y. C. Kim, S. Ryu, J. Seo, and S. I. Seok, "Compositional engineering of perovskite materials for high-performance solar cells," *Nature*, vol. 517, no. 7535, pp. 476–480, 2015.

[308] H. Zhou, Q. Chen, G. Li, S. Luo, T.-b. Song, H.-S. Duan, Z. Hong, J. You, Y. Liu, and Y. Yang, "Interface engineering of highly efficient perovskite solar cells," *Science (80-.).*, vol. 345, no. 6196, pp. 542–546, 2014.

[309] Z. A. Page, Y. Liu, V. V. Duzhko, T. P. Russell, and T. Emrick, "Fulleropyrrolidine interlayers: Tailoring electrodes to raise organic solar cell efficiency," *Sci. (80-.).*, vol. 346, pp. 441–444, 2014.

[310] Z. Xu, L. M. Chen, G. W. Yang, C. H. Huang, J. H. Hou, Y. Wu, G. Li, C. S. Hsu, and Y. Yang, "Vertical Phase Separation in Poly(3-hexylthiophene): Fullerene Derivative Blends and its Advantage for Inverted Structure Solar Cells," *Adv. Funct. Mater.*, vol. 19, no. 8, pp. 1227–1234, 2009.

[311] A. Kumar, G. Li, Z. Hong, and Y. Yang, "High efficiency polymer solar cells with vertically modulated nanoscale morphology.," *Nanotechnology*, vol. 20, p. 165202, 2009.

[312] Z. Yu and L. Sun, "Recent Progress on Hole-Transporting Materials for Emerging Organometal Halide Perovskite Solar Cells," *Adv. Energy Mater.*, 2015.

[313] G.-J. A. H. Wetzelaer, M. Scheepers, A. M. Sempere, C. Momblona, J. Ávila, and H. J. Bolink, "Trap-Assisted Non-Radiative Recombination in Organic-Inorganic Perovskite Solar Cells," *Adv. Mater.*, vol. 27, no. 11, pp. 1837–1841, 2015.

[314] Y. Zhang, M. Liu, G. E. Eperon, T. C. Leijtens, D. McMeekin, M. Saliba, W. Zhang, M. de Bastiani, A. Petrozza, L. M. Herz, M. B. Johnston, H. Lin, and H. J. Snaith, "Charge selective contacts, mobile ions and anomalous hysteresis in organic-inorganic perovskite solar cells," *Mater. Horizons*, vol. 2, pp. 315–322, 2015.

[315] A. Barrows, A. Pearson, C. Kwak, A. Dunbar, A. Buckley, and D. Lidzey, "Efficient planar heterojunction mixed-halide perovskite solar cells deposited via spray-deposition," *Energy Environ. Sci.*, vol. 7, pp. 1–7, 2014.

[316] K. X. Steirer, P. F. Ndione, N. E. Widjonarko, M. T. Lloyd, J. Meyer, E. L. Ratcliff, A. Kahn, N. R. Armstrong, C. J. Curtis, D. S. Ginley, J. J. Berry, and D. C. Olson, "Enhanced Efficiency in Plastic Solar Cells via Energy Matched Solution Processed NiOx Interlayers," *Adv. Energy Mater.*, vol. 1, pp. 813–820, 2011.

[317] A. F. Tillack, K. M. Noone, B. A. Macleod, D. Nordlund, K. P. Nagle, A. Bradley, S. K. Hau, H.-l. Yip, A. K. Jen, G. T. Seidler, and D. S. Ginger, "Surface Characterization of Polythiophene : Fullerene Blends on Different Electrodes Using Near Edge X-ray Absorption Fine Structure," *ACS Appl. Mater. Interfaces*, vol. 3, pp. 726–732, 2011.

[318] N. R. Armstrong, C. Carter, C. Donley, A. Simmonds, P. Lee, M. Brumbach, B. Kippelen, B. Domercq, and S. Y. Yoo, "Interface modification of ITO thin films: organic photovoltaic cells," *Thin Solid Films*, vol. 445, no. 2, pp. 342–352, 2003.

[319] M. T. Greiner, M. G. Helander, W.-M. Tang, Z.-B. Wang, J. Qiu, and Z.-h. Lu, "Universal energy-level alignment of molecules on metal oxides.," *Nat. Mater.*, vol. 11, pp. 76–81, 2012.

[320] J. H. J. Heo, S. S. H. Im, J. H. J. Noh, T. N. T. Mandal, C.-S. Lim, J. A. Chang, Y. H. Lee, H.-j. Kim, A. Sarkar, N. K., M. Gratzel, and S. I. Seok, "Efficient inorganic-organic hybrid heterojunction solar cells containing perovskite compound and polymeric hole conductors," *Nat. Photonics*, vol. 7, pp. 486–491, 2013.

[321] J. H. Heo, D. H. Song, H. J. Han, S. Y. Kim, J. H. Kim, D. Kim, H. W. Shin, T. K. Ahn, C. Wolf, T.-W. Lee, and S. H. Im, "Planar CH3NH3PbI3 Perovskite Solar Cells with Constant 17.2% Average Power Conversion Efficiency Irrespective of the Scan Rate," *Adv. Mater.*, pp. n/a—-n/a, 2015.

[322] D. Chen, A. Nakahara, D. Wei, D. Nordlund, and T. P. Russell, "P3HT/PCBM bulk heterojunction organic photovoltaics: correlating efficiency and morphology.," *Nano Lett.*, vol. 11, pp. 561–7, 2011.

[323] J. Seok, T. J. Shin, S. Park, C. Cho, J.-Y. Lee, D. Yeol Ryu, M. H. Kim, and K. Kim, "Efficient Organic Photovoltaics Utilizing Nanoscale Heterojunctions in Sequentially Deposited Polymer/fullerene Bilayer," *Sci. Rep.*, vol. 5, no. Dcm, p. 8373, 2015.

[324] J. D. Roehling, C. W. Rochester, H. W. Ro, P. Wang, J. Majewski, K. J. Batenburg, I. Arslan, D. M. Delongchamp, and A. J. Moulé, "Material profile influences in bulk-heterojunctions," *J. Polym. Sci. Part B Polym. Phys.*, pp. 1291–1300, 2014.

[325] O. Wodo, J. D. Roehling, A. J. Moulé, and B. Ganapathysubramanian, "Quantifying organic solar cell morphology: a computational study of three-dimensional maps," *Energy Environ. Sci.*, vol. 6, no. 10, p. 3060, 2013.

[326] W.-H. Tseng, H. Lo, J.-K. Chang, I.-H. Liu, M.-H. Chen, and C.-I. Wu, "Metal-induced molecular diffusion in [6,6]-phenyl-C61-butyric acid methyl ester poly(3-hexylthiophene) based bulk-heterojunction solar cells," *Appl. Phys. Lett.*, vol. 103, no. 18, p. 183506, 2013.

[327] G. K. Wertheim and D. N. E. Buchanan, "Reaction of C60 with Metals: W," *Solid State Commun.*, vol. 88, no. 2, pp. 97–100, 1993.

[328] M. Chikamatsu, T. Taima, Y. Yoshida, K. Saito, and K. Yase, "Mg-doped C60 thin film as improved n-type organic semiconductor for a solar cell," *Appl. Phys. Lett.*, vol. 84, no. 1, pp. 127–129, 2004.

[329] H. Wang, J. G. Hou, O. Takeuchi, Y. Fujisuku, and A. Kawazu, "STM observations of Ag-induced reconstruction of C60 thin films," *Phys. Rev. B*, vol. 61, no. 3, pp. 2199–2203, 2000.

[330] A. Devenyi, R. Manaila, and A. Belu-Marian, "Nanocrystalline gold in Au-doped thin C60 films," *Thin Solid Films*, vol. 335, pp. 258–265, 1998.

[331] D. L. Matz, E. L. Ratcliff, J. Meyer, A. Kahn, and J. E. Pemberton, "Deciphering the metal-C60 interface in optoelectronic devices: evidence for C60 reduction by vapor deposited Al.," *ACS Appl. Mater. Interfaces*, vol. 5, pp. 6001–8, 2013.

[332] M. K. Shukla, M. Dubey, and J. Leszczynski, "Theoretical Investigation of Electronic Structures and Properties of C60Gold Nanocontacts," *ACS Nano*, vol. 2, no. 2, pp. 227–234, 2008.

[333] D. Tondelier, K. Lmimouni, D. Vuillaume, C. Fery, and G. Haas, "Metal/organic/metal bistable memory devices," *Appl. Phys. Lett.*, vol. 85, no. 23, pp. 5763–5765, 2004.

[334] G. Kaune, M. a. Ruderer, E. Metwalli, W. Wang, S. Couet, K. Schlage, R. Röhlsberger, S. V. Roth, and P. Müller-Buschbaum, "In situ GISAXS study of gold film growth on conducting polymer films.," *ACS Appl. Mater. Interfaces*, vol. 1, no. 2, pp. 353–360, 2009.

[335] M. Scharnberg, R. Adelung, and F. Faupel, "Influence of top layer geometries on the electronic properties of pentacene and diindenoperylene thin films," *Phys. Status Solidi Appl. Mater. Sci.*, vol. 205, no. 3, pp. 578–590, 2008.

[336] M. Scharnberg, J. Hu, J. Kanzow, K. Rätzke, R. Adelung, F. Faupel, C. Pannemann, U. Hilleringmann, S. Meyer, and J. Pflaum, "Radiotracer measurements as a sensitive tool for the detection of metal penetration in molecular-based organic electronics," *Appl. Phys. Lett.*, vol. 86, no. 2, 2005.

[337] X. H. Zhang, B. Domercq, and B. Kippelen, "Effect of Au deposition rate on the performance of top-contact pentacene organic field-effect transistors," *Synth. Met.*, vol. 159, no. 21-22, pp. 2371–2374, 2009.

[338] S. Fladischer, A. Neuhold, E. Kraker, T. Haber, B. Lamprecht, I. Salzmann, R. Resel, and W. Grogger, "Diffusion of Ag into organic semiconducting materials: A combined analytical study using transmission electron microscopy and X-ray reflectivity," *ACS Appl. Mater. Interfaces*, vol. 4, no. 10, pp. 5608–5612, 2012.

[339] S. Yu, G. Santoro, K. Sarkar, B. Dicke, P. Wessels, S. Bommel, R. Döhrmann, J. Perlich, M. Kuhlmann, E. Metwalli, J. F. H. Risch, M. Schwartzkopf, M. Drescher, P. Müller-Buschbaum, and S. V. Roth, "Formation of Al nanostructures on Alq3: An in situ grazing incidence small angle X-ray scattering study during radio frequency sputter deposition," *J. Phys. Chem. Lett.*, vol. 4, no. 18, pp. 3170–3175, 2013.

[340] A. C. Dürr, F. Schreiber, M. Kelsch, H. D. Carstanjen, and H. Dosch, "Morphology and Thermal Stability of Metal Contacts on Crystalline Organic Thin Films," *Adv. Mater.*, vol. 14, no. 13-14, pp. 961–963, 2002.

[341] a. C. Dürr, F. Schreiber, M. Kelsch, H. D. Carstanjen, H. Dosch, and O. H. Seeck, "Morphology and interdiffusion behavior of evaporated metal films on crystalline diindenoperylene thin films," *J. Appl. Phys.*, vol. 93, no. 9, pp. 5201–5209, 2003.

[342] M. Schwartzkopf, G. Santoro, C. J. Brett, A. Rothkirch, O. Polonskyi, A. Hinz, E. Metwalli, Y. Yao, T. Strunskus, F. Faupel, P. Müller-Buschbaum, and S. V. Roth, "Real-Time Monitoring of Morphology and Optical Properties during Sputter Deposition for Tailoring MetalPolymer Interfaces," *ACS Appl. Mater. Interfaces*, p. 150611090728005, 2015.

[343] R. C. Haddon, "Electronic structure, conductivity and superconductivity of alkali metal doped (C60)," *Acc. Chem. Res.*, vol. 25, no. 3, pp. 127–133, 1992.

[344] G. Zhang, R. C. Huber, A. S. Ferreira, S. D. Boyd, C. K. Luscombe, S. H. Tolbert, and B. J. Schwartz, "Crystallinity Effects in Sequentially Processed and Blend-Cast Bulk-Heterojunction Polymer/Fullerene Photovoltaics," *J. Phys. Chem. C*, vol. 118, no. 32, pp. 18424–18435, 2014.

[345] Y. Tomita and T. Nakayama, "Theory of Metal-Atom Diffusion in Organic Systems," in *Electron. Process. Org. Electron.* (H. Ishii, K. Kudo, T. Nakayama, and N. Ueno, eds.), vol. 209 of *Springer Series in Materials Science*, ch. 14, pp. 303–317, Tokyo: Springer Japan, 2015.

[346] Y. Tomita and T. Nakayama, "Metal-Atom Diffusion in Organic Solids: First-Principles Study of Graphene and Polyacetylene Systems," *Appl. Phys. Express*, vol. 3, p. 91601, 2010.

[347] M. O. Reese, M. S. White, G. Rumbles, D. S. Ginley, and S. E. Shaheen, "Optimal negative electrodes for poly(3-hexylthiophene): 6,6 -phenyl C61-butyric acid methyl ester bulk heterojunction photovoltaic devices," *Appl. Phys. Lett.*, vol. 92, no. 5, p. 053307, 2008.

[348] A. Abrusci, S. D. Stranks, P. Docampo, H.-L. Yip, A. K.-Y. Jen, and H. J. Snaith, "High-performance perovskite-polymer hybrid solar cells via electronic coupling with fullerene monolayers," *Nano Lett.*, vol. 13, pp. 3124–3128, 2013.

[349] B. Bohnenbuck, E. von Hauff, J. Parisi, C. Deibel, and V. Dyakonov, "Current-limiting mechanisms in polymer diodes," *J. Appl. Phys.*, vol. 99, no. 2, p. 24506, 2006.

[350] Y. Shao, Z. Xiao, C. Bi, Y. Yuan, and J. Huang, "Origin and elimination of photocurrent hysteresis by fullerene passivation in CH3NH3PbI3 planar heterojunction solar cells," *Nat. Commun.*, vol. 5, p. 5784, 2014.

[351] Z. Xiao, Q. Dong, C. Bi, Y. Shao, Y. Yuan, and J. Huang, "Solvent Annealing of Perovskite-Induced Crystal Growth for Photovoltaic-Device Efficiency Enhancement," *Adv. Mater.*, vol. 26, pp. 6503–6509, 2014.

[352] J.-Y. Jeng, Y.-F. Chiang, M.-H. Lee, S.-R. Peng, T.-F. Guo, P. Chen, and T.-C. Wen, "CH3NH3PbI3 perovskite/fullerene planar-heterojunction hybrid solar cells.," *Adv. Mater.*, vol. 25, pp. 3727–3732, 2013.

[353] D. Chirvase, Z. Chiguvare, M. Knipper, J. Parisi, V. Dyakonov, and J. C. Hummelen, "Temperature dependent characteristics of poly(3 hexylthiophene)-fullerene based heterojunction organic solar cells," *J. Appl. Phys.*, vol. 93, no. 6, pp. 3376–3383, 2003.

[354] J. Wagner, M. Gruber, A. Wilke, Y. Tanaka, K. Topczak, A. Steindamm, U. Hörmann, A. Opitz, Y. Nakayama, H. Ishii, J. Pflaum, N. Koch, and W. Brütting, "Identification of different origins for s-shaped current voltage characteristics in planar heterojunction organic solar cells," *J. Appl. Phys.*, vol. 111, no. 5, pp. 0–12, 2012.

[355] a. Steindamm, M. Brendel, a. K. Topczak, and J. Pflaum, "Thickness dependent effects of an intermediate molecular blocking layer on the optoelectronic characteristics of organic bilayer photovoltaic cells," *Appl. Phys. Lett.*, vol. 101, no. 14, pp. 0–4, 2012.

[356] A. L. Ayzner, D. D. Wanger, C. J. Tassone, S. H. Tolbert, and B. J. Schwartz, "Room to Improve Conjugated Polymer-Based Solar Cells: Understanding How Thermal Annealing Affects the Fullerene Component of a Bulk Heterojunction Photovoltaic Device," *J. Phys. Chem. C*, vol. 112, pp. 18711–18716, 2008.

[357] G. Juška, K. Arlauskas, and M. Vilinas, "Charge transport in π-conjugated polymers from extraction current transients," *Phys. Rev. B*, vol. 62, no. 24, pp. 235–238, 2000.

[358] S. A. Hawks, B. Y. Finck, and B. J. Schwartz, "Theory of Current Transients in Planar Semiconductor Devices: Insights and Applications to Organic Solar Cells," *Phys. Rev. Appl.*, vol. 3, p. 44014, 2015.

[359] J. C. Aguirre, S. A. Hawks, A. S. Ferreira, P. Yee, S. Subramaniyan, S. A. Jenekhe, S. H. Tolbert, and B. J. Schwartz, "Sequential Processing for Organic Photovoltaics: Design Rules for Morphology Control by Tailored Semi-Orthogonal Solvent Blends," *Adv. Energy Mater.*, p. 1402020, 2015.

[360] J. J. van Franeker, S. Kouijzer, X. Lou, M. Turbiez, M. M. Wienk, and R. A. J. Janssen, "Depositing Fullerenes in Swollen Polymer Layers via Sequential Processing of Organic Solar Cells," *Adv. Energy Mater.*, p. 1500464, 2015.

[361] T. Liu and A. Troisi, "Absolute Rate of Charge Separation and Recombination in a Molecular Model of the P3HT/PCBM Interface," *J. Phys. Chem. C*, vol. 115, no. 5, pp. 2406–2415, 2010.

[362] J. Taylor, *Introduction to error analysis, the study of uncertainties in physical measurements*, vol. 1. University Science Books, 2 ed., 1997.

[363] G. Zhao, Y. He, and Y. Li, "6.5% Efficiency of polymer solar cells based on poly(3-hexylthiophene) and indene-C(60) bisadduct by device optimization.," *Adv. Mater.*, vol. 22, pp. 4355–4358, 2010.

[364] M. a. Faist, P. E. Keivanidis, S. Foster, P. H. Wöbkenberg, T. D. Anthopoulos, D. D. C. Bradley, J. R. Durrant, J. Nelson, and P. H. Wobkenberg, "Effect of multiple adduct fullerenes on charge generation and transport in photovoltaic blends with poly(3-hexylthiophene-2,5-diyl)," *J. Polym. Sci. Part B Polym. Phys.*, vol. 49, pp. 45–51, 2011.

[365] Y. He, H.-Y. Chen, J. Hou, and Y. Li, "IndeneC60 Bisadduct: A New Acceptor for High-Performance Polymer Solar Cells," *J. Am. Chem. Soc.*, vol. 132, pp. 1377–1382, 2010.

[366] D. W. Steuerman, a. Garcia, M. Dante, R. Yang, J. P. Löfvander, and T.-Q. Nguyen, "Imaging the Interfaces of Conjugated Polymer Optoelectronic Devices," *Adv. Mater.*, vol. 20, pp. 528–534, 2008.

[367] M. Dante, J. Peet, and T. Q. Nguyen, "Nanoscale charge transport and internal structure of bulk heterojunction conjugated polymer/fullerene solar cells by scanning probe microscopy," *J. Phys. Chem. C*, vol. 112, pp. 7241–7249, 2008.

[368] J. S. Moon, J. K. Lee, S. N. Cho, J. Y. Byun, and A. J. Heeger, ""Columnlike" Structure of the Cross-Sectional Morphology of Bulk Heterojunction Materials," *Nano Lett.*, vol. 9, no. 1, pp. 230–234, 2009.

[369] C. J. Takacs, N. D. Treat, S. Krämer, Z. Chen, A. Facchetti, M. L. Chabinyc, and A. J. Heeger, "Remarkable order of a high-performance polymer," *Nano Lett.*, vol. 13, no. 6, pp. 2522–2527, 2013.

[370] Y. Sun, G. C. Welch, W. L. Leong, C. J. Takacs, G. C. Bazan, and A. J. Heeger, "Solution-processed small-molecule solar cells with 6.7% efficiency," *Nat. Mater.*, vol. 6, pp. 44–48, 2011.

[371] R. F. Egerton, P. Li, and M. Malac, "Radiation damage in the TEM and SEM," *Micron*, vol. 35, no. 6, pp. 399–409, 2004.

[372] F. Machui, S. Rathgeber, N. Li, T. Ameri, and C. J. Brabec, "Influence of a ternary donor material on the morphology of a P3HT:PCBM blend for organic photovoltaic devices," *J. Mater. Chem.*, vol. 22, no. 1, p. 15570, 2012.

[373] J. Zhu, F. Bebensee, W. Hieringer, W. Zhao, J. H. Baricuatro, J. a. Farmer, Y. Bai, H.-P. Steinrück, J. M. Gottfried, and C. T. Campbell, "Formation of the calcium/poly(3-hexylthiophene) interface: structure and energetics.," *J. Am. Chem. Soc.*, vol. 131, pp. 13498–507, 2009.

[374] F. Bebensee, M. Schmid, H.-P. Steinrück, C. T. Campbell, and J. M. Gottfried, "Toward well-defined metal-polymer interfaces: temperature-controlled suppression of subsurface diffusion and reaction at the calcium/poly(3-hexylthiophene) interface.," *J. Am. Chem. Soc.*, vol. 132, pp. 12163–12165, 2010.

[375] F. Bebensee, J. Zhu, J. H. Baricuatro, J. a. Farmer, Y. Bai, H.-P. Steinrück, C. T. Campbell, and J. M. Gottfried, "Interface formation between calcium and electron-irradiated poly(3-hexylthiophene).," *Langmuir*, vol. 26, pp. 9632–9639, 2010.

[376] P. W. M. Blom, M. J. M. de Jong, and M. G. van Munster, "Electric-field and temperature dependence of the hole mobility in poly(p-phenylene vinylene)," *Phys. Rev. B*, vol. 55, no. 2, p. R656, 1997.

[377] D. Natali and M. Caironi, "Charge injection in solution-processed organic field-effect transistors: Physics, models and characterization methods," *Adv. Mater.*, vol. 24, no. 11, pp. 1357–1387, 2012.

[378] G. F. a. Dibb, M.-A. Muth, T. Kirchartz, S. Engmann, H. Hoppe, G. Gobsch, M. Thelakkat, N. Blouin, S. Tierney, M. Carrasco-Orozco, J. R. Durrant, and J. Nelson, "Influence of doping on charge carrier collection in normal and inverted geometry polymer:fullerene solar cells," *Sci. Rep.*, vol. 3, pp. 1–7, 2013.

[379] J. Bisquert, T. Kirchartz, I. Mora-Seró, and G. Garcia-Belmonte, "Classification of solar cells according to mechanisms of charge separation and charge collection," *Phys. Chem. Chem. Phys.*, 2015.

[380] M. O. Reese, A. M. Nardes, B. L. Rupert, R. E. Larsen, D. C. Olson, M. T. Lloyd, S. E. Shaheen, D. S. Ginley, G. Rumbles, and N. Kopidakis, "Photoinduced Degradation of Polymer and Polymer-Fullerene Active Layers: Experiment and Theory," *Adv. Funct. Mater.*, vol. 20, no. 20, pp. 3476–3483.

[381] G. Amarandei, C. O'Dwyer, a. Arshak, and D. Corcoran, "The stability of thin polymer films as controlled by changes in uniformly sputtered gold," *Soft Matter*, pp. 2695–2702, 2013.

[382] G. Amarandei, I. Clancy, A. Arshak, and D. Corcoran, "Stability of Ultrathin Nanocomposite Polymer Films Controlled by the Embedding of Gold Nanoparticles," 2014.

[383] V. E. Ferry, J. N. Munday, and H. A. Atwater, "Design Considerations for Plasmonic Photovoltaics," *Adv. Mater.*, vol. 22, no. 43, pp. 4794–4808, 2010.

[384] H. A. Atwater and A. Polman, "Plasmonics for improved photovoltaic devices," *Nat. Mater.*, vol. 9, no. 3, pp. 205–213, 2010.

[385] Q. Gan, F. J. Bartoli, and Z. H. Kafafi, "Plasmonic-enhanced organic photovoltaics: Breaking the 10% efficiency barrier," *Adv. Mater.*, vol. 25, no. 17, pp. 2385–2396, 2013.

[386] M. Xue, L. Li, B. J. Tremolet De Villers, H. Shen, J. Zhu, Z. Yu, A. Z. Stieg, Q. Pei, B. J. Schwartz, and K. L. Wang, "Charge-carrier dynamics in hybrid plasmonic organic solar cells with Ag nanoparticles," *Appl. Phys. Lett.*, vol. 98, p. 253302, 2011.

[387] S. Ahn, W. Jang, J. H. Park, and D. H. Wang, "Enhanced performance of layer-evolved bulk-heterojunction solar cells with Ag nanoparticles by sequential deposition," *Org. Electron.*, vol. 24, pp. 325–329, 2015.

[388] S. K. Ghosh and T. Pal, "Interparticle Coupling Effect on the Surface Plasmon Resonance of Gold Nanoparticles: From Theory to Applications," *Chem. Rev.*, vol. 107, no. 11, pp. 4797–4862, 2007.

[389] M. Geng, Y. Zhang, Q. Huang, B. Zhang, Q. Li, W. Li, and J. Li, "Functionalization of C60 with gold nanoparticles," *Carbon N. Y.*, vol. 48, pp. 3570–3574, 2010.

[390] H.-L. Yip and A. K.-Y. Jen, "Recent advances in solution-processed interfacial materials for efficient and stable polymer solar cells," *Energy Environ. Sci.*, vol. 5, no. 3, p. 5994, 2012.

[391] W. J. E. Beek, M. M. Wienk, M. Kemerink, X. Yang, and R. A. J. Janssen, "Hybrid zinc oxide conjugated polymer bulk heterojunction solar cells.," *J. Phys. Chem. B*, vol. 109, no. 19, pp. 9505–9516, 2005.

[392] C. M. Snowden, *Semiconductor Device Modeling*. Springer, 1989.

[393] J. C. Scott and G. G. Malliaras, "Charge injection and recombination at the metal-organic interface," *Chem. Phys. Lett.*, vol. 299, no. 2, pp. 115–119, 1999.

[394] Y.-P. Zhao, G.-C. Wang, T.-M. Lu, G. Palasantzas, and J. De Hosson, "Surface-roughness effect on capacitance and leakage current of an insulating film," *Phys. Rev. B*, vol. 60, no. 12, pp. 9157–9164, 1999.